Design and Operation of Tidal Arrays in Channels

Lei Chen

St Anne's College

University of Oxford

A thesis submitted for the degree of

Doctor of Philosophy in Engineering Science

Trinity 2019

Acknowledgements

Firstly, I would like to thank my supervisor Prof. Thomas Adcock for his supervision and all of his support over the past few years. During the course of this DPhil, his constant and patient guidance has led to many insightful talks and discussions, which advanced both this research and my learning on the subject of tidal energy. With his expertise and suggestions, I was able to overcome many challenges within the project and complete my thesis. I am grateful to the additional oversight provided by Dr. Paul Bonar and Dr. Christopher Vogel who shared their knowledge and feedback as well, which helped tremendously with my understanding of some key concepts and ideas. I must also thank my examiners Dr. Takafumi Nishino and Prof. Alistair Borthwick for their final review of my thesis contents and insightful examination.

Furthermore, I want to extend my thanks to my colleagues in the Tidal Energy Research Group and in Jenkin Room 11. In particular, the support and friendship of Tuo Wang, Bowen Cao, Andrea Schnabl, Tim Tang, Tracy Liang and Qian Ma have been invaluable to my time here at Oxford. The friendly environment at the office and the technical support from the Advanced Research Computing group have made many long days and nights of running simulations there bearable.

Lastly, I would like to thank my family, especially my parents, without whom I would not be here. Their emotional support from a long distance away has always been a large source of my strength and I look forward to them seeing the completion of my DPhil.

Abstract

Tidal currents are a promising source of clean and renewable power in many locations worldwide. In channels with suitable bathymetric conditions for strong currents, arrays of tidal stream turbines have been proposed as a useful method for generating energy. The modelling of tidal arrays is complicated, involving multiple spatial and temporal scales. The large scale deployment of tidal turbines will greatly alter the surrounding flow field, making resource assessment difficult and also complicating the design and operation ('tuning') of tidal turbine arrays. This thesis presents a tidal turbine model that is used to explore the interaction between power extraction devices and tidal flows. The resulting knowledge is used to inform different designs and operational strategies for tidal turbine arrays.

As an introductory work, a model of the Bohai Sea in China is considered. Flow is simulated through the strait using a depth-averaged numerical model and tidal arrays are introduced using an idealised actuator disc model, while turbine arrangement strategies are considered with the goal of maximising the available power to the array. The results of this study have served to direct the focus of the research to the investigation of a more realistic turbine representation and different tuning strategies for array optimisation.

A blockage-corrected blade element momentum theory is implemented to capture more accurately the performance of the tidal turbine. The implementation procedure and key limitations are discussed. A more realistic tidal rotor turbine representation is then used to examine both full-width and partial-width tidal arrays placed within idealised analytical and numerical channel domains. Analysis is undertaken to re-examine and expand on existing theoretical work.

Notable results from this research include the reduced significance of tuning for tidal rotors as compared to actuator discs. This is true for

both temporally fixed and varying tuning strategies, thus suggesting simpler operational strategies to be sufficient as well as more cost-efficient. As well, the maximum amount of power produced by tidal rotors, averaged over the tidal cycle, is typically 60–70% of that produced by actuator discs. This range can potentially serve as a useful correction factor generally applicable to present and future resource assessments of candidate tidal sites.

Finally, through analysis of the optimal arrangement for partial-width arrays under oscillatory flow and the significance of the local blockage effect, it is revealed that the two-scale theory, though appropriate for a majority of realistic turbine deployments, may underestimate the available power in certain flow conditions where the inertia of the flow becomes important. It is hoped that the present results will assist marine energy developers in selecting suitable models with which to determine optimal operation and arrangements for tidal stream turbines and to estimate the amount of tidal energy resource available.

Contents

Nomenclature

Symbol	Unit	Definition
A_C	m^2	Area of channel cross-section
A_D	m^2	Swept area of turbine
A_T	minutes	Actuation time
a_0	m	Amplitude of tidal forcing
a_2	-	Axial induction factor
a_4	-	Wake induction factor
a'_2	-	Tangential induction factor
b_4	-	Wake bypass induction factor
B	-	Blockage ratio
B_A	-	Array blockage ratio
B_G	-	Global blockage ratio
B_L	-	Local blockage ratio
B_r	-	Design rotor blockage ratio
c	m	Chord length of blade section
	m/s	or characteristic wave speed
c_x	-	Local thrust coefficient
C_d	-	Bed friction coefficient
C_D	-	Sectional drag coefficient
C_L	-	Sectional lift coefficient
C_P	-	Power coefficient
C_{PG}	-	Global power coefficient
C_T	-	Thrust coefficient
C_{TG}	-	Global thrust coefficient
D	m	Diameter of turbine
F	-	Tip correction factor
Fr	-	Froude number
g	m/s^2	Gravitational acceleration
h	m	Depth of channel/still water
H	m	Total water depth ($H = h + \xi$)
I	-	Inter-spacing of tuning parameters
k	-	Local resistance coefficient
L	km	Length of channel
m	-	Wake mixing rate
N_R	-	Number of rows
N_R^*	-	Normalised number of rows
n	-	Number of devices in a row
		or number of blades
		or number of sub-tidal cycles
p	N/m^2	Static pressure
P_{av}	MW	Available power

$P_{av,rated}$	MW	Designated rated power
$P_{av,cap}$	-	Normalised rated power
P_{ex}	MW	Extractable power
Q	m^3/s	Flow rate
Q'	-	Non-dimensionalised flow rate
r	m	Spanwise distance along blade section
δr	m	Width of annular ring
R	m	Disc or rotor radius
Re	-	Reynolds number
s	m	Tip to tip spacing
t	s	Time
t'	-	Non-dimensionalised time
T	N	Thrust
	h	or tidal period
TSR	-	Tip speed ratio
u	m/s	Axial inflow velocity
w	m	Width of channel
W	m/s	Relative inflow velocity
X	N	Confining force
x, y	m	Channel stream- and span-wise distance
z_0	mm	Bed roughness length
Z	-	Available tuning parameter options
α	$^\circ$	Angle of attack
α_2	-	Local velocity factor
α_4	-	Wake velocity factor
β	$^\circ$	Blade pitch angle
β_a	$^\circ$	Adjustable blade pitch angle
β_d	$^\circ$	Design blade pitch angle
β_4	-	Wake bypass velocity factor
γ	-	Dimensionless power multiplier
η	-	Basin efficiency
λ_0	-	Natural dynamic balance
λ_1	-	Turbine drag term
ν_T	-	Eddy viscosity coefficient
ξ	m	Elevation of the free surface
ρ	kg/m^3	Fluid density
σ	-	Blade solidity
τ	Nm	Torque
ϕ	$^\circ$	Inflow angle
	$^\circ$	or phase difference between fluid flow
ω	rad/s	Angular velocity of rotor
ω_0	s^{-1}	Frequency of tidal forcing
κ	-	von Kármán constant
Θ	-	Number of actuation points

Abbreviations/Acronyms

Abbreviations	Meaning
AD	Actuator disc
AL	Actuator line
ADCIRC	ADvanced CIRCulation
BEM	Blade element momentum
BC-BEMT	Blockage corrected-Blade element momentum theory
BR	Blade resolved
CFD	Computational Fluid Dynamics
CFL	Courant–Friedrichs–Lewy
DG	Discontinuous Galerkin
FP	Fixed Pitch
LES	Large Eddy Simulation
RANS	Reynolds-averaged Navier–Stokes
RANS-BE	Reynolds-averaged Navier–Stokes embeded Blade Element
RK	Runge–Kutta
SWEs	Shallow water equations
UK	United Kingdom
VP	Variable Pitch

Chapter 1

Introduction

The development of various renewable energy technologies is a point of focus in current research around the world. The key driver for this is the environmental pollution caused by our over-dependence on traditional energy resources. Unlike many alternatives, tidal stream power can be much more predictable (however localised or intermittent they may be), making tidal energy an attractive source of alternative clean energy that has much potential for development. This is especially true in locations featuring high current speeds due to particular geometrical features, such as many well-known tidal channels and headland sites around the UK (Adcock et al., 2013). In addition, such offshore technologies may be even more preferable for coastal cities with a higher population density and intensive land use, such as Zhejiang, China (Wu et al., 2017). Over the last two decades, the interest and attention from governments, industrialists and academics in exploiting this energy resource have grown worldwide.

The magnitude of the commercially extractable tidal stream resource is an important question. This needs to be understood before sites, or the technology as a whole, can be developed. The resource assessment is complicated by the interaction between the turbines and the flow field of the tide, and the dynamic and complex composition of the tidal current itself (Vennell et al., 2015). A balance of the force driving and the resistance to the tidal flow determines the velocity through a tur-

bine, and this in turn determines the power available to a turbine in a tidal system. Large-scale understanding of the tidal dynamics is required for resource assessment and this is only feasible through numerical modelling. Approaches for estimating the available tidal resource at candidate sites are continually developing, aiming to capture the interactions between turbines and tides at relevant scales while still being computationally cost-efficient. Depending on the scale of interest, such a task can usually be achieved with 3D or 2D hydrodynamic models. The former are able to model detailed flow characteristics to analyse the performance of turbines at the scale of an individual device or for a group of turbines, while the latter are more suitable for the analysis of long-term time series of tidal dynamics and their response to the extraction of tidal energy at the scale of the basin. A connected challenge is posed by the requirement to find the optimal array layout and operation strategy for a large array of tidal turbines as they exhibit interactions with the tidal flow in complex ways across multiple scales (Adcock et al., 2015). Thus, considering the great computational effort and cost required, simple 2D numerical models with an idealised domain or lower-order analytical models that describe the leading order physics of array performance in ideal scenarios are preferred.

Many existing theories and works have provided important insights into such topics, but are, to a certain extent, limited by an over-simplistic turbine representation. The widely adopted actuator disc offers only an idealised description of turbine performance, and is expected to provide an overestimation of the power that would be available to an actual turbine. Moreover, as the actuator disc does not account for the characteristics of the turbine blades, it cannot be used to compare between different rotor designs or to capture the realistic turbine behaviour with different operational conditions (Hau and von Renouard, 2003). This thesis uses a more realistic turbine model from which the results are compared to those using the widely-used actuator disc theory.

1.1 Aim and Objectives

The aim of this thesis is to provide new understanding into the complicated problem of optimally designing and operating large arrays of tidal stream turbines for maximum power capture with the implementation of a more realistic turbine representation as an alternative to the frequently used actuator disc. Existing theory and work is further explored and extended both analytically and numerically. Additionally, practical significance of tidal stream power both in terms of resource assessment and the hydrodynamic effects of tidal arrays with their consequential influence on design and operation are re-examined. This research has the following objectives of:

- Exploring the challenging problem of large tidal array optimisation in a real site and identifying key power extraction processes and flow physics that could be major contributors to performance enhancement;
- Implementing a more realistic turbine representation and studying its potential impact on the resource assessment as well as the decision of design and operation strategies;
- Examining the importance of turbine tuning, with the more realistic turbine representation, for varying channel dynamics and array sizes with different tuning strategies, and the impact of tuning on the optimal turbine arrangement; and
- Determining the optimal design of tidal array layout, with the more realistic turbine representation, to enhance power extraction at the basin scale under oscillatory flow conditions, with a focus on the arrangement strategy that maximises local blockage effects.

1.2 Thesis Overview

This thesis is divided into a total of nine chapters. The present chapter outlines the motivation, aim and structure of the thesis. The context of the research is presented in Chapter 2, including a review on the basic principles and development of the tidal stream power resource and its associated technologies, deeper insights into the tidal stream potential of specific sites of interest, and general discussions on various analytical, numerical and experimental techniques for tidal stream power resource assessment. A particular challenge of the present thesis is that the interactions between the turbines and the flow must be modelled over a wide range of length scales — key works across all these scales are introduced.

It has been suggested in previous literature that the optimal array design of a large number of tidal stream turbines for the purpose of maximising their available power in real site has always remained unclear. To better understand the difficulties of optimising turbine deployment, a case study of China's Bohai Sea is undertaken in Chapter 3. A numerical model with detailed calibration and validation is constructed to simulate flow and to explore array design strategies near the Bohai Strait. This study highlights several key physical effects that affect the optimal arrangement, though it is difficult to isolate them in a real site and thus draw useful, general conclusions on array design.

Recognising this, the following chapters focus on idealised domains, where the underlying physics and leading order behaviour of the key physical effects are examined in isolation and in greater detail. Given the highly idealised actuator discs adopted in Chapter 3, a more realistic turbine representation of tidal rotors is introduced in Chapter 4 with a thorough discussion of the implementation and inherent limitations of the model. In Chapter 5, three different tuning strategies are developed for full-width arrays and then extended to incorporate the alternative turbine representation with fixed-pitch and variable-pitch devices. The relative importance

of tuning is examined by considering the results obtained from various conditions of blockage, turbine deployment, and channel dynamics. The accuracy of the actuator disc model, in terms of power estimation, when compared to the more realistic tidal rotor is then analysed for different tuning strategies. Additionally, recommendations are given for the design of tidal stream turbines at basin scale.

However, restrictions on array design may be imposed by other, conflicting uses of the channel, such as shipping. Therefore, a number of more practical arrangements in which the channel is only partially blocked by the turbine array are investigated within different channel dynamics in Chapter 6 to provide a more comprehensive look at the effects of local blockage on tidal turbine array performance. By embedding the partial-width turbine array model into a larger channel model, the predictions from the analytical approach are compared to the numerical simulations. Furthermore, an idealised numerical channel model using the shallow water equations is constructed in Chapter 7 to reassess the practical significance of local blockage effects with a realistic turbine representation and modelling extensions such as the addition of multiple turbine rows. The advanced temporally varying tuning strategy introduced in Chapter 5 has only been explored with a zero-dimensional channel model while the partial-width array in Chapters 6 and 7 has only been explored with the temporally fixed tuning strategy. Therefore Chapter 8 examines the significance of the more advanced tuning strategy with a two-dimensional numerical channel model for a range of fully and partially blocked channel configurations, along with consideration of its impact on the optimal turbine arrangement.

Finally, a summary of the main findings and a discussion of the potential implications of this work for one of the most well-known tidal energy candidate sites are presented in Chapter 9, as well as the possibilities of future extension on this subject. In addition, Appendices A, B and C respectively present an exploration of power capping as an extension to Chapter 5, a detailed discussion of the implica-

tions of Chapter 9 for actual tidal stream power sites (with a focus on the Pentland Firth, UK), and a list of publications from this thesis.

Chapter 2

Modelling of Tidal Stream Energy Extraction

A large amount of research has already been undertaken to tackle the challenges in modelling tidal turbine arrays and accurately capture the interactions between the turbines and the tides at three principal scales. Understanding the mechanics of the fluid through and around individual turbines at the device scale, the additional inter-turbine effects through interactions with fluid flow at the array scale, and the further complications due to realistic bathymetry and tidal forcing at the basin scale are all crucial to ensure a profitable development plan and deliver performance as planned. To simplify the complex modelling problem of multi-scale fluid behaviour, assumptions and compromises are made in the attempt to study simpler, decoupled interactions between flow and turbines over a reasonable computational timescale.

In this chapter, an introductory review on the formation of tides and existing tidal energy technologies is presented in Sections 2.1 and 2.2, respectively. For the purpose of this thesis and specifically the work undertaken in Chapter 3, a brief analysis of tidal stream energy sites in China is discussed in Section 2.3. Following the general discussion, more detailed review of previous key and informative work is considered by separating models in terms of their type, whether they are analytical

(Section 2.4) or numerical and experimental (Section 2.5). Within each modelling review, the sections are also separated by the model scale into the aforementioned scales of the device, array and basin.

2.1 Formation of Tides

The relationship between oceanic tides and the movement of celestial bodies has been studied for centuries, with both the Sun and the Moon playing key roles in this interaction. As the two celestial bodies move relative to the Earth, temporal variations in gravitational forces lead to oscillations in the water level on the surface of the Earth (Wright et al., 1999). Considering only an Earth-Moon system, the largest gravitational force on Earth is experienced at the shortest distance between the two bodies, while the largest centrifugal force, from the rotation around the mass centroid of the two body system, is felt on the opposite end (Pugh, 1987). These forces are balanced by the water deforming above mean sea level at regions both closest and furthest away from the Moon. For a stationary observer on Earth, the Moon takes 24 hours and 50 minutes to completely rotate relative to Earth; over this time, two 'bulges' in water level occur over a single location, making the period of the resulting wave half the lunar day. This is the principal lunar semi-diurnal tide, M_2, and is typically the largest constituent of oceanic tides. However, this simplified two-body model tends to underestimate the amplitude of the tides as it neglects the effect of the other contributing celestial bodies. One such contributor is the similar, but weaker, phenomenon occurring between the Sun and the Earth, which leads to the principal solar semi-diurnal constituent S_2.

When the Sun and the Moon are aligned, their effect is constructive, leading to higher water levels in line with the Sun-Moon axis — this phenomenon is known as a 'spring tide'. In contrast, when the Sun and the Moon are at 90° in relation to the Earth, there is destructive interference between the generated tides and this leads to

a ‘neap tide’. The period over which this variation occurs is related to the amount of time it takes for the Moon to rotate around the Earth, which is 29.5 days. Over a lunar month, there will be two instances of both spring and neap tides, with the length between successive tidal extremes approximately 14 days long.

Further complexities are introduced when the model departs from an idealised Sun, Moon and Earth system, and the influence of other celestial bodies, ocean bathymetry, continents, bed friction and Coriolis effects are accounted for. As a result of these factors, there are significant variations between the tidal ranges around the world from the reflection and shoaling of waves around the continental shelf. Tides are also amplified within channels and inlets due to interference between incoming and reflected components, and the narrowing constriction and resonance between the inlet and the deep ocean (Marshall and Plumb, 1989). The effective extraction of energy at these locations requires an understanding of how the system responds in relation to changes introduced by implemented tidal energy devices, as this will affect the optimum choice of technology and its operation. See Pugh (1987) for more information on the generation of tides on Earth.

2.2 Tidal Energy Technologies

There are two main approaches to extract power from tides — tidal range technologies and tidal stream technologies. The former extracts the potential energy from the hydraulic head difference between flood and ebb tide levels, much in the same way as hydro dams operate in rivers. The latter, which is the focus of the thesis, exploits the energy from rapidly moving tidal streams in a manner superficially similar to wind energy, although with important differences as discussed in this chapter.

Tidal energy extraction dates back many years, with tidal barrages being a particular well-established and understood tidal range technology. One such application is the La Rance power plant in France, the first commercial-scale tidal range

structure dating back over 40 years. This plant provides 240 MW of generating capacity to meet 0.12% of France's annual energy demands (Rourke et al., 2010). Whilst this technology is well understood, there is a high capital and environmental cost required to dam an estuary at a commercially viable scale. Such technologies also risk disrupting the natural sediment and nutrient transportation, and interrupting aquatic migration patterns (Hooper and Austen, 2013; Rourke et al., 2010). More recent tidal energy plans have focused on tidal stream devices due to their reduced environmental impact when compared to tidal barrages. Tidal stream devices work in a similar fashion to wind power where a device, commonly a turbine, is placed directly in locations that have relatively high-speed tidal flows in order to extract power. Accordingly, the technology used in tidal stream power generation has largely followed the development of wind energy systems, with the refinement of the design tackling problems that are unique to underwater application.

Tidal stream devices can be further categorised into two main types — axial flow and cross flow turbines (although other device types, such as oscillating hydrofoil devices, have been considered) (Adcock et al., 2015). Similar to the Darrieus wind turbine, cross flow devices extract energy from flow that is perpendicular to the axis of rotation. The nature of these devices allows them to occupy a greater area of a channel cross-section, but this advantage of high 'blockage' is offset by their relatively low hydrodynamic efficiency when compared to axial devices. This results from two main contributors: firstly as the blades rotate, a significant portion of each rotation positions the blades at an unfavourable angle of attack; secondly, unsteady loading occurs during the period of rotation where the blades are moving against the flow as they pass through the wakes of the other blades. Both these processes occur for a significant portion of each rotation, contributing to undesirable hydrodynamic efficiency and opposing drag (Muchala, 2018). Some examples of cross flow turbines include the Transverse Horizontal Axis Water Turbine (THAWT) concept

developed at the University of Oxford (McAdam, 2011) and the TidGen device by the Ocean Renewable Power Company.

Whilst the technology of tidal stream turbines is still currently in the early stages and no single device has emerged as superior, axial flow turbines are, perhaps, the furthest developed devices (Borthwick, 2016). The reason for this is partially due to the technology's overlap with the widely adopted axial wind turbine, which extracts energy as currents flow past the blades and generate lift forces, causing the blades to rotate. An example of a prototype device is the two 16-m diameter 'SeaGen' turbines designed by Marine Current Turbines (Douglas et al., 2008), which have been successfully tested in Strangford Lough in 2008 with a rated power of 1.2 MW. Successful testing of these devices has driven the investigation into larger deployments by companies like MeyGen, who have the approval for the phase 1 installation of an 86-MW tidal turbine array (MeyGen Ltd., 2014). Given the success of the axial flow turbine, these devices will be the focus for the remainder of this thesis, though many of the results may be relevant to other types of turbines.

2.3 Review of Tidal Stream Resources

Globally, the exploitation of tidal energy resources is restricted to select locations that have suitably high tidal stream velocities, such as the UK, Canada and New Zealand (Adcock et al., 2013; Pearce, 2005; Vennell and Adcock, 2014). Investment into tidal stream technologies is dependent upon the results of resource assessments, which provide a time-dependent prediction of power output at ideal tidal sites. Uihlein and Magagna (2016) have made an effort to summarise the resource assessments in several countries around the world, making progress in their global documentation. In China, a number of studies have also been commissioned in recent years to quantify the tidal resource available at various candidate sites. To demonstrate its magnitude at the scale of a nation, a brief study of the Chinese tidal

energy resource is presented.

2.3.1 Sites of interest in China

As a geographical region, China shares approximately 18,000 km of coastline with four seas in the western side of the North Pacific Ocean — the South China Sea, East China Sea, Yellow Sea, and the Bohai Sea. Tidal currents in the coastal regions of these seas can exceed 2 m/s during spring tides due to the shape of the landmass in the area (e.g. numerous islands), and this level of current velocity has been suggested as an acceptable threshold for the development of tidal stream devices (Adcock et al., 2015). The realisation of this prospect has prompted the government of China to support research investigations into tidal stream energy in the coastal regions surrounding China (Zheng et al., 2015).

Commonly, tidal stream resource assessments fall under two classifications: field measurements and simulations (analytical or numerical). Whilst a costly exercise, field data assessments provide a direct methodology for obtaining average velocity and mean kinetic energy flux measurements, which are the key data for tidal energy assessments. Beginning in the mid-1900s, a total of four national surveys have been conducted in China regarding the exploitation of tidal energy and the relevant resource assessments that would need to be performed (Wu et al., 2017). The first of these surveys, held in 1958, led to the implementation of several small-scale power plants that employed the usage of tidal barrages. However, due to undeveloped and inappropriate design and operation skills, the facilities were deemed a failure and operations ceased (Li et al., 2010). Following this, another survey was carried out in 1989. Based on a preliminary assessment from this survey, two special funds later emerged in 2004 and 2010, respectively titled the 'Marine Comprehensive Investigation and Assessment in China (MCIAC)' and the 'Marine Energy Special Fund (MESF)' (Wu et al., 2017). As a result of these surveys and

funds, tidal current characteristics such as spatial and temporal variations in major channels in China were observed, analysed and recorded in an attempt to examine potential sites for tidal power extraction. Most notably, it was found that the highest velocity of tidal currents exists in the East China Sea, followed by the Bohai and Yellow Seas, and then the South China Sea (Zhang et al., 2014b). However, variations in the flow field due to the complex bathymetry of the seas can cause the full resolution of the flow from solely field measurements to be both difficult and impractical. Therefore, site assessments based on analytical and numerical simulations are required in order to model the entire area of interest at a reasonable cost. These assessments typically include an analysis of the interaction between the flow and tidal array as well as the environmental impact resulting from the extraction of energy. Studies carried out on the East China Sea and the Bohai Sea are reviewed below.

2.3.1.1 East China Sea

The coast of the East China Sea has strong tidal currents, dominated by a semi-diurnal tide regime (Larsen et al., 1985). A number of sites in the East China Sea have measured current velocities of approximately 3-4 m/s (Li et al., 2010), such as the Hangzhou Bay, Zhoushan Archipelago, and some coastal areas near the provinces of Zhejiang and Fujian. Of these locations, the Zhoushan Archipelago contains several channels that showcase the strongest tidal current data. In particular, the channels of Xihoumen, Guanmen, Guishan, and Jintang are said to have the most plentiful marine energy resource in all the coastal areas around China (Xu et al., 2016), with average maximum flow velocities reaching 3.7 m/s (Wu et al., 2017). Thus, these sites offer significant potential for the harnessing of tidal current power.

The first studies on the tidal characteristics of the Zhoushan Archipelago stem from the 1989 national survey, which has since been followed by another study of

the tidal current energy distribution approximately 20 years later (Xu et al., 2016). Wang et al. (2010) claimed that a total of 8.46 MW of power can be extracted from the tidal stream in the Guishan Channel, and that the exploitation of both the Guanmen and Gaoting Channels by extracting the maximum available tidal energy would be able to support 6-7% of Zhoushan City's electrical energy needs in 2005 (Hou et al., 2015). Nevertheless, these numbers are largely based on analytical calculation methods with insufficient considerations of various realistic properties, such as the spatially varying bathymetry and tidal flow, and thus are not sufficient to meet all the needs of actual, realistic projects (Yu et al., 2017).

More recently, in 2014, Hou et al. (2015) created a 2D Finite Volume Coastal Ocean Model (FVCOM) for the purpose of numerical modelling. Specifically in Zhoushan, multiple in-stream turbine rows were analysed to calculate a total extractable tidal energy of 10.2 MW in the Hangmen Channel. Subsequently, in 2016, Xu et al. (2016) used a high-resolution Regional Ocean Modelling System (ROMS) to perform an assessment of the different channels in the Zhoushan Archipelago, while taking into consideration a comparison of their currents and turbulent kinetic energy. The results from this study also conclude that the Guishan Channel is the best area in the Zhoushan Archipelago for the purpose of tidal energy extraction.

2.3.1.2 Bohai Sea

In comparison with the East China Sea, the Bohai Sea has both diurnal and semi-diurnal tides, with velocities in the approximate range of 0.5-1 m/s (Li et al., 2010). In most areas in the Bohai region, the velocity of tidal currents is less than 0.77 m/s; the only exception lies in certain water channels in the Bohai Strait, which is a body of water connecting the Bohai Sea to the Yellow Sea, as high current velocities that exist in the range of 3.6-4.2 m/s can be seen around Laotieshan, located at the north end of the strait (Zhang et al., 2014b). The Bohai Strait is a broad passage, approximately 90 km in length and 19 m in average depth, which

is further separated into a number of channels by small islands. With the division into these smaller channels, the velocity of tidal flow can be significantly increased (Yang et al., 2011). Even though the hydrodynamic and hydrographic conditions of the Bohai Gulf have been studied extensively (Bian et al., 2016; Fang et al., 2004; Li et al., 2016; Zhang et al., 2014a), only a few preliminary studies have been performed on the Chengshantou Cape and Laotieshan Channel in their unexploited state (i.e. no turbine implementation) (Wu et al., 2011, 2010), while no studies to the present author's knowledge have examined the corresponding available tidal stream power and possible turbine arrangements until Chapter 3 of this thesis.

2.4 Low-Order Hydrodynamic Models

Both analytical and numerical modelling of tidal energy systems have been used extensively in recent years with the goal of understanding the underlying physics of tidal devices and the hydrodynamic response to energy extraction. Although detailed numerical models (discussed in Section 2.5) may provide more accurate solutions to specific features of tidal arrays, it is often the case that simple theoretical models provide the most useful insights into the power extraction process with mathematical simplicity and minimal computational cost. As such, a variety of analytical models have been utilised to understand how tidal energy devices interact with the tidal resource. In this section, recent theoretical models of tidal turbines are reviewed for the three different scales of the device, array and basin (see Adcock et al., 2015).

2.4.1 Device scale

The modelling of a single energy extraction device focusing on any specific aspect of a tidal turbine, such as the performance of a specific rotor design, is considered to be at the device scale. Device-scale modelling tends to be the basis of models at the larger array and basin scales.

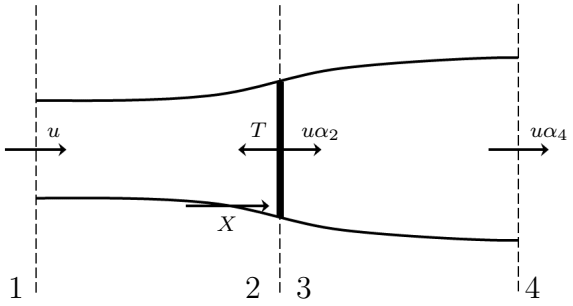

Figure 2.1: Side/plan view for a classic actuator disc model of a turbine in unbounded flow, adapted from Houlsby et al. (2008).

2.4.1.1 Unbounded actuator disc model

The actuator disc theory provides a simplified description of an axial flow turbine by representing a rotor, which comprises a number of blades rotating about a central hub, as a simple porous disc that presents a uniform resistance to the passing flow. This theory was first used by Rankine (1865) and Edmund Froude (1889) to gain insights into the flow field around a driving ship propeller, followed by Joukowsky (1920) and Betz (1920) who independently modified it to investigate wind turbine performance. In the present thesis, the nomenclature of Houlsby et al. (2008) is used to study tidal turbines. Figure 2.1 presents the four defined stations in a laterally unbounded flow: station 1 at a location far upstream of the disc, stations 2 and 3 at locations immediately upstream and downstream of the disc respectively, and station 4 at a location sufficiently downstream of the disc that the static pressure in the wake is equalised whereas the velocity is not. This model assumes a uniform 'core flow' that passes through the disc, encased by a uniform 'bypass flow'. Streamlines between these two flows illustrate the axisymmetric flow expansion as it passes through the turbine. As such, the mass flux is conserved within the core flow streamtube such that:

$$A_1 u = (A_D u_2 = A_D u\alpha_2) = (A_4 u_4 = A_4 u\alpha_4), \tag{2.1}$$

where A, u and α denote cross-sectional area, axial flow velocity and velocity factor, respectively, and the subscripts indicate different stations (D for the disc plane between stations 2 and 3). The velocity factor α_n is a measure of the remaining upstream flow velocity at its denoted station, and another common quantifier used in literature as well as this thesis is the induction factor $a_n = 1 - \alpha_n$. As derived from the equation, the induction factor represents the reduction in upstream velocity at its denoted station. Note that this model does not account for points beyond station 4 where turbulent mixing processes are assumed to occur as the streamlines become straight and parallel. A detailed account of the underlying theory can be found in the work of Burton et al. (2011).

In this analytical model, as the flow is assumed to be inviscid and incompressible with a constant cross-sectional area along the length of the domain, Bernoulli's equation can be considered both upstream and downstream of the disc where energy is conserved. Applying the conservation law to sections between stations 1 and 2 and stations 3 and 4 gives:

$$p + \frac{1}{2}\rho u^2 = p_2 + \frac{1}{2}\rho \left(u\alpha_2\right)^2, \;\; p_3 + \frac{1}{2}\rho \left(u\alpha_3\right)^2 = p + \frac{1}{2}\rho \left(u\alpha_4\right)^2, \tag{2.2}$$

where ρ is the fluid density and p is the static pressure with subscripts indicating different stations. Combining these equations gives an expression for the applied thrust, T:

$$p_2 - p_3 = \frac{T}{A_D} = \frac{1}{2}\rho u^2 \left(1 - \alpha_4^2\right). \tag{2.3}$$

The conservation of momentum is applied between stations 1 and 4 on the core flow streamtube to derive an alternative expression for T. This is expressed as follows:

$$T - X = \rho A_D u^2 \alpha_2 \left(1 - \alpha_4\right). \tag{2.4}$$

For the unbounded actuator disc model, the domain is assumed to be sufficiently

large relative to the size of the actuator disc that the device has no effect on the surrounding bypass flow. This implies that pressure can be treated as ambient outside the core flow, meaning that the forces in the model come entirely from the actuator disc. The force X is therefore negligible and omitted in Equation 2.4. Using this assumption, Equations 2.3 and 2.4 can be combined such that:

$$\alpha_2 = \frac{1 + \alpha_4}{2}. \tag{2.5}$$

With this relationship, the applied thrust T and removed power P, as well as the corresponding dimensionless coefficients C_T (ratio of T to the integrated upstream dynamic pressure $\frac{1}{2}\rho u^2 A_D$) and C_P (ratio of P to the upstream kinetic energy flux $\frac{1}{2}\rho u^3 A_D$), can be expressed in terms of a single parameter, α_4:

$$T = \frac{1}{2}\rho A_D u^2 \left(1 - \alpha_4^2\right) = \frac{1}{2}\rho A_D u^2 C_T, \tag{2.6}$$

$$P = Tu\alpha_2 = \frac{1}{2}\rho A_D u^3 \left(1 - \alpha_4^2\right)\left(\frac{1 + \alpha_4}{2}\right) = \frac{1}{2}\rho A_D u^3 C_P. \tag{2.7}$$

The Lanchester-Betz Limit is a result from the above derivations, which is generally applicable for wind turbines and states that, for a single device in isolation, the maximum percentage of kinetic energy that can be captured from the wind is $\approx$ 59.3%. This limit is achieved when a turbine operates such that the wind speed at the far wake is equal to one-third of the free-stream speed (i.e. $\alpha_4 = 1/3$).

2.4.1.2 Bounded actuator disc model

Having proven a useful tool for the analysis of wind turbines, it is reasonable to expect that the actuator disc theory can be used to investigate the performance of tidal turbines due to similarities between the two technologies, as they both remove momentum from axial flow (Draper, 2011). However, additional complexity is introduced into the theory given that the shallow water flow is constrained by a uniform free surface, channel bed and sidewalls, etc.

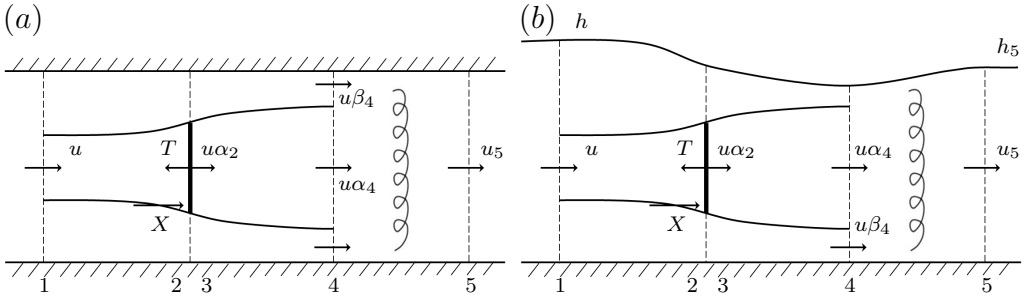

Figure 2.2: Side/plan view for a bounded actuator disc model of a turbine in: (a) rigid lid, and; (b) open channel flow, adapted from Houlsby et al. (2008).

The underlying assumptions of the bounded actuator disc model are similar to those of the unbounded case. However, due to the introduction of the flow boundaries, the assumptions of constant pressure around the core flow and a return to ambient pressure in the wake become invalid. In order to account for the effects introduced by blockage, Garrett and Cummins (2007) extended the actuator disc theory by replacing the unbounded flow field with the assumption of a volume-flux-constrained flow field, described as a 'rigid lid' (Figure 2.2a), which is a free surface that does not deform in response to energy extraction.

One of the key parameters introduced in this bounded disc model is the local blockage ratio B_L, which is defined as the ratio of turbine frontal area A_D to the cross-sectional area of its local flow passage (Nishino and Willden, 2012*b*). As the core streamtube expands, the confining (blockage) effects of the flow boundaries and adjacent turbines lead to a contraction of the bypass streamtube, which subsequently results in an increase in the bypass wake velocity and a reduction in the static pressure of bypass flow in order to conserve mass and energy, respectively. A wake bypass velocity factor, β_4, can be derived through geometric relationships between the streamtubes, which is expressed as:

$$\beta_4 = \frac{1 - B_L \alpha_2}{1 - B_L \left(\alpha_2 / \alpha_4\right)}. \tag{2.8}$$

In addition to the equations of conservation that describe the core flow (which are used for the unconfined model), Bernoulli's equation can also be applied along the bypass flow between stations 1 and 4 as no energy has been lost. Moreover, since the static pressure in the wake bypass flow can no longer be assumed ambient, the confining force term X in Equation 2.4 is not negligible and is now positive and finite for all B_L, as noted by Houlsby et al. (2008). These can be combined to show that α_2 is no longer a simple function of just α_4, but is now a function of both B_L and α_4 as expressed by:

$$\alpha_2 = \frac{1 + \alpha_4}{(1 + B_L) + \sqrt{(1 - B_L)^2 + B_L \left(1 - (1/\alpha_4)\right)^2}}. \tag{2.9}$$

Therefore for a given B_L, the turbine performance can be defined solely in terms of the parameter α_4, which is often referred to as the 'tuning parameter' for the resistance of the actuator disc. Investigations into device performance can be made through adjustments of α_4, in order to determine optimal parameters over a wide range of operation conditions. An interesting finding resulting from the confined model is that across all B_L, $\alpha_4 = 1/3$ still gives the maximum possible power coefficient (Draper, 2011), the equation for which is given as:

$$C_{P,max} = \frac{16}{27} \frac{1}{(1 - B_L)^2}. \tag{2.10}$$

An alternative expression for the tuning parameter is the local resistance coefficient k, which is related to α_2, α_4 and β_4 by using the local velocity at the disc, $u\alpha_2$, instead of relating thrust to the upstream velocity u. The expression for k is given by:

$$k = \frac{T}{\frac{1}{2}\rho A (u\alpha_2)^2} = \frac{\beta_4^2 - \alpha_4^2}{\alpha_2^2}. \tag{2.11}$$

Draper et al. (2014a) showed that the maximum C_P as a function of k is achieved

by tuning the turbines such that $k = 2(1 + B_L)^3/(1 - B_L)^2$, giving an optimal value of $k = 2$ for the unbounded flow case ($B_L = 0$), from which the well-known Betz limit is derived. This alternative tuning representation has the added advantage of relating the resistance coefficient to the geometry of a porous disc (Draper and Nishino, 2014; Whelan et al., 2009), providing a more physically intuitive description of disc porosity than α_4. For the actuator disc theory in the case where α_4 approaches zero, k will approach infinity.

As can be observed from Equation 2.10, the available power increases with blockage to provide a performance enhancement proportional to $(1 - B_L)^{-2}$. Physically, this blockage effect results from the confinement introduced by the flow boundaries on the bypass streamtube, generating a pressure gradient in the streamwise direction; this is balanced by an equivalent pressure gradient in the core streamtube. As a result, there is an increased difference in static pressure on either side of the disc, allowing more power to be extracted from the flow. It is therefore not surprising that the maximum C_P exceeds the Betz limit as the disc extracts power from both the kinetic flux and pressure head (Draper, 2011).

It is also anticipated that, at some point downstream of the turbine, the wake will completely remix with the bypass flow — for the purpose of this analysis, a section sufficiently far downstream from the disc is defined where complete mixing has taken place (station 5). Given that the process of wake remixing introduces additional and unavoidable energy losses, the power extracted by the disc (available power P_{av}) will not be equal to the total power removed from the flow (extractable power P_{ex}) (see definition by Adcock et al., 2013). As tidal energy is a finite and limited resource, the percentage of generated power from the total power removed from fluid flow is an important performance indicator for an energy extraction device. This is defined as basin efficiency η (Nishino and Willden, 2012*b*), which, to

the leading order, is also the ratio between the power and thrust coefficients:

$$\eta = \frac{P_{av}}{P_{ex}} = \frac{C_P}{C_T} = \alpha_2. \tag{2.12}$$

It is worth noting that $C_{P,max}$ is achieved with a basin efficiency of $\eta = 2/3(1 + B_L)$, implying that a turbine will extract more power, albeit less efficiently, at a high value of B_L. This is due to the greater mixing required by the increased difference in core and bypass flow velocities, caused by the larger thrust applied in the highly blocked flow. Thus, the relevant implications when assessing the power generated from rows of tidal turbines in a larger channel are noted in Section 2.4.3, where an overall consideration of C_T, C_P and η is essential for the performance optimisation. This consideration is explored in greater detail in Chapter 5 along with different operation strategies.

A limitation to this model is the rigid lid assumption, which does not allow for a change in depth along the channel and thus contradicts the spatial variation in hydrostatic pressure, as highlighted by Houlsby et al. (2008). Due to this limitation, the model is only applicable for a small Froude number ($Fr = u/\sqrt{gh}$, where h is the local water depth and g is the gravitational acceleration) to ensure that the change in surface elevation Δh corresponding to the energy extraction is sufficiently small compared to the total depth of the fluid (i.e. $\Delta h \ll h$). As blockage increases, this requirement tends to be harder to maintain due to the increased bypass flow speed resulting in a greater disturbance in water level.

In order to address this limitation, two extensions have been studied to refine the constrained actuator disc model in enabling the deformation of the free surface. The first, described by Whelan et al. (2009), permits the free surface to deform through the pressure drop across the rotor, allowing C_P to be expressed implicitly as a function of B_L, α_4 and upstream Fr. However, in this representation, downstream

wake mixing is ignored; as such, in the realistic case where the stream has a non-zero Froude number, basin efficiency cannot be determined and the relationship between upstream and downstream flow conditions cannot be accurately modelled.

The second extension was implemented by Houlsby et al. (2008), which effectively combined the volume-flux-constrained model of Garrett and Cummins (2007) and the free surface model of Whelan et al. (2009), resulting in a laterally constrained model that enables both downstream mixing and free surface deformation to be considered as shown in Figure 2.2*b*. This combined model accounts for both the reduction in water depth when energy is removed from a sub-critical flow and the corresponding increase in velocity (White, 2009). Furthermore, as with previous unbounded and bounded models, maximum power occurs at an optimal tuning of $\alpha_4 = 1/3$ for all B_L (Draper, 2011).

Similar to the rigid lid model, flow passing through the turbines experiences a loss of momentum as power is extracted. This momentum sink now leads to a change in water depth, given by (Houlsby et al., 2008):

$$\frac{1}{2}\left(\frac{\triangle h}{h}\right)^3 - \frac{3}{2}\left(\frac{\triangle h}{h}\right)^2 + \left(1 - Fr^2 + \frac{C_T B_L Fr^2}{2}\right)\left(\frac{\triangle h}{h}\right) - \frac{C_T B_L Fr^2}{2} = 0. \tag{2.13}$$

It should be noted that, as Fr of the flow decreases and Δh further reduces, the open channel model converges towards the rigid lid model. Practically, most candidate sites for tidal stream devices have a flow velocity around 2 m/s and the channel depth required is between 25-50 m (Lewis et al., 2015). This minimum depth may be obtained from the anticipated size of a turbine (diameter of $D = 15$ m) and the minimum allowable tip submersion depth required to allow shipping and prevent cavitation (specified as 8 m for MeyGen Ltd., 2014). The maximum depth is typically derived with consideration of installation and maintenance expenditures, especially in the case of bed mounted devices, for which both costs can be quite

substantial. The current velocity and channel depth requirements suggest that a value of $Fr \leq 0.15$ would generally be expected at real sites, which is supported by Black and Veatch (2005), who suggest that typical UK tidal resources have a Froude number of $0.1 \leq Fr \leq 0.2$. Furthermore, due to various practical constraints in the actual installation of turbines, it is likely that $B_L \leq 0.4$ in realistic scenarios (Flores Mateos, 2019). The combination of low Fr and moderate blockage suggests that, for most real candidate sites of interest, the flow tends to be exclusively subcritical and that the mathematically simpler rigid lid model may be an appropriate approximation to the open channel model.

Despite the wide application of actuator disc models in both analytical and numerical studies of wind and tidal stream power, a simple porous disc offers only an idealised description of turbine performance. This representation does not account for inner rotor mechanisms and is therefore expected to provide an overestimation of the power that would be available to an actual turbine. A more advanced approach utilising the blade element momentum theory (BEMT) has been derived to model a more realistic turbine representation without excessive computational cost. Though the BEMT was initially developed to analyse wind turbines and does not take into account blockage effects, Vogel et al. (2018) have extended the unbounded BEMT to incorporate volume-flux-constrained flow for use with tidal turbines. Referred to as the blockage-corrected blade element momentum theory (BC-BEMT), this derivation accounts for the static pressure difference in the flow passage that results from blockage. As an alternative turbine representation, the BC-BEMT model considered in later chapters of this thesis (beginning with its implementation and limitations discussed in Chapter 4) has provided a better understanding of the operation and performance of real tidal stream turbines.

2.4.2 Array scale

Analogous to the operation of wind farms, tidal turbines can also be implemented in groups of two or more to form tidal turbine arrays with the goal of increasing their power output. However, while turbine spacing in wind farms is generally selected to minimise interactions between devices, the same arrangement is impractical for tidal arrays due to the complex bathymetry of water channels, limited spacing constraints (Cooke, 2016). Instead, understanding the interactions between turbines to optimise their performance is a priority for the commercial development of a tidal array. This section considers steady channel flow only; oscillatory flow will be considered in Section 2.4.3.

Two types of array configurations are typically investigated to explore the optimum arrangement of tidal turbines at this scale: full-width arrays, where turbine rows are spread evenly across the channel width, and partial-width arrays, where the rows only span a fraction of the channel. In reality, the complete blockage of a channel cross-section with a full-width array is likely to be infeasible given requirements for shipping lanes and wildlife. Thus, partial-width arrays are considered a more realistic arrangement.

2.4.2.1 Two-scale separation model

In order to analyse the performance of partial-width arrays, the work of Garrett and Cummins (2007) has been extended by Nishino and Willden (2012*b*) to consider a two-scale actuator disc model. Similar to the individual device model, there is an array-scale core flow that is slowed by the combined thrust from the turbines and an array-scale bypass flow that is accelerated around the array to maintain the conservation of mass flux. As these two flows move at different speeds, array-scale wake mixing is introduced in a region downstream of the entire turbine array.

The two-scale model analyses the flow at two principal length scales for the case of the partial-width array. As shown in Figure 2.3, it is assumed that there is

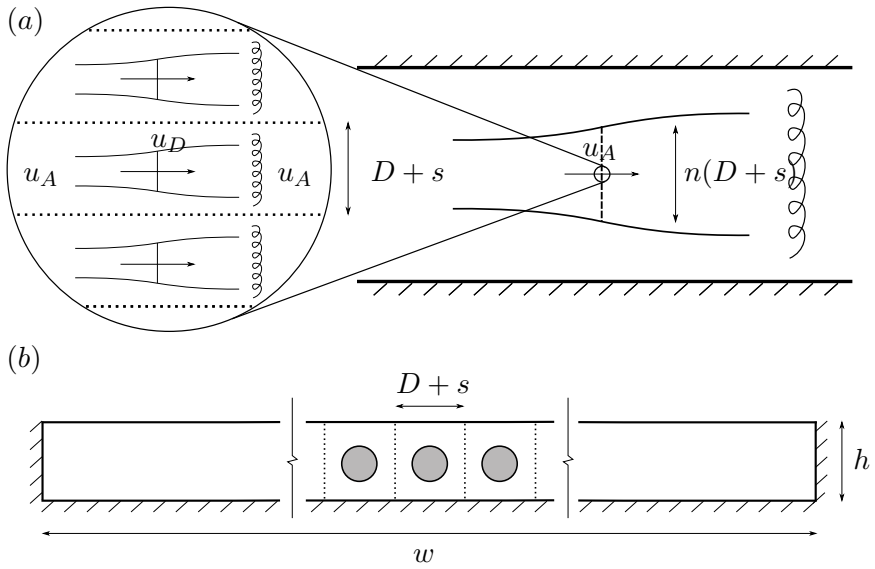

Figure 2.3: Schematic representation of the two-scale actuator disc model showing: (a) plan view of the device-scale (left) and array-scale (right) flows, and; (b) streamwise cross-sectional view of the partial-width tidal turbine array, adapted from Nishino and Willden (2012*b*).

an array of n identical turbines with diameter D and uniform tip to tip spacing s spread laterally in a single row. On the device-scale, localised flow is analysed as it passes through each turbine, while on the larger array-scale, flow is considered to pass through an array width of $n(D + s)$. Assuming that there is a sufficient number of turbines in the array ($n(D+s) \gg D$) and that the array-scale phenomena occur over a much longer space and time than the device-scale phenomena, Nishino and Willden (2012*b*) were able to introduce a concept of scale separation. They proposed the replication of the device-scale model into the larger scale of the array while keeping the same model for device-scale, forming two loosely-coupled disc models at different flow scales, in order to investigate the optimal arrangement and operation of partial-width arrays. The model requires that the array length scale is sufficiently large to allow velocity and hydrostatic pressure recovery to be achieved uniformly across all n device-scale flows prior to any array-scale mixing occurring. This requires the upstream and downstream velocities at the device boundaries to be equal to u_A (Figure 2.3a) in order to provide a kinematic matching point to the

array-scale flow. It is also implicitly assumed that the channel should be sufficiently long, compared to the array wake length, in order to allow for complete array-scale mixing.

Turbine characteristics, such as C_T, C_P, α_2, α_4 and B are denoted with the subscripts L, A, and G to identify them, respectively, at the local (device), array, and global (basin) scales. For example, the value of B_L used in the previous section, defined by the new variables introduced here, is a ratio of $\pi D^2/4$ to $h(D+s)$. Meanwhile, B_A is the ratio of the array cross-sectional area, $hn(D+s)$, to the channel cross-sectional area, hw, where w is the width of the channel. Additionally to B_L and B_A, a global-scale blockage ratio is also introduced, defined as $B_G = B_A B_L = n\pi D^2/4hw$, indicating the total swept area. It is inferred from the equation that, for a full-width array where $B_A = 1$, $B_G = B_L$.

In order to solve the coupled two-scale model, the total array thrust must equal the sum of the thrust from individual turbines. This compatibility condition allows the model to be solved numerically to determine the performance of an array using two of the blockage ratios and the array-scale wake velocity factor α_{4A}:

$$C_{TA} = \alpha_{2A}^2 B_L C_{TL} = (1-\alpha_{4A}) \left[\frac{1+\alpha_{4A}-2B_A\alpha_{2A}}{\left(1-B_A\left(\alpha_{2A}/\alpha_{4A}\right)\right)^2} \right]. \tag{2.14}$$

From the two-scale model, Nishino and Willden (2012*b*) have shown that, for a given B_G, there is an optimal combination of B_L, B_A and α_{4L} that achieves the maximum amount of power. For example, Nishino and Willden (2012*b*) have illustrated that in a laterally unbounded flow, the change in the global power coefficient C_{PG} is a function of both α_{2G} ($= \alpha_{2L}\alpha_{2A}$) and B_L. From the perspective of achieving maximum C_{PG}, there is an optimum α_{2G} for any constant value of B_L as C_{PG} increases then decreases with decreasing α_{2G}; likewise, these results also indicate that there is an optimal B_L when B_G is fixed. Fundamentally, the optimisation of partial-width arrays requires a balance between maximising the beneficial effects of local

blockage while minimising the detrimental effects of excessive array-scale flow diversion and mixing. It has been noted that $C_{PG,max}$ usually occurs at a small value of α_{2G} (which also indicates the global extraction efficiency according to Equation 2.12), demonstrating that optimal power extraction occurs close to the peak of the optimal thrust coefficient curve (Bonar et al., 2019). This model also finds that the maximum possible value for a laterally unbounded channel is $C_{PG,max} = 0.798$, a significant improvement on the Betz limit of 0.593.

Further work by Nishino and Willden (2013) re-examined the assumption on row length in the two-scale theory to better understand flow interactions across different scales for shorter partial-width arrays, where the expansion of local flow channel for each individual device can no longer be neglected and two-scale separation is less well-defined. Another extension by Draper and Nishino (2014) considered the possibility of multiple rows of turbines in an array with 'staggered' versus 'centred' configurations, under the condition that the streamwise spacing between the turbines is sufficient for pressure to equalise but not for complete device-scale wake mixing to occur. In this work, it was concluded that, for a given total swept area, a single row of turbines has the best performance for maximum power capture. This is followed in performance by a staggered arrangement in a multi-row configuration, which is in turn superior to a multi-row centred configuration as downstream turbines can benefit from the accelerated local bypass flow of the staggered upstream turbines. It was also reported that, for rows of turbines with constant values of B_L and B_A, the optimal B_L for a single row of turbines is much higher than that for two rows. Later, Nishino and Draper (2019) were able to further develop the theoretical model to estimate the efficiency of a large array in fully developed flow consisting of either centred or staggered rows of turbines with varying row spacing. This was achieved by using a hybrid inviscid-viscous actuator disc model for the wake mixing process between turbine rows. The existence of an optimal row spac-

ing (corresponding to an optimal mixing rate m) for the staggered configuration was also discovered in the model, and this optimal row spacing was found to decrease with increasing B_L.

Other improvements to the two-scale theory include studies by Vogel (2014) to investigate a deformable free surface with finite Froude numbers and by Cooke (2016) to represent the realistic case of a single row of turbine clustered into several sub-arrays, which all suggest the local blockage effect to be significant. Applications of this two-scale model have also moved beyond the field of tidal energy and into the wind industry to examine the effect of local blockage on wind turbines (Nishino, 2016; Nishino and Draper, 2015).

2.4.3 Basin scale

In the case of a wind farm, the extent of the atmospheric system is sufficiently large compared to the size of the turbines for the boundary imposed by the atmosphere to be considered infinite. Thus, it is often assumed that the kinetic energy flux provides a sufficiently accurate indication of the power available to a wind farm.

This assumption is no longer justifiable for the case of a tidal channel system as the area of the channel cross-section is in a similar scale to the swept area of the turbine array. Garrett and Cummins (2004) have shown that the relationship between the averaged kinetic flux and maximum available power is no longer a simple correlation, which seems intuitive due to the power extraction by an array of turbines resulting in the reduction of flow (Blunden and Bahaj, 2007; Garrett and Cummins, 2008). According to Vennell et al. (2015), for most channels, a blockage ratio between 0.02 to 0.05 for a single-row array can significantly alter the channel dynamics, and this value is lower for a multi-row array. Furthermore, the channel cross-section A_C will vary along the streamwise direction, leading to a variation in the kinetic energy flux that is proportional to the inverse square of A_C; therefore,

there will be a spatially-dependent variation in the kinetic energy flux (Garrett and Cummins, 2008). As such, the ideal steady-flow assumptions used in the analytical models are not entirely accurate, meaning that their findings may not be applicable in more realistic flow conditions. To fully understand the tidal hydrodynamics, it is vital to conduct a basin-scale (or channel-scale) analysis.

2.4.3.1 Simple tidal channel

To overcome the deficiencies of the simplistic kinetic flux approach, Garrett and Cummins (2005) proposed an analytical model to describe head-driven flow through an idealised tidal channel connecting two infinite oceans. Their model has been used extensively in other theoretical studies of tidal stream power (e.g. Vennell and Adcock, 2014). The velocity of the current passing through the channel as well as the drag produced by the turbines are assumed to exhibit no dependence on the turbine's spanwise position within the channel, which requires the entire cross-section of the channel to be blocked by turbines. This allows for the application of the one-dimensional (1D) shallow water approximation to the momentum equation, expressed as:

$$\frac{\partial}{\partial t}\frac{Q}{A_C} + \left(\frac{Q}{A_C}\right)\frac{\partial}{\partial x}\left(\frac{Q}{A_C}\right) + g\frac{\partial \xi}{\partial x} = -F \tag{2.15}$$

where x is the streamwise location along the channel, Q is the flow velocity as a function of flow cross-sectional area $A_C(x)$, g is acceleration due to gravity, t is the time, ξ is the elevation of the free surface and F is the opposing force on the flow, per unit mass, which is the combination of bed friction and resistance from turbines. Despite being a simplistic representation, this model is able to capture the leading order effects of energy extraction on channel dynamics and calculate the maximum power that can be extracted from the flow at a low computational cost. This greatly simplifies the process of optimising turbine deployments and resource assessment.

Similar to previous studies, a number of assumptions are made to simplify the analysis. Firstly, the channel is assumed to be sufficiently short such that Q does

not vary along its length, which is a reasonable assumption for most tidal channels due to the long wavelength of the tide. Secondly, the channel Fr is required to be sufficiently small so that a first-order approximation for depth and velocity is only a function of the position. Finally, it is assumed that both the cross-section and the length of the channel do not vary with time and changes in the channel flow rate do not affect the tides and elevations in adjoining basins. Integrating Equation 2.15 along the length of the channel and assuming the drag to be proportional to velocity squared yields the following equation of motion for flow through the channel:

$$c\frac{dQ}{dt} - g\xi_0 = -\int_0^L F_t dx - \delta_0 Q|Q|, \quad \delta_0 = \int_0^L C_d \left(hA_C^2\right)^{-1} dx + \frac{1}{2}A_e^{-2} \quad (2.16)$$

where $c = \int_0^L A_C^{-1} dx$, ξ_0 is the water level difference between two tidal basins (assumed to vary with t as $\xi_0(t) = a_0 \cos(\omega_0 t)$, where a_0 is the amplitude and ω_0 is the frequency of the forcing), and $\int_0^L F_t dx = \delta_1 Q|Q|$ is a drag term, proportional to the square of the velocity, used to represent the force of the turbine array on the flow. The term C_d is the drag coefficient of the channel and A_e is the cross-sectional area of the flow at the exit, which is assumed to form a jet into the lower tidal basin and is therefore associated with an energy loss (Garrett and Cummins, 2005); the exit loss may vary with channel dynamics and can be tuned by introducing an additional tuning factor.

Assuming a single-constituent tide and negligible drag from turbine support structures, Equation 2.16 can be presented in dimensionless form by equating the variables $Q' = \frac{\omega_0 c}{g a_0} Q$, $\lambda_0 = \frac{g a_0}{(\omega_0 c)^2}\delta_0$, $\lambda_1 = \frac{g a_0}{(\omega_0 c)^2}\delta_1$, and $t' = \omega_0 t$. The equation thus becomes:

$$\frac{\mathrm{d}Q'}{\mathrm{d}t'} + (\lambda_1 + \lambda_0)Q'|Q'| = \cos(t'), \quad (2.17)$$

which can be solved numerically. The non-dimensional parameter λ_0 represents the combined background roughness and exit losses while λ_1 is the turbine drag. In the

absence of turbines, λ_0 describes how the tidal forcing is balanced by the inertial and drag forces. The value of λ_0, known as the channel's 'natural dynamic balance', can fall between the inertial limit ($\lambda_0 = 0$) and the quasi-steady limit ($\lambda_0 \to \infty$). At the inertial limit, the forcing is balanced by the acceleration and therefore the phases of pressure forcing and velocity are separated by almost 90°, whereas for the quasi-steady limit, the forcing is instead balanced by the energy losses in the channel and the phase shift is close to zero. The non-dimensional term λ_0 can be used to categorise and describe real sites, to leading order, by defining it as follows:

$$\lambda_0 = \frac{ga_0}{\omega_0^2 Lh} C_d. \tag{2.18}$$

where L and h are the length and depth of the channel, respectively. Analysing this equation, it may be inferred that small and shallow channels typically exhibit values of $\lambda_0 > 1$, leading them to be categorised as 'drag-dominated', whereas large and deep straits usually imply that $\lambda_0 < 1$ and are often categorised as 'inertia-dominated'. For example, a large strait like the Cook Strait in New Zealand may have $\lambda_0 \approx 0.1$ and conversely, a small channel such as the Tory Channel in New Zealand may have $\lambda_0 \approx 5$ (Vennell et al., 2015). Nevertheless, a full and accurate description of real sites may not be possible using a simple non-dimensional framework due to variability in current across the cross-section of the channel and also its bathymetry. The λ_0 value does, however, prove useful as a first approximation to describe the dynamics of the unexploited channel (Adcock and Draper, 2014).

Analytical calculations using this zero-dimensional (0D) model has determined that the upper bound to energy extraction from a tidal channel is within $\approx 10\%$ of $\gamma(= 0.22)\rho g a_0 Q_{max}$, where γ is a multiplier that depends on the λ_0 and Q_{max} is the maximum volumetric flux through the unexploited channel (Garrett and Cummins, 2005). This estimate arrives from the fact that γ ranges between 0.21 for the inertial limit and 0.24 at the quasi-steady limit. Ultimately, this study has provided

a simple description of the relationship of channel geometry and large-scale flow to the extraction of power, and also further highlighted that the unexploited kinetic flux is not the only contributor to power production as power is instead more closely related to the work done by the tidal forcing.

Extensions of the Garrett and Cummins (2005) model include the work done by Blanchfield et al. (2008) to adjust the inflow and outflow channel boundaries to resemble an infinite ocean at one end and a bay at the other. Results from the study suggest that, even though there is slightly greater variance, the new channel boundary configuration does not affect the previously averaged upper limit in extractable energy (i.e. $0.22\rho g a_0 Q_{max}$). Further work by Smeaton et al. (2016) looked at the effect on channel constriction through adjustments to the cross-sectional width and depth between the open ocean and ocean-lagoon boundaries. This study showed that in general, constrictions reduce the power available, with a reduction in depth having a greater potential power loss than a reduction in width. An exception to this outcome was found when an constriction was applied in a channel connecting an ocean boundary to a smaller lagoon, in which case it was determined that some resonant modes exist with the possibility of enhancing the channel's peak power potential. The most recent extension discussed here is a study by Kreitmair et al. (2019), who used this simple channel model to show how uncertainty in the value of specific inputs, such as the bed friction coefficient C_d, can propagate through the model to produce uncertain maximum power estimates. Specifically, for a full-width array, it was revealed that uncertainty in the value of bottom friction serves to increase estimates of available power; however, the opposite is true for a laterally unbounded array.

2.4.3.2 Combined models

While device-scale models are useful for providing insights into turbine performance, the installation of turbines resulting in flow reduction contradicts the as-

sumption that the free-stream flow rate is unaffected. Conversely, a basin-scale model, while accounting for the balance of forces that drive currents through a channel, is incapable of capturing the flow diversion around individual turbines and distinguishing between available power and extracted power without the integration of a detailed device-scale model. Therefore, efforts have been made in recent analytical work to combine these different types of models in order to better describe the energy available to a tidal array in a channel and to explore the corresponding optimal arrangement and operation. Work undertaken by Vennell (2010) combined the simple analytical channel model of Garrett and Cummins (2005) with the volume-flux-constrained actuator disc theory of Garrett and Cummins (2007) to analyse the performance of turbine arrays that stretch across a channel. In order to avoid violating the underlying assumptions of these models, Vennell (2010) further assumed that only a short section of the channel is occupied by the turbine array, in which the flow can be considered quasi-steady as the tidal flow reverses relatively slowly. An additional assumption of sufficiently short device-scale wake mixing relative to the turbine row streamwise spacing was made to ensure that wake recovery is complete between turbine rows (equivalent to a mixing rate of $m = 1$ as defined by Nishino and Draper, 2019).

In Vennell's (2010) combined model, the array drag term in Equation 2.16 is related to the thrust coefficient C_T in Equation 2.6 for N_R rows of actuator discs, having a blockage of B and operating at wake velocity factor α_4:

$$\int_0^L F_t dx = N_R \frac{C_T\left(B, \alpha_4\right) B}{2} u^2. \tag{2.19}$$

This equation can also be expressed in the non-dimensional form (similar to Equation 2.17) as:

$$\lambda_1 = \frac{1}{2} N_R^* C_T\left(B, \alpha_4\right) B, \tag{2.20}$$

where $N_R^* = \frac{a_0 g}{\omega_0^2 L^2} N_R$ is the normalised number of rows. Through the coupling of the models by Equation 2.20, this system can be solved numerically. From the perspective of a tidal array within a channel, Vennell (2010) showed that the tuning of turbines is required to obtain maximum power capture as the isolated device-scale optimal resistance of $\alpha_4 = 1/3$ can no longer maximise the output of an entire array. Instead, the optimal α_4 should depend on N_R and B. With additional consideration of the channel dynamics, there are two extremes for achieving optimal power extraction: in the case of a small array in a drag-dominated channel, only $C_{P,max}$ is targeted for optimal performance; in contrast, for large arrays in an inertia-dominated channel, α_4 may approach unity in order to balance η with $C_{P,max}$ (Vennell, 2010). Given the assumption that all individual turbines are identical within the array and that the main aim of this thesis is simply to compare different turbine representations with various arrangement and operation strategies (where, within each comparison, the only varying parameter is the turbine representation), turbine performance characteristics at the local scale may be regarded as a sufficient indication of the global-scale behaviour. Thus, unless otherwise specified, the variables C_T, C_P and η without any subscripts still imply the scale of the device, which is true for all chapters in this thesis.

As the number of rows in an array is increased and turbine tunings are continuously adjusted to maintain optimal performance, P_{av} from the array will continue to increase, but with a diminishing return (i.e. the addition of each new row will result in a monotonically reducing increment in performance, see Vennell, 2010). The existence of this phenomenon is an important consideration when deciding on the maximum N_R of an array that is economically viable for a given site. As such, with regards to the array arrangement, work from Vennell (2010) showed that it is more efficient to fill up existing rows to their greatest potential rather than creating additional rows, indicating that the optimal arrangement is to maximise B_L and

minimise N_R.

Extended work by Vennell (2011) allowed turbine rows to be tuned individually — each turbine row tuned 'in-concert' with other turbine rows — in both laterally constricted and unconstricted channels, which resulted in marginally higher power capture. Especially in a drag-dominated channel, the magnitude of this additional power output is largely inconsequential as the performance is equal to or just slightly greater than the uniform tuning case. A greater performance increase was hypothesised by Vennell (2016) following Adcock (2012), where a temporally-varying tuning strategy was proposed to enhance significantly power extraction from an inertia-dominated channel. Vennell (2012) also adopted the constricted channel model to investigate the energy losses resulting from bed friction, support structure drag, mixing, and energy extraction within tidal arrays. With the category of tidal channels divided into shallow channels and large straits, the results showed that different energy losses influence the two channel types in significantly different ways and that large straits tend to have a greater potential for energy extraction given that bed friction does not dominate the channel behaviour.

The 0D combined model of Vennell (2010) made the assumption of a full-width turbine array, which, in reality, is not feasible. Willden et al. (2014) were the first to expand the work of Vennell (2010) by considering partial-width tidal arrays and replacing the volume-flux-constrained actuator disc model with the two-scale separation model of Nishino and Willden (2012*b*); the subsequent combination of the coupled disc model with the simple channel theory of Garrett and Cummins (2005) led to a new approach for the modelling of array power output as a function of channel dynamics and blockage. This work was followed by Gong et al. (2018), who concluded that the significance of local blockage is reduced with the consideration of channel dynamics. The validity of this approach and its ability to reconcile the underlying assumptions of the model are examined in Chapter 6 of this thesis.

Whilst the analytical models are suitable for providing an understanding of the physics involved in tidal-stream power extraction and for quickly estimating available power for a given layout and turbine tuning, they are limited in the physics that they are able to capture. For instance, simplifying real flow behaviour by using velocity factors does not account for phenomena such as vortex streets and meandering of the wakes. Instead, numerical models are designed with the capability to perform such assessments, and they will be briefly reviewed in the following section.

2.5 Computational Models and Experimental Tests

With the complexity of realistic bathymetry and flow dynamics, the challenges that analytical models face can be resolved by implementing a variety of two-dimensional (2D) and three-dimensional (3D) numerical schemes, which enable the process of power extraction to be accurately investigated across different scales. Numerical modelling is also a more economical way to determine resource characterisation when compared to field data collection and scaled laboratory analysis, though scaled testing with realistic tidal behaviour is still essential for the validation and development of both analytical and numerical models. Following the format of Section 2.4, a review is conducted of existing numerical models and experimental tests of tidal turbines operating at the three different scales.

2.5.1 Device scale

Three-dimensional computational fluid dynamics (CFD) is a powerful tool in the modern study of tidal stream power production at scales involving both the device and the array. The governing Navier-Stokes (NS) equations can be directly solved with numerical methods, albeit at high computational and storage costs in order to resolve accurately spatial and temporal scales of turbulence. This limits the application of the analysis to simple flow problems at relatively low Reynolds num-

ber. Instead, the Reynolds-Averaged Navier-Stokes (RANS) equations, which apply a statistical average to the NS equations, and the Large Eddy Simulation (LES), which resolves the turbulence above a certain scale, are widely used (Schluntz, 2014). The problem of turbulence closure within these equations is usually solved by a turbulence-viscosity model that is based on the Boussinesq assumption (Vogel, 2014). It is worth noting that the accuracy of RANS simulations is highly dependent on the choice of turbulence model (e.g. Apsley et al., 2018).

As discussed previously, tidal turbines can be approximated by a uniform actuator disc that acts as a sink for the axial momentum from the fluid flow. Thus, it is appropriate to combine the actuator disc (AD) theory with the RANS solver for investigating large-scale effects of turbines on the flow. Work by Sun et al. (2008), Harrison et al. (2010) and Rahman et al. (2018) compared the wake characteristics of the RANS-AD model against experimental data measured behind a porous disc, and found that the model and experimental results were similar. Nishino and Willden (2012*a*) also used this type of model to investigate effects of the channel aspect ratio and turbulent wake mixing on the tidal power output. This model, which included the effects of blade-induced turbulence, demonstrated that a higher strength of near wake mixing increases the power extraction whereas the aspect ratio of the channel only has a minor effect. However, limitations of this simplified model restrict the turbine representation such that details of the blade structure and the azimuthal velocity component are neglected. Therefore, effects such as near wake profiles, the trailing of vortices from the edges of blades, and the mechanical motion of the rotor on the turbine performance cannot be studied without further parameterisations.

One such parametrisation is the blade element (BE) theory, which discretises the uniform actuator disc into azimuthally averaged concentric annular rings and introduces rotational source terms. The force on each ring is determined from the

incoming flow velocity and turbine parameters, including rotational speed, pitch angle, blade twist profile and 2D sectional lift and drag coefficients (defined within a sub-grid model, details of which are described in Chapter 4). BE theory imposes realistic tidal turbine characteristics and operating conditions, allowing variations in rotational flow velocities and pressure drops across the disc to be modelled. A number of corrections were later introduced to improve the model's accuracy, such as corrections for discrete blade effects (Glauert, 1935), 3D tip losses (Shen et al., 2005), and heavily loaded blades (Schmitz and Maniaci, 2016). The inclusion of the BE theory into a RANS solver to model the tidal flow field is commonly referred to as the RANS-BE method. Batten et al. (2013) and Lavaroni et al. (2014) modelled wake characteristics using the RANS-BE method, resulting in better agreement with experimental measurements than using the AD model. Work by McIntosh et al. (2011), Schluntz and Willden (2015) and Cao et al. (2018) also used this methodology to design tidal turbines that exploit the effects of blockage.

Another numerical parameterisation for turbine performance comes from the work of Sørensen and Shen (2002), who introduced the actuator line (AL) method in order to represent an axial flow turbine by modelling the blade forces as momentum source terms along time-varying, rotating lines. Similar to the RANS-BE method, viscous effects on the blade surfaces are captured through 2D lift and drag coefficients. Compared to the BE method, this model does resolve transient physical phenomena such as tip vortices and therefore is able to provide better estimates of the near wake flow field (Wimshurst and Willden, 2016*b*).

As the numerical model increases in complexity (from AD to BE to AL methods), additional parameters are required to represent the turbine, improving the accuracy of the model but also increasing its computational time. Though effective tools, these models do not completely resolve the flow field around the turbine blades; effects such as root and tip vortices, which are difficult to parameterise, are

not properly accounted for. Therefore, blade-resolved (BR) computations are required to model the complete blade and rotor geometries, providing a significantly greater level of accuracy. Compared to the BE and AL models that require 2D lift and drag coefficients to determine blade forces, the BR model can directly resolve the resulting forces and, more importantly, account for 3D and unsteady effects that are significant around the blade tip and root regions (e.g. Wimshurst and Willden, 2017). However, the high computational cost of this method greatly limits its application to the parameter space of a single device, especially when wake recovery and the blade surface have to be resolved with sufficient accuracy. Afgan et al. (2013) and McNaughton (2013) conducted a BR analysis of an experimental rotor from Bahaj et al. (2007b) using RANS and LES models, from which the results showed good agreement with experimental data. In addition, the BR model was able to resolve detailed flow behaviour such as the interaction between the blade vortices and the turbine support structure (Muchala and Willden, 2018).

Experimental models of tidal turbines (including porous discs and scaled rotor devices) are also important for the study of tidal power extraction and to validate both analytical and numerical studies. Similar to an actuator disc in numerical simulations, a porous disc in an experimental model is only able to apply thrust to the flow, resulting in a non-rotational wake. Despite this limitation, a porous disc may be appropriate when considering large-scale effects such as those in the work of Bahaj et al. (2007a), who used this method to simulate the far wake region behind a tidal turbine. Whelan et al. (2009) used both porous discs and scaled rotor experiments to study the effects of free surface deformation on the flow surrounding turbines and validate their analytical model. Mycek et al. (2014) conducted experimental studies on a scaled rotor to investigate the effects of different free-stream turbulence intensities on turbine performance, and showed that turbulence intensities have minimal effect on the averaged power coefficient but have considerable

influence on wake characteristics.

2.5.2 Array scale

The simplicity of the actuator disc offers a computationally efficient way of investigating large-scale flow effects, undertaking preliminary studies of wake interactions and power generated from different array configurations. This methodology allows a large number of arrangement parameters to be investigated, which would be otherwise infeasible with other numerical models. For instance, Bai et al. (2009) used a RANS-AD model to investigate seven different array arrangements of up to seven discs and found that benefit can be obtained by adding turbines in the spanwise direction while the streamwise spacing of the array can be a parameter to optimise. Nishino and Willden (2013) also employed the RANS-AD model to study a single-row array of up to 40 discs to validate their two-scale model, which suggests that the two-scale dynamics described in the analytical model are reasonably accurate compared to the array behaviour obtained using RANS computations. This is further confirmed by a similar RANS-AD study done by Perez-Campos and Nishino (2015) with eight actuator discs in a vertically sheared flow.

BE model is able to improve accuracy in the modelling of near wake mixing, which plays an important role in determining downstream turbine array power. Turnock et al. (2011) used the RANS-BE method to investigate the spanwise and streamwise spacing of multi-row turbine arrays and showed that power is optimised when turbines are placed far apart in the streamwise direction but closely packed in the spanwise direction. Vogel and Willden (2018) predicted the power performance of a four-turbine array optimally designed for different blockage ratios using the RANS-BE model and discovered that the turbines designed for moderate blockage maximise the array power coefficient as a result of the balance between the device-scale and array-scale flow phenomena.

However, without the detailed and transient representation of turbine blades, the error in the predicted wake characteristics using the RANS-BE method may be amplified when flow passes through multiple downstream turbine arrays, as suggested by Olczak et al. (2016). Therefore, the AL method is also used in the study of near wake interactions in tidal arrays. Churchfield et al. (2013) combined the AL method with LES to study the power from an array in staggered and centred configurations, and showed that performance is better with staggered arrangements, supporting the finding of Draper and Nishino (2014). Due to the high computational cost of BR models, very few studies have been conducted with this method to study the performance of entire tidal arrays (e.g. Nuernberg and Tao, 2018).

As discussed above, the optimal array layout proves to be a challenging problem as the complex interactions between turbines significantly influence overall array performance. Especially for a large array, running multiple optimisation iterations with 3D techniques may be impractical at present. Therefore, lower-order flow modelling and turbine parameterisations are favoured over 3D approaches for turbine arrangement studies. A 2D method, introduced by Funke et al. (2014), incorporates a gradient-based adjoint approach with an objective function to optimise the time-averaged available power ($\overline{P}_{av}$) from tidal turbine arrays. This approach uses the steady shallow water equations (SWEs) to model the tidal flow at the basin scale, discussed in detail in Section 2.5.3, in which the turbine is treated as an additional bed friction term within numerous small discrete drag elements. The model was then used by Coles et al. (2017a), Funke et al. (2016), and Goss et al. (2019) to investigate turbine array configurations for various idealised scenarios and real sites, resulting in a significant performance increase due to the optimisation process. Jacobs et al. (2016) further compared the optimisation results from the SWE model with the LES model of Divett et al. (2013) and determined that even though the SWE model tends to over-predict power production, its estimated performance

enhancement is still similar to that of the 3D simulations.

Limited experimental studies have also been conducted to understand the flow effects within tidal turbine arrays, though spacing requirements and the costs associated with experimentation are key restrictions to the number of turbines and their arrangements that can be tested. As such, these experiments are commonly used solely to validate analytical and numerical array models. Cooke (2016) experimentally determined that the power of an array of eight porous discs is maximised when the discs are in a closely packed configuration in the spanwise direction; in addition, Cooke also found that array-scale and device-scale wake mixing occur almost simultaneously. McNaughton et al. (2019) studied an array of two closely packed turbines and found that, when compared to the single-turbine operation, the array arrangement increases the power coefficient of each turbine by 20%.

2.5.3 Basin scale

The RANS and LES numerical schemes implemented with either a low-order disc model (AD, BE or AL) or a BR model focus on localised spatial and temporal flow characteristics specifically for the analysis of blade loading, turbine performance, and array-scale wake interactions. However, the modelling complexity and costs severely limit their applications in large basin-scale investigations and long simulations of multiple tidal periods, which account for the wider region around a tidal energy site including non-uniform bathymetry and oscillatory tidal forcing. For this scale of modelling, the 2D SWEs are used to model basin-scale tidal flows in bodies of shallow water (Adcock et al., 2013; Coles et al., 2017b; Walters et al., 2013). This method has proven to be reliable and is therefore employed in this thesis as one of the key modelling approaches. Experimentally, Draper et al. (2013b) modelled rows of porous discs stretching a wide channel (with and without a headland) in both steady and oscillatory flows. In general however, it presently remains difficult

to find experimental data at basin scale because of the size of the facility required.

2.5.3.1 Shallow water equations

Flows in coastal regions are often well approximated as having a small vertical acceleration (assuming hydrostatic pressure) in comparison to that in the horizontal direction, and a shallow water depth when compared to the wave length of the tide (Draper et al., 2010). In these conditions, flows can be described with a 2D depth-integrated version of the RANS equations to reduce the computational load because the third (vertical) dimension is effectively neglected. The 2D SWEs are derived by vertically integrating the incompressible Reynolds-averaged continuity and momentum conservation equations with respect to depth (Falconer, 1993). Mathematically, the conservative and non-conservative forms of the SWEs differ by a product rule for derivatives. However for coastal applications, the conservative form is usually used in numerical modelling due to its robust formulation. In the numerical approximations, the discretisation of the two forms of equations are performed differently, and for a conservative form discretisation, the derivative requires the terms across the grid to cancel, leaving only the terms at the boundary; this is a more robust form than the non-conservative approach as the model mass and momentum are inherently conserved. The conservative SWEs used in this thesis are:

$$\partial_t(\xi) + \partial_x(Hu) + \partial_y(Hv) = 0, \tag{2.21}$$

$$\begin{aligned} &\partial_t(Hu) + \partial_x\left(Hu^2 + \tfrac{1}{2}g\left(H^2 - h^2\right)\right) + \partial_y(Huv) = g\xi\partial_x(h) \\ &-C_d u\sqrt{u^2+v^2} + \nu_T\left(2\partial_{xx}(Hu) + \partial_{yy}(Hu) + \partial_{xy}(Hv)\right) \end{aligned}, \tag{2.22}$$

$$\begin{aligned} &\partial_t(Hv) + \partial_x(Huv) + \partial_y\left(Hv^2 + \tfrac{1}{2}g\left(H^2 - h^2\right)\right) = g\xi\partial_y(h) \\ &-C_d v\sqrt{u^2+v^2} + \nu_T\left(\partial_{xx}(Hv) + 2\partial_{yy}(Hv) + \partial_{xy}(Hu)\right) \end{aligned}, \tag{2.23}$$

where $H = h + \xi$ is the total depth considering both still water depth h and the elevation of the free surface above the still water level ξ, u and v are the depth-averaged x and y components of velocity, and ν_T is the horizontal eddy viscosity

coefficient. The variable ν_T is based on the Boussinesq approximation and, for simplicity, is assumed to be spatially and temporally constant over the domains considered in this thesis to describe the array-scale mixing, which is reasonable to be modelled within the 2D framework as the array width is much greater than the channel depth. Though not considered in this work, it is possible to use alternative models to account for the variations in ν_T (e.g. Stansby, 2003). The horizontal eddy viscosity coefficient ν_T and natural bed friction coefficient C_d could be determined from calibration (Borthwick and Barber, 1992; Soulsby, 1997). Coriolis effects and other source terms can be straightforwardly added to the SWE model.

2.5.3.2 Limitations of shallow water equations

Though SWE models are capable of simulating tidal flows in channels and coastal regions in a computationally efficient way, the depth-averaged scheme neglects some physics that may impact resource assessment. For instance, the lack of consideration for vertical currents means that flow features such as secondary currents around sharp bends are ignored (Blanckaert and de Vriend, 2005). While there is a velocity profile that is implicitly assumed when deriving C_d, the internal fluid shear stress that affects inflow speed at the turbine rotor depth and the consequential impacts on turbulent mixing are neglected. This limitation was investigated by Stansby (2006), who analysed the wake behind a conical island simulated with a SWE model, and the poor resolution of the flow field around the island was determined to be a result of the assumed logarithmic velocity profile that relates the bed shear stress to the depth-averaged velocity. This relationship implies a proportional and in-phase linkage between these parameters, which is not the case when large-scale horizontal shear flow structures are important (Draper, 2011). In reality, it is also suggested by Draper (2011) and Owen (1980) that the velocity near the sea bed can be significantly different to the depth-averaged velocity both in magnitude and sign, leading to a lag-in-phase frictional loss at the sea bed (Serhadlıoğlu et al.,

2013).

Another limitation to the SWE model is its representation of turbulence. Whilst several turbulence models such as the depth-averaged $k-\epsilon$ turbulence model (Rodi, 1984) and the mixing length model based on fully turbulent flow (e.g. Stansby, 2003) have been proposed to improve the accuracy of the 2D SWE model, fundamentally it is still unable to capture properly the phenomenon of 3D mixing. Therefore a simplistic approach is still preferred at basin scale, as the resolution of bathymetry and the coastline tends to be more important than that of variances in turbulence (Vogel, 2014).

Finally, basin-scale simulations may have difficulty in resolving the wake behind a turbine due to the complex 3D nature of this flow field and insufficient model resolution in both the temporal and spatial sense. This may not be important where the localised wake region is sufficiently far from other energy devices so as to not impact the power assessment, which is the assumption made throughout this thesis. Nevertheless, as a result of these limitations, care must be taken when interpreting the results from a 2D depth-averaged model (Draper, 2011).

2.5.3.3 Numerical solutions of shallow water equations

A range of methods have been developed to solve the SWEs numerically. As the selection of an appropriate numerical scheme is important for both the accuracy of the model and the computational efficiency, the discontinuous Galerkin (DG) finite element method has been chosen as the primary technique used in this thesis for the reasons discussed in this section.

The DG method discretises the domain into elements and applies discontinuous polynomial basis functions over the elements in order to solve the underlying partial differential equations and achieve a higher-order spatial accuracy. Continuity in this model is maintained within each individual element and flux between neighbouring elements occurs at the shared edge (Hesthaven and Warburton, 2007; Serhadlıoğlu

et al., 2013). The DG method was selected over the continuous Galerkin method due to the greater model efficiency that results from its favourable convergence rate, capacity to improve performance using parallel computations, and its greater reliability (Draper, 2011; Kubatko et al., 2009). A more important consideration leading to the selection of this model is that mass and momentum are conserved for each element, providing the capability to implement sub-grid-scale tidal turbine models without violating continuity (Draper, 2011). There is, however, a well-known disadvantage of the DG method resulting from the use of discontinuous polynomial basis functions — these functions lead to an increased computational cost when compared to the continuous Galerkin finite element method. Nevertheless, this is outweighed by the performance enhancements from the use of parallel computations.

Explicit numerical schemes, such as the Runge-Kutta (RK) method, are used to march the solution forward in time with high temporal accuracy (Shu, 1987). Due to its explicit nature, stability within this model is achieved by restricting the time step limit based on the Courant-Friedrichs-Lewy (CFL) condition (Kubatko et al., 2008), which is:

$$|c|\frac{\Delta t}{\Delta x} \leq \frac{1}{2p+1}, \quad c = u \mp \sqrt{gH} \tag{2.24}$$

where c is the characteristic wave speed, Δx is the grid spacing, Δt is the time step and p is the polynomial degree. Additionally, gradient limitations can be applied in the RK method to prevent non-physical oscillations from being introduced into the model by higher-order polynomial approximations (Bunya et al., 2009; Serhadlıoğlu et al., 2013).

It should be noted that most of the practical difficulties experienced in modelling basin-scale tidal hydrodynamics do not come from solving the SWEs, but instead arise from the handling of boundary conditions. Particularly, the modelling

of wetting and drying in the inter-tidal regions has always been a complicated computational problem, involving the balance of numerical stability, computational efficiency and scientific accuracy (Dick et al., 2013; Medeiros and Hagen, 2013).

2.5.3.4 Tidal turbine representations

Various approaches have been used to represent the effects of tidal turbines in numerical SWE models. One of the simplest approaches is to model the turbines as an additional friction coefficient, as Garrett and Cummins (2005) have indicated that the depth-averaged drag force imparted by the turbines is proportional to the square of the flow rate. This bed friction method is easily applicable and capable of providing a more realistic upper-bound power estimate when the turbine parameters are empirically or experimentally determined (Serhadlıoğlu et al., 2013). Several studies have been conducted to assess real-site power potential using the bed friction method, such as those in the Johnstone Strait and the Minas Passage in the Bay of Fundy, both in Canada (Karsten et al., 2008; Sutherland et al., 2007).

The alternative method of the 'momentum sink' approach, similar to the unbounded uniform actuator disc method, models the turbine as a sink term by taking axial momentum from the flow. This method is able to include the directionality of the flow when removing momentum as flow passes through the turbines, which is an improvement to the bed friction model as it allows the model to account for the flow directionality (Draper, 2011; Flores Mateos, 2019). The momentum loss is included into the SWEs through an external force term that is modified to account for the axial thrust coefficient of the turbine and the drag force from the support structure. This approach has been used by Ahmadian and Falconer (2012) to assess the impacts of tidal array layout on coastal environment and by Martin-Short et al. (2015) to study the effects of tidal arrays on sediment deposition in the Pentland Firth.

However, it should be noted that neither the bed friction nor the simple momen-

tum sink approach accounts for blockage effects and viscous effects such as wake mixing. The power estimated from these models is referred to as P_{ex}, whereas the power extracted by the turbine, P_{av}, and the effects of turbine operation and blockage on P_{av} remain unknown to these two simplistic models. An extension to the momentum sink method by Vogel et al. (2013) included a correction based on the simple momentum theory representation of a turbine array, allowing the momentum sink term to incorporate properly the effects of blockage and viscous wake losses.

Draper (2011) developed the alternative 'line momentum sink' method, which does not modify the source terms in the SWEs. Instead, the energy extraction from the turbines is applied as a pressure drop, or head loss, in the SWEs at the location of the turbine. Consequently, the DG solver, which is adapted to handle discontinuities, enables the effective coupling between the channel dynamics and the turbine model. In the DG solver, the line sink of momentum that portrays a sub-grid turbine model is represented by a line segment at the edge of a triangular element in the channel mesh, which modifies the momentum of the flow passing through. The work of the open channel actuator disc theory is incorporated to specify turbine characteristics B_L, Fr and α_4, allowing the important distinction between P_{av} and P_{ex} to be made.

The application of the line momentum sink approach requires some simplifying assumptions (Draper, 2011). Firstly, the device-scale mixing length is required to be sufficiently small (compared to the size of the mesh elements) so as to be described as a sub-grid-scale process, and the variation in flow through the turbines is required to be sufficiently gradual so as to be considered quasi-steady. Additionally, this method assumes that the tidal devices are evenly spaced within each element of the turbine array. When tested in laboratory-scale physical experiments (Draper et al., 2013b), the validity of these assumptions in the sub-grid model has been shown to hold and thus the model has been adopted in other studies that are discussed in the

following section.

2.5.3.5 Modelling examples with line momentum sink approach

Following the development of the line momentum sink approach, a number of studies have been carried out in both idealised domains and actual locations to investigate turbine performance for a variety of hydrodynamic conditions within channels.

By implementing the line momentum sink approach into the DG-ADCIRC model (following works by Draper et al., 2010; Kubatko et al., 2009, 2006), Serhadlıoğlu et al. (2013) first investigated the headland site of the Anglesey Skerries and the roles of array configuration (series versus parallel) and location, as well as turbine operation, on power extraction. Results showed that greater available power extraction is achieved with the array located closer to the Skerries and it was recommended that rows are arranged in parallel rather than in series configuration. Adcock et al. (2013) adopted Serhadlıoğlu's modified code to assess the potential of tidal channel sites in the Pentland Firth, and estimated that 1.9 GW of P_{av} may be achieved across the entire Firth with economically-viable values of N_R and B_L, which may cause up to a 30% reduction in flow rate. Subsequently, Wang and Adcock (2018) considered power and thrust capping strategies for a full-width array across the Pentland Firth and concluded that, while it is sensible to adopt simultaneous power and thrust capping, the strategy can be highly complicated due the complexity of the real site. A similar approach was adopted by Bonar et al. (2018) to explore tidal resources in the Malacca Strait between the Malay Peninsula and the Indonesian island of Sumtra. The results of this study deemed the size of the resource in the tidal stream to be insignificant when considering Malaysia's total energy requirements, but it has the potential for small-scale projects to generate off-grid electricity using low-speed rotors.

The line momentum sink approach has also been used to explore the optimal array operation and layout within an idealised channel as it offers a reasonable bal-

ance between model accuracy and computational cost. Draper et al. (2013a) studied the performance of a partial-width array next to an idealised headland and identified that, although the shape of the headland can have a considerable impact on available power, power is maximised as the array becomes densely blocked (similar to the case of a tidal channel). However, there is a noticeable asymmetry of flow behaviour between the open ocean side and the headland side, and it was discovered that the available power is severely limited by the flow diversion around the array. This limitation is more pronounced with higher B_L as the flow is met with a larger thrust force. More recently, Bonar et al. (2019) used an idealised channel model with the line momentum sink method to explore the blockage effect under oscillatory flow and was able to demonstrate a side-by-side oscillation of the array core and bypass flows, resulting in a significant performance enhancement referred to as the 'reversal boost' that is discussed in greater detail in Chapter 6.

Preceded by the extensive investigations performed by other researchers, the highly developed and widely adopted line momentum sink approach will also serve as the basis for the model developed in this thesis.

2.5.3.6 Three-dimensional coastal ocean model

Whilst 2D numerical models are useful approximations to realistic flow conditions, the resolution of complex 3D flows may require the use of a higher-order model. A 3D coastal model, which typically solves a 3D form of the SWEs, achieves this by discretising the water column into vertical layers (with thickness either specified, varying with the percentage depth, a hybrid of the two, or varying by fluid density (Miglio et al., 1999)) and solving the partial differential equations to resolve all velocity components within each layer. This usually requires the vertical velocity component to be small, otherwise the inclusion of vertical momentum equations is needed for the non-hydrostatic components.

The application of 3D SWE models allows complex flow features, such as sec-

ondary currents around bends and the formation of salt wedges in estuaries (with the appropriate density coupling model) to be simulated (Kärnä et al., 2017). It also allows for resolution of the velocity profile, an important consideration when modelling real flows as the bed and surface currents may be in opposing directions due to the wind and other forcings. Such features can be important when considering the depth in which to place a turbine and which is required for more accurate resource assessments. The drawback to this methodology is the increased computational cost as the size of the problem is increased with each vertical layer. Furthermore, an adequate turbulence model and additional site-dependent inputs are required for accurate 3D modelling, including temperature and salinity information and the presence of any freshwater inflows, which can be difficult to obtain (Adcock et al., 2015).

An example of a 3D coastal model applied to tidal energy resource assessment comes from Chen et al. (2015), who simulated a tidal array near the island of Zhaitang, off the east coast of China, using the Delft3D model. The turbines were modelled by the momentum sink method and results showed comparable findings to that of previous studies, underpinning the finding by Vennell (2010) that for a fixed number of turbines, a single row outperforms multiple rows.

Chapter 3

Array Design Strategies in the Bohai Gulf *

Arranging a large number of tidal stream turbines with the goal of maximising tidal energy extraction is a challenging problem, with the optimal arrangement depending on a variety of hydrodynamic, operational and environmental factors. Therefore, determining such an arrangement becomes an iterative process due to the complex interactions occurring between the tidal turbines and the surrounding flows that serve to generate power.

In this chapter, new array design algorithms are explored, based on key theoretical results obtained from Chapter 2, to maximise the collective power available to turbines placed in a narrow tidal strait. It should be noted, however, that instead of aiming to refine array design algorithms, the main purpose of this chapter is to use some simplistic approaches to arrange turbines at a real site and identify, at a high level, how complex features, such as bathymetry and tidal dynamics, complicate the design process for a tidal array. This allows the real challenges posed by an actual candidate site to be assessed, which will lay the foundation for the work undertaken in this thesis. As such, this chapter is considered an introductory study to the design

*The discussions in this chapter have been published as a conference paper — see Chen et al. (2018b) from Appendix C.

of tidal arrays at a specific site of interest.

The discontinuous Galerkin version of the open-source hydrodynamic model ADCIRC (DG-ADCIRC) is used to simulate flow through the site model, with the tidal turbines simulated using a sub-grid scale actuator disc model with a line momentum sink approach that follows the work of Serhadlıoğlu (2014). Three algorithms are then used to design turbine arrays for the Bohai Strait, which is considered to be one of China's most promising candidate sites for tidal stream power extraction. An analysis of the potential of the Bohai Strait and the rationale behind its selection have been previously presented in Section 2.3.1. Given that very few studies have analysed the tidal stream resource and potential designs for tidal turbine arrays in the Bohai Strait, this chapter endeavours to examine the site using appropriate modelling techniques and turbine arrangements. Real sites such as this are of course unique but nonetheless, the results of the analysis can be used to draw general conclusions about the optimal design of tidal turbine arrays in tidal straits.

The chapter is structured as follows. Firstly, the numerical model is used to capture the natural hydrodynamics of a real site and to introduce idealised representations of tidal turbines with discussion of the development of the Bohai Strait model in Section 3.1. This is followed by a mesh independence study and detailed discussion on the calibration and validation of the Bohai model against field measurements and data interpolated from literature, in Section 3.2. Finally, different array design algorithms are used to build turbine arrays and analysis is undertaken to determine their performance. A discussion of possible extensions to this work is presented in Section 3.3 before concluding with Section 3.4.

3.1 Bohai Model

3.1.1 Numerical scheme

A 2D hydrodynamic model is developed to simulate the tidal dynamics in China's Bohai region using DG-ADCIRC, which solves the depth-averaged SWEs (Kubatko et al., 2009, 2006). The key reason for the selection of this numerical scheme is its ability to simulate energy extraction by tidal devices; further details of this numerical scheme have already been provided in Section 2.5.3.

For this study, the open channel actuator disc model derived by Houlsby et al. (2008) is used, which is a finite Froude number extension of the volume-flux-constrained actuator disc model of Garrett and Cummins (2007). The power available to the actuator disc in this model is considered an upper bound to the $\overline{P}_{av}$ of a real turbine, which experiences additional losses due to sheared inflow, viscous drag, mechanical and electrical losses, etc.

3.1.2 Model details

Figure 3.1 shows the model domain covering the entire Bohai area, including the Bohai Strait, which connects the semi-enclosed Bohai Sea to the Yellow Sea. A computational mesh comprising piece-wise linear elements is initially developed by using bathymetric contour data provided by the Earth topography five-minute grid (ETOPO5) to inform mesh development within Aquaveo's Surface Water Modelling System (SMS). The land boundary is then carefully adjusted based on the current coastline data sourced from Google satellite imagery. An unstructured mesh comprising 12,618 nodes and 23,885 triangular elements with lengths varying from 1.5 km to 300 m at the location of interest is then generated.

Bathymetry data are obtained from GEBCO's 30 arc-second global grid at a spatial resolution of approximately 950 m. Minor editing of the bathymetry data is required to remove discontinuities, which hinder model stability; this is achieved

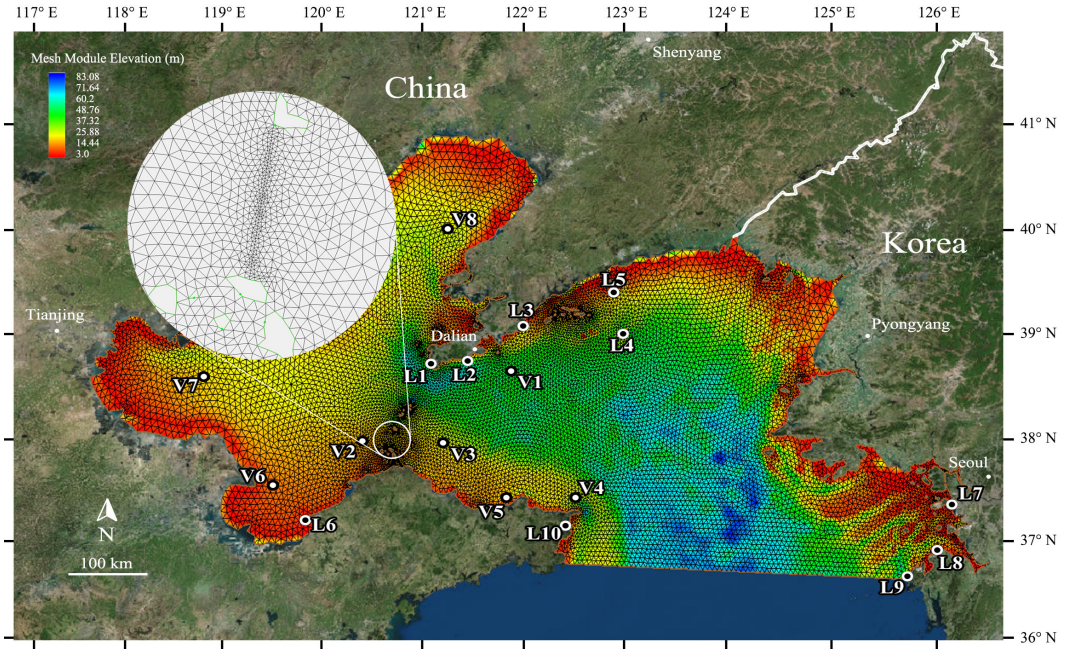

Figure 3.1: Bohai Sea model domain and numerical mesh with contours of bathymetric depth and field measurement markers: the water level and current velocity prediction stations are marked with L and V, respectively.

by manually modifying the data to smooth bathymetry at selected locations. A wetting and drying function is implemented to capture the mass transfer in the inter-tidal zones, following work by Serhadlıoğlu (2014). In order to facilitate comparisons with observation stations in TotalTide (a software package developed by the British Admiralty to predict sea levels and currents), additional alterations to the bathymetry have to be made due to the poor data resolution positioning the stations within inter-tidal zone. In light of this, the bed level in these regions is lowered by 3 m locally to prevent the locations from becoming dry. This allows comparisons to be made with the TotalTide sites without having a significant impact on the tidal dynamics.

Open water boundary conditions for this model are derived from a larger regional-scale model purposely developed to capture the transformation of global tide predictions (obtained from the Le Provost tidal database) into the domain, as discussed further in Section 3.2.2. The model boundary is assumed to be sufficiently far from

the area of interest as to be unaffected by the changes introduced due to the turbines.

3.2 Model Calibration and Validation

Prior to investigating turbine array layouts, the accuracy and fidelity of the numerical model must be verified. This is done by firstly performing a mesh independence study as described in Section 3.2.1. Subsequently, a model calibration is undertaken by analysing various boundary forcing and bed friction coefficients in Sections 3.2.2 and 3.2.3, respectively. The model is then validated by comparing model predictions against published co-tidal charts and various global tide databases in Section 3.2.4. Further validation is carried out to compare the water levels and current velocities predicted by the numerical model with those predicted by the British Admiralty's TotalTide in Sections 3.2.5 and 3.2.6. The data sourced from the TotalTide software is compiled using field measurements of water levels and current velocities to make harmonic predictions. These predictions are made by using a Fourier-like analysis to decompose observed data into discrete frequencies that are associated with key drivers of tidal forcing such as M_2, which is dominant in this region. Each harmonic constituent can be represented by:

$$H_{0n} \cos\left(\omega_n t - \phi_n\right), \tag{3.1}$$

where H_{0n} is the amplitude, ω_n is the frequency, ϕ_n is the phase of the tidal constituent and t is time. Once determined, these constituents can be used to reconstruct the water level at a desired time.

For the purpose of calibration and validation, tides are simulated between 00:00 1 Jan 2016 and 23:55 19 Jan 2016. Following this, results are extracted at selected locations to facilitate comparisons with TotalTide. The numerical model allows the tidal forcing to 'ramp up' over the first 4 days, before running for another day in order to reduce the effect of initial transients. Results from the following 14 days

are extracted for harmonic analysis with observations recorded hourly for each mesh node.

3.2.1 Mesh independence study

A mesh independence study is performed to confirm that the results from the numerical model do not vary with mesh resolution and time step choice. In order to achieve high quality results, greater mesh refinement is needed, which subsequently requires greater computational power due to the corresponding adjustment in the time step needed to accommodate finer resolutions. Mesh resolution and time step are related by the CFL condition, which, in effect, states that in order for a model to remain stable when the element size is reduced, a smaller time step is needed — this results in a higher computational cost.

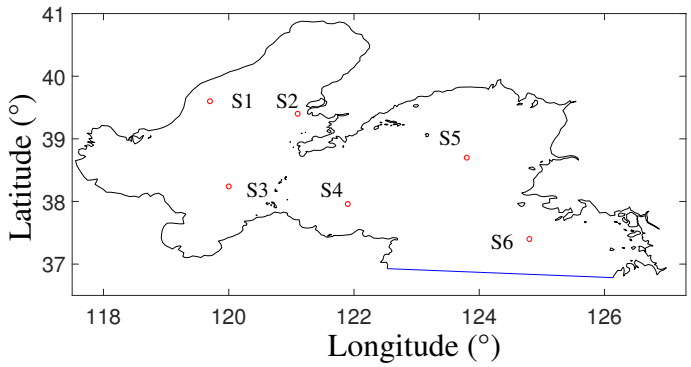

Figure 3.2: Locations for the observation nodes for mesh convergence study.

The mesh independence study is carried out using four unstructured triangular finite element meshes with an identical open boundary resolution, but different numbers of elements. Harmonic analysis is undertaken at six locations in each numerical mesh to determine the effect mesh resolution has on model results, as shown in Figure 3.2. While the error of a hydrodynamic model at a real site is usually determined by comparing results against a reference value obtained from observations, for this study, a complete set of observed data is not available at the specified nodes.

Instead, the results obtained from the finest mesh (U4) are used as the reference value to evaluate mesh-independence by determining the relative error (percentage difference to the reference value) for each location, following Serhadlıoğlu et al. (2013). The results of error measurement are presented in Table 3.1. It has been determined, based on the results achieved, that the small error between U1 and U4 is acceptable given the relative significant difference in computational time. Therefore, U1 is chosen as the most efficient model.

Table 3.1: M_2 tidal elevation amplitude for the meshs used in the independence study.

Grid	Mesh of nodes	S1 (%)	S2 (%)	S3 (%)	S4 (%)	S5 (%)	S6 (%)
U1	12618	1.22	1.34	1.17	1.11	1.12	0.92
U2	21459	0.75	0.91	0.80	0.66	0.82	0.49
U3	59060	0.54	0.57	0.61	0.48	0.56	0.35
U4	132691	-	-	-	-	-	-

3.2.2 Forcing boundary calibration

Li et al. (2016) have noted that the Bohai Sea has four principal tidal constituents — the diurnal K_1 and O_1 tides and the semi-diurnal M_2 and S_2 tides. The Le Provost database is used to reconstruct the water level forcing based on these components at the ocean boundary of the Bohai model (Le Provost et al., 1995). However, given that the predictions from the global tidal model occur over a coarse domain, the results can be inaccurate in some regions. For this reason, calibration of the boundary forcing is undertaken by comparing the forcing on the ocean boundary provided by the Le Provost database against several reference values. These values include a set of numbers from co-tidal charts derived from other papers (Fang et al., 2004) with the relevant interpolation. A comparison is also made with the TPXO database (Egbert et al., 1994) as another comparable global dataset, and a data point at an observation station from TotalTide is taken into account as well. Figure 3.3 plots

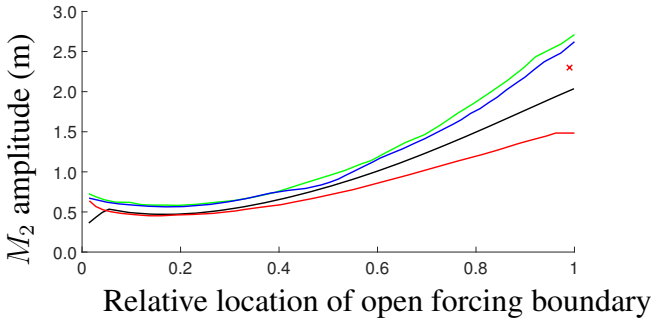

Figure 3.3: M_2 amplitude profile along the open forcing boundary obtained from reference paper (blue curve), global tides database TPXO (black curve), observation station (red cross), and numerically predicted by the pre-calibration model (red curve) and post-calibration model (green curve) with DG-ADCIRC.

the various amplitudes of the M_2 constituent along the open boundary, obtained separately from all of the aforementioned sources as well as numerically predicted by the DG-ADCIRC model both pre-calibration and post-calibration.

By comparing the results obtained using the initial tidal forcing (red curve) with other models for the area obtained from the paper reference (blue curve) and TPXO database (black curve), particularly poor agreement at the eastern side of the ocean boundary is observed. This is further confirmed by a third reference (red cross) provided by the observation station Mohang-Ri in the TotalTide database, located at the eastern end of the open boundary (see L9 in Figure 3.1). This may be due to the pre-calibrated Bohai model's failure to capture the effect of the Coriolis force pushing tides towards the Korean Peninsula, which increases their amplitude.

Therefore, a larger numerical model, covering the Bohai, Yellow, and East China Seas, is built in order to obtain more accurate boundary conditions for the smaller Bohai Sea model. This larger model is forced with a reconstructed water level based off of the four aforementioned key tidal constituents from the Le Provost database. The results from the newer model are then interpolated to drive the water level boundary along the southern extent of the smaller Bohai Sea model. The resulting M_2 amplitude is plotted as the green curve in Figure 3.3 and is shown to be a better

match to the reference values. Thus, this analysis revealed that the Le Provost model does not accurately capture the high tidal amplitude near the Korean Peninsula and a better agreement is found by calibrating the present model with an open boundary forcing driven by a larger model.

3.2.3 Bed friction calibration

As seen in previous studies of the numerical modelling of real sites, the bed friction is a critical model parameter (Gao and Adcock, 2017; Serhadlıoğlu et al., 2013). It is difficult to base this parameter directly on the physics and so it is usually calibrated by comparison to water level measurements (Soulsby, 1997).

The drag on the flow due to bed roughness is given by:

$$F = \int \int_A \rho u|u| C_d dA, \tag{3.2}$$

where ρ is the density of the seawater, A is the area of the seabed, u is the depth-averaged velocity vector and C_d is the dimensionless seabed drag coefficient. In order to simulate the depth-dependency and to maintain model stability, a hybrid non-linear bottom friction law is applied. This best-fit C_d value of 0.001 is set to increase slowly (by a factor of $[1+(10/h)^{10}]^{(1/30)}$) in depths $h < 10$ m, such that the bed friction coefficient increases with decreasing depth in shallow water (Luettich and Westerrink, 2000).

Using the TotalTide constituents for M_2 tidal elevation amplitudes at the ten selected locations (L1-L10 in Figure 3.1), a calibration of model drag is undertaken. This process analyses the Bohai Sea model with three global coefficients of friction for the U1 model: $C_d = 0.001$, 0.00125 and 0.0015 (the reduction of C_d to 0.00075 leads to numerical instability). As indicated by the calculation of the percentage difference between numerical prediction and TotalTide data in Table 3.2, $C_d = 0.001$ produces the best fit. This agrees with past studies identifying the Bohai Sea

Table 3.2: Percentage difference with M_2 tidal elevation amplitudes between numerical prediction and observation data (TotalTide) at different stations using different bed friction coefficients.

Location	$C_d = 0.001$ (%)	$C_d = 0.00125$ (%)	$C_d = 0.0015$ (%)
L1	-11.48	-13.46	-14.32
L2	-11.24	-12.97	-13.48
L3	-7.83	-9.25	-10.35
L4	-7.87	-9.63	-10.76
L5	-1.27	-3.87	-5.43
L6	+0.00	-2.27	-3.57
L7	+11.50	+8.65	+5.97
L8	+11.07	+7.72	+4.64
L9	+15.04	+13.76	+12.9
L10	+2.00	-2.64	-3.87

as a particularly 'smooth' area with a relatively low bed roughness (Teng et al., 2016). However, even though the best calibration value of C_d has been chosen for the model, it does not closely agree at every observation location. As bed friction is typically not constant over a given domain (due to different material types, sediment grain size and marine flora), it is difficult to accurately define a spatially varying bed roughness without information on the seabed composition.

3.2.4 Co-tidal chart comparison

Figures 3.4 and 3.5 show the predicted co-amplitude and co-phase lag lines of both M_2 and K_1 alongside the co-tidal charts presented by Su et al. (2015). As shown in Figure 3.4a, two amphidromic points (positions where the harmonic constituent amplitude tends to zero, implying that water level does not change) of the semi-diurnal tides in the Bohai Sea are located in the proximity of Qinhuang Island and close to the mouth of the Yellow River. It is shown that model predictions give a good visual agreement with co-tidal charts from earlier studies (e.g. Fang et al., 2004; Su et al., 2015; Yao et al., 2012). However, human activities such as land reclamation have resulted in significant changes to the coastline of the Bohai Sea

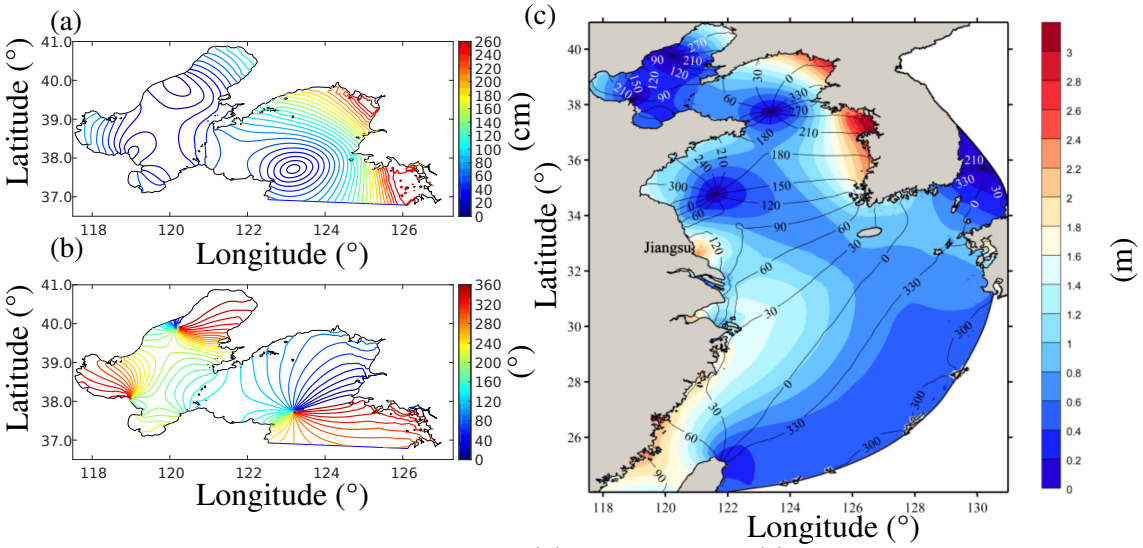

Figure 3.4: Comparison of the M_2 co-tidal (a) amplitude, and (b) phase contours predicted using DG-ADCIRC with (c) M_2 co-tidal chart computed by Su et al. (2015).

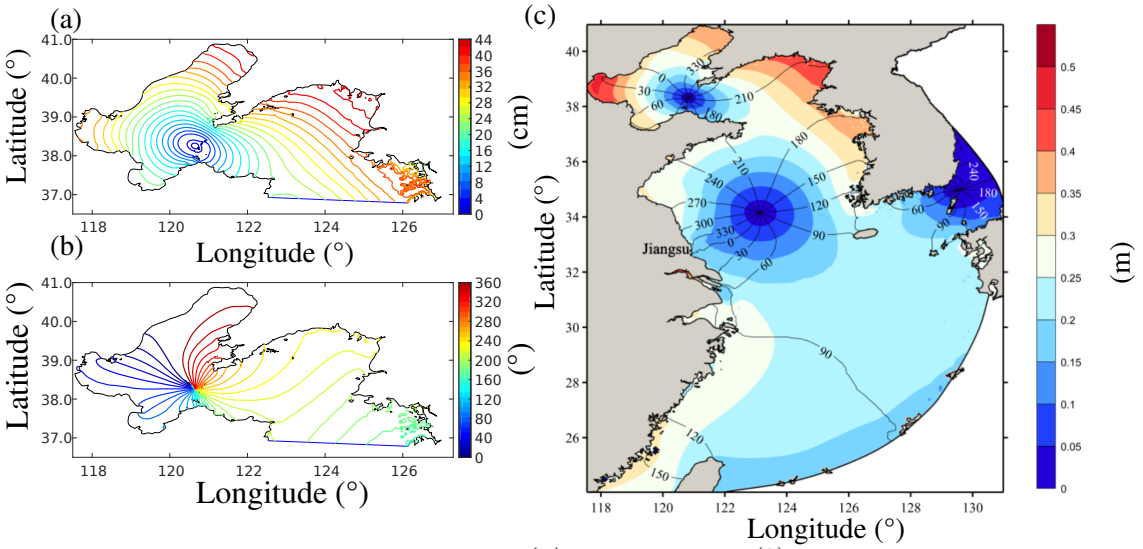

Figure 3.5: Comparison of the K_1 co-tidal (a) amplitude, and (b) phase contours predicted using DG-ADCIRC with (c) K_1 co-tidal chart computed by Su et al. (2015).

in recent years, which have a substantial impact on the entire tidal system (Large-scale land reclamation at the site of interest can be clearly identified from Figure 2 in Zhang et al., 2014a). Furthermore, the model has demonstrated the sensitivity of the area's amphidromic points to the bed drag coefficient. For these reasons, it is possible that the presence of the amphidromic point close to the mouth of the Yellow River is a matter of contention — several findings in the literature have suggested

that it should be located further inland. For the K_1 constituent, there is only one amphidromic point in this area located in the Bohai Strait.

While calibrating the model, the reproduction of the diurnal tides' amphidromic points is found to be less sensitive to the bed drag coefficient than that of the semi-diurnal tides. With the range of bed drag coefficients investigated, the amphidromic point of the diurnal tides varies by $\leq$1 kilometer while the points for the semi-diurnal tides can vary by approximately several kilometers. The pattern of S_2 is similar to that of M_2 and the pattern of O_1 is similar to that of K_1.

3.2.5 Water surface elevation validation

Tidal amplitude and phase predictions from the numerical model are compared with the predictions from TotalTide at the ten water level measurement stations (L1-L10) shown in Section 3.2.3. A comparison between the model-predicted and TotalTide harmonic constituents, M_2 and K_1, is presented in Tables 3.3 and 3.4. Agreement between the predictions is fair, with amplitude errors generally $< 15\%$ and phase errors generally $< 20°$. However, the agreement of several observations is not as good as expected. Some discrepancy is anticipated since these points are located within the inter-tidal zone, where the water is shallow and is more sensitive to factors such as seabed drag, poorly resolved bathymetry — all of which present modelling challenges. Nonetheless, the results indicate that the present model is capable of capturing the key features of tidal elevations.

3.2.6 Tidal currents validation

Several previous modelling studies have demonstrated the inherent problems in validating tidal currents, which include the cost and complexity of oceanography data collection, as well as the significant variation of currents over short length and time scales. Measurements taken closer to the seabed are particularly sensitive to the nature of the underlying floor of the sea, making the extrapolation of measured data

Table 3.3: Predicted water level amplitudes (m).

Station	M_2 tide TotalTide	M_2 tide ADCIRC	M_2 tide Error (%)	K_1 tide TotalTide	K_1 tide ADCIRC	K_1 tide Error (%)
L1	0.61	0.54	-11.48	0.13	0.21	+61.54
L2	0.89	0.79	-11.24	0.23	0.26	+13.04
L3	1.15	1.06	-7.83	0.29	0.34	+17.24
L4	1.27	1.17	-7.87	0.37	0.36	-2.70
L5	1.58	1.56	-1.27	0.35	0.41	+17.14
L6	0.50	0.50	+0.00	0.20	0.24	+20.00
L7	2.87	3.20	+11.50	0.46	0.32	-30.44
L8	2.62	2.91	+11.07	0.40	0.33	-17.50
L9	2.26	2.60	+15.04	0.37	0.31	-16.22
L10	0.50	0.51	+2.00	0.30	0.25	-16.67

Table 3.4: Relative phases of water level signals (°).

Station	M_2 tide TotalTide	M_2 tide ADCIRC	M_2 tide Error (°)	K_1 tide TotalTide	K_1 tide ADCIRC	K_1 tide Error (°)
L1–L2	-27	-29	-2	-36	-34	+2
L2–L3	-18	-20	-2	+342	-15	+3
L3–L4	-22	-28	-6	-16	-14	+2
L4–L5	+3	+8	+5	+10	+4	-6
L5–L6	+14	+128	+114	-139	-133	+6
L6–L7	-132	92	+224	+74	+66	-8
L7–L8	-12	-22	-10	+6	-21	-27
L8–L9	-14	-20	-6	-14	+6	+20
L9–L10	-96	-54	+42	-2	-19	-17
L10–L1	+304	-56	0	-7	-16	-9

to depth-averaged values less reliable. Furthermore, there is a limited amount of data available for the Bohai region, and even those that are available tend to be of relatively poor quality. In regards to the currents, as pointed out by Adcock et al. (2013), their phase can be measured with greater reliability than their magnitude. This is useful as the phase is, to the leading order, dependent on the dynamic balance (ratio of inertia to drag forces). Therefore, this indicates that more weight should be placed on validating tidal current phases rather than magnitudes.

Table 3.5 compares the predicted depth-averaged current velocities at the seven

Table 3.5: Major axis amplitudes (m/s) and relative phases (°) of depth-averaged velocity signals.

Station	Amplitude			Station	Phase		
	TotalTide	ADCIRC	Error (%)		TotalTide	ADCIRC	Error (°)
V1	0.22	0.34	+54.54	V1–V2	92	132	+40
V2	0.18	0.22	+22.22	V2–V3	20	-20	-40
V3	0.65	0.80	+23.10	V3–V4	-113	-125	-12
V4	0.28	0.15	-46.43	V4–V5	78	55	-23
V5	0.25	0.52	+108.00	V5–V6	74	108	+34
V6	0.38	0.50	+31.58	V6–V7	-116	-128	-12
V7	0.41	0.51	+24.39	V7–V1	-35	-22	+13

current measurement stations (V1-V7 in Figure 3.1). These results do not compare favourably with the harmonic constituents derived from TotalTide; however, the quality of the TotalTide measurements are unknown so some discrepancies are expected. The unfavourable comparison with current phase may be due to the limited capability of the DG-ADCIRC model in representing flow turbulence with its inherent assumption that the velocity is uniform over the depth (refer to discussion in Section 2.5.3), thereby restricting the simulation of large-scale eddies that may develop in flows around the islands. Anecdotal evidence from other researchers[†] suggest that modelling this region is more difficult than most, which has also been the experience for this thesis. Despite this, overall the model is found to capture the basic physics of the Bohai Sea reasonably well.

3.2.7 Sources of error

The model developed has two principal sources of error: the quality of the input data requiring simplifying assumptions to be made when building the model, and the quality of the data used for calibration and validation. The accuracy of the model is highly dependent on the accuracy of the bathymetry data, especially in the shallow regions. The resolution of the GEBCO data is insufficient to capture the small, localised tidal dynamics along the complex coastlines and close to the islands where

[†]J.J. Westerink in talk at the 15th International Workshop on Wave Hindcasting and Forecasting.

observation stations are typically located. It is anticipated that improved bathymetry would lead to an improved calibration at these locations. The Le Provost database, which is derived from relatively old measurements, is known to contain inaccuracies and the code may struggle to interpolate correctly tidal frequencies and amplitudes close to the ocean boundary. Furthermore, as the modelling is computationally intensive, it is necessary to compromise the model accuracy. To this end, the model is simplified by smoothing the coastlines, such that the coarse mesh does not fully account for small structures such as bays and estuaries. Another key limitation is the inability of the depth-averaged model to capture the more complicated flows around islands and headlands, where 3D effects should not be neglected (Adcock et al., 2015). In general, locations with more complex forcing, such as fresh water inflows and meteorological conditions (e.g. air pressure and wind), are expected to exhibit more complex 3D effects, which are not modelled in this study. Additionally, in regions of shallow water, non-linear interactions between the constituents may become particularly significant and can be another source of model error.

The raw data used to generate the harmonic constituents in the TotalTide dataset are of unknown age and origin, and therefore care must be taken when using TotalTide for model comparison. However, water level data are generally considered more reliable than current measurements, as supported by data sourced from other papers (Fang et al., 2004). Moreover, the Bohai Sea's coastal zone has witnessed a large amount of economic development in the last ten years, resulting in a significant amount of coastal reclamation work to meet the demands of increased urbanisation and industrialisation. What was previously wetland and tidal flats on the land closest to the seafront has been developed with features such as seawalls and harbours (Zhang et al., 2014a). This means that the TotalTide data may no longer accurately reflect the movements of water in the region.

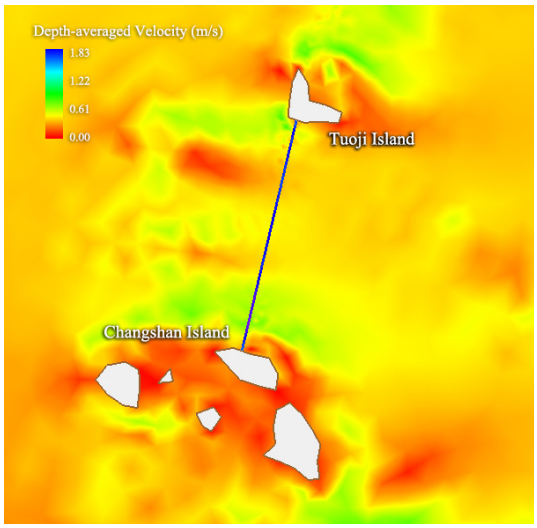

Figure 3.6: Contours of unexploited (near-) peak depth-averaged velocity through the Bohai Strait. The black line marks the channel cross-section for the potential positioning of the array.

3.2.8 Turbine implementation

After model validation and calibration, the numerical mesh is then modified to place rows of tidal turbines in the Bohai Strait (located between China's North Changshan Island and Tuoji Island as seen in Figure 3.6). The distance between these islands is approximately 20 km while the average water depth is approximately 25 m, so the turbines are designed with a diameter of $D = 10$ m. To avoid having to adjust the mesh each time a new row is added, the code is modified to allow multiple rows of turbines to be placed within the edge between adjacent mesh elements, following the work of Adcock et al. (2013). To facilitate this modification, it is assumed that each new row within a given edge is placed directly behind the previous row, and that each row within a given edge experiences the same flow conditions — identical upstream velocity, water depth, and Froude number. Effectively, it is assumed that the rows of turbines are placed in close enough proximity that array-scale mixing for each row occurs concurrently downstream of the entire array (Perez-Campos and Nishino, 2015); this assumption is reasonable because many practical situations require tidal turbines to be closely spaced in the streamwise direction. Such

a modelling approach may have resulted in minor differences in the calculation of power as it neglects the static head variation between turbine rows as a result of energy removal in the open channel model, but these differences are fairly negligible due to the sufficiently small Froude number at this particular site. In addition, the wake mixing length of a tidal turbine is typically $20D$ (Chen et al., 2017), which is smaller than the finest $\approx$ 300-m mesh resolution in this model, though the lack of detail on device-scale mixing should not affect the leading order physics of energy extraction (see discussion of mixing in Chapter 2). Although time-varying tuning strategies are explored in following chapters, α_4, which is also the tuning factor, is held constant throughout the tidal cycle in this chapter.

3.3 Array Design

3.3.1 Strategies

In past research, kinetic energy flux has been considered a useful metric in the assessment of tidal stream resources. This parameter formed the basis of early tidal power assessments (e.g. Blunden and Bahaj, 2006), which multiplied its value by some impact factor (< 1) to give an estimate of the available tidal resource (EMEC, 2009). As noted in Section 2.4.3, this approach is flawed because the natural kinetic energy flux is not directly related to the maximum P_{ex} (which could be even higher than the natural kinetic energy flux), but it is still clearly a useful starting point for resource assessment and the study into the optimal arrangement of tidal turbines. This metric is used as the basis of the new array design strategies within this chapter, which are described below.

The three design strategies investigated in this paper are illustrated in Figures 3.7-3.9. The channel cross-section is divided into 50 sections of equal width and the sections with a mean water depth of less than $1.5D$ are excluded from the analysis. Tidal arrays are then built incrementally by placing turbines in the section of the

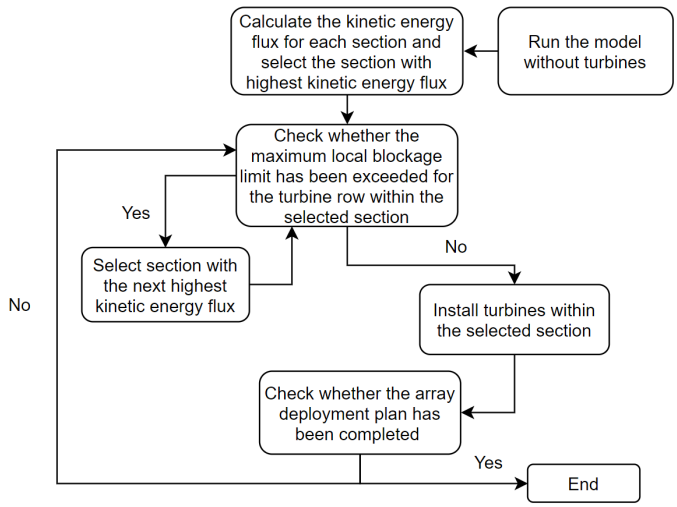

Figure 3.7: Array design algorithm for strategy 1.

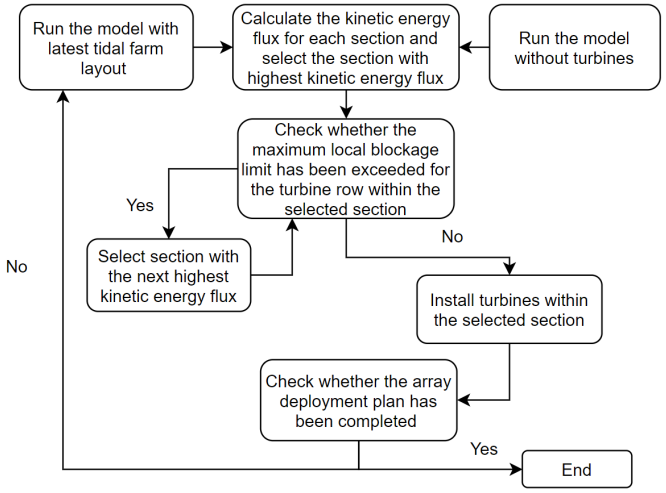

Figure 3.8: Array design algorithm for strategy 2.

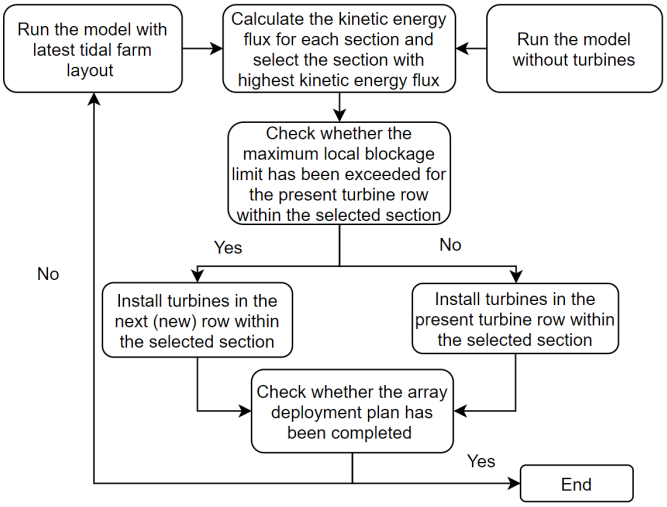

Figure 3.9: Array design algorithm for strategy 3.

highest kinetic energy flux, averaged over the tidal cycle; the local blockage in these array sections is not allowed to exceed the realistically maximum B_L value of 0.4 (Flores Mateos, 2019). The first strategy is based purely on the natural kinetic energy flux and does not account for the feedback between the turbines and the flow. The second and third strategies do account for feedback effects, with the former requiring all the turbines to be placed in a single cross-stream row, while the latter allows the turbines to be deployed in multiple rows (though within a single turbine edge, as discussed in Section 3.2.8).

Strategy 1, which does not take into account the turbine-flow feedback, requires the model to be run only once; in comparison, strategies 2 and 3 require multiple iterative simulations. For this study, 1,000 turbines need to be installed in groups of 10. To facilitate the large number of simulations needed, the problem is simplified — the model is allowed to spin up for 2 days before results from the following 3 days are extracted and time-averaged. The tuning factor of $\alpha_4 = 1/3$ is held constant as the arrays are built, and the flow is driven by a single dominant tidal constituent, M_2. It is also worth noting that the adoption of the adjoint approach (Funke et al., 2014, 2016) typically simplifies the problem further to consider only steady flow. However, this neglects the effects of flow reversal, which work by Bonar et al. (2019), later expanded in Chapter 6, has shown to be significant (not necessarily for the channel considered here but certainly for inertia-dominated channels).

3.3.2 Analysis

Figure 3.10 presents a comparison of $\overline{P}_{av}$ for the arrays built using strategies 2 and 3. For both strategies, $\overline{P}_{av}$ is shown to increase monotonically with the number of turbines installed, and the curves for the two strategies match exactly up to point A. This is expected because both strategies deploy their first 170 turbines (which is the development at point A) in a single cross-stream row. Beyond this point, how-

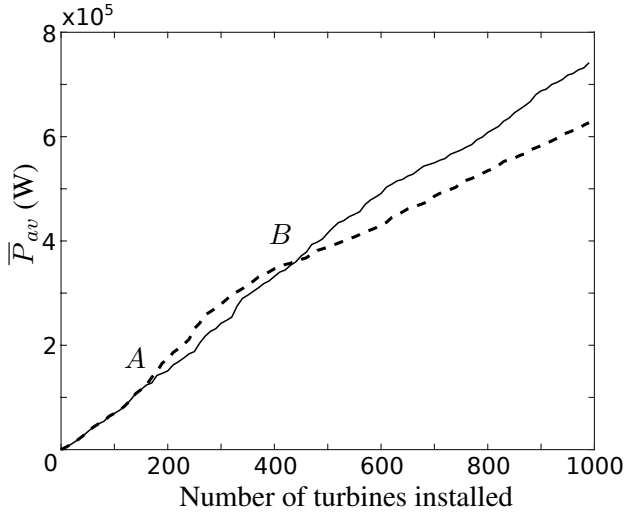

Figure 3.10: Variation in $\overline{P}_{av}$ with number of turbines installed for strategy 2 (dashed line) and strategy 3 (solid line).

ever, $\overline{P}_{av}$ diverges as strategy 2 continues to add turbines to the same row whereas strategy 3 begins placing turbines in a second row behind the first. Between points A (170 turbines installed) and B (440 turbines installed), strategy 2 produces more power than strategy 3, which is somewhat counter-intuitive given that it is the more constrained strategy. Beyond point B, however, strategy 3 begins to outperform strategy 2. The arrays produced by the different strategies for 440 and 1,000 turbines are illustrated in Figures 3.11 and 3.12.

The difference in power produced by the two strategies is explained as the choice between placing turbines only in parallel (strategy 2) or also allowing placement of turbines in series (strategy 3), along with the varying kinetic energy distribution across the channel cross-section. The optimal arrangement is, of course, highly dependent on the site geometry and flow dynamics (Vennell et al., 2015). It was noted by Divett et al. (2014) that, in an idealised site with uniform kinetic energy distribution across the width of the channel, the addition of turbines in a parallel configuration serves to increase their B_G, which results in an increase in $\overline{P}_{av}$ (Garrett and Cummins, 2007). Conversely, the addition of turbines in a series configuration means that a much greater thrust is applied to the flow through a smaller

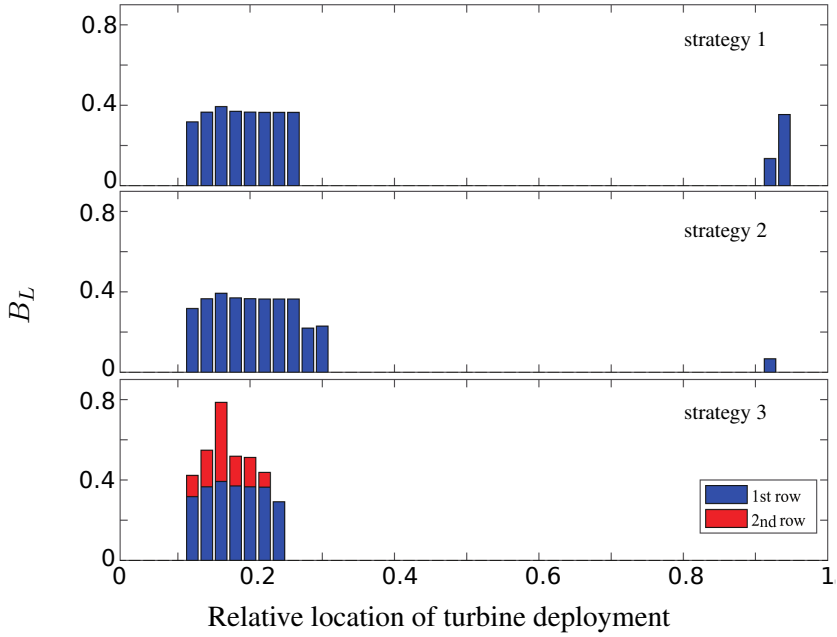

Figure 3.11: Optimal arrangements (cross-sectional views of local blockage distributions) of 440 turbines corresponding to the different development strategies.

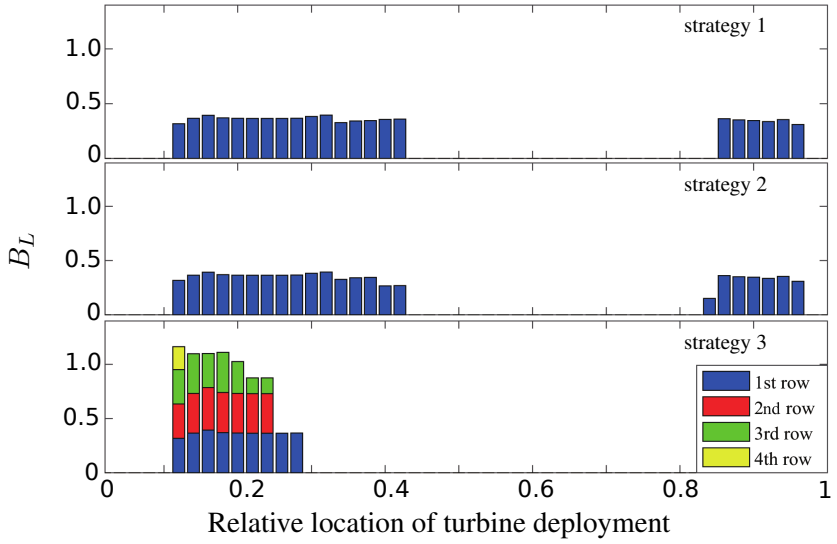

Figure 3.12: Optimal arrangements (cross-sectional views of local blockage distributions) of 1,000 turbines corresponding to the different development strategies.

B_G. Due to the negative interference effect between turbine rows in this placement, the series strategy is generally considered less effective than the parallel strategy. However, at a real site, current velocities vary significantly throughout the channel cross-section; as such, the series configuration is more effective in cases where the kinetic energy flux is higher in certain sections. The initial benefit from the parallel arrangement, between points A and B and due to the global blockage effect, is eventually exceeded by the benefit from the series arrangement, which allows several rows of turbines to be placed at the section with the higher kinetic energy flux. Therefore, it can be seen that, for a certain number of turbines, strategy 2 is better; however, strategy 3 proves to be more beneficial overall, especially for a large number of tidal turbines in the array.

Figure 3.13 plots the spanwise kinetic energy flux profile before and after the installation of the turbine arrays. The figure clearly shows two peaks at the ends of the profile, with the left peak much higher than the right. In strategy 2, the turbines are constrained to be placed within a single row, so the left peak region where there is high kinetic flux is exploited first, before the next deployment is made to exploit the area of the right peak. The placement of turbines is less constrained in strategy 3, which allows for the multi-row installation of turbines in all sections with the highest kinetic flux. It is clear that the increased number of rows installed in strategy 3 affects the kinetic energy flux profile the most, as they serve to reduce the flow through the array and also enhance the array-scale bypass flow. The disadvantage of strategy 2, as compared to strategy 3, is that the turbines must be placed in the sections with lower kinetic energy flux at a later stage.

Figure 3.14 shows the growth of $\overline{P}_{av}$ per turbine (defined as total $\overline{P}_{av}$ divided by number of turbines installed) for strategies 2 and 3, which the global blockage effect serves to initially enhance in addition to the combined power output. However, as each new turbine is placed in a less favourable location for strategy 2, $\overline{P}_{av}$ per

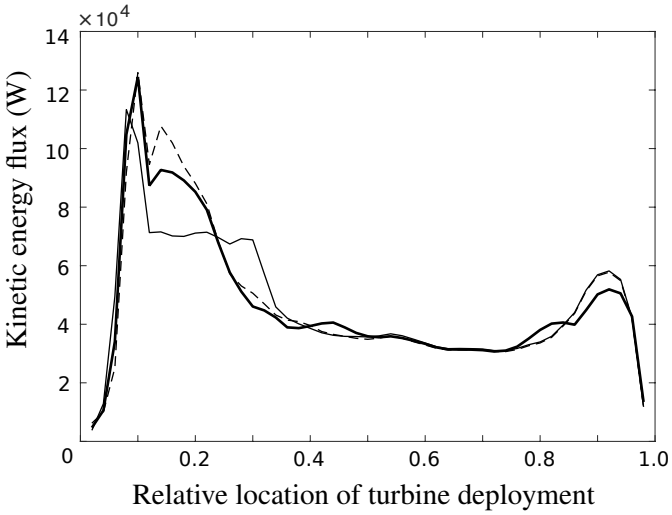

Figure 3.13: Spanwise kinetic energy flux profile for the unexploited case (dashed line) and for arrays of 1,000 turbines built using strategy 2 (thick solid line) and strategy 3 (thin solid line).

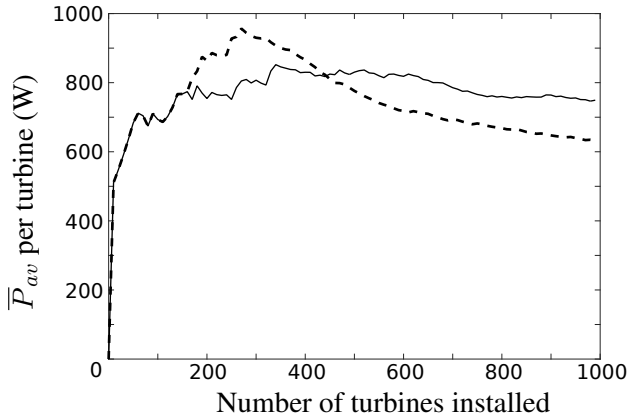

Figure 3.14: Variation in $\overline{P}_{av}$ per turbine with number of turbines installed using strategy 2 (dashed line) and strategy 3 (solid line).

turbine then starts to decline. A similar but less severe reduction in power can be found with strategy 3, caused by the law of diminishing return (Vennell, 2010). It is surprising that the curve for strategy 3 remains relatively flat even after three rows of turbines — since the output power is proportional to the cube of the throughflow velocity, it should be significantly reduced by the thrust from three turbine rows. This suggests that there is no obvious diminishing return on the placement of successive turbine rows in this case. To explain this, some simplifying assumptions about the hydrodynamics of the site are made to enable comparison to the idealised

channel model of Garrett and Cummins (2005). The phase lag between the head difference and current at the site is found to be $\approx 30^{\circ}$, which corresponds to a natural dynamic balance of $\lambda_0 \approx 2$. This implies that the natural impedance of the site is quite high, giving it characteristics similar to a drag-dominated site. Thus, the kinetic energy flux profile appears to be relatively insensitive to the thrust from turbines, allowing multiple rows to be installed in the left peak area. Interestingly, strategy 1 (the naturally-occurring kinetic energy flux approach) is able to produce an optimal array very similar to that produced by strategy 2, as shown in Figures 3.11 and 3.12. Strategy 1 appears effective in this case but this is likely only due to the drag-dominated nature of the site. Therefore it is not recommended that strategy 1 be used more generally.

In the perspective of a resource assessment, results of the power produced per turbine has demonstrated that the energy resource is fairly limited, suggesting that the overall significance and feasibility of the particular site considered here may be low. However, the turbine arrangement methodology developed in this work can still be applied at other candidate sites and provides an approach to inform the design and development of tidal turbine arrays.

3.3.3 Additional tidal constituents

Having explored optimal arrangements for turbines in a simplified flow through the Bohai Strait, a more realistic situation is considered. In this scenario, the model is forced with both M_2 and K_1 tides and is allowed to spin up for 5 days from still water conditions before results from the following 14 days are recorded for analysis. Optimal α_4 values are obtained from the standard cubic spline interpolation following the work of Serhadlıoğlu (2014) to calculate $\overline{P}_{av,max}$, although given the drag-dominated nature of the site, these are found to be close to $\alpha_4 = 1/3$ (see Vennell, 2010). A fourth array design strategy, in which the turbines are distributed

Table 3.6: $\overline{P}_{av}$ (W) for different array design strategies.

Number of turbines	Even	1	2	3
440	2.88 x 10^5	7.86 x 10^5	8.13 x 10^5	7.74 x 10^5
1000	8.29 x 10^5	1.44 x 10^6	1.42 x 10^6	1.51 x 10^6

evenly across the site (i.e. turbines are placed in each section but with variable B_L), is included for comparison. Table 3.6 shows the results obtained for the deployments of 440 and 1,000 turbines using the four different strategies (including the 'even' fourth strategy) for the cases involving the additional tidal constituent and longer model run time.

Even with additional tidal constituents, the results are found to be similar to the finding in Section 3.3.2 — for a deployment of 440 turbines, strategy 2 is shown to be slightly superior, but for the placement of 1,000 turbines, strategy 3 proves to be more beneficial. Moreover, when comparing the even strategy to strategy 2, Table 3.6 shows that $\overline{P}_{av}$ increases by 282% and 171% for the deployment of 440 and 1,000 turbines, respectively. This finding verifies the benefit of the local blockage effect, as suggested by Nishino and Willden (2012*b*). However, it is difficult to distinguish here between the effects of the kinetic energy flux profile and the effects of global and local blockage. These three effects would have contributed in different ways to the different strategies, and it is difficult to separate them in a real site.

3.3.4 Limitations

There are several limitations to the array design strategies proposed above, some of which have already been discussed briefly. Firstly, for many earlier simulations, only the M_2 tide is considered, which may not be sufficient to capture all of the key physics, therefore resulting in some differences in optimal array layout. In an attempt to rectify this problem, additional simulations have been performed in Section 3.3.3 with an additional tidal constituent and a longer simulation run time.

Secondly, in each run of strategies 2 and 3, all of the turbines are assumed to have $\alpha_4 = 1/3$, which is not calibrated for maximum power capture by the whole array over a tidal cycle, due to greater computational requirements. Individualised tuning strategies, such as the 'fixed' and 'dynamic' strategies discussed later in Chapter 5, should be considered.

Thirdly, in these strategies, the intricacy of simulating each turbine placement in relation to the cases immediately before and after it could limit the results of $\overline{P}_{av}$ to localised maxima, instead of a global maximum value that results from all the runs simultaneously. However, due to the design of the strategies, it can be difficult both methodologically and computationally to calculate the global maximum of the available power.

Lastly, even though global and local blockage effects have been included, they are not isolated. Understanding the optimal arrangement of tidal turbines requires consideration of these effects along with the kinetic energy flux profile, which are difficult to differentiate as all three factors affect the results by varying degrees.

3.4 Conclusions

This chapter has explored different strategies for building tidal turbine arrays in China's Bohai Strait. The available tidal resource in this region is relatively small and so it is unlikely to make a promising site for future tidal stream power development. This analysis, however, allows us to examine the difficulties of arranging tidal turbines in real locations with varying bathymetry and more realistic flow patterns. New design strategies based on the kinetic energy flux profiles have been used to design tidal turbine arrays. The optimal arrangements have been found to be highly dependent on both the dynamics of the site and the number of turbines installed. For this drag-dominated site, the results have shown that it is advantageous to concentrate the turbines in the areas of highest kinetic energy flux with a series

configuration, but it is also noted that this may not be the optimal strategy for other candidate sites, especially those that are inertia-dominated.

Several processes that affect the optimal arrangement of tidal turbines at real sites have been identified in this study. The first is the natural distribution of kinetic energy flux, which is particularly important for small deployments of turbines. The second is array-scale flow diversion and reduction, which are closely related to the array operation strategy. Optimising the resistance ('tuning') for different array configurations and channel dynamics is crucial to maximising their power output, which may be found to be more evident in inertia-dominated channels (Vennell, 2010). However, tuning is not fully explored in this chapter due to the computational limit in the optimisation process for a real site. The final point is the consideration of array layout. The importance of local blockage has been briefly demonstrated in the arrangement of turbines within a tidal stream to maximise their collective performance, as increasing the density with which turbines are packed means they can operate with higher C_P. Additionally, the preference between parallel and series turbine placements may be highly dependent on the candidate site and the tidal array development plan proposed.

The optimal arrangement problem remains a complex one. A few different array design strategies have been considered, and an attempt made to analyse the underlying physics, which is especially complicated for actual sites. Whilst strategies based purely on numerical optimisation have their advantages, there is potential to improve these with intermediate, simpler strategies such as those used here and with insights into the key physics of the problem.

3.4.1 Further direction in thesis

It has become apparent from this chapter that determining the optimal arrangement of tidal stream turbines at a real site is challenging, and solving this problem in its

entirety is beyond the scope of this thesis. Instead, the rest of this thesis focuses on several key aspects of the problem by making some simplifying assumptions regarding both the turbine and the tidal flow, while maintaining appropriate conditions for the operation of turbines. One of the key assumptions adopted in the following chapters is the use of a simplified and idealised rectangular channel. This simplified assumption can reduce the computational intensity of the modelling domain, allowing the fundamental behaviours of tidal turbine arrays in channels and their key physics to be studied in greater detail and set apart from the complexities of a real site; this provides useful, general insights on array design and operation. In the following chapters, various optimal tuning strategies and arrangements (with a focus on the local blockage effect) are extended analytically and numerically, particularly with the use of a more realistic representation of the axial-flow tidal turbine highlighted in the next chapter.

Chapter 4

Implementation and Limitations of the Blockage-Corrected Blade Element Momentum Theory *

Accuracy in resource assessment typically requires the development of basin-scale models that can account for the presence of tidal turbines. It is presently computationally infeasible to capture all spatial and temporal details of the flow characteristics through and past a tidal turbine array at such a scale, so idealised models of tidal turbines are usually applied. The actuator disc theory provides a useful starting point for the analysis of tidal turbine performance, and has proven valuable in establishing upper bounds on $\overline{P}_{av}$ for rows of turbines placed at candidate tidal power sites (e.g. Adcock et al., 2013). However, it models the turbine rotor as a uniform disc, which only removes axial momentum from the flow and thus affords only an idealised description of turbine performance.

The purpose of this chapter is to replace the actuator disc model with a more realistic model to provide practical insights into resource assessments as well as various array design and operation strategies. Using CFD or similar approaches

*The discussions in this chapter and Chapter 5 have been published together as a both a workshop abstract and journal paper — see Chen et al. (2018a, 2019a) from Appendix C.

is very costly and coupling them with a large-scale model is generally infeasible. As a compromise, a model that captures the leading order physics of a turbine but is much more computationally simple is proposed; inevitably, it will also contain certain limitations. In this thesis, the blockage-corrected blade element momentum theory (BC-BEMT), which is expanded from the classical unbounded BEMT developed for use with wind turbines by Vogel et al. (2018) to account for blockage effects, is chosen. The model, whilst still an approximation of real turbine operation, contains significantly more underlying physics than the actuator disc theory with only marginally greater computational cost and provides a broader parameter space within which turbine performance can be explored. While this chapter is primarily a method chapter and mainly describes the theory which has been developed and published by others, the detailed discussion of the BC-BEMT implementation and limitation by the author go beyond the material previously published and serve as a foundation for the novel analysis in the subsequent chapters.

This chapter begins with a review of the classical BEMT model in Section 4.1, while the detailed implementation of the BC-BEMT is elaborated in Section 4.2. Section 4.3 introduces the three rotors used in this project, designed using the Reynolds-averaged Navier Stokes equations combined with the blade element model (RANS-BE). Discrepancies between the simulation results produced by both analytical and numerical models, which incorporate the RANS-BE-designed rotors, are explained and considered as well. Finally, the modelling of the actuator disc and tidal rotor turbine representations is described in Section 4.4, where a comparison is first made between the disc and the variable-speed, fixed-pitch (FP) rotor. This is followed by a study on the performance of the variable-speed, variable-pitch (VP) rotor, with different rotor types simulated in design and off-design blockage conditions. This section also includes a discussion of the BC-BEMT in the context of this work, highlighting both its inherent limitations and its inability to handle the

extreme operating conditions found in various operation strategies adopted in the subsequent chapters.

4.1 Blade Element Momentum Model

The BEMT combines the linear momentum theory with the blade element theory to offer a more advanced low-order turbine model to account for the aerodynamic (or hydrodynamic) characteristics of the turbine blades, thus providing a more realistic description of turbine performance compared to the actuator disc theory (Glauert, 1983). A brief description of the theory and its underlying assumptions will suffice for the purposes of this study; see Burton et al. (2011) for further details.

In blade element theory, a turbine of n blades rotating at an angular velocity of ω is modelled as a disc, which is divided along its spanwise length R into i blade elements, the swept areas of which take the form of i concentric annular rings (Figure 4.1a). The lift force and drag force on each blade element are calculated from 2D aerofoil (or hydrofoil) characteristics by specification of the axial induction factor a_{2i}, tangential induction factor a'_{2i}, relative inflow velocity W_i, blade pitch angle β_i, and the angle of attack α_i (Figure 4.1b). Following the convention of the BEM analysis, induction factors are used throughout this chapter instead of velocity

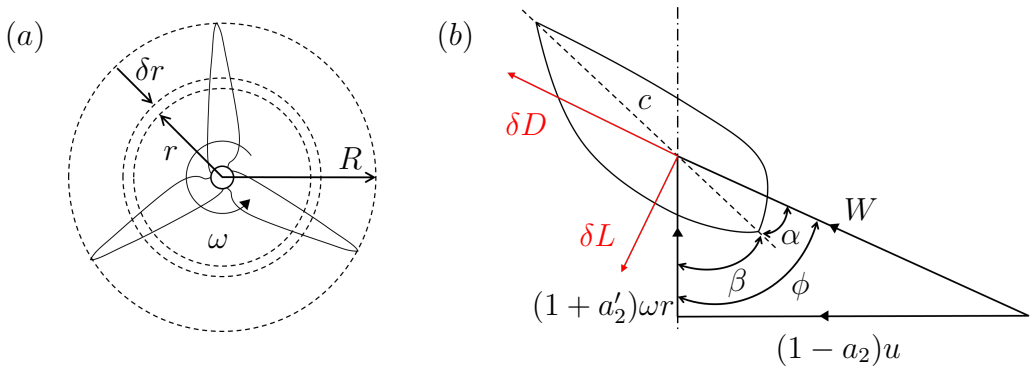

Figure 4.1: Schematic diagrams showing: (a) the discretisation of the turbine rotor into blade elements and annular rings, and; (b) the resolution of lift and drag forces on the blade section. Adapted from Burton et al. (2011).

factors.

Neglecting spanwise velocities and 3D flow effects, the axial and tangential velocities experienced by each blade element are given by $(1-a_{2i})u$ and $(1+a'_{2i})\omega r$, respectively, in which u is the axial inflow velocity and r is the radial (or spanwise) distance from the centre of the rotor. The sectional lift δL, which acts on a spanwise length of δr of the blade and in a direction normal to that of the relative W_i, is then given as:

$$\delta L = \frac{1}{2}\rho W_i^2 c_i C_{Li} \delta r, \tag{4.1}$$

in which c_i is the chord length of the blade section, and C_{Li} is the lift coefficient (Burton et al., 2011). The sectional drag δD, which acts on the spanwise length δr and in the direction of W_i, is then given by:

$$\delta D = \frac{1}{2}\rho W_i^2 c_i C_{Di} \delta r, \tag{4.2}$$

in which C_{Di} is the drag coefficient of the force on the blade. Based on the geometric relationships from Figure 4.1b, the relative W_i approaching the blade element at an inflow angle of $\phi_i = \alpha_i + \beta_i$ may be calculated as:

$$W_i = u\frac{1-a_{2i}}{\sin\phi_i}. \tag{4.3}$$

In the BEMT, the forces acting on each annular ring are related to the change in the momentum of the fluid passing through the rotor. Since spanwise velocities are neglected, it is assumed that there is no momentum transfer between annular elements. The theory also assumes that all fluid particles passing through a given annular element experience the same change in momentum, neglecting the gaps between the n rotating blades (Burton et al., 2011). To account for this, a simple tip correction method is used to derive the azimuthally averaged induction variables required by momentum equations from the blade element analysis: the blade-local

a_{2i} and a_{4i} are multiplied by a dimensionless tip correction factor, F_i, which is given by (Glauert, 1983):

$$F_i = \frac{2}{\pi}\cos^{-1}\left[\exp\left[\frac{n(1-(R/r))}{2\sin\phi_i}\right]\right]. \tag{4.4}$$

Using this function, the value of F is set to unity for most of the blade span, where the gaps between the blades are assumed to be small, but decreases to zero at the blade tip, where the gaps are much larger (Eggleston and Stoddard, 1987).

Blade element theory also gives expressions for the sectional axial thrust δT and tangential torque $\delta\tau$ acting on the spanwise length δr. These are equated to the changes in the axial and angular momentum of the flow passing through a given annular element, following the work of Burton et al. (2011), to give:

$$\delta T = \frac{1}{2}\rho W_i^2 n c_i (C_{Li}\cos\phi_i + C_{Di}\sin\phi_i)\delta r = 4\pi r \rho u^2 (1-a_{2i}F_i)a_{2i}F_i\delta r, \tag{4.5}$$

$$\delta\tau = \frac{1}{2}\rho W_i^2 n c_i (C_{Li}\sin\phi_i - C_{Di}\cos\phi_i) r\delta r = 4\pi r^3 \rho u (1-a_{2i}F_i)a'_{2i}F_i\omega\delta r. \tag{4.6}$$

Integrating δT and $\delta\tau$ over all the blade elements gives the total thrust T and power P of the rotor, and consequently the rotor thrust and power coefficients, C_T and C_P, which have been defined in Chapter 2.

4.2 Blockage-Corrected Blade Element Momentum Model

The BEMT provides a more physically accurate description of turbine performance than the actuator disc theory, because it accounts for the spatial variations in the flow and attempts to model the forces developed by real turbine blades (Burton et al., 2011). However, the classical BEMT does not account for the effects of flow confinement (blockage). Unconfined flow is a reasonable approximation for wind

turbines, which normally take up a negligible part of the atmospheric boundary layer. However, for tidal turbines, the blockage effect has a significant influence on their performance and cannot be ignored in the analysis (Garrett and Cummins, 2007; Nishino and Willden, 2012*a*). To address this issue, Vogel et al. (2018) have recently extended the classical BEMT to take into account the constrained flow field (also see Vogel, 2014). More specifically, the blade element theory is used to model the turbine, which incorporates the turbine hydrodynamic characteristics, and is coupled with the analytical volume-flux-constrained momentum theory developed by Garrett and Cummins (2007).

In the classical, unbounded linear momentum theory, it is assumed that the static pressure in the near wake of the turbine recovers to the level of the upstream static pressure in the far wake, which results in the velocity deficit in the far wake being twice that at the turbine plane. For bounded flow, however, the acceleration of the confined bypass flow results in the development of a streamwise static pressure difference along the flow passage, which enables the turbine to apply a higher thrust coefficient and thereby achieve a higher $C_{P,max}$. The BC-BEMT accounts for this greater pressure difference by equating the axial thrust predicted by blade element theory to the change in fluid momentum predicted by the volume-flux-constrained linear momentum theory, whilst the analysis of tangential components remains the same as in the classical BEMT (Vogel et al., 2018).

Figure 4.2 illustrates the side view of the BC-BEMT model, where the actuator disc is similarly assumed to be separated into concentric annuli and a bypass flow surrounds a number of annular streamtubes of width δr. Although it is possible for the flow speed between each annular streamtube and the bypass flow to differ, the downstream boundary of the model exists at a point where the streamwise static pressure across all annular streamtubes and the bypass flow is equalised. Similar to the work done by Garrett and Cummins (2007), the flow past the rotor is analysed

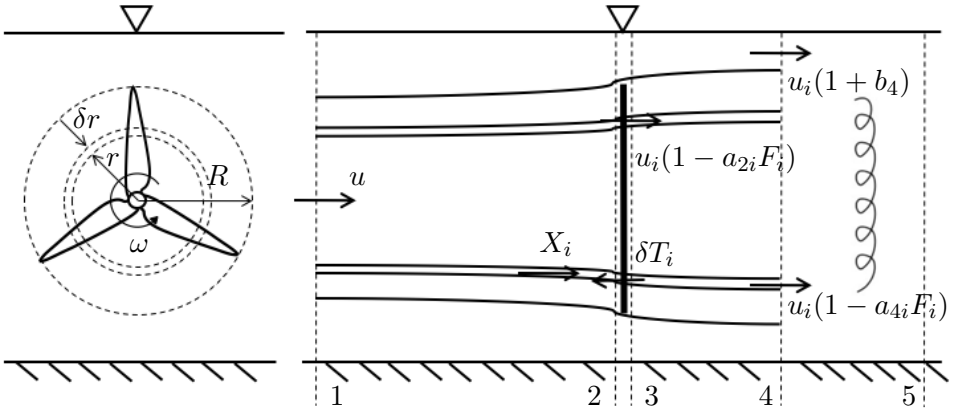

Figure 4.2: Schematic diagram (streamwise and cross-stream views) of the BC-BEMT model, adapted from work by Vogel et al. (2018).

at five different stations. In each annular streamtube, the conservation of mass, momentum, and energy are considered and enforced.

As with the classical BEMT, expressions for a_{2i} and a'_{2i} can be obtained by equating both thrust and torque on the blade elements to the momentum flux through the i^{th} annulus. Being a net effect of the change in static pressure and thrust, the change of momentum in the i^{th} streamtube is expressed as:

$$p_1\delta A_{1i} - p_4\delta A_{4i} + p^*\delta A^* - \delta T_i = -\rho\delta A_i u^2(1-a_{2i}F_i)a_{4i}F_i, \tag{4.7}$$

where $p^*\delta A^*$ is the confining force X_i due to the expansion of the streamtube between station 1 and station 4. A further assumption by Nishino and Willden (2013) approximates the term $p_1\delta A_{1i} + p^*\delta A^*$ as:

$$p_1\delta A_{1i} + p^*\delta A^* = p_1\delta A_i(1-a_{2i}F_i) + p^*\delta A^* \approx p_1\delta A_{4i}. \tag{4.8}$$

By applying the conservation of mass, the following relationship can be obtained:

$$\delta A_{4i} = \frac{1-a_{2i}F_i}{1-a_{4i}F_i}\delta A_i. \tag{4.9}$$

Utilising the Bernoulli equation in the bypass flow yields:

$$p_1 - p_4 = \frac{1}{2}\rho u^2(b_4^2 + 2b_4). \tag{4.10}$$

Combining Equations 4.9 and 4.10, the momentum balance in Equation 4.7 can be rearranged to obtain:

$$\delta T_i = \rho\pi r_i u^2 \frac{1 - a_{2i}F_i}{1 - a_{4i}F_i}(b_4^2 + 2(b_4 + a_{4i}F_i) - 2a_{4_i}^2 F_i^2)\delta r. \tag{4.11}$$

By equating this calculated change of momentum to that subjected by the sectional thrust generated in the i^{th} annulus (Equation 4.5), an expression for a_{2i} can be derived:

$$a_{2i} = \frac{(2\frac{\sigma_i\mu_i}{\sin\phi_i^2}(1 - a_{4i}F_i) - F_i\gamma_i) - \sqrt{\gamma_i(F_i^2\gamma_i - 4\frac{\sigma_i\mu_i}{\sin\phi_i^2}(1 - a_{4i}F_i)(1 - F_i))}}{2\frac{\sigma_i\mu_i}{\sin\phi_i^2}(1 - a_{4i}F_i)}, \tag{4.12}$$

where $\sigma_i = nc_i/2\pi r_i$ is the blade solidity, $\gamma_i = (b_4^2 + 2(b_4 + a_{4i}F_i) - 2a_{4i}^2F_i^2)$, and $\mu_i = C_{Li}cos\phi_i + C_{Di}sin\phi_i$. Similarly, a'_{2i} can be derived as:

$$a'_{2i} = \frac{\sigma_i(C_{Li}\sin\phi_i - C_{Di}\cos\phi_i)(1 - a_{2i})}{4\sin\phi_i\cos\phi_i F_i(1 - a_{2i}F_i) - \sigma_i(C_{Li}\sin\phi_i - C_{Di}\cos\phi_i)(1 - a_{2i})}. \tag{4.13}$$

Closure of the equations is achieved by using the actuator disc theory from Garrett and Cummins (2007) and considering that the change in momentum predicted by the volume-flux-constrained actuator disc theory is equal to the total axial thrust predicted by blade element theory.

Figure 4.3 illustrates the calculation procedure for the BC-BEMT. Before performing the calculations, it is necessary to provide details of the rotor geometric and hydrodynamic characteristics, including the number of blades, the blade solidity and twist profiles, and the lift and drag coefficients of the constituent hydrofoil. The simulation settings include the operating condition, such as the axial inflow ve-

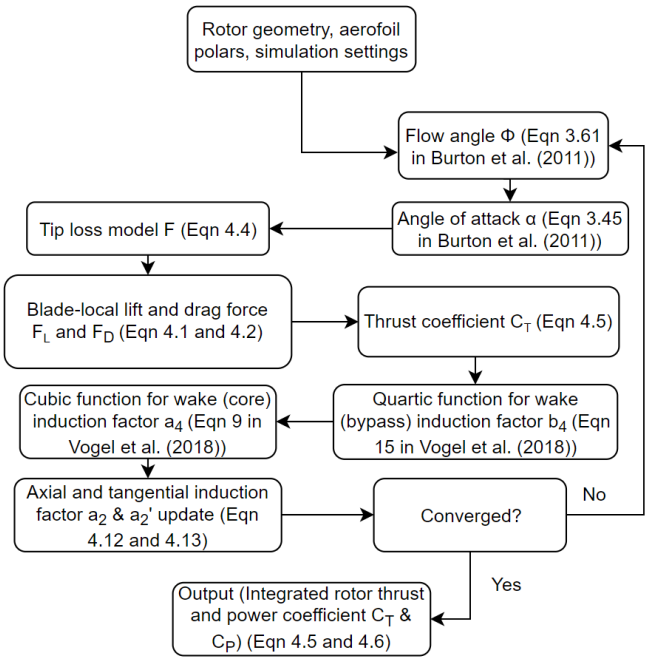

Figure 4.3: Flow chart of the BC-BEMT calculation procedure.

locity u, the blockage ratio B, and the tip speed ratio TSR (which is defined as the ratio of the rotational speed of the blade tip, ωR, to u). The initial estimates of a_2, a_2' and a_4 are set to 0.3, 0.01 and 0.6, respectively. These initial guesses are based on the common range of the relevant parameters found in the classic unbounded BEMT (Vogel et al., 2018).

The calculation begins by computing ϕ, α, F, and the sectional lift and drag forces on each blade element. As in the classical theory, δT and are integrated over all blade elements to obtain C_T. The model then solves cubic and quartic equations to obtain a_4 and the corresponding wake bypass velocity factor, b_4 (see Equations 9 and 15 in Vogel et al., 2018). Finally, the values of a_2 and a_2' are updated and fed back into the calculation sequence. The iteration continues until the convergence criteria of a relative error $<10^{-6}$ is achieved for both a_2 and a_2'. The 3D blade-resolved CFD simulations have been used to compare the results of the BC-BEMT model (Vogel et al., 2018). In these simulations, the performance of a rotor designed

for unblocked conditions (in which the rotor design blockage ratio B_r is 0.01) has been investigated in four different blockage ratios. The results show that the BC-BEMT provides reasonably good agreement in terms of the C_P and C_T predictions of the rotor.

In this study, two types of rotor devices are considered. Firstly, the Fixed Pitch rotor (FP) boasts mechanical simplicity as it offers a potential reduction in costs by eliminating variable-pitch components and reducing maintenance requirements, while also offering greater reliability. The FP rotor blades are installed at a prescribed value of β and the turbine is controlled by altering its TSR. The Variable Pitch rotor (VP), on the other hand, is frequently adopted by large-scale wind turbine designs and may be more desirable for current tidal turbine developments (Boukhezzar et al., 2007). Though more complex, the VP rotor generally offers superior performance, particularly in off-design operating conditions, because its β can be varied and there is an extra degree of freedom in the design with which to manipulate the turbine characteristics.

As with actuator disc theory, the key variables for the BC-BEMT are B and the tuning parameter. In blade element theory, however, the tuning factors are replaced by variables more closely related to the operation of the rotor: TSR and $\beta = \beta_d + \beta_a$, which comprises the design pitch angle β_d (relevant to both FP and VP operation), and the adjustable pitch angle β_a (for VP operation only). To enable direct comparison between the actuator disc theory and the BEMT, the area-weighted average value of turbine resistance, k, can be calculated for the rotor as:

$$k = \frac{\int_{r_{nace}}^{R} \delta k_i 2\pi r dr}{\pi(R^2 - r_{nace}^2)}, \tag{4.14}$$

where k_i is the local thrust coefficient at each annular ring and r_{nace} is the radius of the turbine nacelle. For a given rotor, k may be increased by increasing TSR, so as to increase the rotational speed of the blades, and/or by reducing β_a, so as to

pitch the blades to 'stall'. Conversely, k may be reduced by decreasing TSR and/or increasing β_a, so as to pitch the blades to 'feather'.

4.3 Rotor Inputs

As noted in Chapter 2, a higher-order blade element model may be obtained by using the 3D steady RANS equations (known as the RANS-BE method) to model the flow field rather than the four stations described in the simple analytical model. By modelling the disc in a highly resolved numerical flume, this method has been widely used in studies investigating the performance of tidal turbines and arrays (Schluntz and Willden, 2015; Turnock et al., 2011; Wimshurst and Willden, 2016*a*).

A RANS-BE model has been developed by McIntosh et al. (2011), in which a blade element code has been implemented as a user-defined function embedded into ANSYS FLUENT. The rotor is modelled as a disc with a number of cells and the annular ring is constructed by counting the cell at the same azimuthal radial distance. The force experienced by each cell depends on the flow field at the disc plane, which is calculated by the blade element code and exerted on the flow field by applying a static pressure difference and swirl velocity across each cell. The resulting changes to the flow field are then captured by the RANS equations, which consequently alters the flow field at the disc plane and thus the force generated by the disc (Cao et al., 2018). The iteration proceeds until the coupled blade element calculation and RANS simulation converge. Belloni (2013) uses this RANS-BE tool to design tidal rotors for open-centre and ducted turbines. Schluntz and Willden (2015) have applied this model to design tidal turbine rotors for operation in different channel cross-sectional blockage conditions and to assess their performance. Cao et al. (2018) further utilised this model to investigate the effects of turbulence intensity and the blockage ratio on tidal turbine performance.

With the RANS-BE model as a design tool, the model of McIntosh et al. (2011)

aimed to achieve the maximum power coefficient, $C_{P,max}$. For a given set of design conditions, including u, TSR and B, the model includes an iterative tool that can repeatedly adjust the chord length and twist angle on each annular ring such that the desired local thrust coefficient, c_{xi}, is achieved and the optimal angle of attack, α_{opt}, is maintained on each annular ring. The value of α_{opt} depends on the hydrofoil lift and drag coefficients used for the blade and is usually specified as the angle corresponding to the maximum lift to drag ratio.

The value of c_{xi} represents the thrust coefficient found locally to each annular ring (Schluntz and Willden, 2015), which is effectively the same as the k_i introduced in the BC-BEMT section above. Belloni (2013) has found a negligible difference between the varied and constant local thrust coefficient specification along the blade, so it has been decided that the value of c_{xi} can remain constant over the blade for all three rotor designs adopted here (Cao et al., 2018; Schluntz and Willden, 2015). For each c_x, the optimisation tool will return a rotor design with its C_P. The optimal rotor design to obtain $C_{P,max}$ for a given B can then be found by comparing the C_P from a range of different c_x. The value of c_{xi} is defined as:

$$c_{xi} = \frac{\delta T}{\frac{1}{2}\rho \delta A_{disc} {u_{xi}}^2}, \tag{4.15}$$

where u_{xi} ($= u(1 - a_{2i}F)$ in Figure 4.2) is the local axial velocity experienced by each annular ring and δA_{disc} is the area of each annular ring, which can be approximated by $2\pi r \delta r$ (Cao et al., 2018).

The three rotors used in this work are taken from published literature. They have been designed specifically for a low blockage of 0.01 (virtually unblocked), a moderate blockage of 0.16, and a very high blockage of 0.314, using the RANS-BE design tool. The rotors designed for the two former cases are obtained from Cao et al. (2018) and they have been validated against blade-resolved simulations, with satisfactory agreement found in the thrust and torque distribution comparisons. As

Cao et al. (2018) did not have a rotor designed for higher blockage, the rotor design for high blockage is obtained from the work of Schluntz and Willden (2015). By investigating a range of target TSR values for the three blockage ratios under the same design inflow speed of $u = 2$ m/s, the optimal values of TSR for the rotors of $B_r = 0.01$, $B_r = 0.16$, and $B_r = 0.314$ have been found to be 5.5, 5.5, and 5, respectively. All rotors for this work have $D = 20$ m and a nacelle of diameter $0.15D$ has been included, which results in a range of $0.15D/2 < r < D/2$ for the entire span of the rotor blades, with no transition or cylindrical blade sections employed. The constituent hydrofoil is the Risø-A1-24 profile, which offers a realistic ratio of maximum thickness to chord length and a smooth post-stall region. The values of C_L and C_D are obtained with a Reynolds number of $Re = 12 \times 10^6$ for the current study from the work of Wimshurst and Willden (2016*a*), as representative of a full-scale tidal turbine operation. As shown in Figure 4.4, a large range of α values is investigated due to the wide range of off-design conditions that will be studied in later sections and the requirements of numerical stability.

The findings by Vogel et al. (2018) have touched on the capability of the BC-BEMT model in capturing the general trend for both axial and tangential force distribution along the blade obtained from blade-resolved simulations. However, with the assumption that the stages of wake expansion (station 3 to 4 in Figure 4.2) and wake mixing (station 4 to 5) are completely separated, the analytical model is unable to resolve the complex wake characteristics. For example, the model cannot resolve the interaction between enhanced shear flows and the expansion of the wake, which may affect the blockage effect (Cao et al., 2018). Thus, when applying both the analytical BC-BEMT simulation and the numerical RANS simulation with the same rotor design, it is expected that the discrepancy of the rotor performance between the two techniques is smaller for the low-blockage case, while the difference is enlarged at high blockages. It should be noted that the complex physics of the

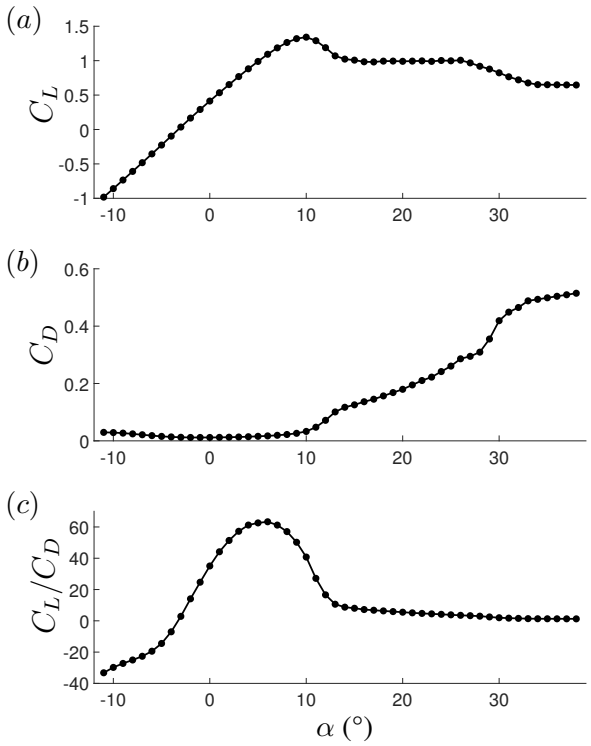

Figure 4.4: Variations with α in: (a) C_L; (b) C_D, and; (c) C_L/C_D, for the Risø-A1-24 hydrofoil and $Re = 12 \times 10^6$, adapted from Wimshurst and Willden (2016*a*).

constrained flow field at high blockage conditions may be currently imperfect for both modelling techniques and a higher fidelity CFD numerical model (e.g. blade-resolved simulation) is still required if all the relevant physics are to be accurately simulated. Reflecting on the works of Cao et al. (2018) and Vogel et al. (2018), the discrepancy can be observed by comparing the torque distribution along the blade of the blade-resolved simulation to the BC-BEMT and RANS-BE simulations, in which the former tends to underestimate the results while the latter tends to overestimate them.

The variation found in comparison can also be attributed to the complexity of the flow around the blade tip. As flow diverts around the blade tip, radial flow is increased (and thus the axial component is reduced) at the outermost edges of the disc — the BC-BEMT model is unable to reflect this phenomenon, whereas it is apparent in the RANS-BE model (Belloni, 2013). In addition, the effect of the

Glauert tip correction model in the BC-BEMT reduces a_2 to zero near the blade tip and hence the flow velocity is equal to the free stream velocity. However, for the RANS-BE model, the velocity near the blade tip can exceed the free-stream flow speed in high blockage conditions due to the accelerated bypass flow.

Thus, due to the different flow physics that the two methods take into account, when the optimal rotors designed by the RANS-BE method are analysed using the BC-BEMT method, their performance may be sub-optimal even in their design conditions. The proposed BC-BEMT model can potentially become a useful and cost-efficient tool for tidal rotor design, as long as its deficiencies when compared with the RANS-BE method and its own restrictions and limitations are well understood and fully considered (Section 4.4.2). Nevertheless, without incorporating additional correction models or conducting detailed validations, the feasibility of the rotor designed by the BC-BEMT model remains questionable. As such, the following studies in this thesis use the rotors designed using the RANS-BE method.

4.4 Rotor Operations

The BC-BEMT model provides us with a valuable opportunity to re-examine the representational accuracy of the actuator disc, and also the flexibility to explore the parameter space in design and off-design turbine operation modelling. This section of the chapter will mainly aim to discuss two findings, the first of which is the resulting difference in C_P, C_T and η curves between the idealistic disc and the more realistic rotor with a FP mechanism. Secondly, the investigation is extended to rotors with a VP mechanism, which afford a greater degree of operational flexibility and allows the rotors to be simulated over a wide, yet still restricted, range of operating conditions. The performance curves and surfaces for both types of rotors will form the foundation for the analysis in the following chapters. In addition, different rotor designs are simulated in both design and off-design blockage conditions,

which may provide some valuable insight into the sensitivity of the results from Chapter 5.

The BC-BEMT is known to provide a less accurate description of turbine performance in capturing off-design and highly blocked flow conditions. Some of the limitations are caused by inherent issues within the BEMT model itself, which are illustrated in Sections 4.4.2.1 and 4.4.2.2, while others are due to the inability of the BC-BEMT model to simulate extreme off-design conditions, some of which are discussed in Sections 4.4.2.3-4.4.2.5, and are further explored by different operating strategies in Chapter 5.

Since the wide range of off-design conditions are achieved by altering both the rotational speed and the pitch angle of the rotor blades, in order to somewhat account for these limitations, less accurate and non-physical flow solutions are precluded by restricting the range of values to $3 \leq TSR \leq 8.5$ and $-5° \leq \beta_a \leq 9°$, outside of which the rotor C_P and C_T are set to zero. Even within these ranges, however, there exist certain operating conditions for which rotor performance results must be treated with caution. With additional consideration for realistic site constraints along with the limitations of the BC-BEMT, another restriction is also imposed on the maximum allowable value of blockage with a cap of $B_L \leq 0.35$ for the operation of tidal rotors in this thesis.

4.4.1 Power and thrust curves and surfaces

For the different turbine properties within various channel dynamics, $\overline{P}_{av}$ is defined by C_P, C_T and η. The differences in performance between the tidal rotors and equivalent actuator discs are most clearly shown in Figures 4.5 and 4.6, which compare the variations in C_P, C_T and η with tuning, k, between FP rotors and discs operating in $B_L = 0.16$ and 0.314 flow conditions.

In the graphs of C_P and C_T, it is observed that the magnitudes of C_P, C_T and η

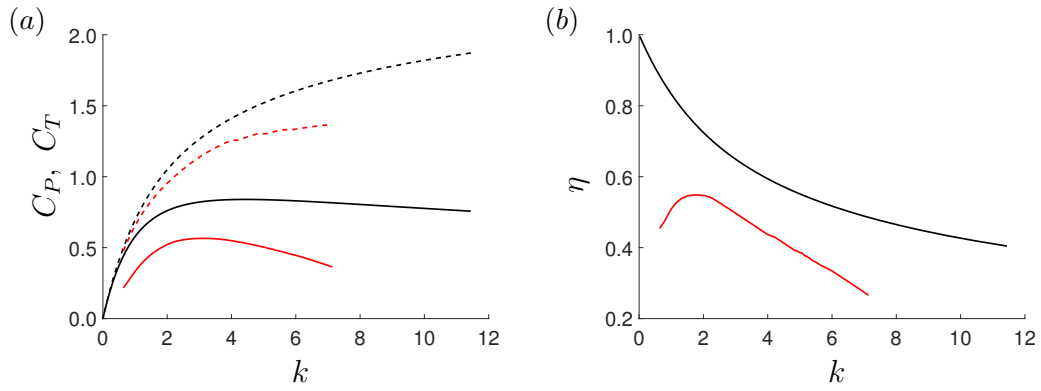

Figure 4.5: Variations with k in: (a) C_P (solid lines) and C_T (dashed lines), and; (b) η, for an actuator disc (black lines) and FP rotor (red lines) with $3 \leq TSR \leq 8.5$ in moderately blocked ($B = 0.16$) flow.

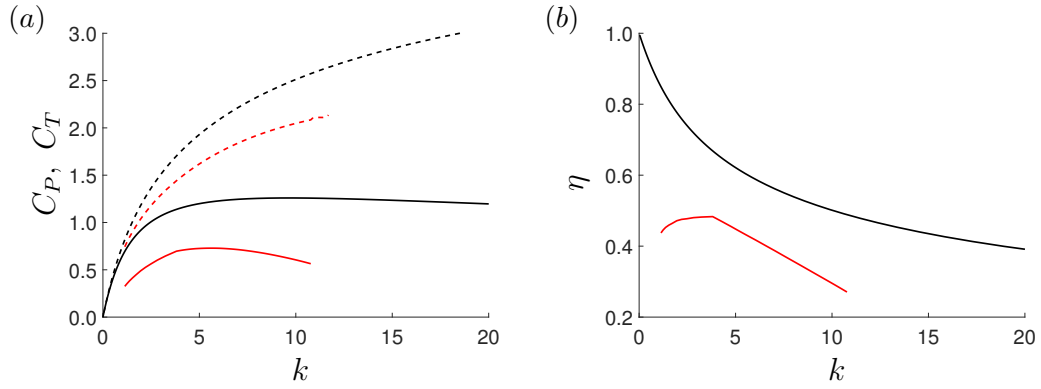

Figure 4.6: Variations with k in: (a) C_P (solid lines) and C_T (dashed lines), and; (b) η, for an actuator disc (black lines) and FP rotor (red lines) with $3 \leq TSR \leq 8.5$ in highly blocked ($B = 0.314$) flow.

are significantly different, as the results from the rotors are much lower than those predicted by the discs. This is due to the fact that the rotating rotor, unlike the idealised disc, comprises a discrete number of blades and incorporates a rotational wake. The implication of this is that the rotor will experience various losses, such as loss in the rotating wake as well as tip loss, where the assumption of an infinite number of blades no longer holds. Additionally, the blades are based on a constituent hydrofoil and thus they experience both lift and drag, which causes the rotor to experience drag loss when operating with higher k or significant stall loss when operating with lower k (Burton et al., 2011). In comparison, the actuator disc only assumes loss in the wake mixing Garrett and Cummins (2007).

Another key difference concerns the variations in η (Figures 4.5b and 4.6b). For the disc, there is a simple inverse relationship between k and η: as k increases, so does C_T and thus the amount of power dissipated in local-scale wake mixing increases, and η decreases. Whereas for the FP rotor, the relationship between k and η is not quite so simple: as k (which is represented here solely by TSR) increases, η initially increases and then decreases as the rotor emerges from a stalled flow condition (in which C_P and C_T estimates are less accurate), attains an initially large but decreasing C_P/C_T ratio, and then shuts off as the maximum permissible value of TSR is achieved. As with C_P and C_T, the absolute value of η is also lower for the more realistic rotor than for the idealised disc.

For VP rotors, the performance curves take the form of 3D surfaces, with β_a on the x-axis, TSR on the y-axis, and C_P, C_T, and η on the z-axis (Figures 4.7-4.9). The value of C_T is shown to increase with both increasing TSR and decreasing β_a, in contrast to η, which increases with decreasing TSR and increasing β_a. The value of C_P should peak at $\beta_a = 0$ with $TSR = 5.5$ or 5 (depending on the rotor design), but marginally higher values may be attained for different values of TSR for which c_x is no longer constant along the blade span (Schluntz and Willden, 2015). Specifically in this study, as the rotor designed by the RANS-BE method has been applied in the BC-BEMT model, this can also contribute to the offset in design values.

It may be of interest to also examine some rotor performance in off-design environments. A series of simulations are conducted to compare the performance of rotors designed for $B_r = 0.01$ and $B_r = 0.314$ with the deemed optimised rotor of $B_r = 0.16$, in a domain with a blockage ratio of $B_L = 0.16$. For each case, a range of operating conditions are studied with both FP rotors (Figure 4.10) and VP rotors (Figures 4.11-4.13), and the corresponding $C_{P,max}$ are presented in Table 4.1. In the case of FP rotors, both Figure 4.10a and the tabulated values show that, for the

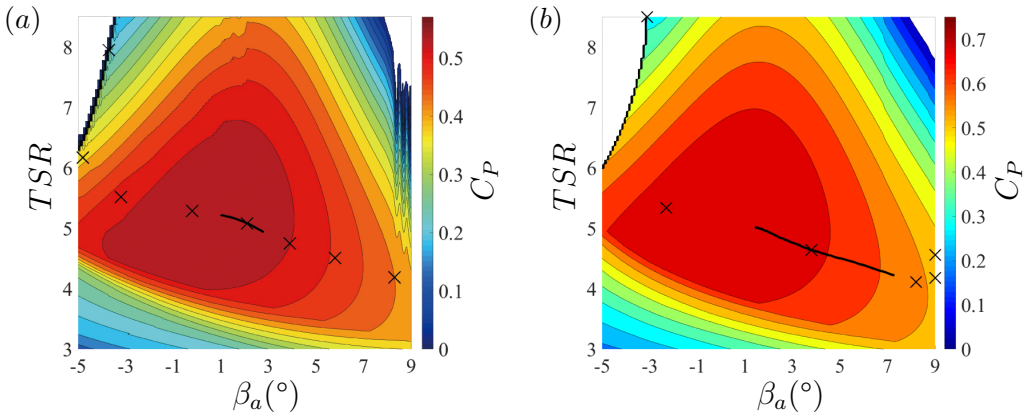

Figure 4.7: Variations in the C_P surface with TSR and β_a for: (a) $B_r = B_L = 0.16$, and; (b) $B_r = B_L = 0.314$, for a VP rotor. Solid lines indicate the range of operation for 'fixed' turbine tuning while crosses indicate the same for 'dynamic' turbine tuning.

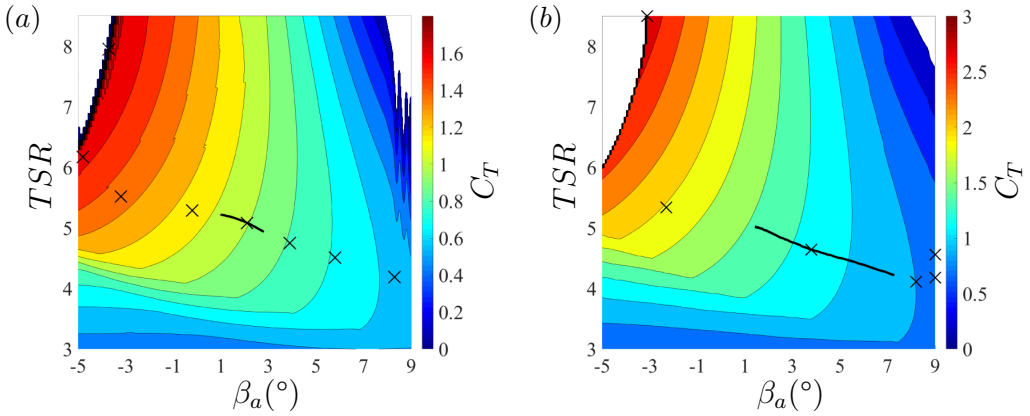

Figure 4.8: Variations in the C_T surface with TSR and β_a for: (a) $B_r = B_L = 0.16$, and; (b) $B_r = B_L = 0.314$, for a VP rotor. Solid lines indicate the range of operation for 'fixed' turbine tuning while crosses indicate the same for 'dynamic' turbine tuning.

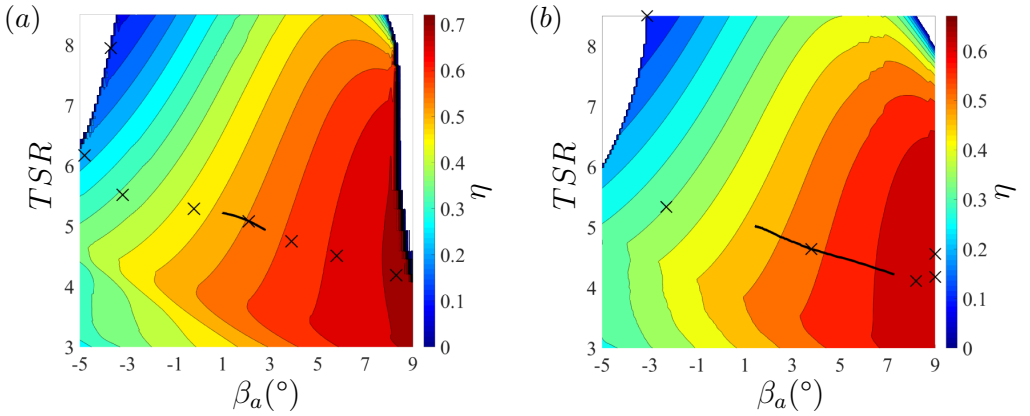

Figure 4.9: Variations in the η surface with TSR and β_a for: (a) $B_r = B_L = 0.16$, and; (b) $B_r = B_L = 0.314$, for a VP rotor. Solid lines indicate the range of operation for 'fixed' turbine tuning while crosses indicate the same for 'dynamic' turbine tuning.

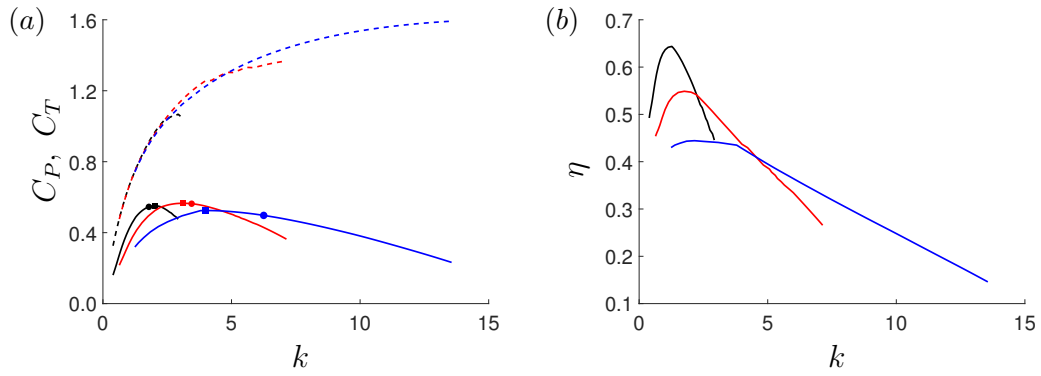

Figure 4.10: Variations with k in: (a) C_P (solid lines) and C_T (dashed lines), and; (b) η, for $B_r = 0.01$ rotor (black lines), $B_r = 0.16$ rotor (red lines) and $B_r = 0.314$ rotor (blue lines) in moderately blocked ($B_L = 0.16$) flow. The dots indicate the corresponding k for $TSR = 5.5$ or 5 (circle) and $C_{P,max}$ (square) for each FP rotor.

two off-design scenarios, $C_{P,max}$ is not achieved at the design value of TSR. The points on the C_P curves mark the values of $C_{P,max}$ when $TSR = 5.5$ and 5, and it is observed that TSR has to be either increased or decreased (thus altering k) for C_P to reach its peak. More specifically, it is found that, compared with the design scenario of $B_r = B_L = 0.16$, a higher TSR (with decreasing β_a for VP rotors) is required to achieve $C_{P,max}$ for the low blockage rotor design ($B_r = 0.01$) while the opposite is true (lower TSR, with increasing β_a for VP rotors) for the high blockage rotor design ($B_r = 0.314$). To explain this, taking the highly blocked rotor design as an example, a lower TSR in moderate blockage conditions allows it to operate at an α that is closer to its α_{opt} by achieving less thrust and thus enhancing the approaching flow speed; a similar idea applies to the low blockage rotor design. Identical findings have been published by Schluntz and Willden (2015) and Vogel and Willden (2018). Although all rotors exhibit values of $C_{P,max}$ relatively close in range, the highest $C_{P,max}$ is found to correspond with the VP rotor with $B_r = 0.01$. This is somewhat counter-intuitive as the optimised rotor with $B_r = 0.16$ is expected to have the highest performance (as is the case with FP rotors); however, at its peak C_P region, the rotor actually tends to operate at slightly lower TSR with increasing β_a. This may be caused by the aforementioned fact that the rotor used

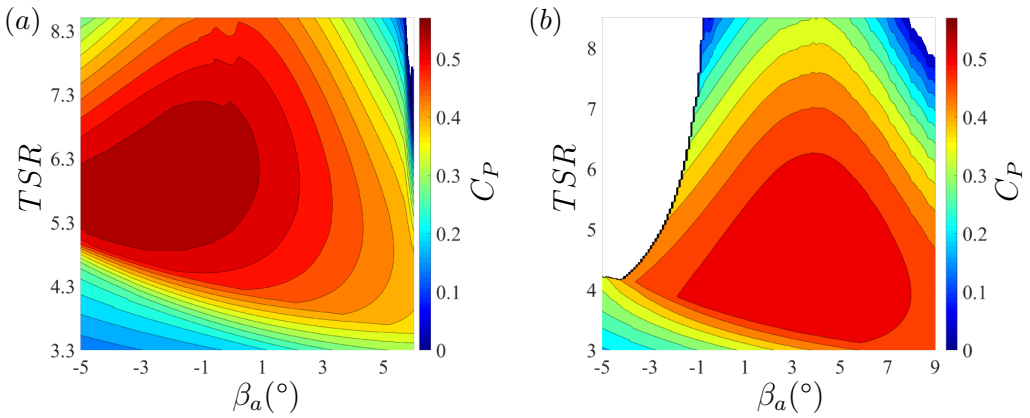

Figure 4.11: Variations in the C_P surface with TSR and β_a for: (a) $B_r = 0.01, B_L = 0.16$, and; (b) $B_r = 0.314, B_L = 0.16$, for a VP rotor.

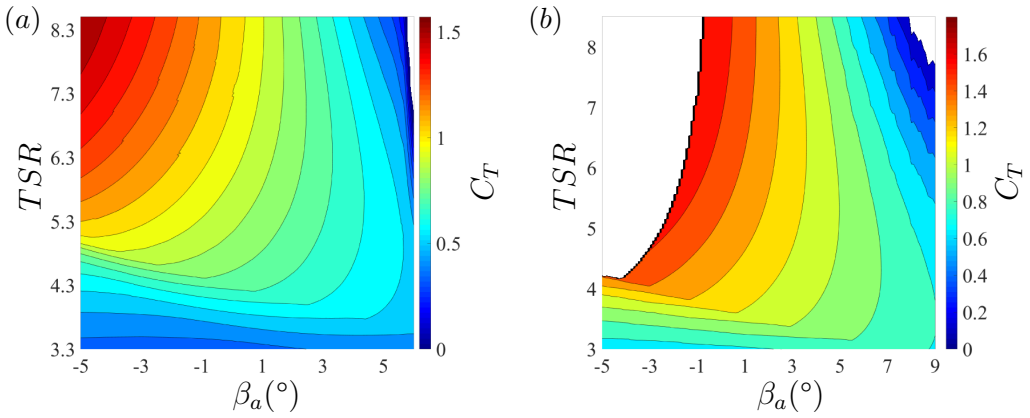

Figure 4.12: Variations in the C_T surface with TSR and β_a for: (a) $B_r = 0.01, B_L = 0.16$, and; (b) $B_r = 0.314, B_L = 0.16$, for a VP rotor.

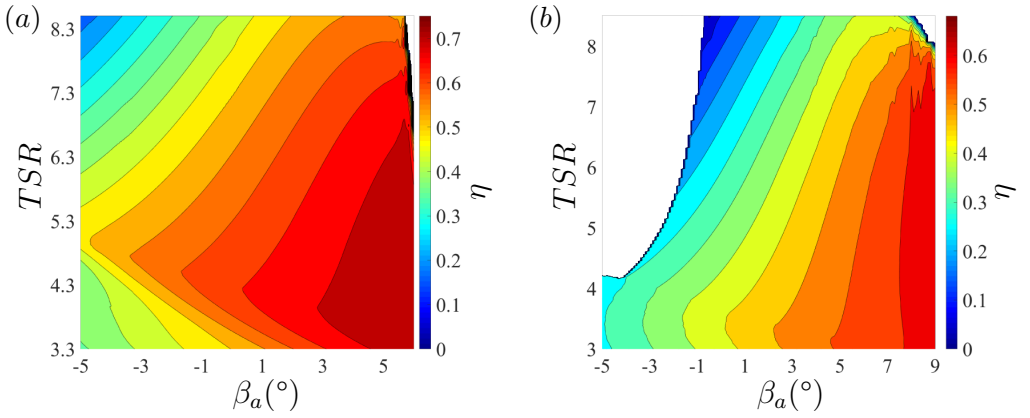

Figure 4.13: Variations in the η surface with TSR and β_a for: (a) $B_r = 0.01, B_L = 0.16$, and; (b) $B_r = 0.314, B_L = 0.16$, for a VP rotor.

by the BC-BEMT model is designed within RANS-BE and is therefore sub-optimal when analysed using the BC-BEMT model.

The variation in $C_{P,max}$ reduces from 7.2% for FP rotors to less than 3.8% for

Table 4.1: $C_{P,max}$ and corresponding parameters for each rotor in $B_L = 0.16$.

B_r	Device type	$C_{P,max}$	$C_T(C_{P,max})$	$TSR(C_{P,max})$	$\beta_a(C_{P,max})$ (°)
0.010	FP	0.552	0.970	6.2	0.0
0.160	FP	0.566	1.152	5.1	0.0
0.314	FP	0.525	1.225	3.8	0.0
0.010	VP	0.567	1.106	5.9	-2.6
0.160	VP	0.566	1.130	5.3	0.6
0.314	VP	0.545	1.104	4.5	3.6

VP rotors. Conversely, the corresponding η values vary greatly and Figure 4.10b indicates that, in a moderately blocked environment, the FP rotors designed for low blockage are generally superior to the rotors designed for high blockage in terms of η.

Likewise, some conclusions can be drawn from the results simulated with VP rotors. For example, when operating a rotor that is designed for low blockage conditions in a higher blockage domain ($B_r = 0.01$, $B_L = 0.16$), its C_T surface will be lower overall than that of a rotor initially designed for this domain; on the other hand, its η is higher overall. Nonetheless, for both parameters, the performance surfaces of the two off-design rotors rarely ever intersect in their 3D parameter space. However, for the C_P surfaces, while most values are lower for a rotor designed for lower blockage conditions, if the rotor is operated with higher TSR and decreasing β_a, its surface is found to largely intersect in that region with the C_P surface of the optimised rotor.

This phenomenon can be explained by considering the physics of the turbine's performance, which produces power according to the amount of resistance that the turbine provides against the flow. As the increase of rotational speed essentially reduces the porosity of a turbine, a rotor designed with a lower blockage ratio can also achieve the level of power produced by a higher-blockage rotor due to its higher solidity. However, such an operation is generally inadvisable because of the mechani-

cal problems and cavitation that may arise from the high operating speed (Buckland et al., 2013). Thus, the improvement in performance for a rotor designed for low blockage in a higher blockage configuration is ultimately limited.

4.4.2 Limitations

In general, the BC-BEMT model is able to provide appropriate C_P, C_T and η over a wide range of TSR and β_a values. However, it tends to fail in extreme conditions as shown in the three small regions situated in the corners of the VP rotor performance plots (e.g. Figure 4.7). Specifically, these are conditions of low TSR with low β_a, high TSR with high β_a, and high TSR with low β_a, where the model fails to predict the turbine performance. Along with these restrictions, other limitations also exist within the theory itself. For instance, the assumption of annular independence is appropriate for midsections of the rotor blade, but it tends to fail near the blade tip and the root regions where unsteady flow conditions, such as separated flow, and 3D flow effects are predominant; in such situations, 2D lift and drag coefficients cannot be used without the necessary corrections. All of these limitations will be explored below.

4.4.2.1 Tip correction

One major limitation of the classic BEMT is its inability to predict accurately the blade force and model the complex 3D flow physics near the blade tip region. The model ignores the effects of discrete blades on the localised flow field as well as the spanwise component, which is the area where the most power is produced. A tip correction model for the correction of discrete blade effects has been developed by Glauert (1983), which has been incorporated into the BC-BEMT to account for the reduction in momentum change at the tip of the turbine blades. Even though the current model contains the Glauert tip correction, it cannot thoroughly capture the losses due to spanwise flows caused by pressure equalisation around the

blade tip. Empirical spanwise flow correction, either isotropic (Shen et al., 2005) or anisotropic (Wimshurst and Willden, 2017), may be added as an extra tip correction but these are formally only for low blockage.

However, existing tip correction models lack generality and cannot be applied broadly, as they depend on specific rotor geometry, blade tip shape and blockage ratio. In addition, the effect of the Glauert tip correction model is to reduce the axial and tangential induction factors as the radial flow approaches the tip of the rotor blade. As such, the velocity (and corresponding momentum) deficit reduces to zero towards the blade tips, essentially forcing the free stream velocity at the blade tip to be equal to the upstream velocity. This is incorrect considering the inherent constraining assumptions of the BC-BEMT.

4.4.2.2 Blade root correction

Beginning with the experiments performed by Himmelskamp (1945), it has been commonly observed in literature that, in the root region of a rotating blade, the values of the measured lift force and thrust observed on an operating turbine are significantly higher than those predicted with 2D theory (at the same value of α). This is because the classical BEMT often fails to capture the rotational augmentation caused by favourable pressure change due to a centrifugal pumping phenomenon, and the separation points shifting towards the trailing edge as a result of the flow separation condition (Guntur, 2013). Even though at present, stall is not usually used as a control mechanism due to the development of pitch regulation, it is still unavoidable in the root regions of the rotor blade.

Additionally, it is not possible for the BEMT to capture the flow acceleration effect at the turbine hub as well as the effect of root vortex shed from the hub, which are phenomena commonly observed in numerical simulations (Muchala, 2018). In fact, the behaviour near the hub is likely to be strongly dependent on the actual complex 3D geometry of the hub-blade connection and nacelle, which is difficult to

represent in the BC-BEMT model. Since limitations within the root region generally do not affect power calculations by a meaningful amount, given the small radius and hence small torque for a given force, there are currently no root correction or hub loss models applied in the simulations.

4.4.2.3 Extreme operating condition: low TSR with low β_a

Vogel et al. (2018) have developed the BC-BEMT model to simulate a rotor designed for $TSR = 5$ and observed that a considerable portion of the blade will be stalled with low values of TSR ($TSR \leq 4.5$) based on the 2D hydrofoil characteristics and calculated values of α. A similar phenomenon has been observed here, as evidenced by the results from Figures 4.7-4.9.

The three figures show that there is a significant drop of C_P, C_T and η in the low-TSR region, which is enhanced further by the decrease of β_a into negative values. When both the TSR is lowered and the rotor blades are pitched to stall, a significant fraction of the blade surfaces are operating with a very large α, resulting either from the increase of ϕ or the reduction of β. Under such an extreme stall condition, the flow will separate from the surface of the blade to such a degree that the power and thrust predictions obtained from 2D hydrofoil characteristics will not be representative of actual turbine performance.

However, in reality, a rotating blade would stall at a higher α value due to a physical phenomenon known as the 'stall delay effect' (Guntur, 2013). The centrifugal force exerted by the blade in rotation allows a spanwise component of flow to develop on the suction surface along the entirety of the blade. Due to this favourable force, the separation point of the trailing flow is shifted and results in the delay of turbine stall. This physical effect has not been considered in this study, and thus under low TSR conditions, estimations of turbine performance are often difficult due to the inaccuracy of stall prediction. It may be possible to improve the agreement between simulation results and experimental data in this region by correcting the

2D hydrofoil characteristics used in the BC-BEMT model to take into account the effects of spanwise flow. This is commonly conducted by applying a stall delay correction to the 2D lift and drag coefficients or extracting the coefficients at different radial locations from the blade-resolved simulations (Vogel et al., 2018).

Whilst many popular correction models, including those by Snel and van Holten (1995), Lindenburg (2004), Dumitrescu et al. (2007), Du and Selig (1998), Chaviaropoulos and Hansen (2000) and Bak et al. (2006), have been proposed to correct for stall delay effects, they are ultimately insufficient for the prediction of tidal turbine performance and the results using different models are mostly inconsistent with each other (Guntur, 2013). Given that the main purpose of the work in this thesis is to investigate leading order turbine effects, it has been decided that none of these schemes will be included in the final model.

4.4.2.4 Extreme operating condition: high TSR with high β_a

The simulation results of C_P, C_T and η under a condition of high TSR and high β_a are also clearly presented in Figures 4.7-4.9, indicated by observations in the upper right corner. As TSR and β_a both increase, it is noted that all parameters rapidly drop to zero (i.e. blank regions in the upper right corner of Figures 4.7-4.9 and 4.11-4.13), with an abnormal trend appearing along the right border of the figures.

Unlike the previous operating condition, choice of a high value of TSR in combination with a large, positive value of β_a leads to ϕ and α becoming small or even negative. The calculation sequence will encounter certain numerical instabilities (while still physically relevant, the numerical solution scheme is unable to solve the equations) and breaks down. Where this happens, the result is obtained through second-order polynomial extrapolation, since the flow physics of this phenomenon can still be explained. It can be speculated that the extrapolation process is the cause of the abnormal black region that appears at the right border of the graphs. Despite having to use extrapolation, the flow remains attached to the blade and therefore the

data is more reliable than the results at the turbulent wake state and extreme stall condition where the model cannot capture the real physics.

Beyond a certain point, however, the BC-BEMT model results become less meaningful as the rotor attains a negative induction factor. This could bring the model to another inefficient operation state — the propeller state — where the streamtube is contracting. The thrust force is directed downstream and acts as a propulsion device, and the current BC-BEMT model is unable to provide physically meaningful results. As it is obvious that the model does enter the propeller state at the top right corner of the graphs (where C_P, C_T and η all go to zero), the model is manually adjusted in this situation to set the magnitude of all three parameters to zero or invalid.

It is worth noting that the performance maximisation strategies adopted herein will generally avoid the two extreme operating conditions mentioned in this section and Section 4.4.2.3. The solid lines and crosses in Figures 4.7-4.9 indicate the maximum ranges of operation for VP rotors with 'fixed' and 'dynamic' tunings (introduced in the next chapter) and show that, for the range of flow conditions considered in this study, at least, maximisation of array power does not require the combinations of low TSR and low β_a or high TSR and high β_a.

4.4.2.5 Extreme operating condition: high TSR with low β_a

The last of the three extreme operating conditions can be observed in the upper left corner of Figures 4.7-4.9 and 4.11b-4.13b, where a high value of TSR is paired with low β_a. It is noticeable from all three surfaces that there is a cutoff line where all values drop immediately to zero (i.e. blank regions), as specified by the model upon entering what is known as the turbulent wake state, achieved by this specific combination of operational environment.

In the BC-BEMT, solutions of the 1D momentum equations are only valid for small induction factors (windmill state) as the model is unable to represent accu-

rately the process when turbines experience a turbulent wake (Vogel et al., 2018). Values of $a_2 > 0.5$ (resulting in a negative a_4) imply wake reversal, which contradicts the assumption of an enclosed streamtube. Therefore, an empirical Buhl high-induction correction (Buhl, 2005) may be applied to adjust the relationship between C_T and a_2 in this high-induction state. Similar empirical models have not yet been developed for confined flows, since the transition for bounded flows to turbulence in the rotor wake is expected to occur at a higher C_T as the wake velocity increases with blockage for a given level of thrust (Vogel et al., 2018). Though a full understanding of the influence of blockage on the turbulent transition is beyond the scope of this study, it is important to try to account, in some way, for the effects of confinement on the flow condition in the rotor wake.

Non-physical flow solutions may arise when the rotor is operating with a high TSR and low β_a. In order to confine the modelling of the turbine to a relatively meaningful operation state, the rotor is switched off when the majority of the primary power-producing area of the blade exceeds the blockage-corrected turbulent wake threshold. Following the Buhl correction (Buhl, 2005), it is assumed that the model stops once the majority (i.e. 60%) of the primary power-producing area of the blade ($0.3 < r/R < 0.85$) exceeds $a_2 > 0.6$. In the simulations, this is represented by, once again, manually setting all values to zero when the upper limit of a_2 is surpassed.

Furthermore, the 3D plot surfaces of C_P and C_T contain discontinuities near the high TSR and low β_a region, which is an anomaly from the other parts of the graphs connected by smooth curves. By comparing the C_P and C_T surfaces at $B_r = B_L = 0.16$ and $B_r = B_L = 0.314$, clearer observations of this feature can be found from the lower-blockage rotor.

In explanation, the tip section of the blade is first considered, which has the greatest rotational speed. Higher TSR can lead the tip region into a propeller-like

state in the tangential direction, decreasing ϕ with reference to Equation 4.6. Specifically in the tangential direction, since $\cos\phi/\sin\phi$ becomes exceedingly large and surpasses C_L/C_D as ϕ decreases, a negative torque is obtained at the tip due to the small ϕ. This phenomenon has also been corroborated by the findings of Muchala (2018). Coupled with the fact that the flow is less confined at lower blockage ratios, less water is forced through the turbine and hence the tangential velocity would be lower. This corresponds to smaller value of ϕ and subsequently smaller α. As β_a becomes more negative, ϕ may decrease further and thus it is more likely to observe the discontinuities.

4.5 Conclusions

The BC-BEMT model developed by Vogel et al. (2018) has been implemented in this work, in which a blade element theory is coupled with the volume-flux-constrained momentum theory. The model allows the accommodation of flow constraints imposed by neighbouring turbines or seabeds, and approximates the free surface as a rigid lid. By comparing with results from blade-resolved simulations, Vogel et al. (2018) have shown that the BC-BEMT model agrees reasonably well in terms of predicting the power and thrust coefficients of tidal turbines.

For the work in this thesis, several RANS-BE-designed rotors from literature have been simulated with the BC-BEMT model in domains with three different levels of blockage. The simulations operate a range of TSR and β_a values to examine the power and thrust characteristics of the idealised disc, the FP rotor, and the VP rotor under both designed and off-design operation conditions. Generally, for FP rotors, compared to the actuator disc, the BC-BEMT predicts relatively conservative C_P and C_T values due to its realistic representation of the turbine where more energy losses are considered. For the VP rotors, the BC-BEMT provides more flexible and appropriate values of C_P and C_T for most of the operating conditions. By vary-

ing the operating conditions, a rotor in an off-design condition can achieve similar $C_{P,max}$ values as a rotor specifically designed for that blockage ratio, though this is not necessarily advisable.

However, when rotors are operating under extreme conditions (a few specific combinations of high/low TSR and β_a), the BC-BEMT model tends to struggle in predicting turbine performance due to its inability to consider the stall delay effect and various extreme turbine states such as the propeller state and the turbulent wake state. Under the operation strategies proposed in this study, some of the extreme operating conditions can be avoided, and steps have been taken to address the others. Given that the BC-BEMT captures the leading order physics of tidal rotors within a meaningful range of operation, this analysis should provide useful, general insights into the performance of more realistic turbine representations. Most importantly, the BC-BEMT model used here clearly contains more realistic turbine physics than the actuator disc models typically used in tidal stream resource studies.

Chapter 5

Operation and Performance of Tidal Rotors in Channels *

Much of the global tidal stream power resource is located in narrow channels where the energy from the tidal flow is concentrated to produce fast tidal streams (Vennell et al., 2015). The design of tidal turbine arrays is complicated by the fact that the presence of such devices in a large quantity will provide a significant influence on the surrounding environment, including the flow from which power can be exploited. These interactions need to be understood both for accurate resource and environmental impact assessments but also to understand the best operation strategy for turbines.

Vennell (2010) was the first to show that maximising the performance of a tidal turbine array requires the turbine resistance to be 'tuned' for a given channel and turbine arrangement. By combining the simple tidal channel and the bounded actuator disc models of Garrett and Cummins (2005, 2007), Vennell has shown that for turbines in channels, the maximum averaged available power depends not only on C_P but also on C_T. The two parameters, together with the channel's natural dynamic balance λ_0, determine the velocity of the flow through turbines. Vennell

*The discussions in this chapter and Chapter 4 have been published together as a both a workshop abstract and journal paper — see Chen et al. (2018a, 2019a) from Appendix C.

(2010) has also shown that large, optimally tuned turbine arrays can realise most of a channel's energy potential and later demonstrated, following the work of Adcock (2012), that varying the tuning over the tidal cycle can produce a higher power output, often without increasing the maximum loading on the turbines whilst also maintaining a higher channel flow rate (Vennell, 2016).

This chapter aims to take this analysis to the next stage by incorporating physics more representative of real tidal stream turbines, using the BC-BEMT model developed by Vogel et al. (2018) described in the previous chapter. This more advanced low-order model may be used to consider different approaches to turbine tuning, which include varying the rotational speed and/or pitch angle of the turbine blades. The introduction of the more representative tidal rotor affords the opportunity to re-examine the importance of tuning for tidal turbines in channels, and to compare the actuator disc, which has been used extensively in theoretical and numerical models of tidal stream power, with a more realistic model of turbine performance.

This chapter is structured as follows. Firstly, Section 5.1 introduces the different tuning strategies proposed in this chapter, and details both the physics behind and the implementation of each individual strategy. The importance of tuning is considered in Section 5.2 by comparing two types of tidal rotors, FP and VP, where the tuning parameter is either temporally fixed or varying, against the results of the equivalent actuator disc. In order to perform a comprehensive study, the two turbine representations are modelled in a variety of conditions with different blockages and turbine deployments, within different tidal channels. Taking into account the findings from this chapter, general conclusions are drawn from this work to inform the design of tidal stream turbines from a basin-scale perspective.

5.1 Tuning Strategies

The design and operation of tidal turbine arrays will affect the power performance of the turbines. The term tuning was introduced by Vennell (2010), which suggests that, at different locations, slightly different turbine characteristics are desirable because there is a feedback between the tidal stream turbines and the tidal flow — applying too much thrust to the flow can reduce the tidal current at the site in such a way that a lower thrust condition might provide more power. Following the work of Vennell (2016), three different turbine tuning strategies are used to maximise the time-averaged available power, $\overline{P}_{av}$. A factor that is neglected here for the sake of simplicity is power capping, which is likely to be adopted in the design of tidal turbine arrays (Vogel et al., 2018) and further discussed in Appendix A.

5.1.1 Strategy A: impatient tuning

Commercial applications of modern wind energy typically adopt the maximum power point tracking (MPPT) approach, which seeks to obtain the maximum available power from the wind by continually adjusting the tuning of the turbine according to the instantaneous wind velocity upwind of the turbine rotor (Thongam and Ouhrouche, 2011). This particular tuning strategy has also been adapted for tidal turbines, which adjusts the the turbine resistance k for operation at their local $C_{P,max}$ throughout the tidal cycle. Although it tends to be effective for wind farms due to the variability of wind velocity and the limited capacity to alter the dynamics of the wind by the turbines themselves, it has been shown to be less beneficial for tidal turbines (Vennell, 2016). Therefore in this chapter, this tuning strategy, termed as the 'impatient' strategy following Vennell (2016), is used simply as a baseline for comparison.

5.1.2 Strategy B: fixed tuning

The second tuning strategy, which has been termed the 'fixed' strategy, seeks a temporally fixed turbine resistance (a value of k that is constant with time) that maximises $\overline{P}_{av}$ over the tidal cycle. This fixed tuning strategy was used by Vennell (2010), and has since formed the basis of a number of resource assessments of candidate tidal power sites (e.g. Adcock et al., 2013).

Compared to the impatient strategy, the fixed strategy typically presents a lower resistance to the incoming flow, and so relatively less power is generated around slack water when incoming flow velocity is low. However, the application of a lower resistance early in the tidal cycle enables greater flow acceleration, which means that more relative power can be produced later in the tidal cycle when incoming velocity is higher. In fact, this enhanced power production later in the tidal cycle more than compensates for the reduced power production earlier in the tidal cycle, as will be discussed in this chapter.

5.1.3 Strategy C: dynamic tuning

The third strategy, termed the 'dynamic' tuning strategy, is slightly more complex and was introduced by Adcock (2012) and further developed by Vennell (2016). This strategy seeks a time-varying k that maximises the benefits of stronger currents later on in a tidal cycle by adjusting the turbines earlier on to allow for a lower flow resistance during periods of the cycle with slack water.

With dynamic turbine tuning, k typically varies over half a tidal cycle as follows. Around the turn of the tide, when velocities are still low, k is set to zero so that the turbines do not present additional resistance to the developing flow. As the incoming velocity begins to increase over time, k is gradually increased to a maximum near the end of the half tidal cycle, when the velocity has reduced almost to zero. Garrett and Cummins (2005) have shown that, at a given point in space, the amount

by which the peak velocity lags the peak tidal forcing decreases with increasing resistance to flow. With this strategy, it is possible to use the turbine resistance to decrease this phase difference, so that the velocity follows the tidal forcing more closely, and experiences a longer period of acceleration as a result (Vennell and Adcock, 2014). This longer period of acceleration results in higher inflow velocities and thus a higher $\overline{P}_{av}$ for the turbines. Dynamic turbine tuning is most effective where the effects of turbine resistance are most significant; that is to say, for the combination of large blockage B_L, large number of turbine rows N_R^*, and small λ_0 (Vennell, 2016).

5.1.4 Tuning strategy implementation

All three of the suggested tuning strategies are conducted in a dimensionless channel with a single-constituent tide, a quadratic seabed drag, and neglecting the parasitic drag from turbine support structures. If k is held constant throughout the tidal cycle, the task of maximising $\overline{P}_{av}$ is trivial — a fixed tuning is used to achieve a certain C_P and hence $\overline{P}_{av}$, the value of which may be maximised by selecting the optimal fixed tuning. For strategy A, a simple 'max' function is able to yield $C_{P,max}$ for both the actuator disc and the tidal rotor, and the operation parameters that correspond to this $C_{P,max}$ are used during the tidal cycle and across different channel dynamics. Considering strategy B, the Nelder-Mead simplex algorithm ('finsearch' function) is used to find a temporally fixed tuning that can output the overall $\overline{P}_{av}$ over a tidal cycle. An advantage of the Nelder-Mead method is its ability to provide significant improvements within a small number of iterations, and thus very quickly produce the desired results (Lagarias et al., 1998). The output turbine tuning with the corresponding tuning parameters is constant over the tidal cycle but varies with different channel dynamics due to the different feedback received.

The task of maximising $\overline{P}_{av}$ becomes quite complex, however, if the tuning pa-

rameters are allowed to vary in time. To simplify this more complicated optimisation problem, strategy C can be applied in the form of a Fourier series with respect to time (or similar transformations) to represent the tuning parameters, following work by Adcock (2012), Vennell and Adcock (2014), and Vennell (2016). An alternative which produces similar results is to divide the tidal cycle into M equal sub-cycles. Although this means that the turbine properties do not vary continuously over the cycle, it provides advantages at the end of sub-cycles by allowing a discontinuity in the operation. Within each of these shorter periods, the turbine resistance is held constant and a simple optimisation algorithm, which begins with a selection of pseudorandom variables, is used to determine the set of fixed tunings that maximise $\overline{P}_{av}$. In this way, n fixed tunings over n sub-cycles (time blocks) are used to approximate the temporally varying k, which is regarded as the near-optimal solution. The Global Optimisation Toolbox within MATLAB is used for obtaining the optimal n fixed tunings as it can successfully process the high-dimensional nature of the task. Out of the number of optimisation methods offered by the toolbox, two techniques are employed in this work: gradient-based methods and a 'derivative-free' direct search method. In terms of gradient-based optimisation, the actuator disc calculations utilise both 'GlobalSearch' and 'MultiStart', which differ in that the former is most efficient on a single-core machine while the latter has a parallel version that allows it to operate on multi-core machines (Agnarsson et al., 2013). Both algorithms generate multiple starting points followed by the function 'fmincon' (being the only gradient-based local solver that considers constrained optimisation problems), which finds the local optima. The point that has the lowest objective value, that is also feasible, is chosen to be the global optimum. For the more direct optimisation technique, MATLAB performs a 'Pattern Search' operation by picking a point and searching the surrounding mesh for a point that provides better objective solutions, and then moving to that point and repeating the process until the global

optimum is found. This derivative-free technique is more effective when the objective function is non-differentiable, such as the case of the non-smooth performance surfaces generated by the BC-BEMT model.

The resulting value of $\overline{P}_{av}$ is found to be insensitive to the initial set of pseudorandom variables as well as the optimisation techniques chosen and the function used to describe the temporally varying turbine parameters. Model solutions depend only weakly on the choice of n, and a sensitivity test is conducted with the resulting value of $\overline{P}_{av}$ found to converge with increasing n. Increasing the value of n above 20 is found to yield increases in $\overline{P}_{av}$ of $< 1\%$, and so a value of $n = 20$ is chosen for the ease of computation.

5.2 Tuning of Tidal Rotors

The results from the simulations performed in this work are shown in this section in terms of the parameters $\overline{P}_{av}$ and k of an actuator disc model relative to a more realistic turbine model. Sections 5.2.1 and 5.2.2 examine the relative importance of tuning and further differences between FP and VP turbines, respectively. Section 5.2.3 considers the degree to which the actuator disc over-predicts the power available to tidal rotors operating under different strategies, with consideration of different rotor designs and rotor sensitivity. Through the discussion, it is hoped that the importance of tuning for different turbine representations can be investigated to provide more insight into the operation of tidal turbine arrays.

5.2.1 Optimal tuning

In order to investigate the results of the three tuning strategies, the relative importance of tuning on $\overline{P}_{av}$ and the overall effect of tuning are considered. The performance of the three different tidal turbine representations (disc, FP rotor and VP rotor) are analysed and compared. Two primary tuning strategies are then used to maximise $\overline{P}_{av}$, by means of optimal fixed and dynamic tuning parameter, k. The

results of $\overline{P}_{av}$ are normalised, in this case, by those obtained using the impatient tuning strategy, in order to examine the relative importance of tuning for each of the three turbine representations (i.e. how much additional power can be gained by tuning, compared to strategy A).

Though the tuning strategies focus solely on maximising $\overline{P}_{av}$, turbine performance is discussed in terms of the three key parameters of C_P, C_T and η. The relative importance of these parameters is determined by the three variables that define the ratio of turbine drag to natural drag, B_L, N_R^* and λ_0, for which a broad range of values are assumed ($B_L = 0.16$ and 0.314, $N_R^* = 1$ and 5, and $0 \leq \lambda_0 \leq 10$).

5.2.1.1 Fixed tuning

The significance of tuning is first examined by comparing the variations in maximum $\overline{P}_{av}$ and optimal temporally fixed k obtained using the actuator disc, FP rotor and VP rotor with different combinations of B_L, N_R^* and λ_0 (Figures 5.1 and 5.2).

The most notable result is that, for all turbine models considered, the importance of tuning increases with increasing B_L, increasing N_R^*, and decreasing λ_0. This finding is consistent with existing theoretical work — Vennell (2010) has shown that when the natural drag (represented here by λ_0) is relatively low and the turbine drag (represented here by B_L and N_R^*) is relatively high, the effect of tuning is greater because the throughflow velocity, and hence $\overline{P}_{av}$, is more dependent on the turbine resistance. Moreover, whilst substantial increases in $\overline{P}_{av}$ are available for large B_L, large N_R^*, and small λ_0, in cases where the turbine resistance is less significant (such as most practical scenarios), the fixed tuning strategy is shown to provide only slightly more power than the impatient tuning strategy.

It is also clear that, as compared to the actuator disc, the increase in power that may be achieved by adopting a fixed tuning strategy is significantly lower for the rotors (Figures 5.1a and 5.2a), showing that the importance of tuning is greatly re-

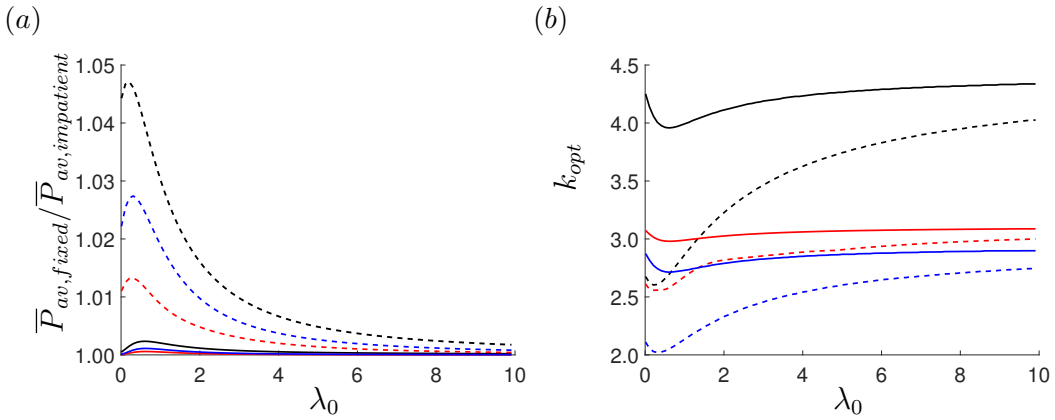

Figure 5.1: Variations with λ_0 in: (a) normalised maximum $\overline{P}_{av}$, and; (b) optimal temporally fixed k, for one (solid lines) and five (dashed lines) rows of actuator discs (black lines), FP rotors (red lines), and VP rotors (blue lines), in moderately blocked ($B_L = 0.16$) flow with the fixed strategy.

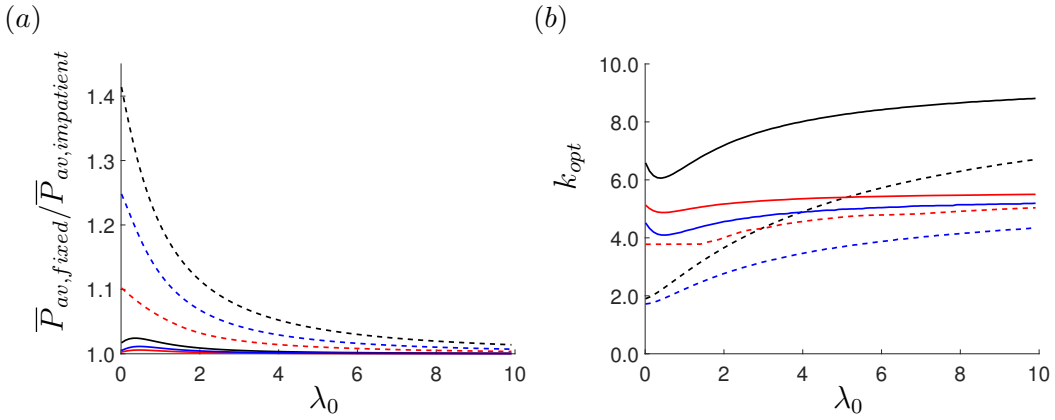

Figure 5.2: Variations with λ_0 in: (a) normalised maximum $\overline{P}_{av}$, and; (b) optimal temporally fixed k, for one (solid lines) and five (dashed lines) rows of actuator discs (black lines), FP rotors (red lines), and VP rotors (blue lines), in highly blocked ($B_L = 0.314$) flow with the fixed strategy.

duced using more realistic turbine representations. For instance, in the case where $B_L = 0.314$, $N_R^* = 5$, and $\lambda_0 = 0.01$ (where tuning has particularly significant benefits), fixed tuning provides $\approx 10\%$ more power to the FP rotor than the impatient strategy, compared to $\approx 41\%$ for the disc. The VP rotor performs better, with $\approx 25\%$ power increase in this case, but still displays less significant increases for smaller values of B_L and N_R^*, and larger λ_0.

To understand why the potential increase in power is lower for the rotors than the disc, it is useful to consider the variations of k with λ_0, which attempts to define

how the turbines operate based on channel dynamics and different turbine properties (Figures 5.1b and 5.2b). Vennell (2010) has explained that when the turbines are installed in a drag-dominated channel (high λ_0), the turbines are of less importance in the overall flow dynamics and therefore will tend to maintain the optimal flow resistance that will achieve the best power coefficient (i.e. operating at $C_{P,max}$). As λ_0 reduces and the effects of turbine resistance become more significant, if the turbines still operate at $C_{P,max}$, then their collective drag will slow the flow to the point where a significant amount of power in the undisturbed channel cannot be harnessed. Therefore the thrust needs to be reduced, and thus the optimal fixed k for the disc generally decreases, especially for cases with high N_R^* and high B_L due to the relationship between flow velocity and consequential $\overline{P}_{av}$. This reduction in turbine resistance (C_T) will result in both stronger flow rate increment as well as better η, which, in combination, outweighs the sacrifice of the optimum local turbine performance ($C_{P,max}$). Therefore, in an inertia-dominated channel where λ_0 is low, the maximum $\overline{P}_{av}$ becomes more dependent on C_T and η rather than C_P.

There is also an exception to this rule. For very small values of λ_0, a small upward tail in the optimal k curves (Figures 5.1b and 5.2b), which departs from the general trend, is observed, especially for cases with lower N_R^* and B_L. This phenomenon is mainly related to the nature of unexploited flow rate impedance in the extreme-inertia region (i.e. $\lambda_0 = 0.01$), as shown at the left end of the graph in Figure 5.3. The slope of $\overline{Q'}_{unexploited}$, the non-dimensional time-averaged naturally occurring flow rate (See Section 2.4.3.1), is seen to decrease and eventually flattens with decreasing λ_0, meaning that the channel flow rate becomes less sensitive to the turbine resistance again, just as it does in the drag-dominated channel. As the slope decreases in steepness, the change of average flow rate with respect to the change in λ_0 also lessens, and therefore the significance of turbine tuning is lowered by the insensitivity of $\overline{Q}$ with respect to the domain. As such, the optimal k increases as

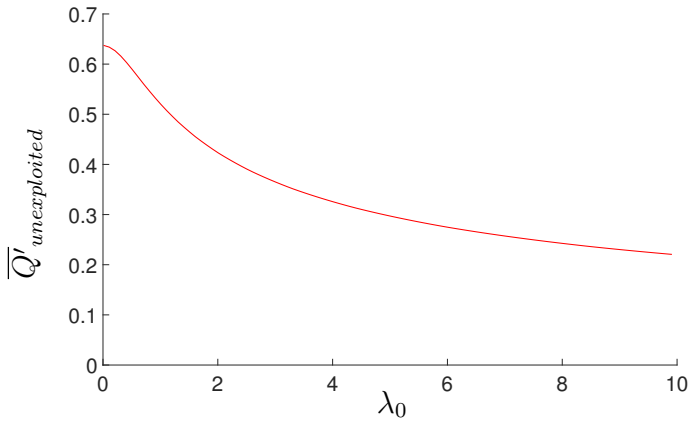

Figure 5.3: Variation in $\overline{Q'}_{unexploited}$ with λ_0.

the benefits of C_P prevails over the costs of lower C_T and η.

For the tidal rotors, with k as the dependent variable, it is clear to see that the optimal fixed k is lower and undergo less variation with λ_0 than for the disc. To demonstrate, for the VP rotor case with $N_R^* = 5$ and $B_L = 0.314$ (Figure 5.2*b*), which are the conditions for the largest variation in k, the value of Δk from the lowest to highest point on the curve is 45% less than that of the actuator disc.

The relative insignificance of tuning using tidal rotors, as compared to actuator discs, can be explained by considering the channel and turbine physics. For large λ_0, the optimal k for the rotor is lower than for the disc because, for the more realistic turbine model, C_P peaks at a lower value of k and corresponding C_T (Figures 4.5*a* and 4.6*a*). For $B_L = 0.314$ as an example, it is clear that the values of $k(C_{P,max}) = 9.6$ and $C_T(C_{P,max}) = 2.5$ for the disc is much greater than the values for the rotor, $k(C_{P,max}) = 5.6$ and $C_T(C_{P,max}) = 1.7$, meaning that the tidal rotor cannot provide as much thrust as the actuator disc when operating at $C_{P,max}$; therefore its relative volumetric flow rate increment achieved by tuning the turbine away from its point of $C_{P,max}$ will not be as evident as with the actuator disc.

Additionally, as mentioned in Section 4.4.1, there is also a difference between the three turbine representations in terms of η, especially for small λ_0. In Figures

4.5b and 4.6b, there is a clear inverse relationship between k and η for actuator discs, such that when the turbine is tuned towards smaller λ_0, both higher flow rate and η are achieved concurrently. However, for FP rotors, although a similar inverse relationship exists over a range of k, the improvement of η is not as rapid in comparison (i.e. the disc has a steeper inverse relationship). Furthermore, η drops below a certain value of k as lower TSR brings a large portion of the rotor to stall. In this case, while shifting the focus parameter from $C_{P,max}$ to lowest C_T, the basin efficiency η, due to its decrease, becomes an unfavourable consideration that is in opposition with C_T. Partially for this reason, the tuning curve of the $N_R^* = 5$ case in Figure 5.2b plateaus at $k \approx 3.8$ with small λ_0, showing strong resistance before flow separation is due to occur over the blade. Hence, varying from large to small λ_0, for realistic rotors, the effects of turbine resistance on the throughflow velocity and the increment of η (caused by a reduction in k and thus C_T) become less significant.

For the FP rotor, which has no other means of controlling k, the TSR decreases significantly as the optimal k reduces, and there is a significant reduction in power. For the VP rotor, however, this limitation is lifted as pitching the blades to feather allows k to be reduced with a much smaller reduction in TSR (explained in Section 5.2.2). Effectively, more flexible turbine control allows for the coexistence of lower C_T and better η, similar to the performance characteristic of the actuator disc. Thus for fixed tuning, the VP rotor performs better than the FP rotor, particularly for small λ_0; however it still has lower performance compared to the disc, as it is impossible for the efficiency modelled by the tidal rotor simulations to reach the level modelled by the actuator disc simulation.

5.2.1.2 Dynamic tuning

The importance of tuning is next examined by comparing the variations in $\overline{P}_{av}$ and the optimal dynamic tuning, k, obtained for the actuator disc, FP rotor, and VP rotor. As before, different combinations of B_L, N_R^* and λ_0 are considered (Figures

5.4 and 5.5), and the results of $\overline{P}_{av}$ are normalised by those obtained using the impatient tuning.

Compared to impatient tuning, dynamic tuning is shown to provide considerably more power to the tidal rotors than fixed tuning (Figures 5.4a and 5.5a). Whereas, for $B_L = 0.314$, $N_R^* = 5$ and $\lambda_0 = 0.01$, fixed tuning provides $\approx 10\%$, $\approx 25\%$, and $\approx 41\%$ more power to the FP rotor, VP rotor, and actuator disc than impatient tuning, the corresponding increases for dynamic tuning are $\approx 34\%$, $\approx 61\%$, and $\approx 103\%$. As with fixed tuning, however, the potential increases in power are signifi-

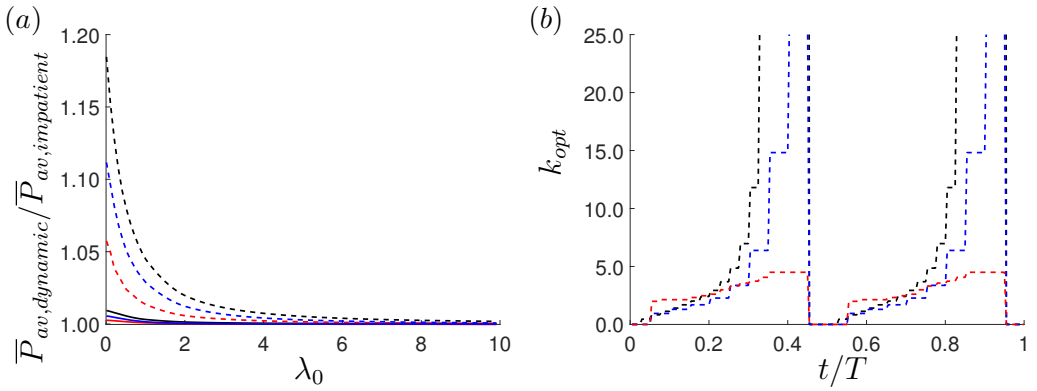

Figure 5.4: Variations in: (a) normalised maximum $\overline{P}_{av}$ with λ_0, and; (b) optimal k with the relative time over a tidal cycle t/T for $\lambda_0 = 0.1$, for one (solid lines) and five (dashed lines) rows of actuator discs (black lines), FP rotors (red lines), and VP rotors (blue lines), in moderately blocked ($B_L = 0.16$) flow with the dynamic strategy.

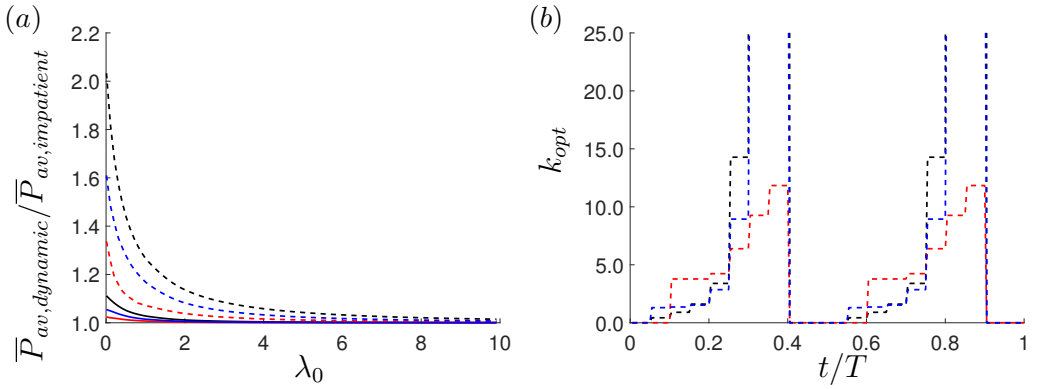

Figure 5.5: Variations in: (a) normalised maximum $\overline{P}_{av}$ with λ_0, and; (b) optimal k with the relative time over a tidal cycle t/T for $\lambda_0 = 0.1$, for one (solid lines) and five (dashed lines) rows of actuator discs (black lines), FP rotors (red lines), and VP rotors (blue lines), in highly blocked ($B_L = 0.314$) flow with the dynamic strategy.

cantly lower for the more realistic rotors than for the idealised disc, and also smaller for the vast majority of cases in which the turbine resistance is less significant.

To understand why the potential increase in power using dynamic tuning is lower for the rotors than for the disc, it is useful to consider the variations with time, t, of the corresponding optimal tunings, k (Figures 5.4b and 5.5b, where $N_R^* = 5$ and $\lambda_0 = 0.1$). Vennell (2016) has shown that in the optimal dynamic tuning of an actuator disc, the relative importance of C_P, C_T and η varies over the tidal cycle. As such, the half tidal cycle may be divided into four main phases: phase 1, in which C_T is set to zero to allow the flow to accelerate uninhibited; phase 2, in which a large η is required, as in the case of small λ_0; phase 3, in which a large C_P is required, as in the case of large λ_0, and; phase 4, in which C_T is set to its maximum value in order to stop the flow sooner and thus ensure an extended period of flow acceleration for the next half tidal cycle. There is practically no difference in optimal k between the rotor and disc during phase 1, because the turbines are not operating. However, in the latter phases, certain conditions or combinations of C_P, C_T and η for a certain phase will be clearly advantageous over the other phases if discs are installed. For the tidal rotors, however, the three parameters are still fairly competitive over the entire half-cycle. Thus, tidal rotors will give a very limited range of k in comparison, and tuning is naturally deemed to be less important.

Again, the results obtained using rotors are enhanced by the VP mechanism, as it enables the rotors to more closely approximate the idealised optimal k variations over the tidal cycle as predicted by the disc. However, as the maximum k for idealised disc actually goes to infinity while the value remains limited for the VP rotor (to $k \approx 28$ for $B_L = 0.16$ and $k \approx 45$ for $B_L = 0.3$, neither shown due to figure sizing limitations), there still exists a significant difference between the VP rotor and the actuator disc.

As a common finding across both the previous section and this section, it should

be noted that, for all tuning strategies, the amount of power produced per row (or per turbine) decreases as additional rows (from $N_R^* = 1$ to 5) are added. This finding can be attributed to the phenomenon of a diminishing return (Vennell, 2010), in which each additional row of turbines results in a decreased increment in performance. It is worth noting that the dynamic strategy has the most gradual diminishing return, as a larger N_R^* within the strategy effectively enhances the thrust that can be applied in phase 4 and thus benefits the strategy as a whole (Vennell, 2016).

5.2.2 Fixed-pitch and variable-pitch rotors

Further understanding of the differences in operation between a FP and VP rotor is useful. Effectively, by adopting a VP device, an additional degree of freedom is gained with β_a. Referring back to Figures 5.1b-5.5b, for each value of k output by the tidal rotors, a value of TSR and/or β_a exists for the calculation of the optimal tuning parameter. For fixed tuning, Figures 5.6 and 5.7 show the domain-dependent variation of optimal TSR and β_a for both FP and VP rotors under different turbine deployments; likewise, Figures 5.8 and 5.9 depict the same trendlines for dynamic tuning, with temporally varying k.

It is first noted that, for the fixed tuning strategy, as the channel moves from high to low λ_0, the optimal TSR value for FP rotors drops drastically compared with VP rotors. Although, due to the relationship between TSR, flow velocity u, and angular velocity ω, the decrease of TSR coupled with an increase in u (less resistance to flow in an inertia-dominated channel) will result in an overall gain in the average value of ω. For a VP rotor, ω can increase up to three times its original value across different channel dynamics, while a FP rotor sees a slightly lower increase.

In the case of a FP rotor when turbine effects are predominant in the channel (large B_L, large N_R^*, small λ_0), as β_a is constant while ϕ is increasing due to the decreasing TSR, α must increase. This is an undesirable phenomenon, as stall

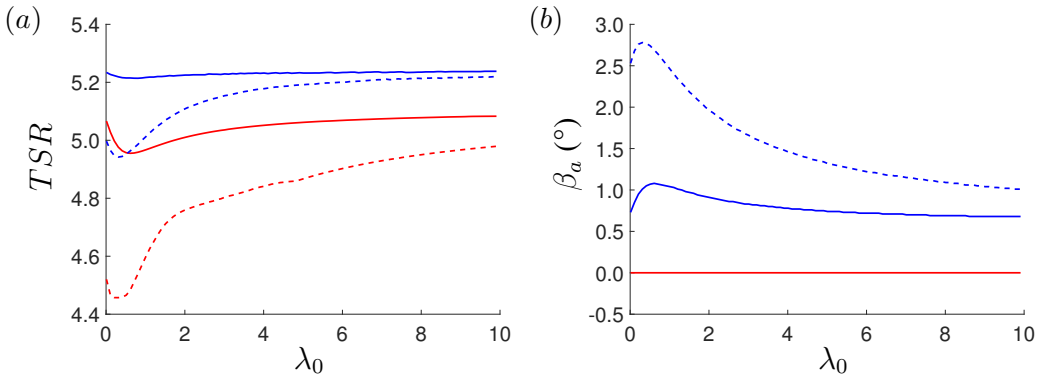

Figure 5.6: Variations with λ_0 in: (a) optimal fixed TSR, and; (b) optimal fixed β_a, for one (solid lines) and five (dashed lines) rows of FP rotors (red lines) and VP rotors (blue lines), in moderately blocked ($B_L = 0.16$) flow with the fixed strategy.

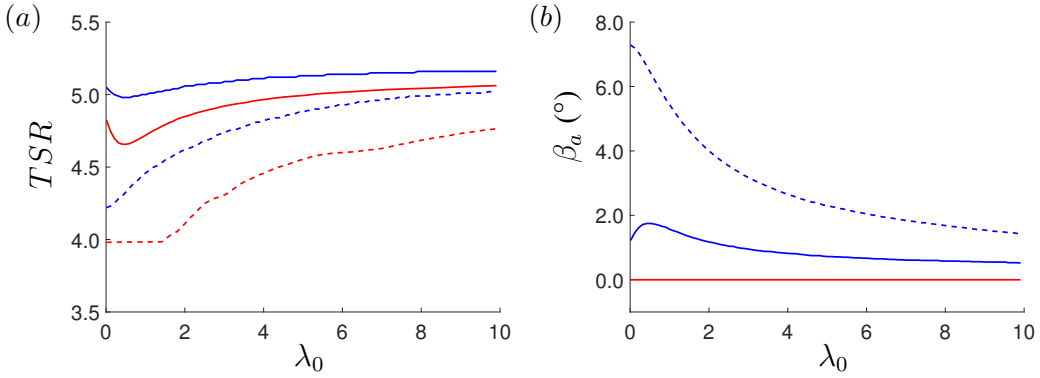

Figure 5.7: Variations with λ_0 in: (a) optimal fixed TSR, and; (b) optimal fixed β_a, for one (solid lines) and five (dashed lines) rows of FP rotors (red lines) and VP rotors (blue lines), in highly blocked ($B_L = 0.314$) flow with the fixed strategy.

will occur due to the flow separation from the suction surface of the blade (Burton et al., 2011), which can result in a significant loss of power, since the C_L/C_D ratio is affected by the large amount of increase in the drag and decrease in the lift. However, in the case of a VP rotor, coupled by the increase of β_a, α stays fairly constant in the desired design range. More importantly, by controlling the pitch angle, the VP rotor observes less turbine thrust (refer to Figure 5.12) and also an improvement in η when compared to the FP rotor. The lowered flow rate reduction and higher control in maintaining the value of TSR and resulting torque provides additional power, especially under the condition of small λ_0 with lower values of k.

In the operation of a VP rotor within the dynamic tuning strategy, maximum

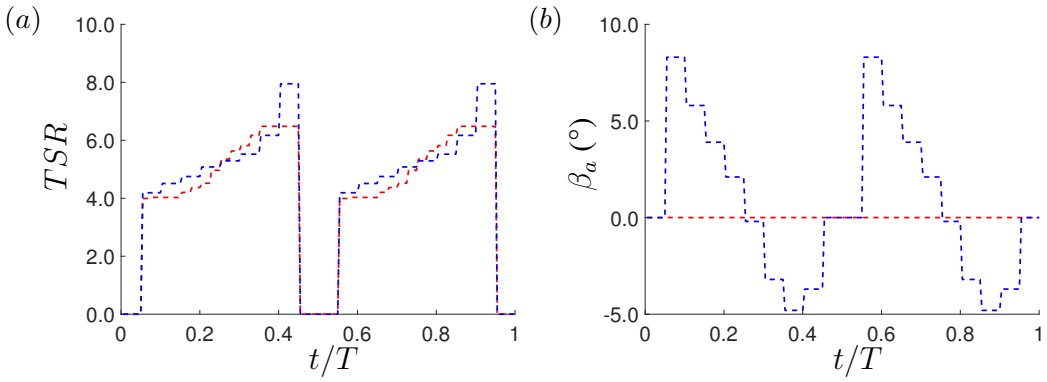

Figure 5.8: Variations with the relative time over a tidal cycle, t/T, in: (a) optimal dynamic TSR, and; (b) optimal dynamic β_a, for $\lambda_0 = 0.1$ and five rows of FP rotors (red lines) and VP rotors (blue lines), in moderately blocked ($B_L = 0.16$) flow with the dynamic strategy.

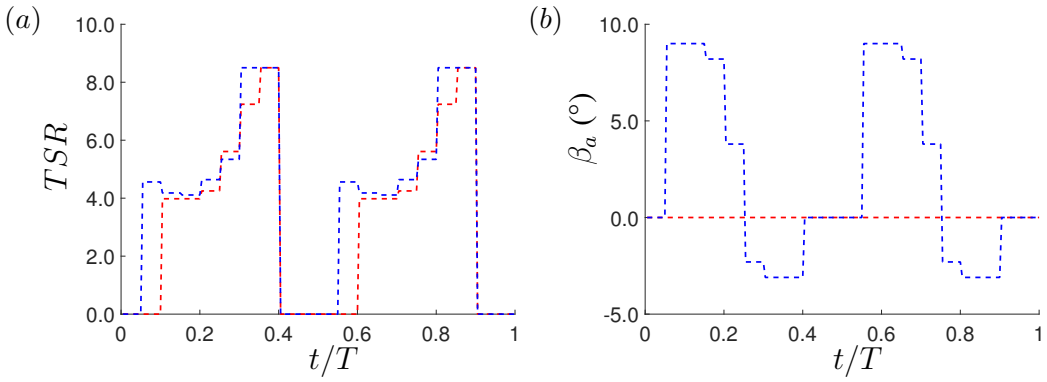

Figure 5.9: Variations with the relative time over a tidal cycle, t/T, in: (a) optimal dynamic TSR, and; (b) optimal dynamic β_a, for $\lambda_0 = 0.1$ and five rows of FP rotors (red lines) and VP rotors (blue lines), in highly blocked ($B_L = 0.314$) flow with the dynamic strategy.

efficiency is physically achieved by allowing low flow resistance (increasing β_a) after the turn-off status at flow reversal to allow for flow to build up uninhibited, and later operating with decreasing β_a and TSR to apply maximum resistance. The required change in TSR and β_a to achieve the optimal k, while maintaining a reasonably favourable α over the tidal cycle, are plotted for different blockage conditions in Figures 5.8 and 5.9.

Overall, the VP rotor is a favourable option as it allows the turbine to adjust to operation states that are more beneficial to operation efficiency and power production. More specifically, with the single degree of freedom limitation that the FP

rotor has, it is only comparable to the idealistic actuator disc in terms of thrust. In order to better match both levels of thrust and power, the VP rotor with two degrees of freedom is able to achieve better results. There are, of course, many other advantages and disadvantages to FP and VP rotors beyond those studied within the scope of this work.

5.2.3 Disc and rotor power comparison

Finally, the amount of $\overline{P}_{av}$ produced by the more realistic tidal rotor is compared directly with the amount produced by the idealised actuator disc. For different combinations of B_L and N_R^* in both strategies, Figures 5.10 and 5.11 show the variations with λ_0 in $\overline{P}_{av,rotor}$, normalised by $\overline{P}_{av,disc}$, as a measure of agreement between of the actuator discs and tidal rotors in terms of power production. In a similar fashion, Figures 5.12 and 5.13 display outputs of time-averaged rotor thrust $\overline{T}_{rotor}$ normalised by disc thrust $\overline{T}_{disc}$ as well as the time-averaged flow rate of the disc and rotor simulations normalised by the time-averaged unexploited channel flow rate $\overline{Q'}_{unexploited}$, both for the fixed tuning strategy across a range of channel dynamics. On the other hand, Figures 5.14-5.19 compare the fixed and dynamic tuning strategies in terms of P_{av}, T and Q' over the tidal cycle. For both moderately and highly blocked flow conditions, the installation of five rows of discs and rotors are examined within two specific sampled channel dynamics ($\lambda_0 \approx 0.1$ as in the Cook Strait and $\lambda_0 \approx 1.0$ as in the Pentland Firth, see Vennell and Adcock, 2014). In most of the power and thrust figures for dynamic tuning, the appearance of jagged and non-smooth curves are due to the 'step' method used in section 5.1.4, where the tidal cycle has been divided into a finite number of time blocks. Table 5.1 presents the capacity factors corresponding to Figures 5.14 and 5.17, which are defined as the ratio of the time-averaged available power with the power capping strategy, $\overline{P}_{av,rated}$, to the rated power, $P_{av,rated}$. The rated power is a designated value used in the oper-

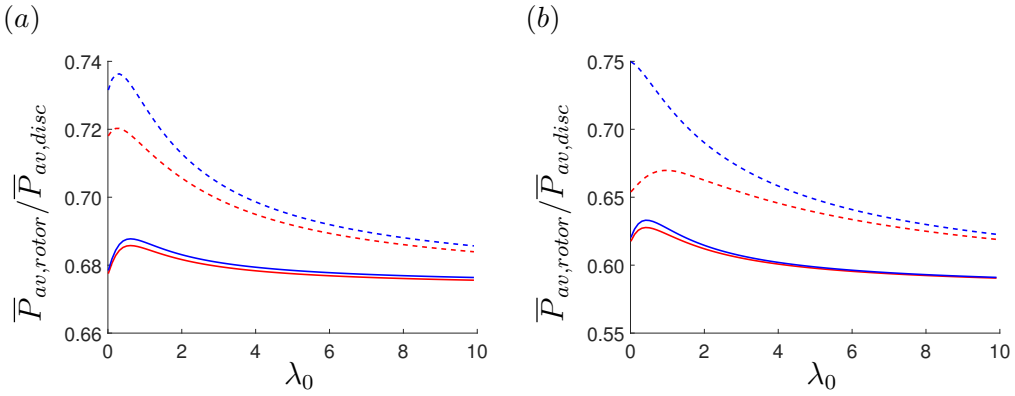

Figure 5.10: Variations in normalised maximum $\overline{P}_{av}$ with λ_0, for one (solid lines) and five (dashed lines) rows of FP (red lines) and VP (blue lines) rotors with fixed tuning strategy, in: (a) moderately blocked ($B_L = 0.16$) flow, and; (b) highly blocked ($B_L = 0.314$) flow.

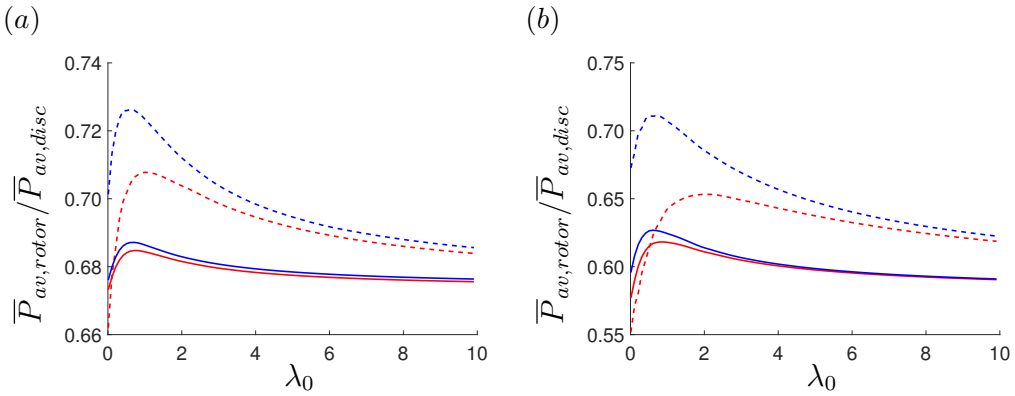

Figure 5.11: Variations in normalised maximum $\overline{P}_{av}$ with λ_0, for one (solid lines) and five (dashed lines) rows of FP (red lines) and VP (blue lines) rotors with dynamic tuning strategy, in: (a) moderately blocked ($B_L = 0.16$) flow, and; (b) highly blocked ($B_L = 0.314$) flow.

ation of power capping to indicate the maximum allowable power (see Appendix A for detailed discussion), so when rated power is fully extracted, the capacity factor is at unity and it decreases with increasing time that turbines operate below rated power. See Wang and Adcock (2019), Vogel et al. (2018), and Vogel et al. (2019) for more discussion of the capacity factor.

The results show that, as expected, the idealised disc consistently overestimates the amount of time-averaged power available to the more realistic rotor. Across the range of variables considered, and for the specific designs chosen, $\overline{P}_{av}$ produced by the rotors is typically 60-70% of the amount produced by the disc. Additionally, for

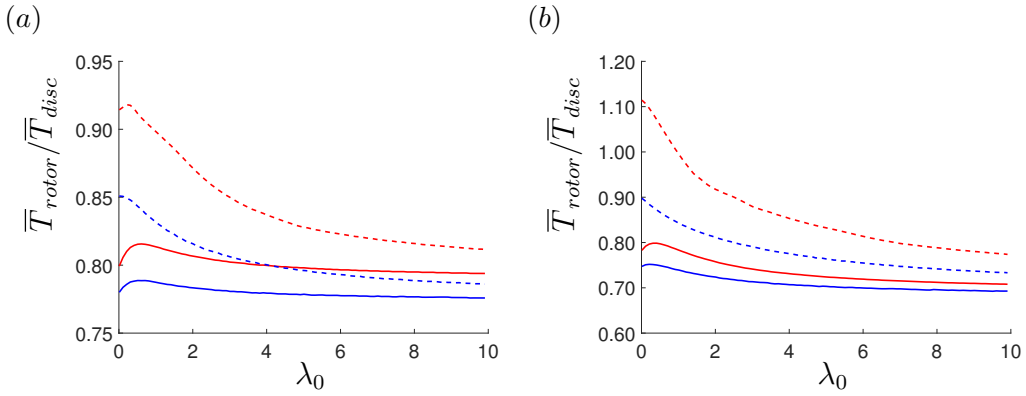

Figure 5.12: Variations in normalised $\overline{T}$ with λ_0, for one (solid lines) and five (dashed lines) rows of FP (red lines) and VP (blue lines) rotors with fixed tuning strategy, in: (a) moderately blocked ($B_L = 0.16$) flow, and; (b) highly blocked ($B_L = 0.314$) flow.

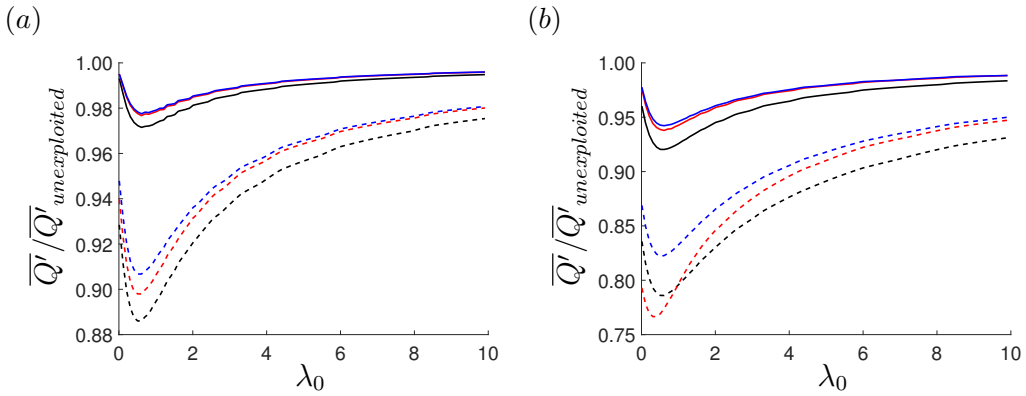

Figure 5.13: Variations in normalised $\overline{Q'}$ with λ_0, for one (solid lines) and five (dashed lines) rows of actuator discs (black lines), FP rotors (red lines), and VP rotors (blue lines) rotors with fixed tuning strategy, in: (a) moderately blocked ($B_L = 0.16$) flow, and; (b) highly blocked ($B_L = 0.314$) flow.

the fixed tuning strategy, it is apparent that the actuator disc also tends to overestimate the flow reduction caused by turbines, and will thus tend to overestimate their environmental impacts. With the dynamic tuning strategy, however, it is possible for actuator discs to experience a certain period within the tidal cycle where the flow rate through the disc resumes the level found in the unexploited channel, albeit with a greater phase shift, as suggested by Figures 5.16 and 5.19. Across both tuning strategies, the diminishing return for the rotor is also found to be more gradual than that for the disc.

The more idealistic disc is generally found to overestimate the rotor power by

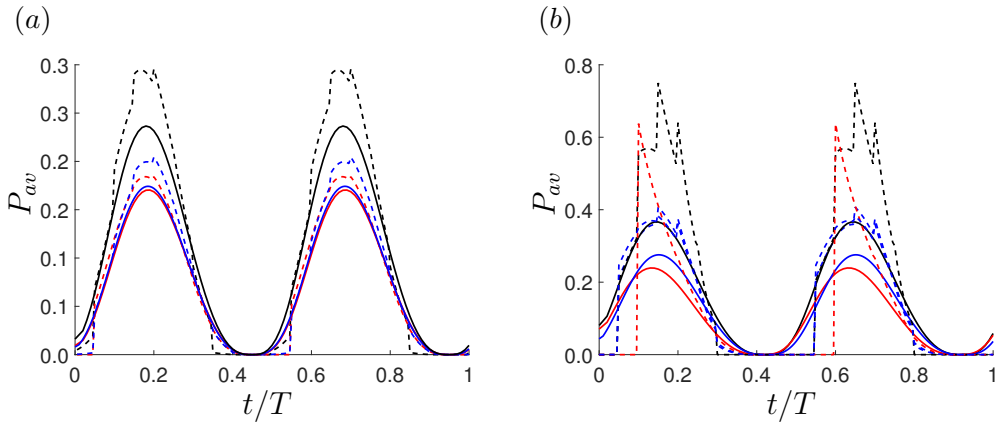

Figure 5.14: Variations in P_{av} with the relative time in a tidal cycle, t/T, in: (a) moderately blocked ($B = 0.16$), and; (b) highly blocked ($B = 0.314$) flow, for $\lambda_0 = 0.1$ with fixed (solid lines) and dynamic (dashed lines) tuning strategies for five rows of actuator discs (black lines), FP rotors (red lines), and VP rotors (blue lines).

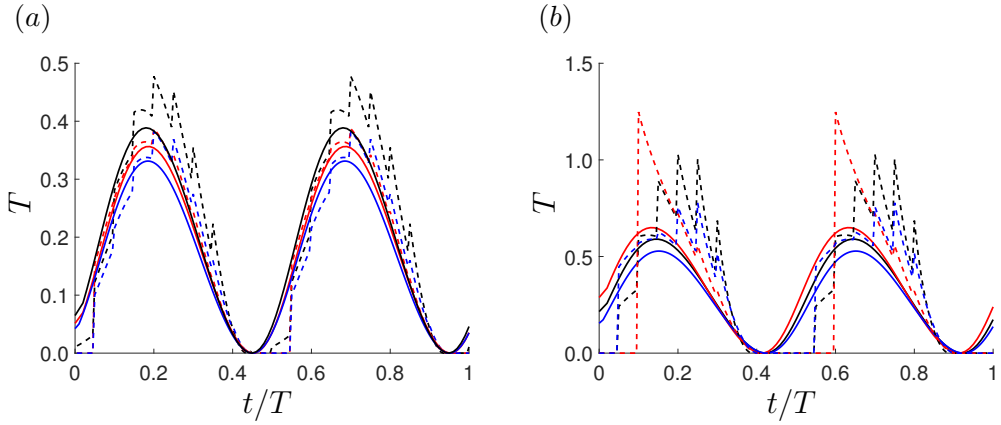

Figure 5.15: Variations in T with the relative time in a tidal cycle, t/T, in: (a) moderately blocked ($B = 0.16$), and; (b) highly blocked ($B = 0.314$) flow, for $\lambda_0 = 0.1$ with fixed (solid lines) and dynamic (dashed lines) tuning strategies for five rows of actuator discs (black lines), FP rotors (red lines), and VP rotors (blue lines).

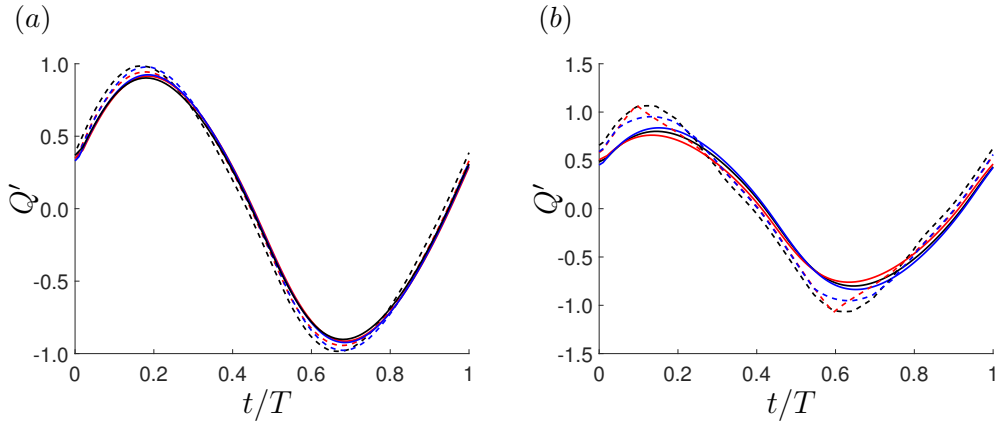

Figure 5.16: Variations in Q' with the relative time in a tidal cycle, t/T, in: (a) moderately blocked ($B = 0.16$), and; (b) highly blocked ($B = 0.314$) flow, for $\lambda_0 = 0.1$ with fixed (solid lines) and dynamic (dashed lines) tuning strategies for five rows of actuator discs (black lines), FP rotors (red lines), and VP rotors (blue lines).

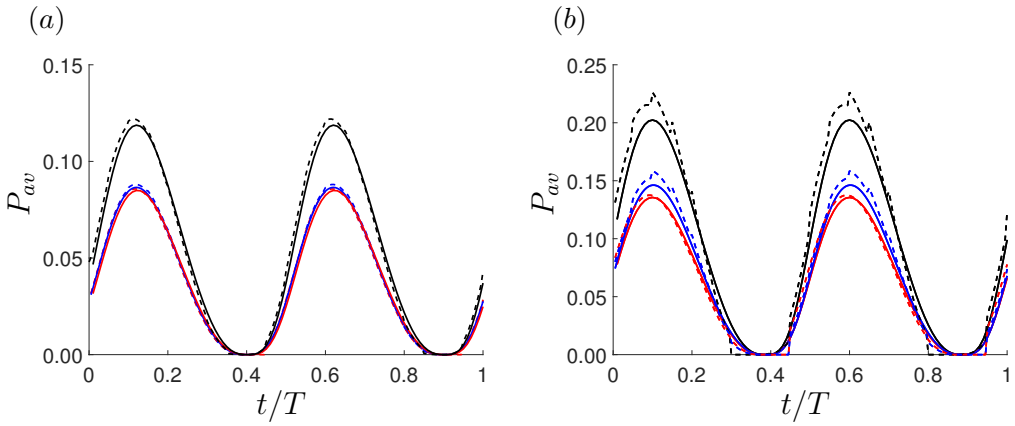

Figure 5.17: Variations in P_{av} with the relative time in a tidal cycle, t/T, in: (a) moderately blocked ($B = 0.16$), and; (b) highly blocked ($B = 0.314$) flow, for $\lambda_0 = 1.0$ with fixed (solid lines) and dynamic (dashed lines) tuning strategies for five rows of actuator discs (black lines), FP rotors (red lines), and VP rotors (blue lines).

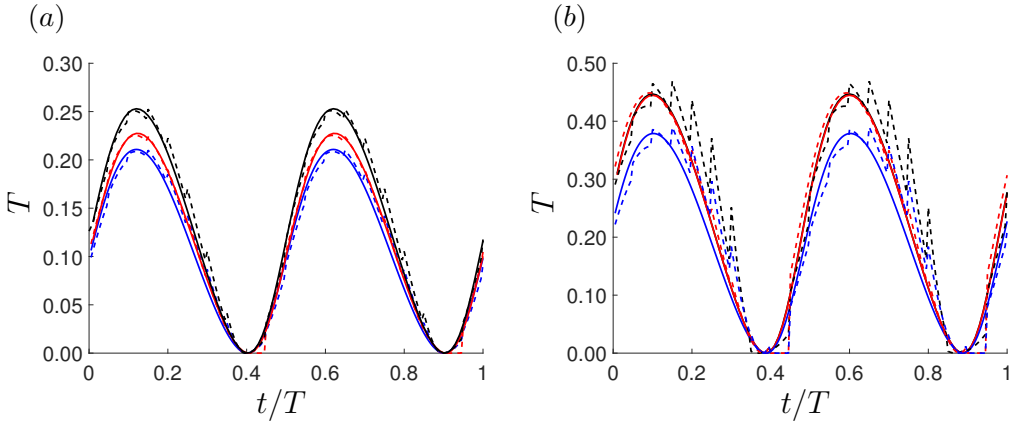

Figure 5.18: Variations in T with the relative time in a tidal cycle, t/T, in: (a) moderately blocked ($B = 0.16$), and; (b) highly blocked ($B = 0.314$) flow, for $\lambda_0 = 1.0$ with fixed (solid lines) and dynamic (dashed lines) tuning strategies for five rows of actuator discs (black lines), FP rotors (red lines), and VP rotors (blue lines).

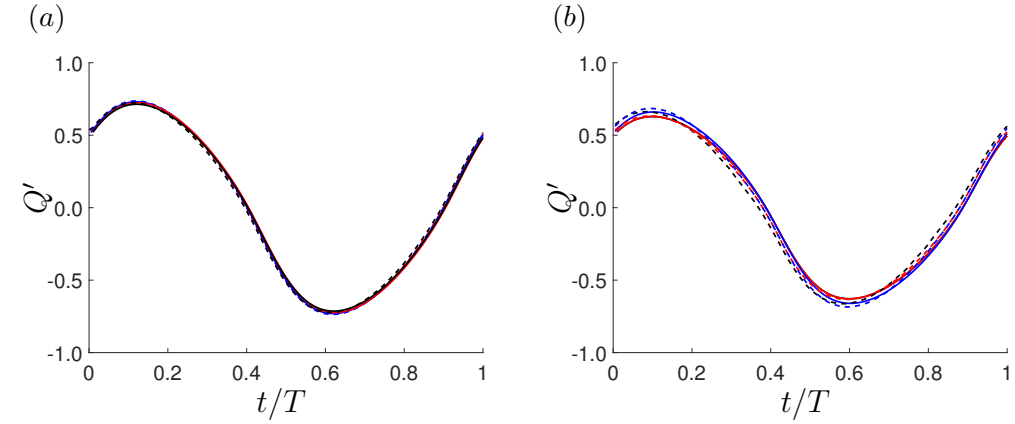

Figure 5.19: Variations in Q' with the relative time in a tidal cycle, t/T, in: (a) moderately blocked ($B = 0.16$), and; (b) highly blocked ($B = 0.314$) flow, for $\lambda_0 = 1.0$ with fixed (solid lines) and dynamic (dashed lines) tuning strategies for five rows of actuator discs (black lines), FP rotors (red lines), and VP rotors (blue lines).

Table 5.1: Capacity factors for the conditions corresponding to Figures 5.14 and 5.17.

B_L	λ_0	Turbine	Fixed tuning	Dynamic tuning
0.16	0.1	AD	0.42	0.38
		FP	0.42	0.39
		VP	0.43	0.41
0.314	0.1	AD	0.44	0.28
		FP	0.44	0.19
		VP	0.43	0.38
0.16	1.0	AD	0.44	0.44
		FP	0.44	0.44
		VP	0.44	0.44
0.314	1.0	AD	0.45	0.42
		FP	0.45	0.45
		VP	0.45	0.43

a greater amount when the turbine resistance is less significant and the optimal k is high, and by a lesser amount when the turbine resistance is more significant and the optimal k is low. As previously noted, the VP rotor is found to provide closer agreement with the disc model than the FP rotor, because the operation of varying the blade pitch allows the rotor to approximate more closely the performance of the idealised disc.

For sufficiently large λ_0, the main apparent strength of the actuator discs is the high maximum C_P that can be attained and, in comparison, the maximum C_P difference with the tidal rotors. The normalised available power will tend to the ratio of maximum rotor C_P to disc C_P, the value of which will generally decrease with with higher blockage, as the difference between the maximum C_P values of discs and rotors become larger, regardless of tuning strategy. As discussed in Chapter 4, the rotor achieves an optimal value of maximum C_P for a given B_L when the rotor is optimally designed for that blockage configuration. From the results of Schluntz (2014), it can be inferred that, by increasing B_L, the mass flow rate through the rotor designed for higher blockage with higher c_x (and σ) is decreased when compared to

the rotor designed for the original, lower blockage with lower c_x (and σ). According to Equation 4.6, the consequential decrease in both ϕ and W for the higher-blockage rotor may compete with the increasing blade solidity and therefore may affect the value of τ, while the idealisation of the disc allows it to freely apply higher thrust without realistic consequences.

For small λ_0 and fixed tuning, the degree of agreement depends more on the ratio of rotor C_T to disc C_T, as well as the difference in η between the two models, although the ratios between the two parameters for disc and rotor will vary independently from the decrease of k. For small λ_0 and dynamic tuning, however, the determination of the key relationship is more complicated because the rotor and disc models differ not only in terms of C_P, C_T and η, but also in the relative importance of these variables, which changes throughout the tidal cycle.

For fixed tuning, as k decreases in operation (with the value for the disc dropping faster than the rotor), the relative level of resistance and therefore C_T, which determines the change of momentum in the channel, decreases while η, which determines the relationship between power and flow speed, increases (refer to Figures 4.5 and 4.6). Following these trends, the $\overline{P}_{av}$ calculated by the actuator disc model is found to approach those of the tidal rotors. From Figure 5.12a, it is also observed that the thrust level of a FP rotor matches almost exactly with that of the actuator disc representation in the region with small λ_0, meaning that the difference between the absolute values of thrust between the two models is decreasing (especially for the scenario of $B_L = 0.3$ and $N_R^* = 5$, as evidenced by the value of $\overline{T}_{rotor}/\overline{T}_{disc}$ reaching unity). However, the power levels predicted by the two models are still inconsistent due to the difference in η, for which the curves of the two models contract until k reduces to a certain point. Therefore, at this point, the $\overline{P}_{av}$ estimations produced by the actuator disc model will be closer to that predicted with a more realistic model. With VP rotors, even greater improvement can be observed and

this has been explained in Section 5.2.2.

For the dynamic tuning strategy, in phases 1 and 2, similar improvements can be expected due to operation under small k values. In phases 3 and 4, however, higher k is required and the advantage of the disc is enhanced by producing unrealistically large C_T and C_P. Therefore, the inverse trend of the normalised $\overline{P}_{av}$ curve for the dynamic tuning strategy is less steep and less obvious than that of the fixed tuning strategy (comparison between Figure 5.10 and Figure 5.11). Generally speaking, dynamic tuning is able to achieve higher performance as it produces greater power with similar or even lower levels of thrust than required by the fixed tuning strategy. Although high C_T is needed at the end of each half tidal cycle, with the rapid flow rate decline before the flow reversal, the overall thrust provided by the turbines remains low, as shown in Figures 5.15 and 5.18. However, it is worth noticing that in the case of a large number of turbine rows in an inertia-dominated channel ($N_R^* = 5$, $B_L = 0.314$, $\lambda_0 = 0.1$), Figure 5.15b and Table 5.1 indicate that a significant increase in power is only achieved through low capacity factors along with heavy structural load. Therefore the feasibility of such turbine operation without power capping remains questionable.

It is possible for the normalised $\overline{P}_{av}$ curves in Figures 5.10 and 5.11 to increase overall, instead of decrease, with increasing λ_0 for both fixed and dynamic tuning strategies. For a FP rotor under conditions of higher N_R^* or higher B_L using the fixed tuning strategy, as k tends to zero, the rotor will approach the highest point on its η curve whilst the disc will follow its own increasing η curve and η_{disc} goes to unity. With the progressive increase of N_R^*, the value of η_{rotor} will pass its peak point and begin to drop as the large incremental thrust becomes too much of an impedance to flow, and some efficiency must be given up to maintain an acceptable level of flow rate. Thus, C_T becomes the most prioritised factor in comparison to the contrasting C_P and η, further enlarging the ratio of η_{rotor} to η_{disc}. Ultimately, both FP and VP

rotors are set to fail below certain values of TSR due to the inner limitation of the BC-BEMT (see Section 4.4.2), thus they will not be able to reach the practically zero C_T of the disc. Therefore, when N_R^* or B_L become unrealistically large, for the fixed tuning strategy, the $\overline{P}_{av}$ ratio of rotor to disc is essentially dependent on the corresponding ratio of C_T for $C_{T,disc} \rightarrow 0$ and the corresponding ratio of η for $\eta_{disc} \rightarrow 1$. On the other hand, for the dynamic tuning strategy, due to the infinite amount of thrust in phase 4, the flow acceleration closely overlaps with the pressure forcing. Thus in the power comparison graphs of Figures 5.10 and 5.11, when λ_0 is small, it is possible for the curves to veer toward either direction on the y-axis.

5.2.3.1 Rotor sensitivity and design

Since the determining factor for the shape of the normalised $\overline{P}_{av}$ curves varies with the channel dynamics for both strategies, it is ultimately reliant on the rotor design and different hydrofoil properties. In order to investigate the optimal rotor design for different channel dynamics and different tuning strategies, the three FP and VP rotors designed by the RANS-BE method for different blockages (mentioned in Chapter 4) are simulated with $N_R^* = 1$ and 5, and $B_L = 0.16$.

Figure 5.20 plots the $\overline{P}_{av}$ curves of different rotor designs normalised over the $\overline{P}_{av}$ of the equivalent disc. For the fixed tuning strategy, a relatively large variation is observed between the three different FP rotors. When turbine resistance is of lower importance ($N_R^* = 1$), the FP rotor with $B_r = 0.16$ is consistently superior in performance, which can be expected as it is the optimised rotor with the highest $C_{P,max}$ for the simulated domain blockage. However, when the importance of turbine resistance is increased (smaller λ_0 and $N_R^* = 5$), the performance of the $B_r = 0.01$ rotor exceeds that of the optimised rotor as it has a higher relative η and this is beneficial in these circumstances for the reason explained in Section 4.4.1. The last rotor with $B_r = 0.314$ is generally inferior in all cases when compared with the other two as it possesses neither high C_P nor η.

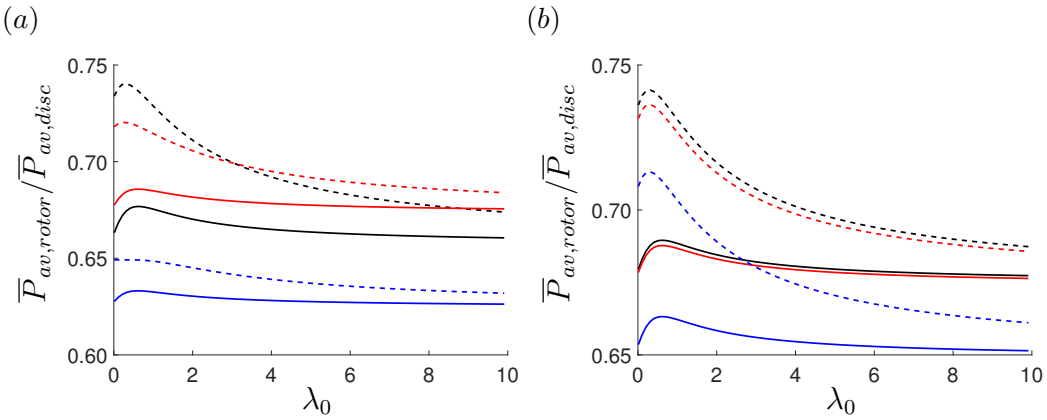

Figure 5.20: Variations in normalised maximum $\overline{P}_{av}$ with λ_0, for one (solid lines) and five (dashed lines) rows of (a) FP rotors, and; (b) VP rotors, designed for $B_r = 0.01$ (black lines), $B_r = 0.16$ (red lines) and $B_r = 0.314$ (blue lines) in moderately blocked ($B_L = 0.16$) flow.

While this variation also exists for VP rotors, it is much more limited as the spread in the $\overline{P}_{av}$ curves between the three VP rotors is much smaller. This relative similarity in performance can be explained physically by, for example, considering the $B_r = 0.314$ VP rotor. While this rotor (which has higher c_x, resulting in a higher solidity profile and lower twist profile) is operating, since TSR is decreasing and β_a is increasing for better efficiency, it essentially becomes a rotor with design properties for lower blockage, i.e. in the physical sense, it is equivalent to a more porous disc applying less thrust to the flow, similar to the rotor designed for lower blockage ratios.

Even though variations in power between the different rotors for both strategies have been observed, in most practical scenarios, the amount of turbine drag will be sufficiently small compared to the amount of natural drag. As such, for each value of λ_0, the high-C_P rotor will produce a largely similar amount of power to the high-η rotor given the flexibility of tidal rotors under different operating conditions (however, the approximation of rotors estimating 60-70% of the power produced by discs is still true for all rotors). Still, the high-η rotor design will afford benefits of lower structural costs and higher extraction efficiency.

For the dynamic tuning strategy, a clear choice of rotor design becomes more complex due to the different performance characteristics needed for different phases of the strategy. Realistically, a single rotor will not be able to accommodate perfectly the entire strategy, especially as some of the required characteristics are contradictory during different phases. A rotor optimised for a certain blockage ($c_x = c_{x,optimal}$) naturally has better C_P in those blockage conditions (see Schluntz and Willden, 2015), while an over-designed rotor ($c_x > c_{x,optimal}$) is expected to have higher C_T and an under-designed rotor ($c_x < c_{x,optimal}$) will have lower C_T and better η. Despite having the option of a VP rotor that will be able to make certain adjustments, it is difficult to achieve the designed performance while operating under off-design conditions. To analyse the different phases in the dynamic tuning process, the high-blockage, over-designed rotor is generally favourable for phase 4 as it allows for greater flow to build up for the early stage of the next half tidal cycle. However during phase 2, the higher relative value of C_T will give more resistance to the flow and thus worsen the flow condition later on in phase 3; as phases 2 and 3 are the periods where most of the power produced, the over-designed rotor is generally found to be inferior to the rotor designed for a lower blockage. Therefore a low-blockage, under-designed rotor is generally favourable for phase 2, as better efficiency allows the turbine to extract more power after its start-up. Additionally, a lower C_T will allow for better flow conditions in the following phase within the half tidal cycle, but it will not be able to provide as much thrust as an over-designed rotor does at the end of the cycle. Thus, it follows that an optimally designed rotor will be favourable for phase 3, but its advantage within the tidal cycle is not as prominent as the favourable choices for the other phases. From this analysis, it is concluded that there is generally a trade-off in the rotor design when considering the overall dynamic strategy.

5.3 Conclusions

In this chapter, the works of Vennell (2010, 2016) have been extended to incorporate a more realistic turbine representation, which is based on the BC-BEMT of Vogel et al. (2018). Naturally, the results presented here depend on the design of the rotor, which uses the approach of McIntosh et al. (2011). A number of rotor designs have been used in this work beyond those presented here, and across the range of flow conditions and turbine deployments considered, the $\overline{P}_{av}$ results appear to be insensitive to the exact specifications of rotor design. The study also incorporates a number of simplifying assumptions and limitations inherent in the BC-BEMT, as described in the current and previous chapters. However, given the appropriate rotor design and operation range considered, the accuracy of the BC-BEMT and thus the comparisons between disc and rotor remain fair. As such, the overall findings should be relevant to a broad range of turbines and practical scenarios. With this model, the significance of tuning for tidal turbines and its role in maximising the power available from tidal channels have been explored.

For all the tuning strategies considered, tuning is shown to be less important for the tidal rotor than for the actuator disc. For the idealised disc, large variations in k may be used to produce extreme variations in C_T and thus C_P and η. Depending on the flow condition, the disc may be assigned either a very large k, so as to produce a very large C_P (or simply a very large C_T, in the case of dynamic tuning), or a very small k, so as to produce a very large η. For the more realistic rotor, however, the corresponding values of C_P, C_T and η are typically much lower, and undergo less variation with k. As a result, the range of optimal k is smaller and the potential benefits of a given tuning strategy are less significant. In terms of the power production predicted by two turbine representations, it has been observed that, as expected, the idealised disc consistently overestimates the amount of power available relative to the more realistic rotor. Across the range of variables considered,

the power produced by the rotors is typically 60-70% of the amount produced by the disc — this range of values can potentially serve as a general correction for current and future resource assessments. The degree of agreement between the two turbine representations depends on the specifics of the rotor design, but for the fixed strategy the disc is generally found to overestimate the rotor power by a lesser amount when the turbine resistance is relatively significant (that is to say, when λ_0 is small and B_L and/or N_R^* are large) and by a greater amount when the turbine resistance is relatively insignificant (as in most practical scenarios). Similarly, in the case of dynamic tuning, a significant overestimation of the rotor power is observed for the disc. In addition, for both tuning strategies, the disc also tends to over-predict the diminishing return that has been found to occur with increasing N_R^*, though the extent of over-prediction is lessened with the dynamic strategy.

With greater flexibility in its operation, the VP rotors can more closely approximate the performance of the disc. The adjustable value of β_a enables the rotor to vary the value of k while maintaining a near-optimal TSR, which yields benefits in terms of both power production and extraction efficiency, particularly in off-design operating conditions and cases where turbine resistance is significant. The results also provide a general understanding of tuning that may be used to better inform the design of tidal turbines. If a fixed tuning strategy is adopted, then $\overline{P}_{av}$ is maximised by designing the rotor to produce either a high C_P if λ_0 is large, or a high η if λ_0 is small. Thus a regular rotor design process is deemed to best suit the drag-dominated channel, whereas in comparison, an under-designed rotor is generally desirable for the inertia-dominated channel, with its relatively higher η and lower C_T. On the other hand, if a dynamic tuning strategy is adopted, the task of optimal design is complicated by the fact that the rotor must provide different, and perhaps contradictory, performance characteristics throughout the tidal cycle.

Chapter 6

Simplified Models of Local Blockage Effects in Oscillatory Channel Flow *

In order to investigate efficiently the design of tidal turbine arrays, a variety of theoretical models have been developed to predict and maximise the extraction of tidal power. As reviewed in Chapter 2, Garrett and Cummins (2007) used an actuator disc model to show that for a single turbine (or full-width turbine array) in volume-flux-constrained flow, the maximum P_{av} depends on the value of B_L. Nishino and Willden (2012*b*) later extended this actuator disc model to examine the maximum P_{av} that may be produced by tidal turbine arrays spanning only part of the channel cross-section. By assuming that array-scale flow events take place over much greater length scales than device-scale flow events, Nishino and Willden (2012*b*) were able to describe the performance of a partial-width array using a two-scale actuator disc model. The authors then showed that for each global blockage, there exists an optimal local blockage (or equivalently, an optimal array blockage) that maximises P_{av}. This optimal B_L can be achieved by optimising the cross-stream

*The discussions in this chapter have been published as a joint journal paper — see Bonar et al. (2019) from Appendix C — in which Lei Chen was the second author. The 2D numerical results in this chapter were kindly provided by the main author Dr Paul A. J. Bonar but this chapter aims to present only Chen's contribution to this work, though the collaborative nature of the analysis herein is emphasised.

spacing between the turbines within the array (Nishino and Willden, 2012*b*).

The two-scale actuator disc theory can be used to predict the optimal arrangement of, and maximum power available to, tidal turbines arranged in a single cross-stream row. However, these predictions are limited by the simplifying assumptions of the theory that neglect the important interaction between the turbines and the channel-scale flow (Vennell, 2010). In order to investigate more realistic oscillatory flow conditions, the two-scale theory can be coupled with the channel model of Garrett and Cummins (2005), which describes the interactions between the resistance presented by the array and the bulk flow through the channel. Though simplistic, the channel model is capable of capturing the leading order physics of tidal energy extraction and channel-scale dynamics at low computational cost. However, even though this analytical approach advanced the turbine model one step further, more realistic flow conditions and channel dynamics, as well as the interaction between the turbines within an array require the complexity of a more detailed numerical approach. This is especially true for the case of a partially blocked channel, where the analysis of the flow field can no longer simply be considered as 1D problem (Bonar et al., 2019).

This chapter provides a detailed investigation into the effects of local blockage on tidal turbine array performance by comparing a semi-analytical model that incorporates channel dynamics following the work of Willden et al. (2014), with results from a shallow water model developed by Bonar (2017). The details of the semi-analytical coupling scheme are discussed in Section 6.1 and the 2D numerical model is briefly reviewed in Section 6.2. Following this, a comparison between two hydrodynamic modelling approaches with varying values of tidal forcing amplitude a_0 and channel background roughness C_d are presented and discussed in Section 6.3.

6.1 One-Dimensional Analytical Channel Model

As reviewed in Chapter 2, Garrett and Cummins (2005) proposed an idealised theoretical model to describe the extraction of energy from a simple tidal channel. In this 1D theory, the tidal forcing is assumed to be unaffected by changes in the channel flow rate, and the turbine array, which is modelled as a simple opposing force, is assumed to completely span the channel width. Vennell (2010) later combined this simple model with the volume-flux-constrained actuator disc theory and showed that array power production benefits from the arrangement of tidal turbines in a single cross-stream row.

The model presented by Vennell (2010), adopted in Chapter 5, is useful for assessing the performance of full-width tidal arrays. However, it is more realistic to consider partial-width arrays because tidal channels are not normally fully occupied, owing to the presence of shipping lanes, bathymetric variations, etc., are not normally fully occupied. Following the work of Willden et al. (2014) (see also Gong et al., 2018), the semi-analytical model developed and presented in this chapter has been embedded into the two-scale actuator disc theory of Nishino and Willden (2012*b*) with the simple channel theory of Garrett and Cummins (2005). The coupled model is solved by relating the values of the array-scale C_T with the channel-scale turbine drag coefficient δ_1. This provides the representation for a partial-width array configuration and thus allows for a more accurate study of tidal turbine performance to be carried out.

6.2 Two-Dimensional Numerical Channel Model

The semi-analytical model requires numerous simplifying assumptions, such as the use of a single value of Q that varies in time but is uniform across the channel cross-section and along its width (Draper, 2011; Garrett and Cummins, 2005). Some of these assumptions have been relaxed by Bonar (2017), who used a shallow water

model to simulate channel dynamics with a partial-width array of actuator discs modelled by the line momentum sink approach. The model simulates an idealised rectangular tidal channel with a length of 20 km, width of 4 km and a depth of 20 m (Bonar, 2017). The water level at the eastern boundary has been set to remain constant while the water level at the western boundary has been raised and lowered to drive flow through the channel; channel walls have been modelled as slip boundaries. For the model validation, varying cases of high, medium and low C_d have been simulated in conjunction with varied a_0 across the unexploited channel. In general, the results from the numerical model have shown reasonable agreement with the analytical results of Garrett and Cummins (2005) provided by the author. More details on the numerical model can be found in Bonar (2017) and Bonar et al. (2019).

6.3 Modelling of Local Blockage Effects in Oscillatory Flow

Having considered the two models for channel-scale dynamics, a comparison is made to examine the capacity of the analytical scheme in capturing the local blockage effect in oscillatory flow. This is achieved by comparing the results of maximum $\overline{P}_{av}$ achieved with different array arrangements from the 1D model with the results predicted numerically by the 2D model.

Channel dimensions are held constant between the analytical and numerical models in order to facilitate a direct comparison of the simulation results. The maximum $\overline{P}_{av}$ is determined for various arrangements of single-row arrays, simulating a range of values for both B_A and B_L whilst maintaining a constant B_G value of 0.1. The range of values investigated for B_L varies from 0.1 to 0.8 (an unrealistically high upper value, as noted by Willden et al., 2014) whereas the corresponding

range of B_A varies from 1 to 0.125. This variation in local blockage is consistent with the case where the number of turbines in the array is reduced while their size is increased or, similarly, where the distance between turbines is decreased; as such, the packing density becomes higher while the array length shortens. The turbines are tuned with the fixed tuning strategy to suit the varying B_L in order to obtain the maximum $\overline{P}_{av}$ over the tidal cycle. An analysis is then performed with different values of a_0 and C_d.

Analytical and numerical results of $\overline{P}_{av}$ are presented in Figures 6.1-6.3. The simulations are conducted with optimally tuned turbines operating with a fixed tuning strategy in oscillatory flow for the range of specified B_L. For comparison, the results of an analytical combined model by Vennell (2010) are also presented, which assumes a full-width array (where $B_G = B_L$) that consists of a single row of turbines with varying channel widths. For clarity, each of the three models will be referred to in a certain way herein: 'analytical combined partial-array model' for the combined semi-analytical two-scale model of Nishino and Willden (2012*b*) with the 0D channel model of Garrett and Cummins (2005); 'numerical model' for the 2D shallow water model of Bonar (2017), and; 'analytical combined full-array model' for the combined model of Vennell (2010).

For $B_L = 0.1$, in which turbines span the entire channel, it is observed that all three models produce near identical results. This is expected for both of the analytical combined models as they are identical in formulation for the case of a full-width turbine array. The numerical results are also consistent with the other models for this array configuration, with only small discrepancies observed that are discussed in further detail in Section 7.2.1. However, as B_L increases, a comparison of the analytical combined partial-array model and the numerical model shows that the prediction of $\overline{P}_{av}$ begins to diverge; the results from the analytical model exhibit a consistent under-prediction of $\overline{P}_{av}$. It is also observed from the plots that the ana-

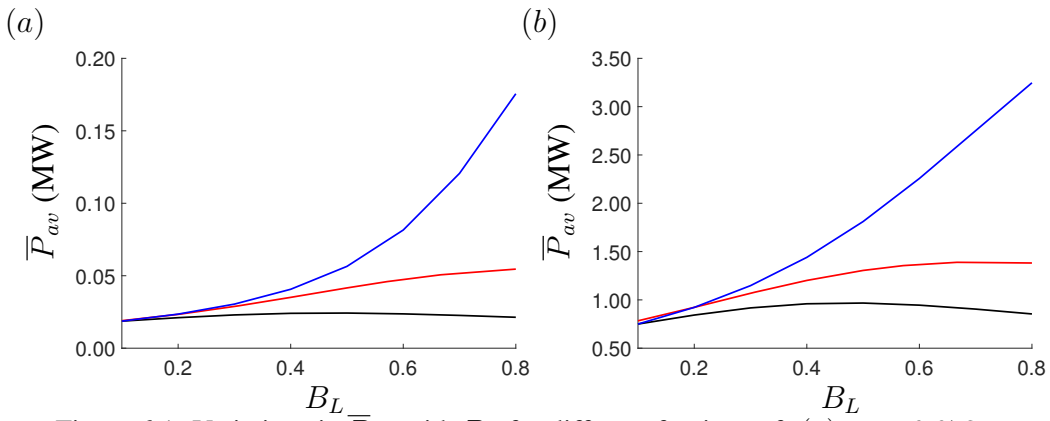

Figure 6.1: Variations in $\overline{P}_{av}$ with B_L for different forcings of: (a) $a_0 = 0.073$ ($\lambda_0 \approx 0.27$), and; (b) $a_0 = 0.31$ ($\lambda_0 \approx 1.16$), for $C_d = 0.003$, predicted by the analytical combined partial-array model (black lines), the numerical model (red lines), and the analytical combined full-array model (blue lines).

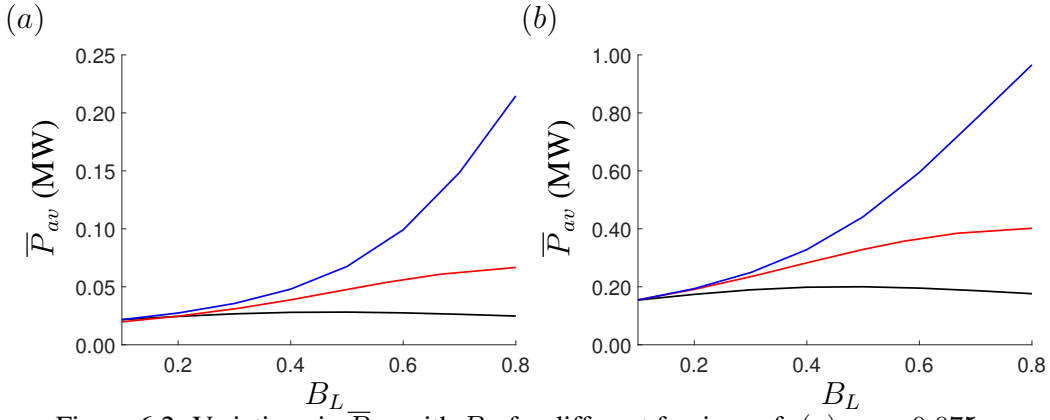

Figure 6.2: Variations in $\overline{P}_{av}$ with B_L for different forcings of: (a) $a_0 = 0.075$ ($\lambda_0 \approx 0.09$), and; (b) $a_0 = 0.145$ ($\lambda_0 \approx 0.18$), for $C_d = 0.001$, predicted by the analytical combined partial-array model (black lines), the numerical model (red lines), and the analytical combined full-array model (blue lines).

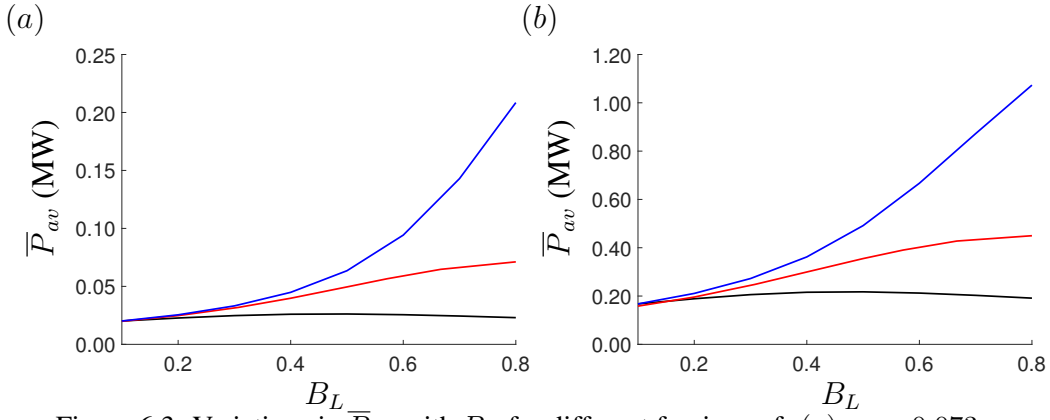

Figure 6.3: Variations in $\overline{P}_{av}$ with B_L for different forcings of: (a) $a_0 = 0.073$ ($\lambda_0 \approx 0.05$), and; (b) $a_0 = 0.148$ ($\lambda_0 \approx 0.09$), for $C_d = 0.0005$, predicted by the analytical combined partial-array model (black lines), the numerical model (red lines), and the analytical combined full-array model (blue lines).

lytical combined partial-array model has an optimum value for B_L that allows the array to capture maximum power from the flow, whereas the curves produced by the numerical model show a much greater increase in power with local blockage. The trend for the numerical model suggests that the phenomenon of the 'reversal boost' (explained below) may increase in magnitude with increasing B_L and that maximum $\overline{P}_{av}$ can be achieved at blockage ratios of $B_L \geq 0.8$. Following this result, the optimal arrangement strategy would be to group the turbines close together so as to maximise the effects of local blockage and take full advantage of the array-scale flow dynamics. It is interesting to note that the numerical model results are bounded by the analytical combined full-array and partial-array models as upper and lower bounds, respectively.

A possible reason for the discrepancy between the analytical combined partial-array and numerical models may be due to the analytical coupling scheme operating over a 1D domain, meaning that it is unable to capture the 2D phenomenon of the 'reversal boost' as described by Bonar (2017). Bonar observed that in oscillatory flow, there is a phase shift between the array-scale core flow and bypass flow as a result of the two fundamental terms that govern the phase of the flow — the inertia and the combined drag of background roughness and turbine thrust. Simplistically, the relationship between these two terms results in a phase lag. Assuming that the tidal cycle is at a point in time when the flow is moving from left to right, at a further point in time, providing that the channel is of sufficient length, the tide will start to reverse due to oscillation with both the core and bypass flows coming to a stop before reversing directions. The core flow will turn sooner than the bypass flow, for two reasons — it turns more easily due to the presence of turbine thrust lowering its velocity more rapidly in the left-to-right direction, and it is also phase-shifted ahead of the bypass flow. The consequence of this is that the leading core flow becomes the 'path of least resistance' for the lagging bypass

flow, and the inertia of the bypass flow causes a fraction of itself to redirect into the core region in preference to flowing back along its original trajectory. The resultant additional flow through the turbines enhances the performance each time the tide changes direction (for better visualisation, see Figure 7.8 in Bonar, 2017). The discrepancy in the $\overline{P}_{av}$ curves has also been found to vary with different channel dynamics; for instance, the difference is most enhanced in Figure 6.3a, which is simulated with the lowest λ_0, and it is least observable in Figure 6.1b, which has the highest λ_0. This reveals that the reversal boost may be more significant within an inertia-dominated channel, as the velocities of the array-scale core and bypass flows in such a domain are increasingly dependent on turbine resistance instead of background roughness. In contrast, turbine arrays in a drag-dominated channel may be incapable of generating a sufficient amount of phase shift between their core and bypass flows for the effect of the reversal boost to be considered important. The results discovered here are consistent with the findings in Bonar (2017).

It is difficult to capture this reversal boost phenomenon with the analytical simulations as its existence contradicts the underlying assumptions made by the 1D models. Vennell (2010) assumed that the turbines present a uniform resistance to the flow and that there is no cross-stream flow variation, and thus the array-scale flow always moves simultaneously across the length of the array cross-section in a seamlessly adjacent manner (referred to as having 'locked' status), indicating that no mass nor momentum transfers in the spanwise direction along the array. In contrast, the analytical combined partial-array model revealed that the array-scale core and bypass flows may have different magnitudes (but not phase) due to flow diversion around the array to the bypass flow (referred to as being 'separated' in status), leading to a definite transfer of both mass and momentum between the two flows, otherwise known as array-scale mixing. However, the findings of Bonar (2017) suggest that realistic 2D dynamics within a partial-width array in oscillatory flow

may be a combination of the flow conditions caused by two opposing separated flows, dynamically balanced over the course of a tidal cycle. Specifically, there is a beneficial separate-flow condition following the reverse of the tide as the array-scale bypass flow redirects into the array core. This phenomenon, being the key driver of the reversal boost, is not accounted for in the analytical combined partial-array model and is mainly responsible for the discrepancy between the analytical partial-array model and numerical model results. Subsequently, however, due to array-scale flow diversion, the core flow is redirected into the bypass flow once more and resumes a detrimental separate-flow condition, which is in fact captured by the analytical combined partial-array model. Thus, this phenomenon is mainly responsible for the large discrepancy between the analytical combined partial-array and full-array models. Noting this theoretical interpretation, the result of the numerical $\overline{P}_{av}$ curve being bounded by the two analytical curves, as well as the way they represent the assumption of two extreme flow dynamics, can be justified. In this case where the results of the analytical combined full-array model tend to be greater than those of the numerical model, it may be inferred that, when partial-width arrays are considered, the advantage gained from the beneficial array-scale bypass flow diversion is not sufficient to overcome the negative impact from the array-scale core flow diversion.

In addition to the reversal boost phenomenon, the $\overline{P}_{av}$ discrepancy in results between the two modelling approaches can also be attributed to differences in the array-scale representation, given that the numerical and analytical models use similar approaches at the turbine scale. Firstly, the analytical combined model neglects bed friction as the model assumes that natural losses within an array are dominated by turbine drag. Conversely, the numerical model includes background roughness, the presence of which allows the array-scale bypass flow resistance to increase (Bonar et al., 2019; Creed et al., 2017). This greater resistance helps fa-

cilitate more flow through the turbines, which improves the turbine performance C_P in the numerical simulation. Secondly, as the flow is 2D, it no longer travels straight through the turbine, as is the case in the analytical model. As a result, the variation in the effective cross-sectional area of the array is not accounted for due to the yaw angle variation in oscillatory flow; this process is captured by the numerical model. Thirdly, the analytical model is built on the assumption that the additional array-scale mixing is much longer than the device-scale mixing (Nishino and Willden, 2012*b*). However, in oscillatory flow where the tidal period is taken into consideration, it is possible that the reversal of the tide can occur before complete establishment of array-scale mixing, which means the underlying assumption of the scale-separation theory is less applicable. Finally, the experimental work conducted by Cooke (2016) has shown that significantly less power is generated at the ends of a turbine array due to the 'end effect' — a flow leakage around the end of arrays resulting from a high-pressure area upstream of the array. This end effect is analogous to the tip effects on rotor blades and may influence the results obtained from both models if accounted for.

6.4 Conclusions

The two-scale separation model of Nishino and Willden (2012*b*) has been extended, following Willden et al. (2014), to incorporate channel-scale flow dynamics. A comparison of this model with the 2D numerical model by Bonar (2017) has been undertaken and an observable discrepancy in the results of $\overline{P}_{av}$ produced by the turbines simulated using these two approaches has been found. This discrepancy is attributed to the newly identified two-dimensional phenomenon of a reversal boost, which develops around a partial-width turbine array in oscillatory flow, found by Bonar et al. (2019). This difference highlights the significance of the simplifying assumptions required by the two-scale separation model — such as requiring 1D,

steady flow — which results in the model neglecting important flow features that are otherwise present. In addition, the key differences between these models and the margin of observed error suggest that for cases of high B_L, the coupled solution scheme of the simple channel model and two-scale separation model does not capture all of the leading order physics involved in oscillatory flow and may limit the applicability of their findings.

However, within the realistic range of local blockage ratios investigated ($B_L \leq 0.4$), the analytical combined partial-array model has provided similar results to the numerical model for the optimal turbine arrangement with respect to the local blockage, and the unrealistically large benefits from the numerical model outside of this range may be inconsequential. Despite this, encouraging performance enhancement is suggested by the numerical simulation of a single-row actuator disc array operating with the fixed tuning strategy, which presents the potential for the local blockage effect (due to the existence of the reversal boost) to be investigated in the following chapters.

Chapter 7

BC-BEMT Model of Local Blockage Effects in Oscillatory Flow *

The local blockage effect is a useful phenomenon that can be used to arrange turbines for maximum power capture. Effectively, local blockage allows a given total turbine swept area to extract more power at an approximately similar array construction cost. By comparing the results predicted by the analytical combined partial-array model with those of the numerical model developed by Bonar et al. (2019), Chapter 6 has identified that both the optimal array operation and potential for enhanced power capture can be quite different under certain oscillatory flow conditions. While the representation of turbines as porous discs in the previous chapter only provides an idealised description of turbine performance, the more advanced blade element momentum model for tidal rotors will be able to better capture realistic turbine behaviour.

In this chapter, the works of Nishino and Willden (2012*b*) and Bonar et al. (2019) are extended to consider a more realistic turbine representation, which is based on the volume-flux-constrained BEMT of Vogel et al. (2018), along with the modelling of multiple-row arrays. Specifically, the performance characteristics of

*The discussions in this chapter have been published as a conference paper — see Chen et al. (2019b) from Appendix C.

realistic tidal rotors are embedded within two different channel domains: the 0D analytical channel described by Garrett and Cummins (2005), and a 2D numerical channel following the work of Bonar et al. (2019). Different turbine arrangements are considered for both steady and oscillatory flow conditions, and the maximum $\overline{P}_{av}$ is compared between two turbine representations. These comparisons are then used to provide a better understanding of the effects of local blockage on the performance of realistic tidal rotors in tidal channels.

Section 7.1 of this chapter briefly analyses the performance between an actuator disc and a tidal rotor for different values of B_L. Section 7.2 presents the results for both analytical and numerical models of tidal stream turbine arrays in partially blocked channels. The numerical model considered in this section is verified against the analytical model of a simple channel (Garrett and Cummins, 2005) and array model (Vennell, 2010). Finally, Section 7.3 investigates the balance between the beneficial effects of local blockage and detrimental effects of 'array choking', alongside examination of the reversal boost and optimal array operation with both actuator discs and tidal rotors.

7.1 Turbine Performance with Local Blockage Effects

The performances of actuator discs and tidal rotors are compared across a range of B_L values. As Schluntz and Willden (2015) have demonstrated the importance of designing turbines for a specific blockage ratio, the work in this chapter also uses a rotor that has been designed specifically as input into the BC-BEMT model for a moderate blockage. This seems appropriate for accommodating the range of blockage ratios studied here, as the design blockage falls into the middle of the range. Following work by Cao et al. (2018), this rotor is designed for $u = 2$ m/s, $B_L = 0.16$, and $TSR = 5.5$, basing its blade cross-section on the Risø-A1-24 hydrofoil, the same as was adopted in Chapters 5. The simulated rotors in this

study operate with FP blades. Whilst varying the pitch of rotor blades can lead to improved performance, the additional variable introduced into the optimisation problem comes at an increased computational cost. The additional cost required to optimise for the inclusion of VP operation is determined to be impractical due to the numerical model being several orders of magnitude longer to run than the analytical model adopted in Chapter 5 and the number of additional arrangements that need to be considered. As a result, only the mechanically simple FP devices are considered here.

Simulations are performed for the rotor ($B_r = 0.16$) operating under different conditions of B_L and further comparison with the equivalent actuator disc is undertaken. Table 7.1 shows a comparison of the maximum power coefficients $C_{P,max}$ between the disc and the rotor under three sample local blockage ratios ($B_L =$ 0.1, 0.2 and 0.3), along with the corresponding optimal thrust coefficient C_T, efficiency η, local resistance k, and induction factor a_2 (calculated similarly to the area-weighted k in Equation 4.14) for each $C_{P,max}$. Observing the results from the table, as the absolute values for $C_{P,max}$ are higher for each condition with higher blockage, both the disc and the rotor are deemed capable of capturing the blockage effect. For an isolated actuator disc at the optimal operation condition of $C_{P,max}$, there is a simple and direct relationship between B_L and the optimal a_2, as well

Table 7.1: $C_{P,max}$ values for tidal rotors and actuator discs operating with $B_L = 0.1$, 0.2, 0.3, and their corresponding optimal values of C_T, η, k, and a_2.

B_L	Turbine	$C_{P,max}$	$C_T(C_{P,max})$	$\eta(C_{P,max})$	$k(C_{P,max})$	$a_2(C_{P,max})$
0.1	Rotor	0.51	1.05	0.50	2.85	0.39
0.1	Disc	0.73	1.21	0.61	3.29	0.39
0.2	Rotor	0.60	1.23	0.49	3.37	0.39
0.2	Disc	0.93	1.67	0.55	5.40	0.45
0.3	Rotor	0.71	1.43	0.49	3.76	0.38
0.3	Disc	1.21	2.39	0.51	8.96	0.49

as B_L and the optimal k, indicating that flow through the disc will decrease with increasing B_L. As discussed in Chapter 4, this can be simply explained by considering that an increase in blockage allows a larger flow rate to be sustained through the turbine swept area, allowing a greater value of optimal k to be applied, thus resulting in a higher $C_{P,max}$ and increased optimal a_2. The reduction in the optimal η is a result of larger mixing losses due to the higher B_L (Draper, 2011; Garrett and Cummins, 2007).

Interestingly, for the tidal rotor, the relationship between B_L, k and a_2 is no longer quite as simple; instead as B_L increases, the optimal k will also increase (at a slower rate than the disc) and the optimal a_2 will decrease. The reason that k increases is twofold. Firstly, as discussed in the previous paragraph, greater confinement within the array means that it is more difficult for the flow to divert around the turbine, leading to an increase in optimal k. Secondly, k also needs to be increased due to the change in the angle of attack, α, of the blade — the increased mass flow rate through the rotor swept area that results from higher B_L will further increase α. Additional resistance needs to be applied to reduce incoming flow rate and therefore reduce α back to its optimal value (Wimshurst, 2018). The degree to which the optimal k should be increased with blockage is limited as a larger k may lead to an over-correction of α, leading to a negative impact on the rotor performance. In the case where the increase in mass flow rate due to the increasing B_L is greater than the drop in flow rate due to resistance applied by the rotor with increased optimal k, there will be a decrease in a_2; a similar finding has been provided by Schluntz and Willden (2015) and Wimshurst and Willden (2016*a*). Here, the slight increase in axial flow velocity is still smaller than the angular velocity increase (as increasing k for FP operation means increasing TSR) resulting in a decrease in α along the blade to below the optimum, thus reducing the C_L/C_D ratio. This may also explain why it is observed that even though both the absolute value of optimal k

and the corresponding $C_{P,max}$ of the rotor are higher for increasing blockage, the increment is still less than that of the disc. For instance, increasing B_L from 0.1 to 0.3 results in a $\approx 70\%$ increase in $C_{P,max}$ for the disc but only a $\approx 40\%$ increase for the rotor. Another notable finding is that the actuator disc tends to extract more power at a higher B_L albeit less efficiently (lower optimal η) due to greater mixing losses (Draper, 2011). In contrast, the optimal η remains relatively constant with the variation in B_L for the tidal rotor. This may also result from the restrictions placed on k for realistic turbine properties constraining the variation of k to a small range, in turn reducing the variation in optimal η. The turbine design should also be considered in relation to this finding as it may be design-specific, due to the fact that the rotor is not optimally designed for each of the B_L values studied here.

7.2 Analytical and Numerical Combined Models

The work by Vennell (2010) has been extended to partial-width arrays by replacing the volume-flux-constrained actuator disc theory of Garrett and Cummins (2007) with the two-scale actuator disc theory of Nishino and Willden (2012*b*), which has been discussed in Chapter 6. An assumption made by Vennell (2010) is that additional rows are not affected by the wakes of upstream rows (i.e. the wakes are fully mixed before reaching the downstream row of turbines (i.e. mixing rate $m = 1$), see Nishino and Draper, 2019). With this assumption, the single-row array model of Nishino and Willden (2012*b*) can be extended to arrays with identical multiple turbine rows by equating the thrust coefficient at local scale with the thrust coefficient at array scale (Perez-Campos and Nishino, 2015):

$$C_{TA} = N_R(1 - a_{2A})^2 B_L C_{TL}, \tag{7.1}$$

where the subscripts L and A indicate the local and array scales (used for turbine performance characteristics with the assumption defined in Section 2.4.1), and N_R

is the number of turbine rows. It has been noted by Draper and Nishino (2014) that this is an important consideration as turbines located in rows toward the back of arrays that lie in the wakes of upstream turbines will see a decrease in power available, though staggered turbine configurations may ameliorate the situation. More importantly, a further extension in this chapter has replaced the actuator discs with the more realistic tidal rotors, modelled using the BC-BEMT, in a similar way to Chapter 5.

Following the methodology of Bonar et al. (2019), this study also employs a 2D numerical channel model, which solves the depth-averaged SWEs using DG-ADCIRC (Kubatko et al., 2009, 2006). Based on the work of Draper et al. (2010), the turbines are embedded within the SWE model at the sub-grid scale, and the extraction of energy is represented as a discontinuous reduction in fluid depth. Local-scale mixing is resolved in the sub-grid scale, whilst array-scale mixing is simulated numerically by means of a spatially and temporally constant eddy viscosity coefficient. Though simplistic, this line momentum sink approach has been verified experimentally (Draper et al., 2013b), and has been widely used in numerical studies, as discussed in Section 2.5.3. The numerical code used in this study is a modified version of the code provided by Schnabl et al. (2019), which is based on the DG-ADCIRC code used by Serhadlıoğlu et al. (2013). The modified code has been adapted to allow the turbine properties to be specified using power and thrust curves, which serves as a more flexible simulation tool as it allows the user to specify external turbine performance coefficients that can be extracted from analytical models, high-fidelity numerical models or experimental data; further details of the modified code are provided by Schnabl et al. (2019). Using this approach, a hydrodynamic channel model is simulated with various turbine models, which allows for different turbine representations to be studied and compared under various array layouts.

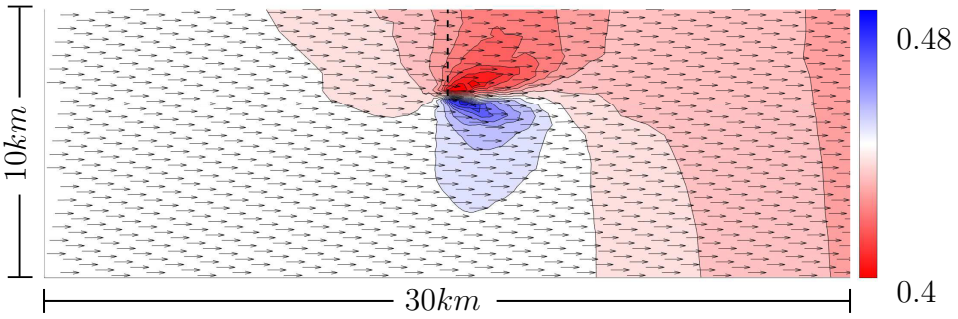

Figure 7.1: Plan view of the idealised model domain, showing the contours of streamwise depth-averaged velocity (m/s). The location of array deployment is depicted by the dashed lines for the case $N_R = 1$ and $B_L = 0.3125$, while the thin black arrows illustrate the magnitudes and directions of velocity factors u and v.

Figure 7.1 presents the geometry of the computational mesh for the 30-km long, 10-km wide, and 30-m deep channel. The domain is divided into 2,042 triangular elements that vary in size from 200 m around the turbine array to 1 km at the channel boundaries; a time step of 1 s is also specified. The channel walls are assigned slip boundary conditions. A realistic value of bed friction $C_d = [\kappa/\left(1 + \ln\left(z_0/h\right)\right)]^2 =$ 0.002 is chosen following the work of Soulsby (1997), based on values of $z_0 \approx$ 1.5 mm for the mean roughness length with very coarse sand and κ = 0.4 for the von Kármán constant. It is important to note that this is the same as $C_d = 0.004$ when using the alternative convention typical of mechanical engineering applications where the 1/2 term is included. The turbine array is located in the middle of the channel, with a distance of 400 m separating each row of turbines in the streamwise direction. This value is adopted assuming the wake mixing length of a tidal turbine is typically 20 times its diameter (Chen et al., 2017). Steady flow is driven by assigning a constant flow rate of 1 m/s at the model inlet. This boundary condition is used to facilitate comparison with the two-scale actuator disc theory, which assumes that the mass flux through the channel is unaffected by turbine resistance (Nishino and Willden, 2012*b*). For oscillatory flow simulations, the flow is driven by varying the water level at the model inlet sinusoidally with an amplitude of $a_0 =$

0.2 m and a period of $T = 12.42$ h. For each simulation, the model is allowed to spin up for 2 days. The simulations then continue for another 8 days before the results from the last two complete tidal cycles are extracted and time-averaged for analysis. The value of λ_0 for the idealised model is determined to be ≈ 0.2, categorising this channel as relatively inertia-dominant (Garrett and Cummins, 2005). Under this condition, it is expected that the reversal boost will be more pronounced than for a drag-dominated channel (Bonar et al., 2019), as explained in the discussion in Chapter 6.

7.2.1 Two-dimensional channel model verification

The length of the idealised numerical model studied is deemed sufficiently short in comparison to the wavelength of the tidal oscillations so that changes in the rate of flow within the channel are independent of position (Vennell, 1998). Consequently, a number of simulations are performed using different values of a_0 and C_d in oscillatory flow to examine how the unexploited and exploited channel in the numerical scheme perform against the analytical channel model (Garrett and Cummins, 2005) and array model (Vennell, 2010). Five verification scenarios are run with varied a_0 and C_d while maintaining the same channel dimensions and oscillatory tidal period. For the unexploited channel, simulation results of the maximum flow rate, Q, and the phase lag between peak surface elevation and peak velocity, ϕ, are extracted. A single-row full-width array is modelled for the case of the exploited channel to compare the maximum values of $\overline{P}_{av}$.

Tables 7.2 and 7.3 compare values estimated by the analytical and numerical models for the unexploited and exploited channel, respectively. It is clear that both numerical models show good agreement in all cases, with the values of Q, ϕ and $\overline{P}_{av}$ all agreeing to within 1.5% of the predictions from the respective analytical models. Thus the numerical full-width array model is confirmed to be able to reproduce

Table 7.2: Numerical and analytical (Garrett and Cummins, 2005) predictions of maximum Q and ϕ for a specific unexploited channel.

C_d	a_0	Q (m^3/s)	$Q_{(GC05)}$ (m^3/s)	ϕ (°)	$\phi_{(GC05)}$ (°)
0.001	0.2	141.099 $\times 10^3$	139.206 $\times 10^3$	82.45	83.24
0.002	0.2	138.306 $\times 10^3$	137.285 $\times 10^3$	76.42	77.45
0.004	0.2	131.402 $\times 10^3$	131.018 $\times 10^3$	65.47	66.85
0.002	0.1	70.157 $\times 10^3$	69.603 $\times 10^3$	82.43	83.24
0.002	0.4	263.205 $\times 10^3$	262.036 $\times 10^3$	65.06	66.84

Table 7.3: Numerical and analytical (Vennell, 2010) predictions of maximum $\overline{P}_{av}$ for a specific full-width array configuration with actuator discs and tidal rotors.

C_d	a_0	Turbine	$\overline{P}_{av}$ (MW)	$\overline{P}_{av(V10)}$ (MW)
0.001	0.2	Disc	0.4661	0.4702
0.002	0.2	Disc	0.4426	0.4458
0.004	0.2	Disc	0.3856	0.3887
0.002	0.1	Disc	0.0580	0.0582
0.002	0.4	Disc	3.0645	3.0945
0.001	0.2	Rotor	0.3269	0.3287
0.002	0.2	Rotor	0.3139	0.3153
0.004	0.2	Rotor	0.2740	0.2750
0.002	0.1	Rotor	0.0410	0.0411
0.002	0.4	Rotor	2.1754	2.1906

closely the results of the analytical model and is deemed a suitable choice for the extension of theoretical works. This agreement is also a check on the numerics and set-up of both model codes.

Further observation reveals some small discrepancy in the comparison between the analytical and numerical models, both with the unexploited and exploited channel cases. This difference may result from the boundary conditions of the model (oscillatory water level and fixed water level boundary conditions are placed at opposite ends of the channel) with the assumption of approximately constant flow rate along the length of the channel. A variation in the streamwise cross-sectional area at the array occurs as a result of the oscillatory boundary and this contrasts with the rigid lid assumption used in the analytical channel model (Garrett and Cummins,

Table 7.4: M_2 tidal elevation amplitudes (m) of the central node for a partial-width array.

Number of elements	0.5 s	1 s	2 s
1067	0.1001554	0.1000553	0.1000551
2042	0.1002003	0.1002002	
8168	0.1002261		

Table 7.5: M_2 tidal elevation amplitudes (m) of the end node for a partial-width array.

Number of elements	0.5 s	1 s	2 s
1067	0.1001250	0.1001247	0.1001242
2042	0.1001772	0.1001755	
8168	0.1002027		

2005). This variation in the array cross-sectional area may also explain the slight power asymmetry from flood and ebb tides.

A mesh resolution and time independence study is undertaken on the numerical model for both full-width ($B_L = 0.1$, $B_A = 1$) and partial-width ($B_L = 0.2$, $B_A = 0.5$) single-row array configurations using three different meshes and time steps. Two additional meshes are generated by halving and doubling the original mesh node spacing, and each mesh is tested using time steps of 0.5, 1 and 2 s to generate a total of nine test cases. As in Chapter 3, the harmonic analysis results at two node locations, one at the centre (for both full-width and partial-width arrays) and one at the end of the array (partial-width array only), are computed and extracted in order to evaluate the convergence rate. Tables 7.4 and 7.5 present the M_2 tidal elevation amplitudes at the observed locations for each simulation, and these results show consistency when the number of elements and time steps are doubled or halved. The results for the full-width array also show a high level of agreement with errors of less than 0.2%. Thus, it can be confirmed that that the model is accurate in solving the SWEs and that the results discussed in Chapters 7 and 8 are due to the physics of the problem and not the numerical code.

7.3 Results and Discussion

Analytical and numerical methods are now used to explore the potential for local blockage effects to enhance the performance of turbine arrays comprising one and five rows of actuator discs and tidal rotors in steady and oscillatory channel flow. A constant global blockage of $B_G = 0.1$ is specified, and simulations are performed using eight different combinations of B_A and B_L. Beginning with a full-width array ($B_L = 0.1$, $B_A = 1$), B_L is then increased to a value of 0.3125, which corresponds to a reduced B_A of 0.32 so that the area of the turbine is unchanged. The value of k is held constant in time within a simulation but varied between simulations to obtain the maximum $\overline{P}_{av}$ by performing a standard cubic spline interpolation, as in Chapter 3. Dynamic turbine tuning over the tidal cycle, such as that presented by Vennell and Adcock (2014), will be considered in Chapter 8. Array performance is measured in terms of maximum $\overline{P}_{av}$ for oscillatory flow, and in terms of the maximum global power coefficient per row (turbine), $C_{PG,max}$, for steady flow, which is defined as the ratio of maximum $\overline{P}_{av}$ per row (turbine) to the channel-scale kinetic energy flux ($\frac{1}{2}\rho u^3 A_C B_G$). It is important to note that the analysis of multiple turbine rows ($N_R = 5$) is performed to simulate a higher array C_T and subsequently higher array resistance, as the further increment of B_L within a single row is limited by the validity of the BC-BEMT. Despite the substitution, this method of simulating additional rows is less effective in terms of maximising $\overline{P}_{av}$ than increasing B_L within an array (Draper and Nishino, 2014; Vennell, 2010).

7.3.1 Steady flow

Figure 7.2 shows the variations in $C_{PG,max}$ with B_L for one and five rows of actuator discs and tidal rotors operating in steady flow. Figure 7.3 normalises the results of $C_{PG,max}$ by the values obtained for equivalent full-width arrays ($B_L = 0.1$) in order to isolate the effects of local blockage on array performance. Figure 7.4a depicts

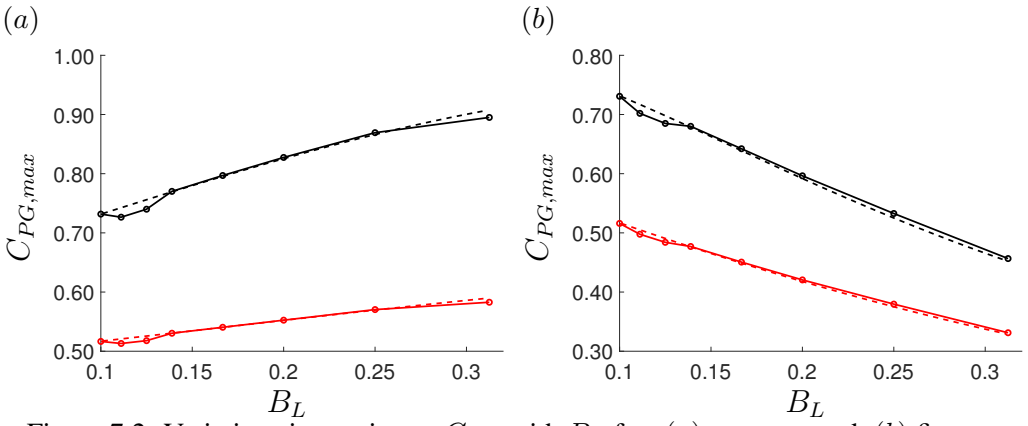

Figure 7.2: Variations in maximum C_{PG} with B_L for: (a) one row, and; (b) five rows of actuator discs (black lines) and tidal rotors (red lines) in steady flow predicted using numerical (solid lines) and analytical (dashed lines) models.

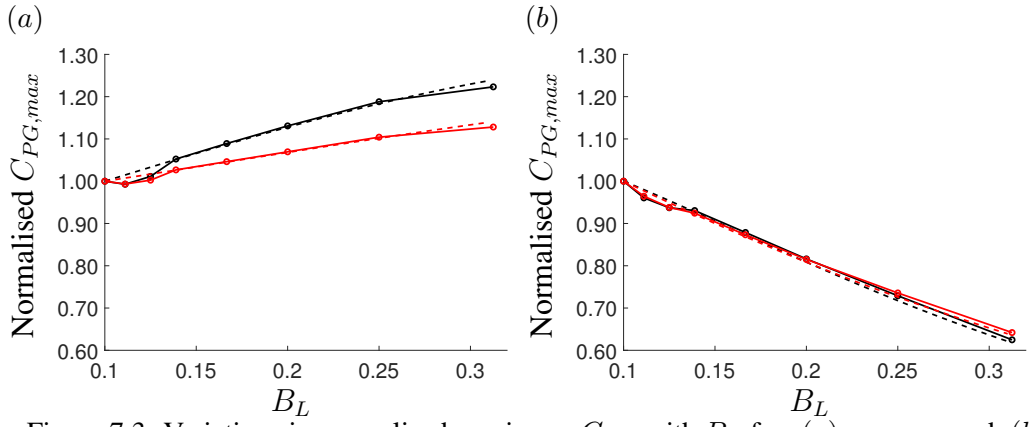

Figure 7.3: Variations in normalised maximum C_{PG} with B_L for: (a) one row, and; (b) five rows of actuator discs (black lines) and tidal rotors (red lines) in steady flow predicted using numerical (solid lines) and analytical (dashed lines) models.

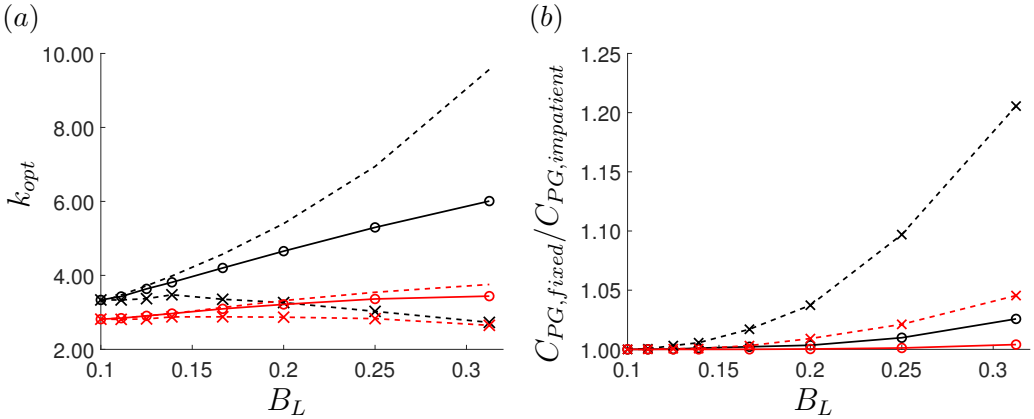

Figure 7.4: Variations with B_L in: (a) optimal k, and; (b) normalised maximum C_{PG}, for one (circles) and five (crosses) rows of actuator discs (black lines) and tidal rotors (red lines) in steady flow. Specifically for (a), the plain dashed lines represent the use of the impatient strategy.

the variations in optimal k with B_L that correspond to Figure 7.2.

Figure 7.2 shows very good agreement between the analytical and numerical models, for both actuator discs and tidal rotors and for both one and five rows of turbines. Small differences are apparent at both ends of the curves for the cases of small and large B_L, which are most likely due to the different dimensional orders of the two channel models and their underlying physics (such as the 2D shallow water model including end effects and flow non-normal to the turbine array), as mentioned in Chapter 6. Despite this, as noted by Perez-Campos and Nishino (2015), Bonar et al. (2019), and Cooke (2016), the two-scale theory is found to predict the results of the numerical model and laboratory-scale experiments reasonably well.

It is also clear that both turbine representations respond similarly to increasing B_L. For both discs and rotors, $C_{PG,max}$ is shown to increase with B_L for $N_R = 1$ and decrease with B_L for $N_R = 5$. This finding shows that, as is consistent with existing work, the effects of increasing local blockage vary with the number of turbine rows (Divett et al., 2014; Draper and Nishino, 2014). Nishino and Willden (2012*b*) have shown that, by reducing the lateral spacing between turbines (i.e. increasing B_L), $C_{PG,max}$ will initially increase due to the higher flow confinement, which results in greater flow resistance in the bypass region that diverts more flow through the rotor. However, as B_L increases even further (modelled here by the $N_R = 5$ array), $C_{PG,max}$ may begin to reduce. As the turbine resistance progressively increases, a larger amount of flow will be diverted around the entire array and the detrimental effects of array-scale flow diversion will outweigh the beneficial effects of the increase in turbine-scale flow confinement, such that less power will result from the reduced core flow. Moreover, two-scale flow dynamics are introduced by shortening a full-width array to a partial-width array as there are array-scale core and bypass flows that mix together some distance downstream of the array. Effectively, the local blockage effect shifts from being a beneficial factor of power production

to being a detrimental 'array choking' effect, with an overall negative impact on array performance. Therefore, the optimal B_L is much lower for a multi-row array than for a single-row array, which is in accordance with the finding by Draper and Nishino (2014).

Similar to the discovery in Chapter 5, it is found that the idealised actuator discs tend to overestimate $C_{PG,max}$ when compared to the more realistic rotors. More importantly, it is also apparent that the performance enhancement with increasing B_L (that is to say, the significance of local blockage effect) for the rotor is overall lower than that predicted by the disc, evidenced by the gain in $C_{PG,max}$ (slope of the curves) indicated by the normalisation process in Figure 7.2. To understand this relative insignificance of the local blockage effect when considering the rotor in relation to the disc, the corresponding variation in the optimal value of k (Figure 7.4a) should be considered. Nishino and Willden (2012b) have explained that, as B_L increases, the optimal k initially increases due to the greater confinement of flow enabling higher optimal thrusts (with decreasing potential for flow diversion), which is the trend depicted by the case when $N_R = 1$. However, for sufficiently large numbers of turbine rows (i.e. $N_R = 5$, which has a similar effect on the flow to increasing B_L), optimal k decreases as the array choking effect becomes a significant enough consideration to necessitate the lowering of optimal thrust levels as a means by which to compensate for the much higher resistance presented by the array.

Figure 7.4a also shows that, for the case of $N_R = 1$, the optimal k varies less with increasing B_L for the rotor than the disc. By considering the variation of $C_{P,max}$ and $C_{T,opt}$ across the different blockage ratios in Table 7.1, it may be inferred that although the C_P of the rotor is higher for increasing B_L, this increase in performance is less than that of the disc. Ultimately, as B_L increases, the optimal k increases rapidly for the disc because it is able to produce freely higher power;

whereas for the rotor, optimal k increases less rapidly because it accounts for the reduction in performance due to the change in operation lowering the angle of attack below its optimal value as well as additional energy losses (e.g. drag loss) that are intensified at higher k and B_L. Similarly, when the optimal array thrust reduces for $N_R = 5$, the corresponding reduction in optimal k is also less for the rotor — increasing B_L from 0.1 to 0.3 results in an $\approx 18\%$ decrease in optimal k for the disc but only a $\approx 5\%$ decrease for the rotor, because of its lower C_T, which requires a smaller tuning correction. For $N_R = 5$, the performance of the rotor is less sensitive to the effects of local blockage than the disc as realistic turbines do not apply sufficiently high thrust on the flow for their resistance to be significant.

In order to examine the importance of tuning, Figure 7.4*b* shows the curves of maximum C_{PG} for the fixed tuning strategy normalised by the results of the impatient strategy. As Chapter 5 has found, it can be observed from the figure that tuning is more significant for higher B_L and N_R. More importantly, tidal rotors benefit much less from tuning when compared to actuator discs. For the idealised disc, as B_L increases, its η reduces significantly at the local scale and subsequently global scale, which will necessitate a considerable reduction in its optimal k in order to maintain performance (Nishino and Willden, 2012*b*). However, the same is not true for the rotor, because η stays relatively constant (Table 7.1). In effect, for a given change in B_L, the importance of tuning is found to be less significant for the rotor than for the disc.

Lastly, it can be inferred from Figures 7.2 and 7.3 that, when $N_R = 1$, the actuator disc overestimates the performance of the tidal rotor by a greater amount when B_L is large, and by a lesser amount when B_L is small, whilst the opposite is true for $N_R = 5$. In explanation, when the array consists of a single row and the local blockage effect is still dominant and beneficial to power production, higher optimal k is required with the increase of B_L, enhancing the idealised strength of the

disc by producing unrealistically large C_T and C_P. For $N_R = 5$, however, optimal k decreases with increasing B_L because the applied thrust by the multi-row array is sufficiently large that $C_{PG,max}$ can only be increased by applying a lower array thrust. The above finding is explained, then, by the realisation that when optimal k is small, the more realistic rotor is able to match more closely the performance of the highly idealised disc as discussed in Section 5.2.3. The physics behind such trends may partially explain the overall better agreement found between the two turbine representations in Figure 7.3*b*, though this may be case-specific as more divergence may be expected if the optimal k drops sufficiently low.

7.3.2 Oscillatory flow

Figure 7.5 shows the variations in maximum time averaged available power, $\overline{P}_{av,max}$, and optimal k with B_L for one and five rows of actuator discs and tidal rotors operating in oscillatory flow. Figure 7.6 normalises the variations in $\overline{P}_{av,max}$ by the values obtained from the equivalent full-width arrays ($B_L = 0.1$). Figure 7.7*a* depicts the variations in optimal k with B_L that correspond to Figure 7.5. When compared to the results from the steady flow simulations, it is clear that the two-scale theory no longer closely matches the results of the numerical model. Figure 7.6 shows that in oscillatory flow, partial-width turbine arrays ($B_L > 0.1$) yield considerably more power than the equivalent full-width arrays. Moreover, the trends suggest that turbine arrangements with higher B_L than those considered here ($B_L \geq 0.3125$) can produce even more power. The departure from theory is most noticeable for $N_R = 5$ (Figure 7.6*b*), where the two-scale theory predicts that $\overline{P}_{av,max}$ should decrease with increasing B_L but the numerical model shows $\overline{P}_{av,max}$ to increase instead. These findings match those presented in Chapter 6 and are consistent with the work of Bonar et al. (2019), who provided a detailed description of the two-dimensional array-scale dynamics underlying this significant increase in power production.

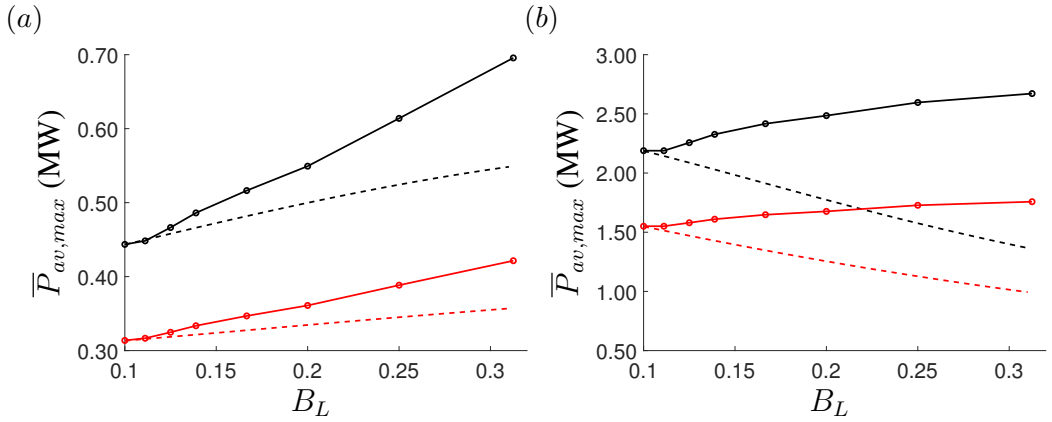

Figure 7.5: Variations in $\overline{P}_{av,max}$ with B_L for: (a) one row, and; (b) five rows of actuator discs (black lines) and tidal rotors (red lines) in oscillatory flow predicted using numerical (solid lines) and analytical (dashed lines) models.

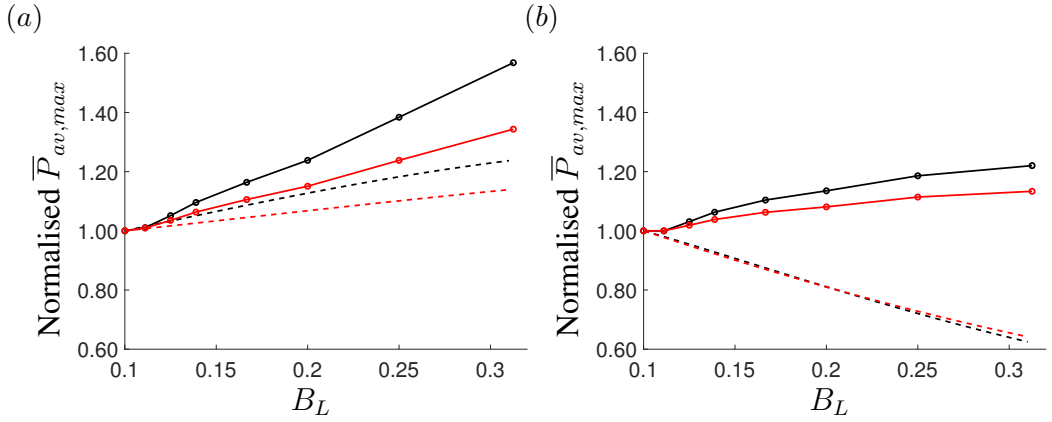

Figure 7.6: Variations in normalised $\overline{P}_{av,max}$ with B_L for: (a) one row, and; (b) five rows of actuator discs (black lines) and tidal rotors (red lines) in oscillatory flow predicted using numerical (solid lines) and analytical (dashed lines) models.

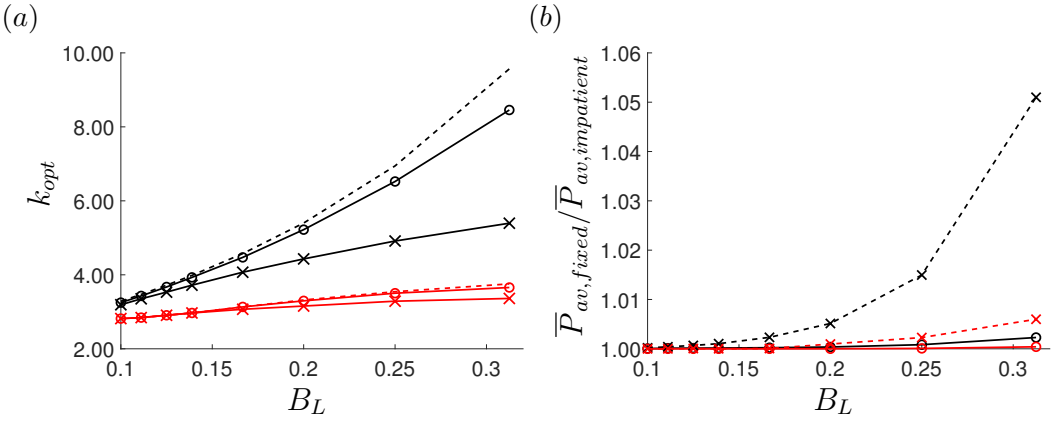

Figure 7.7: Variations with B_L in: (a) optimal k, and; (b) normalised maximum $\overline{P}_{av}$, for one (circles) and five (crosses) rows of actuator discs (black lines) and tidal rotors (red lines) in oscillatory flow. Specifically for (a), the plain dashed lines represent the use of the impatient strategy.

In the case of steady flow, Nishino and Willden (2012*b*) have shown that the partial-width array divides the channel-scale flow into array-scale core and bypass flows. In the case of oscillatory flow, Bonar et al. (2019) have found that these array-scale flows oscillate side-by-side but with their peak velocities separated by a phase difference, resulting in a cross-stream diversion of array-scale bypass flow through the array. This reversal boost mechanism can considerably enhance the power available to short and highly blocked turbine arrays. However, as discussed in Chapter 6, this two-dimensional phenomenon cannot be captured using the existing lower-order theories, which explains the large differences in power observed for large B_L.

Extending the previous studies that have only considered single-row arrays of actuator discs, Figures 7.5 and 7.6 show that, under oscillatory flow and within the studied range of local blockage, considerably more power is still available to higher-blockage arrays. This is true not only for a single row of turbines but also five rows and not only actuator discs but also tidal rotors, although it is clear that the discs again overestimate the performance of the rotors as well as the significance of local blockage effect. Increasing B_L from 0.1 to 0.3125, for instance, provides $\approx 10\%$ more power for the rotor (as compared to $\approx 20\%$ more for the disc) when $N = 5$, and $\approx 35\%$ more power for the rotor (as compared to $\approx 60\%$ more for the disc) when $N = 1$.

The significant enhancement of the local blockage effect due to the beneficial reversal boost can be verified by considering the corresponding variations in optimal k (Figure 7.7a). Previously, for steady flow, where the effects of array-scale diversion are detrimental to power production, Figure 7.4a has shown that the optimal values of k to maximise the power available to the array (solid lines) are quite different from those that maximise the power coefficient of the individual turbine (dashed lines). In contrast, for oscillatory flow, Figure 7.7a shows that these two

sets of optimal k align more closely — this is because whereas in steady flow, the thrust from the turbines should be carefully calibrated so as to slow but not choke the flow through the array, in oscillatory flow, it may be more beneficial to apply a larger thrust so as to increase both the differences in the velocity amplitude and the phase between the core and bypass flows. This allows a greater amount of bypass flow to be funnelled through the array core at the turn of the tide, yielding more power and maximising the effect of the reversal boost (Bonar, 2017; Bonar et al., 2019).

It is therefore expected that the importance of the tuning is generally limited in oscillatory flow as compared to steady flow. This is confirmed with the comparison between Figures 7.4b and 7.7b, in which Figure 7.7b shows the curves of maximum $\overline{P}_{av}$ for the fixed tuning strategy normalised by the results of the impatient strategy. The comparison suggests that the importance of tuning is significantly over-predicted in steady flow conditions. A common finding between steady and oscillatory simulations is that, even though the importance of tuning is enhanced with increasing B_L and N_R, the more realistic rotor still does not benefit as much from the tuning process as does the idealised actuator disc.

A direct comparison between the power produced by the tidal rotors and the actuator discs can be found in Figures 7.5 and 7.6. Unlike the steady flow case, the actuator disc shows a greater rate of performance increase with B_L than the tidal rotor for both the $N_R = 1$ and $N_R = 5$ cases. Generally, the tendency of the actuator disc to overestimate the performance of the tidal rotor, which is based on its higher optimal k, is further enhanced under oscillatory flow as the idealised disc is able to apply considerably more thrust and produce, by means of the reversal boost, considerably more power. This overestimation is less pronounced with $N_R = 5$ as it necessitates the reduction of the optimal k to extract power more efficiently. Additionally, when directly comparing the power produced by the two turbine rep-

resentations, the rotor still predicts approximately 60-70% of the power predicted by the disc.

It should be briefly noted that for the BC-BEMT model, the performance of the turbine also depends on the design of the rotor. One specific rotor design has been applied in the simulation of all blockage conditions considered in this chapter, but a higher performance can be obtained if the rotor was optimised specifically for each configuration (or with the addition of a variable pitch mechanism). However, observation from Figure 7.7a suggests that the optimally designed rotor ($c_x = c_{x,optimal}$) is not necessarily the best option. Instead, an under-designed rotor ($c_x < c_{x,optimal}$) is more suitable for highly packed configurations, which is even more evident for an increasing number of rows. Although, informed by the studies in Section 5.2.3.1 for a range of rotor designs, there may not be a large enough difference in performance and the conclusion drawn in this chapter should still be generally applicable.

It is also worth noting that the numerical model adopted in this chapter is based on several simplifying assumptions, and is therefore unable fully to describe realistic scenarios. For example, for arrays of smaller sizes, there may not be sufficient difference between the scale of the array and the individual device, thus the device and array-scale wake expansions can no longer be treated separately (Nishino and Willden, 2013). Subsequently, the variations in performance characteristics across the spanwise direction of the array may become significant, especially towards the edge of the array, and the turbine element will need to be sufficiently small to capture such end effects (Cooke, 2016). Lastly, the modelling of turbulence is also not well-established in depth-averaged numerical simulations (Vogel, 2014). Bonar et al. (2019) have shown that the $\overline{P}_{av}$ produced by partial-width turbine arrays is relatively insensitive to the value of eddy viscosity. In this study, it was explained that the use of a constant eddy viscosity ν_T, adopted by the 2D model, is predominately driven by the need to describe array-scale mixing rather than local-scale mixing

(Bonar et al., 2019). Intuitively, a higher ν_T may simultaneously lower the effects of both the beneficial and detrimental separated flows (as introduced in Section 6.3) between the array core and its bypass region, and will therefore affect the overall array performance in a contrary way (Bonar et al., 2019; Nishino and Willden, 2012*a*). Although greater detail of turbulent structures may be captured by more sophisticated modelling techniques (e.g. LES), their applicability may be limited to small arrays due to the high computational cost. Thus the current modelling technique is a reasonable compromise. Given the number of simulations run in Chapter 8, the ability to capture the leading order physics of turbine behaviour with a significant computational saving is a crucial consideration. Thus similar approaches are implemented in the following chapter.

Only one specific channel dynamic has been examined in this chapter, further insights into the effects of local blockage on array performance may be realised by considering alternative oscillatory flow regimes (e.g. different values of a_0 or alternative C_d). Based on the finding by Bonar et al. (2019), it is generally expected that both the significance of the local blockage effect and the importance of tuning may further reduce in drag-dominated channels. Array performance may also be improved by adopting dynamic tuning strategies (e.g. Vennell, 2016), which are explored in the following chapter.

7.4 Conclusions

In this chapter, 1D analytical and 2D numerical models have been used to explore the potential for local blockage effects to enhance the performance of turbines in tidal channels. Turbines have been represented using the highly idealised actuator disc theory and the more realistic BEMT. In the case of steady flow, the 2D numerical model has been shown to reproduce very closely the predictions of the two-scale theory. In the case of oscillatory flow, however, the numerical results have shown

that densely packed arrays produce considerably more power than that which is predicted by the 1D theory. These results support the findings of Bonar et al. (2019), who showed that under certain oscillatory flow conditions, the power produced by a partial-width tidal turbine array can be much greater than that predicted by two-scale theory. In oscillatory flow, maximum $\overline{P}_{av}$ has been shown to increase with increasing B_L, a finding which is also consistent with the work of Bonar et al. (2019). This result has been confirmed by using a large number of turbine rows and a more realistic turbine represnetation.

It can be concluded that the importance of the local blockage effect is generally smaller but not negligible for realistic tidal rotors. Under steady flow, the effects of local blockage have been shown to be less significant for the tidal rotors than for the idealised discs, as well as in the case of a large number of turbine rows. A similar conclusion is true for oscillatory flow, though the reasoning is more complex due to the additional consideration of the reversal boost. As for tuning, its significance is also much lower for the rotor than for the disc in both steady and oscillatory flows; nonetheless, considering just the rotor, the importance of tuning is further reduced when comparing the condition of oscillatory flow to steady flow. In terms of the amount of power predicted, in all oscillatory flows considered, the power correction for the rotor still approximates to 60-70% of the power estimated by the disc. The over-predicting nature of the disc is more pronounced under conditions of high B_L, where the performance differences between disc and rotor are more pronounced, while it is less noticeable with a large number of rows, where the contradiction of the negative array choking effect and the positive reversal boost is most prominent.

Chapter 8

Dynamic Tuning in an Idealised Two-Dimensional Channel

Adcock (2012) suggested that a crucial point of consideration in large tidal turbine arrays within a channel is that short-term energy storage is possible by exploiting the inertia of oscillating flow. This additional storage of energy can be used to exceed the maximum available power estimated by previous research that adopted Vennell's fixed tuning strategy, which seeks a constant value of tuning parameter over a tidal cycle to maximise the power production (Vennell, 2010). In consideration of the inertial energy storage, a more advanced strategy, known as the dynamic tuning strategy, has been developed by Vennell and Adcock (2014) and Vennell (2016); discussion of this strategy can also be found in Chapter 5. The dynamic tuning strategy defines a temporally varying tuning curve for the operation of a number of identical tidal turbines in a large array by manipulating the phase of oscillating currents. Similar power extraction dynamics of the dynamic tuning strategy can also be seen in the fixed tuning strategy as well as the process of power capping, albeit unintentional and, in a sense, sub-optimal (Vennell, 2016).

Previous work looking at dynamic tuning for tidal turbines (including Chapter 5) has been undertaken using a simple 0D model with full-width turbine arrays. The

0D model allows for faster computation, meaning that a greater parameter space can be explored to investigate the effects of channel dynamics and array size on the potential benefits of dynamic tuning. The disadvantage of this model is that its simplification means that some key features of the flow physics, which require higher-dimensional models, are ignored. More importantly, partial-width arrays, for which performance is enhanced significantly in oscillatory flow (as discussed in Chapter 6 and 7), have yet to be explored using a dynamic tuning strategy. Thus, this chapter investigates the dynamic strategy by gradually building up model complexity to simulate more realistic conditions. Specifically, a 2D hydrodynamic model is used instead of the 0D model to simulate full-width and partial-width arrays of tidal turbines modelled both as actuator discs and tidal rotors. These models are applied to examine the potential of the dynamic strategy under different configurations with a more advanced numerical model to maximise the power capture over a tidal cycle. This research also aims to investigate how the dynamic strategy changes in accordance with different array layouts, especially for the more complicated flow field around a partial-width array.

The structure of this chapter is as follows. Section 8.1 introduces the improved 'generate-and-test' approach that has been established in order to optimise the dynamic strategy in the 2D model. This section also discusses the additional modification of the numerical model developed in Chapter 7 to enable the variation of turbine characteristics over a tidal cycle. Section 8.2 conducts a comparison between the 0D and 2D hydrodynamic models for simulating a fully blocked channel in order to reproduce the results of the dynamic strategy presented in Chapter 5 with the 2D SWE model; both actuator disc and turbine rotor representations are used in this comparison. Finally, the effect of inertia in oscillatory flow is investigated by exploiting the optimal operation strategy in a 2D partially blocked channel model in Section 8.3. This section explores the combined effect of dynamic tuning (with

the beneficial ‘dynamic boost’) and the reversal boost, while searching for insights as to the optimal arrangement and tuning strategy.

8.1 Development of Dynamic Tuning Strategy

As discussed in Chapter 5, the solution space of the dynamic tuning strategy is complex and metaheuristic methods are required to find the optimal tuning curve. These methods include the gradient-based ‘Global Search’ and the direct ‘PatternSearch’, which are applied to simple 0D models in order to quickly simulate the response of a trial tuning curve and provide feedback for the next iteration (Agnarsson et al., 2013). Variations of these methods, such as the adjoint approach, can improve the time taken to determine the solution for the 0D case (Vennell, 2016). However, such optimisation techniques are largely inapplicable in the more detailed 2D case due to the computational requirements of each simulation being several orders of magnitude greater than the 0D model. Instead, in this chapter, a more straightforward and comprehensive ‘generate-and-test’ method is adopted to optimise the tuning curve.

The conventional ‘generate-and-test’ method is an exhaustive iterative search approach that enumerates all possibilities in the solution domain to find the optimum. Although more computationally intensive than metaheuristic methods, there is independence between the parameter sets of individual simulations, meaning that all simulations can be run in parallel. Despite being highly parallel, however, the generate-and-test algorithm must examine a very large number of combinations in order to determine an optimum. This makes the conventional generate-and-test approach impractical either due to the computational size growing exponentially with the progressive increase of optimisation variables (number of time blocks, trial tuning parameters, actuation time) or due to the processing time increasing significantly when the problem gets more complex for each permutation. Consequently, the optimisation variables chosen to be examined over a tidal cycle should be man-

ageable and targeted to the anticipated solution (Section 8.1.1). Considering the large number of optimisation problems investigated in this chapter and the limited potential of the ARCUS-B supercomputer, a modified version of this generate-and-test approach is adopted to further lessen the computational strain and achieve an optimised parameter set.

8.1.1 Improved generate-and-test approach

When tuning tidal turbines with a dynamic strategy, it is typical that optimal conditions are found where low resistance is applied at the early stage of the tidal cycle while higher resistance is required at the end of each half tidal cycle (Vennell, 2016). By incorporating this information into the generate-and-test approach, the number of simulations can be reduced as only tuning curves that have monotonically increasing turbine resistance have to be simulated. For simulations, the problem is analysed by firstly discretising the half tidal cycle into n blocks (time periods in hours) — the optimal tuning curves are assumed to be symmetric for the following half tidal cycle, as noted by Vennell (2016), for the simplicity of optimisation. Within each block, one value of the tuning parameter (α_{4n} or TSR_n) is chosen amongst Z_n options available. The values of n and Z can be adjusted to balance the trade-off between the accuracy of the results and the computational expense: n varies the size of the time block used, while Z can be varied over each time block to improve the accuracy over specific blocks. Of the potential combinations, only the tuning curves with increasing TSR for the tidal rotor or decreasing α_4 for the actuator disc are simulated as other permutations outside of these sets are discarded as invalid solutions due to their violation of the previous assertion that resistance should be increased over the half tidal cycle for dynamic strategies. The monotonic selection algorithm implemented by the modified generate-and-test approach works as follows:

$$\alpha_{4_1} \geq \alpha_{4_2} \geq \cdots \geq \alpha_{4_{n-1}} \geq \alpha_{4_n}, \tag{8.1}$$

$$TSR_1 \leq TSR_2 \leq \cdots \leq TSR_{n-1} \leq TSR_n. \tag{8.2}$$

This condition effectively reduces the number of combinations of tuning curves run by the generate-and-test method by an order of magnitude. Using this method, an optimisation problem is formulated for the operation of a tidal array with the objective to maximise power capture over a tidal cycle. The optimisation algorithm outputs the optimal tuning parameter, amongst all the valid potential combinations of tuning parameters, at each of the n time blocks.

As discussed in Chapter 5, the strength of the dynamic tuning strategy relies on the capacity to shift the phase of the array-scale core flow by changing the resistance of the array. In order to account for the feedback of phase shifting with the implementation of the dynamic strategy, an additional optimisation variable is constructed by specifying an actuation point, A_T, for dynamic strategy operation, allowing tuning curves to be phase-shifted forward and backward in time by a certain amount. The value of A_T is adjusted such that $\overline{P}_{av,total}$ is maximised for a given tuning curve:

$$\bar{P}_{av,total} = \frac{\sum_{i=1}^{n}[\bar{P}_i(TSR_i, A_T)]}{n} \quad \text{or} \quad \bar{P}_{av,total} = \frac{\sum_{i=1}^{n}[\bar{P}_i(\alpha_{4,i}, A_T)]}{n}. \tag{8.3}$$

8.1.2 Optimisation process

Considering the time required for each simulation and the limitation of computational resources, $n = 5$ is chosen for this work as the initial value; this ensures that a reasonable tuning curve can be determined without excessive computational load, as further refinements on n is found to be contribute $< 2\%$ of performance enhancement. With the array deployed, the model is allowed to spin up for 2 days before results from the following two complete tidal cycles are recorded to calculate the $\overline{P}_{av}$ for each simulation. The optimisation process, with B_L, B_A and N_R as inputs, for both full and partial-width array is presented below in five steps:

1. B_L and N_R are input into the 0D model by Vennell (2010) to calculate a tuning curve assuming a full-width array. This tuning curve is used as the initial guess for the array tuning optimisation in the 2D numerical model. An additional adjustment is made to the initial guess if the highest value of C_T is not at the end of the half tidal cycle — the actuation point A_T is adjusted by order of minutes to satisfy this condition. Whilst the tuning curve is expected to be different between full-width and partial-width arrays, the full-width curve is considered an initial approximation to direct the search and reduce the size of the solution domain.

2. Based on the initial guess extracted from step 1, an upper bound (UB) and a lower bound (LB) for each block n are constructed from the expressions:

$$TSR_{UB,n} = TSR_{initial,n} + \frac{Z_n}{2} I_n \quad \text{or} \quad \alpha_{4UB,n} = \alpha_{4initial,n} + \frac{Z_n}{2} I_n, \quad (8.4)$$

$$TSR_{LB,n} = TSR_{initial,n} - \frac{Z_n}{2} I_n \quad \text{or} \quad \alpha_{4LB,n} = \alpha_{4initial,n} - \frac{Z_n}{2} I_n, \quad (8.5)$$

where I_n is the inter-spacing between each value of the tuning parameter corresponding to a Z_n. The intervals I and Z for each block are carefully selected to balance the model complexity and computational demands with the accuracy of the solution. A series of tuning curves are constructed considering each permutation of the tuning parameter between the bounds for each of the n time blocks. Using the criteria of dynamic tuning discussed earlier in this section, invalid curves are eliminated using this improved generate-and-test method. It should be noted that the results from each iteration serve as an informed initial guess for the next iteration, for which a new set of upper and lower bounds can be calculated for further precision of the most optimal tuning curve.

3. Once all plausible tuning curves have been determined, a phase shift is applied to account for the effect of the arrays on the tidal phase. This is achieved by defining a number, Θ, of actuation points A_T, which are used to shift the entire set of tuning curves from step 2 either forward or backward in time. Although this increases the total number of simulations needed by a factor of Θ, this is done to account for any phase shift of the flow caused by the tuning strategy and to provide confidence that the near-optimal tuning has been achieved.

4. $\overline{P}_{av}$ is calculated over the entire tidal cycle for all tuning curves at each actuation point A_T. The tuning curve and corresponding actuation point with the highest $\overline{P}_{av}$ is selected as the optimal tuning curve. However, if any of the tuning parameters within this curve meets the lower or upper bound, then this tuning curve is used as the initial guess for the next iteration and the algorithm is repeated from step 2. This process is repeated until all of the tuning parameters for the tuning curve with the highest $\overline{P}_{av}$ fall between the lower bound and upper bounds. A sample selection of tuning curves are presented in Figure 8.1, with the corresponding time-varying power, P_{av}, presented in Figure 8.2.

5. Once the optimal tuning curve is obtained, it is possible to further refine the temporal resolution of the curve by reducing the time block size (i.e. choosing $n > 5$) and I for each time block. This step also serves as a convergence check to determine if the change in $\overline{P}_{av}$ by refining n or I is less than a specified tolerance ($< 1\%$). It should be noted that additional controls are added to this process to stop the procedure if the number of simulations exceed a maximum allowable number (e.g. > 5000 simulations for each iteration).

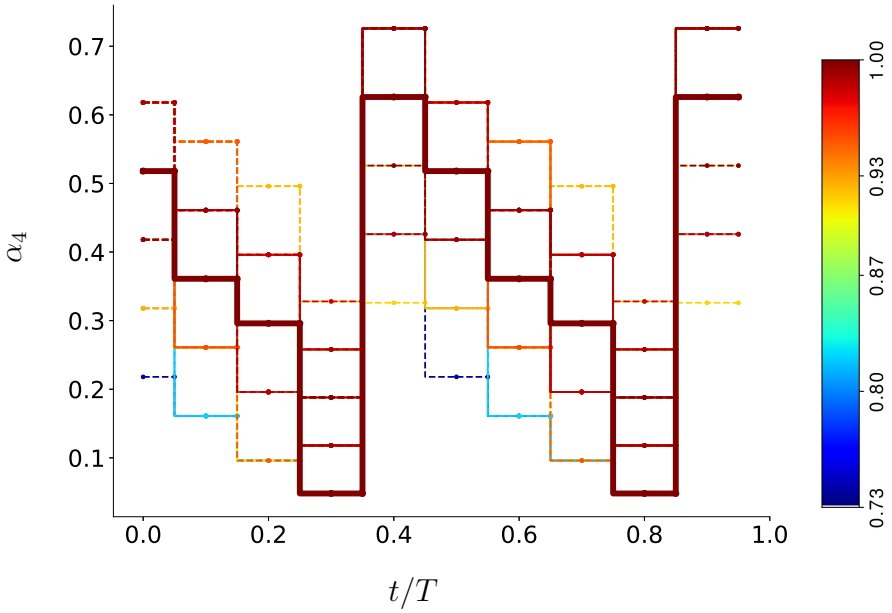

Figure 8.1: Variation of permutations, with the relative time in a tidal cycle t/T, forming the tuning curves for one simulation iteration. The colour of each tuning curve corresponds to its normalised $\overline{P}_{av}$ (MW), which is its $\overline{P}_{av}$ over the maximum $\overline{P}_{av}$ in this simulated range (provided by the bold curve). For presentation clarity, only every fifth tuning curve in order of the normalised $\overline{P}_{av}$ magnitude has been plotted.

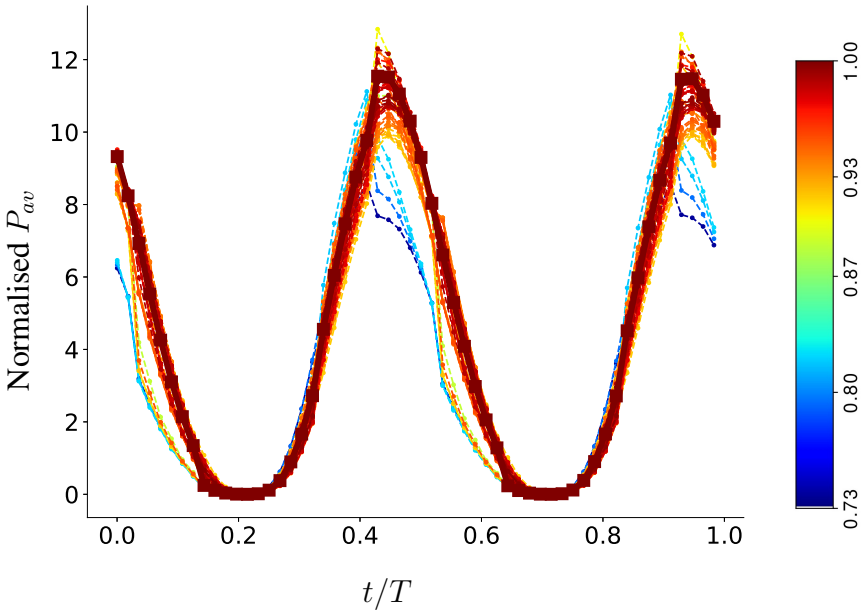

Figure 8.2: Variation of normalised P_{av} calculated using each of the tuning curves shown in Figure 8.1.

8.1.2.1 Modification of DG-ADCIRC source code

The work presented in this chapter follows the same line-discontinuity approach as in the DG-ADCIRC software, implementing a user-defined turbine model based on a modification made by Schnabl et al. (2019), as in Chapter 7. The turbine implementation previously developed by Serhadlıoğlu et al. (2013) and Schnabl et al. (2019) was designed for the fixed tuning operation strategy and was only able to accommodate a single tuning parameter over an entire simulation. An extension to this model is made through improvements to several FORTRAN subroutines, which are modified to relax this restriction. This gives the user more flexibility to control turbine operation over a tidal cycle and enables the inclusion of the dynamic tuning strategy in the DG-ADCIRC model. The user specification for the dynamic strategy is made in the mesh information input file by specifying an n number of time blocks and the corresponding tuning parameter assigned for each time block as well as the actuation point A_T. When the code is executed, this information is automatically read in by an in-built DG-ADCIRC subroutine, which computes a temporally varying tuning curve over the course of the simulation. After time $t = A_T$ into the simulation, the power and thrust coefficients are specified by the assigned tuning parameter.

8.2 Dynamic Tuning of Full-Width Arrays

As highlighted in Chapter 5 as well as in works by Vennell and Adcock (2014) and Vennell (2016), the introduction of a large full-width turbine array operating with a dynamic tuning strategy to maximise power extraction may have significant effects on the hydrodynamics of the channel, where complete resolution of these hydrodynamics may be difficult to capture in analytical models. Chapter 7 has shown that a favourable comparison can be achieved between numerical and 0D analytical models for fixed tuning strategies. When extending the model to incorporate

a dynamic tuning strategy, it remains unknown whether the effects of the 2D flow processes can be fully captured by the simplified 0D model due to the temporally varying turbine resistance over the tidal cycle. By extension, these processes may not be considered when determining the optimal tuning curve for dynamic strategies (and more importantly, predicting the maximum available power produced by a large array) in 0D models. This implies that higher-order 2D or 3D models are required to capture these nuances and to make further improvements to the dynamic tuning strategy. It has been noted in Chapter 5 that the significance of the dynamic strategy can be enhanced as λ_0 is reduced and B_L and N_R are both increased. The idealised channel model adopted in Chapter 7 ($\lambda_0 \approx 0.2$) has been determined to be a reasonably inertia-dominant channel, indicating that a meaningful performance increase is to be expected by operating with a dynamic tuning strategy. With this in mind, a series of full-width arrays with varied layouts (N_R and B_L) are modelled in the same idealised 2D hydrodynamic channel as adopted in Chapter 7. A larger range of N_R (up to $N_R = 10$) than those used in the previous chapter is also considered, and these layouts are shown in Figure 8.3a. Across all simulations, an oscillating head difference across the channel, $a_0 = 0.2$, and a bed drag coefficient, $C_d = 0.002$, are held constant. The difference in turbine representations is also tested in these simulations by seeking optimal tuning curves for both actuator discs and tidal rotors.

For all cases considered, the generate-and-test optimisation process is able to succeed in just one iteration, with the difference between the optimal strategy and initial guess being indistinguishable. This suggests that the optimal tuning curve for the dynamic strategy derived by the 0D model remains optimal for the 2D numerical model. Using this result, a comparison is then undertaken between the 0D and 2D models by applying the same tuning curve. The time-averaged power output $\overline{P}_{av}$ and maximum flow rate Q for both the 0D and 2D cases are presented in Table

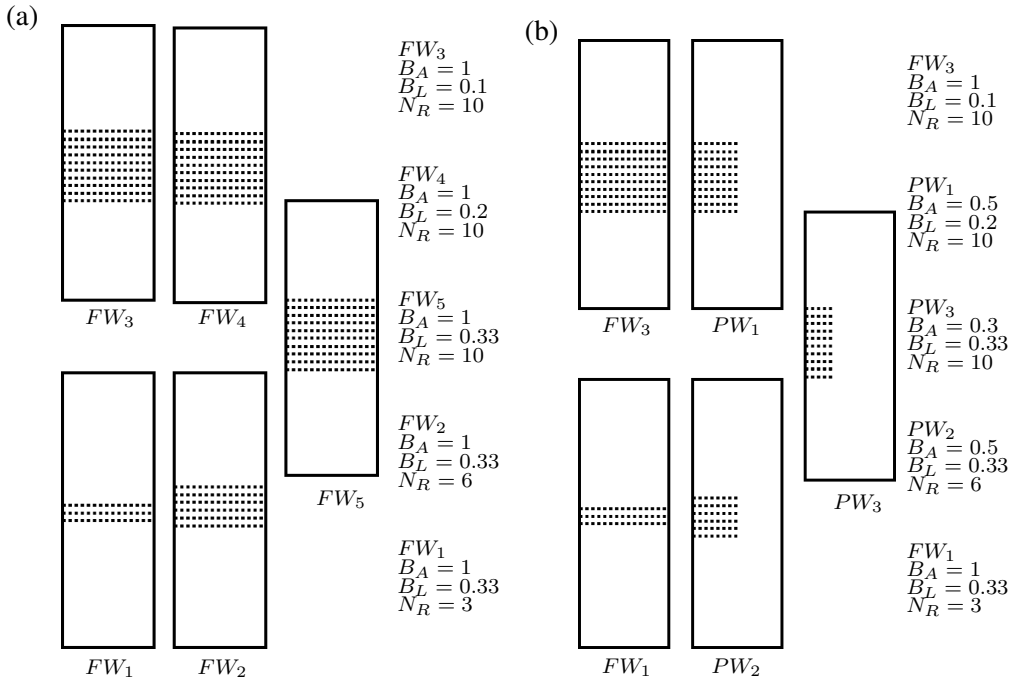

Figure 8.3: Schematic plan views of actuator discs and tidal rotors arranged in: (a) five full-width (FW) arrays with varying total swept area ($N_R B_G = N_R B_A B_L$), and; (b) five full and partial-width (PW) arrays with constant total swept area.

8.1. Table 8.2 compares the two models using a newly defined 'dynamic boost' and the variable $\Delta\phi$. The dynamic boost is defined as the percentage variation of $\overline{P}_{av}$ obtained from dynamic tuning from the corresponding $\overline{P}_{av}$ obtained from fixed tuning, as a way to compare how effective a dynamic strategy is in contrast to a fixed strategy. The values of $\Delta\phi$ are determined by firstly evaluating ϕ, the phase difference between the current and the head, for the dynamic and fixed strategies, then by taking the difference between ϕ for both tuning strategies. A positive $\Delta\phi$ indicates that the current phase for the dynamic strategy has been shifted closer to the head than the fixed strategy.

It is evident from Tables 8.1 and 8.2 that both the disc and the rotor captures a dynamic boost with the 2D hydrodynamic model, with the disc tending to over-estimate the value. A similar finding has been discussed in Section 5.2.1.2, where a lower performance was observed in the tidal rotor relative to the actuator disc, due to the rotor's lower maximum available thrust and the disc being more suitable

Table 8.1: Numerically and analytically predicted $\overline{P}_{av}$ and maximum Q for selected array configurations with actuator discs and tidal rotors.

Array	$\overline{P}_{av}$ (MW)	$\overline{P}_{av(V10)}$ (MW)	Q (m^3/s)	$Q_{(V10)}$ (m^3/s)
FW1 (disc)	7.429	7.595	135.788 $\times 10^3$	134.756 $\times 10^3$
FW2 (disc)	13.828	14.135	134.724 $\times 10^3$	133.278 $\times 10^3$
FW3 (disc)	4.303	4.328	136.586 $\times 10^3$	135.851 $\times 10^3$
FW4 (disc)	10.267	10.325	134.862 $\times 10^3$	133.965 $\times 10^3$
FW5 (disc)	20.903	21.438	132.857 $\times 10^3$	132.519 $\times 10^3$
FW1 (rotor)	4.384	4.442	136.023 $\times 10^3$	135.357 $\times 10^3$
FW2 (rotor)	8.349	8.462	134.174 $\times 10^3$	133.387 $\times 10^3$
FW3 (rotor)	3.052	3.070	136.708 $\times 10^3$	135.942 $\times 10^3$
FW4 (rotor)	6.831	6.853	134.769 $\times 10^3$	134.135 $\times 10^3$
FW5 (rotor)	13.015	13.147	131.476 $\times 10^3$	130.853 $\times 10^3$

Table 8.2: Numerically and analytically predicted dynamic boost and $\Delta\phi$ between dynamic and fixed tuning strategies for selected array configurations with actuator discs and tidal rotors. Values of $\Delta\phi < 0.01°$ are omitted from the table.

Array	Dynamic boost (%)	Dynamic boost$_{(V10)}$ (%)	$\Delta\phi$ (°)	$\Delta\phi_{(V10)}$ (°)
FW1 (disc)	1.02	1.07	0.36	0.48
FW2 (disc)	3.08	3.42	0.66	0.96
FW3 (disc)	0.21	0.23	-	0.03
FW4 (disc)	1.34	1.39	0.45	0.47
FW5 (disc)	5.77	6.83	3.45	4.36
FW1 (rotor)	0.16	0.19	-	-
FW2 (rotor)	0.47	0.48	-	-
FW3 (rotor)	0.08	0.08	-	-
FW4 (rotor)	0.36	0.37	-	-
FW5 (rotor)	1.32	1.36	0.75	0.96

for the proposed operational phases of the dynamic strategy. However, Table 8.2 indicates, contrary to the finding in Chapter 5, that the additional power increase using the dynamic strategy is underwhelming for both turbine representations. This is unsurprising as the number of dimensionless rows (N_R^*) adopted in Chapter 5 (based on the work of Vennell, 2016) is not equivalent to the number of rows (N_R) modelled in this chapter. Overall, the results from the analytical 0D model (Vennell, 2010) and numerical 2D model provide an encouraging level of agreement of within 2% across all configurations. The small level of discrepancy between the models

has been identified before and discussed in Section 7.2.1.

Another possible explanation for the small discrepancy may be attributed to the occurrence of a seiching mode. As discussed by Vennell and Adcock (2014), this is potentially introduced by a high-frequency response from the tide, which can be caused by a rapid change in the drag coefficient of a turbine array such as that applied by the dynamic strategy. This consideration is of broad scale importance for the operation of a turbine array as the effects of the shallow waves introduced not only change the optimal dynamic boost determined by 0D models, but also channel navigability and shoreline erosion. For this reason, the geometry of the channel and fundamental seiche period should be taken into account when analysing such strategies. For the rectangular channel in this study, the fundamental (first mode) seiche period is determined to be 60 minutes in the streamwise direction and 15 minutes in the spanwise direction. A Fast Fourier Transform (FFT) is used to analyse the frequencies for the time-series of modelled surface elevation at a number of locations. This analysis shows no clear observable peak corresponding to the free oscillation period for the first mode in the amplitude spectrum, suggesting that under these conditions, the dynamic strategy does not introduce a seiche. The relatively high bed friction and shallow bathymetry of the channel result in a highly damped system, which may be why these higher frequency waves are not observed.

As presented in Table 8.2, dynamic boost is shown to increase with B_L and N_R for both turbine representations, with the actuator disc achieving a 5.77% dynamic boost with the largest array (FW_5, $N_R = 10$) in comparison to 1.02% with the smallest array (FW_1, $N_R = 3$). A similar result is obtained when $N_R = 10$ is fixed and B_L transitions from a low-blockage layout (FW_3, $B_L = 0.1$) with a bare minimum dynamic boost of 0.21%, to a high-blockage layout (FW_5, $B_L = 0.33$) where a much higher performance enhancement is observed. The reported observation is consistent with previous findings by Vennell (2016).

The underlying reason for this increase is discussed in Section 5.2.1.2. In comparing all the different configurations in this section, FW_5 has superior performance due to it having the highest N_R and B_L out of all the simulations. FW_5 achieves also the largest phase shift in phase 4 due to it having the highest $N_R C_T$, allowing the array to provide higher resistance during the end phase and in turn produce more power. However, even for the FW_5 configuration using actuator discs, little variation in ϕ is found. Thus it may be inferred that, with realistic N_R and B_L considered, an array is not large enough to contribute to a significant phase shift.

Despite slight discrepancies between the 0D and 2D models, the overall close agreement between them while implementing the dynamic strategy suggests that the former is capable of producing similar results as the higher-order hydrodynamics model. In addition, there does not seem to be any major physics associated with the dynamic strategy for the full-width array that has not been captured by the 0D model (Adcock, 2012; Vennell, 2016; Vennell and Adcock, 2014). These results have also shown that the dynamic tuning strategy can be modelled successfully in 2D over a full-width array, leading to the implementation of a partial-width array in the next step of the research.

8.3 Dynamic Tuning of Partial-Width Arrays

As discussed in Chapters 3 and 7, for a given number of turbines with a fixed total turbine swept area $N_R B_G$ and varying array layout, both the local blockage effect and the global blockage effect (i.e. having arrays in series or in parallel configurations) can have a significant impact on the partial-width array performance. In turn, the resistance of the array may need to be adjusted to account for beneficial effects such as the reversal boost while mitigating the possibility of other detrimental effects such as array choking. All previous studies of partial-width arrays have focused on using either the impatient strategy or the fixed strategy, which requires

the turbine tuning to be fixed throughout the tidal cycle; these strategies may not necessarily be able to extract the maximum available power. It is therefore of interest to investigate the significance of the local and global blockage effects with a dynamic tuning strategy. Having already analysed the dynamic tuning strategy with a full-width array in the previous section, it is explored further within several configurations of partially blocked channels as they are more representative of realistic arrangements for tidal turbine arrays.

8.3.1 Configurations

For both actuator discs and tidal rotors, a range of array configurations are considered, each with a fixed total device area as shown in Figure 8.3*b*. For the purpose of studying the local blockage effect, a total of three different array blockages are investigated with a fixed N_R. These array layouts (in order of increasing B_L) are: FW_3, with a B_L of 0.1 and turbines spaced equally across the channel ($B_A = 1$); PW_1, with a B_L of 0.2 and the turbine array blocking half of the channel ($B_A = 0.5$), and; PW_3, with a B_L of 0.33 and densely packed turbines in the channel ($B_A = 0.3$). Furthermore, the effects of global blockage are investigated by analysing two additional highly packed configurations, PW_2 and FW_1, with a fixed B_L of 0.33 to match PW_3.

8.3.2 Effects of local and global blockage

Both fixed and dynamic tuning strategies (considered 'patient' tuning strategies as opposed to the frequently mentioned impatient strategy, termed by Vennell, 2016) are adopted to explore the local and global blockage effects, as well as to examine the dynamic boost across different array configurations. Actuator discs and tidal rotors are also both considered as the tendency of the discs to overestimate results can be useful in understanding the mechanism of the theories studied herein.

The maximum $\overline{P}_{av}$ for each combination of tuning parameters is determined

by deriving the tuning parameter/curve following the standard interpolation method discussed in Chapter 7 for the fixed tuning strategy and the improved generate-and-test method introduced in this chapter for the dynamic tuning strategy. In the case of the fully blocked channel, the computational intensity of the 2D model is significantly reduced due to the available results of the 0D model. This is not the case for the partially blocked channel, however, as the effect of a bypass flow is not included in the 0D model, meaning the full implementation of the following procedure is required. Typically, the fixed tuning parameter requires less than ten simulations to determine its optimal value, while thousands of simulations are needed to derive the dynamic tuning curve for the generate-and-test method. The initial guess used in the generate-and-test method for the partial-width configurations PW_1, PW_2 and PW_3 are adopted from FW_4, FW_2 and FW_5, respectively. Following the optimisation process, the optimally tuned values of maximum $\overline{P}_{av}$ are calculated for each arrangement with fixed and dynamic strategies. These values are plotted both as a function of B_L with constant N_R and as a function of N_R with constant B_L, for the two patient strategies. The plots are separated for each turbine representation with the disc results presented in Figure 8.4 and the rotor results presented in Figure 8.5. The dynamic boost is calculated by normalising the variation of $\overline{P}_{av}$ from the dynamic strategy by the respective $\overline{P}_{av}$ obtained from the fixed strategy, as this provides a way to visualise the benefit of dynamic tuning; this is plotted in Figure 8.6.

A few important observations can be made from the figures. Firstly, for both turbine representations, the results from the two patient strategies show similar trends. There appears to be an optimal value of B_L at which there is a maximum $\overline{P}_{av}$, as observed in both Figures 8.4a and 8.5a (the bars representing, for increasing B_L, the configurations of FW_3, PW_1, and PW_3). And as the global blockage decreases (i.e. configuration transitions from parallel to series by increasing N_R), there is

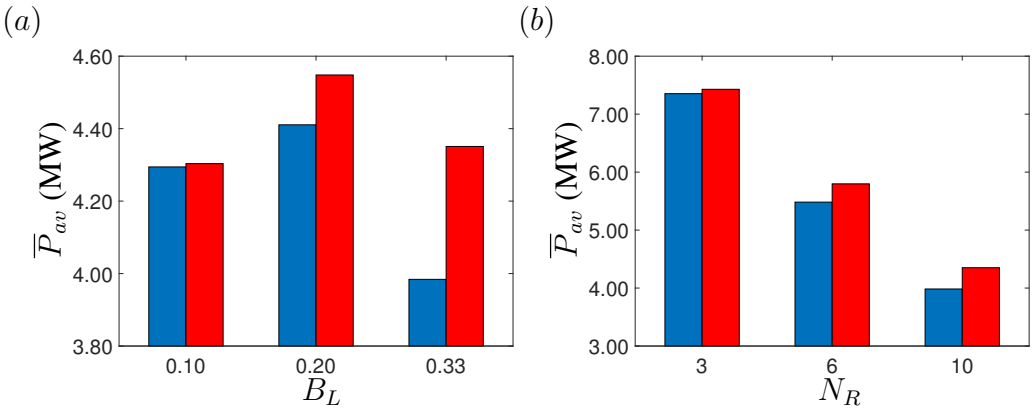

Figure 8.4: Variations in $\overline{P}_{av}$ for actuator discs in different array configurations with: (a) varying B_L and fixed $N_R = 10$, and; (b) varying N_R and fixed $B_L = 0.33$, with fixed (blue bars) and dynamic (red bars) tuning strategies.

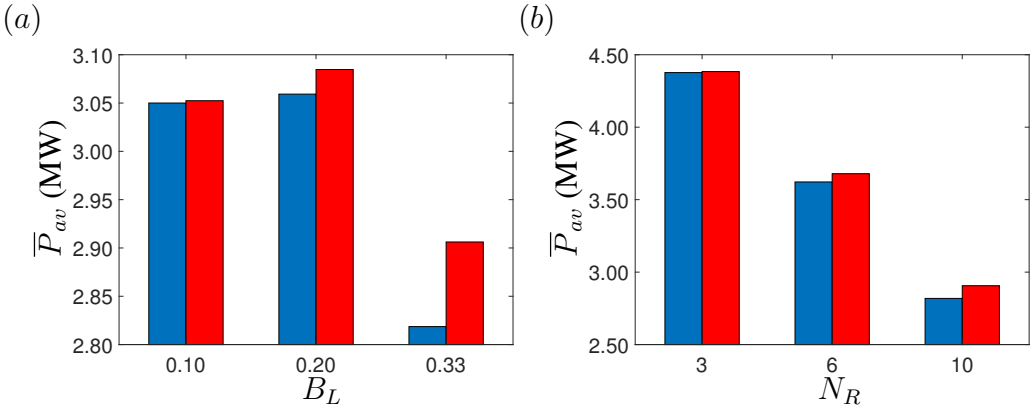

Figure 8.5: Variations in $\overline{P}_{av}$ for tidal rotors in different array configurations with: (a) varying B_L and fixed $N_R = 10$, and; (b) varying N_R and fixed $B_L = 0.33$, with fixed (blue bars) and dynamic (red bars) tuning strategies.

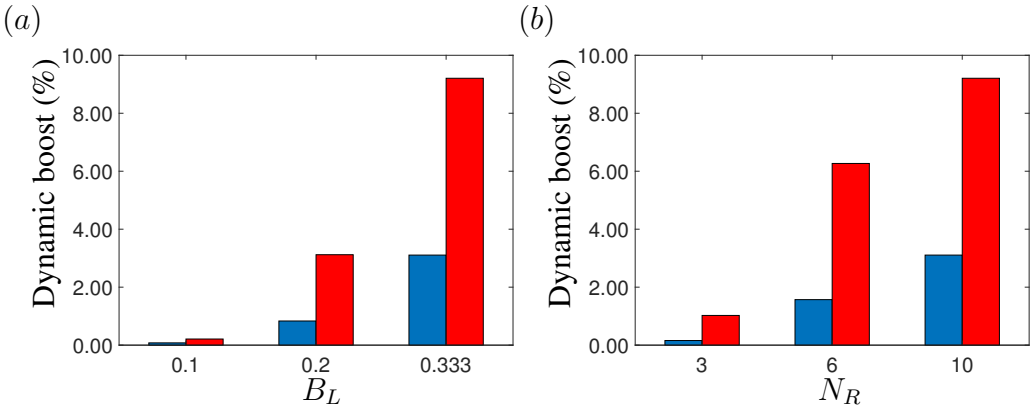

Figure 8.6: Variations in dynamic boost with: (a) varying B_L and fixed $N_R = 10$, and; (b) varying N_R and fixed $B_L = 0.33$, with actuator discs (blue bars) and tidal rotors (red bars) in different array configurations.

a monotonically decreasing trend in $\overline{P}_{av}$ as shown in Figures 8.4b and 8.5b (the bars representing, for increasing N_R, the configurations of FW_1, PW_2, and PW_3). Secondly, the dynamic strategy yields more power than the fixed strategy in both full-width and partial-width arrays, but the degree to which this increase is achieved appears to vary with both B_L and N_R.

Expanding on the first observation from above, it is apparent that for this channel geometry, an optimal B_L can be found between $B_L = 0.1$ and $B_L = 0.33$. This indicates that array configurations of more densely packed turbines may have a negative impact on the performance, consistent with the existing theoretical work by Nishino and Willden (2012*b*). Set against this, recent work by Bonar et al. (2019) and the findings presented in Chapter 7 has suggested that, under certain flow conditions, turbines should be arranged in short and highly blocked rows in order to benefit from a reversal boost effect. However, for a large array (as adopted in this chapter), the turbine resistance may increase excessively by reducing the lateral spacing between turbines, resulting in a significant amount of flow diversion around the array accompanied by array-scale mixing. Ultimately, this array choking effect will outweigh the increase in turbine-scale flow confinement and reversal boost, leading to less power production from the reduced core flow.

The decrease in power with increasing N_R can be understood by looking at the work by Garrett and Cummins (2007). While examining global blockage, it has been found that parallel configurations (which have lower N_R) are usually superior to series configurations due to the higher blockage they provide on a global scale. In a similar manner, the FW_1 and PW_2 arrangements, which also have lower N_R in comparison, perform better than the FW_3 and PW_1 arrangements, respectively. Vennell (2010) and Draper and Nishino (2014) have explained this phenomenon by claiming that, in order to optimise the power from a fixed number of tidal rotors, it is most efficient to align them all in the same row until this is no longer practical, and

only then should a second row be filled, and so on. This result is expected given that the energy flux in each successive row of an idealised channel is reduced due to the presence of the turbines. However it should be noted that, for array connectivity, the results from Chapter 3 suggested conflicting results that favour turbine installation in a series configuration, mainly due to the kinetic energy profile distribution across the channel for the real site of the Bohai Strait. Interestingly, there also exists the 60-70% power correction between the actuator disc and tidal rotor simulations for all configurations, though the over-prediction by the disc is lessened with series configurations.

The primary explanation for the second finding mentioned above lies with the temporally varying operation of the dynamic strategy, as indicated by the tuning curves shown in Figure 8.7. Especially, the optimal tuning curves for PW_1, PW_2 and PW_3 suggest that the tuning strategy for the partial-width array is similar to the four-phase strategy used for the full-width turbine arrays (Vennell, 2016). An example of tuning curve variation with the indication of operation phases 1 - 4 is

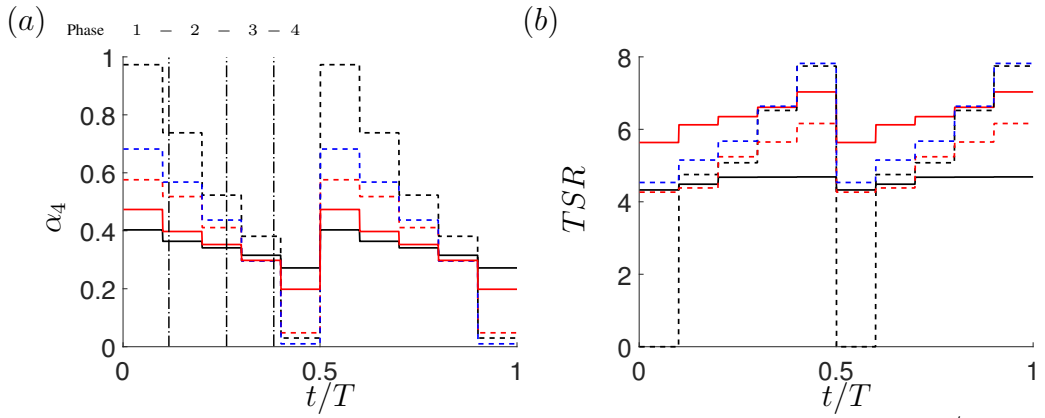

Figure 8.7: Variations of tuning curves with the relative time in a tidal cycle, t/T, for: (a) actuator discs, and; (b) tidal rotors, with different array configurations. Full-width arrays include FW_1 (red solid lines) and FW_3 (black solid lines), while partial-width arrays include PW_1 (red dashed lines), PW_2 (blue dashed lines), and PW_3 (black dashed lines). Operation within each of the four dynamic strategy phases is indicated by the dash-dotted lines.

shown in Figure 8.7a, but the exact weighting of different phases within the tidal cycle may vary with different λ_0 and array configurations. In the figure, the tuning parameters α_4 and TSR are used respectively for the actuator disc and tidal rotor, instead of the k adopted in previous chapters, given that this section focuses heavily on the tuning strategies and less on the comparison between turbine representations. There does, however, exist a significant difference in the variation of the tuning parameter between the actuator disc and tidal rotor models in terms of k, similar to the findings in Chapter 5. This is due to the realistic limitation of the tidal rotor in accommodating the changes needed in the different phases of the dynamic strategy, thereby restricting the potential of the dynamic boost as it appears in the actuator disc model.

In order to better understand the array performance increase due to the dynamic tuning strategy on partial-width arrays, the variations in power production and array-scale core flow are analysed over a complete tidal cycle. The partial-width configuration of PW_3 with actuator discs is chosen to perform this analysis as it yields the highest dynamic boost, approximating to a $\approx 10\%$ gain in power on top of the fixed strategy. Measurements are taken at a turbine installed in the centre of this sample configuration as the representative turbine. The results are examined below.

A substantial increase in both $\overline{P}_{av}$ and the peak velocity of the array-scale core flow is observed in the dynamic strategy, as shown in Figure 8.8. This is due to the four-phase operational mechanism of the dynamic strategy, which generates a considerably higher peak velocity by facilitating flow acceleration during the period immediately following flow reversal. Such an operation leads to a phase shift forward and higher flows later in the half tidal cycle. With respect to the power production, higher P_{av} is generated over a shorter effective production period with a larger $P_{av,max}$ of up to 40% more than the fixed strategy, as shown in Figure 8.8b.

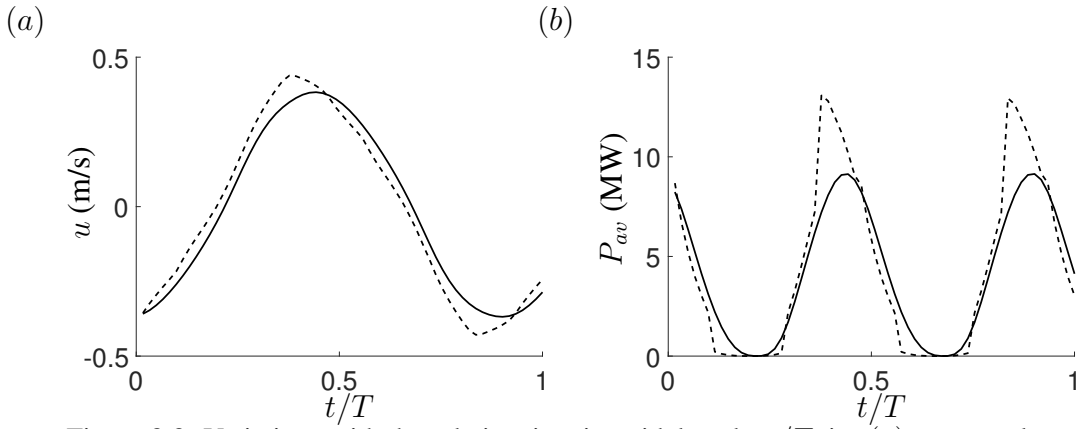

Figure 8.8: Variations with the relative time in a tidal cycle, t/T, in: (a) array-scale core flow, and; (b) P_{av}, for the PW_3 actuator disc configuration with fixed (solid lines) and dynamic (dashed lines) tuning strategies.

How the dynamic tuning strategy differs from the fixed strategy is further understood by a tidal harmonic analysis. Figures 8.9 and 8.10 provide a more complete representation of tidal characteristics across the channel over the simulation period by illustrating the computed amplitude (elevation) and phase (velocity) of the M_2 co-tidal charts. Careful observation between Figures 8.9a and 8.9b shows a very slight difference in contour line density (i.e. slightly more gradual head loss) in Figure 8.9b, indicating that less resistance has been applied with the dynamic strategy on average over the tidal cycle; this allows for the development of stronger array-scale core flow. The difference in contours along the array core between Figures 8.10a and 8.10b suggests that there is an overall phase shift between the fixed and dynamic strategies. The small difference of the phases agrees with a similar finding in Section 8.2, indicating that it may be unlikely that the phase can be manipulated to extract more power when considering a realistic number of rows and blockage.

The results presented in this section have shown that the maximum $\overline{P}_{av}$ can be enhanced by the dynamic strategy as a function of both the local and global blockages across multiple configurations. Specifically, for a constant swept area of turbines and regardless of the layout (whether the installations are partial-width or

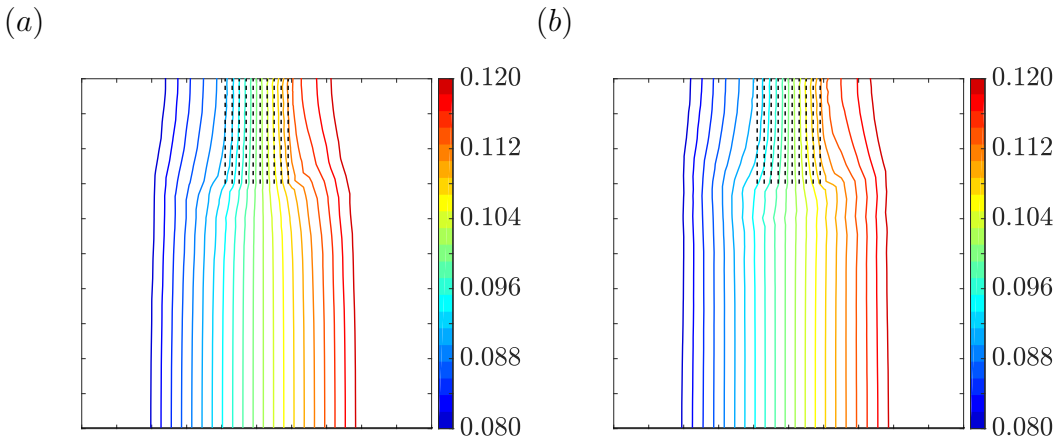

Figure 8.9: Contours of the M_2 co-tidal elevation amplitude (m) predicted using DG-ADCIRC for: (a) fixed tuning strategy, and; (b) dynamic tuning strategy, with the location of array deployment depicted by group of dashed lines.

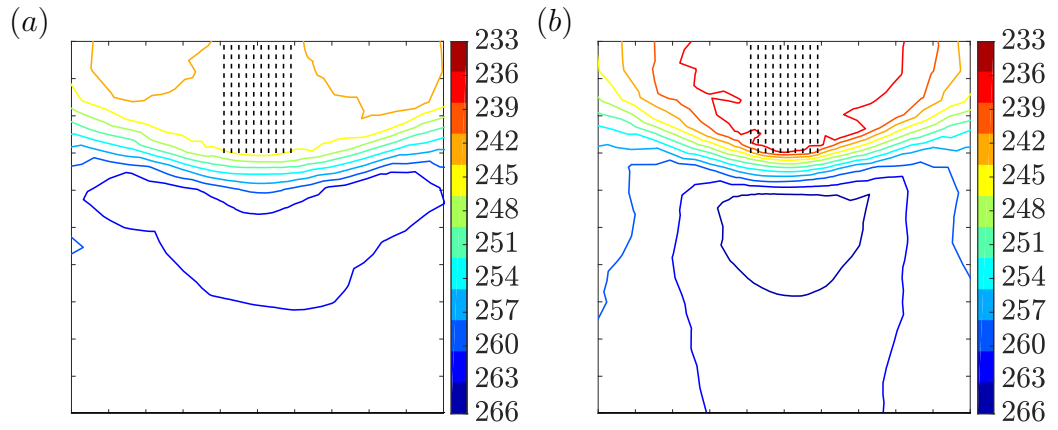

Figure 8.10: Contours of the M_2 co-tidal velocity phase (°) predicted using DG-ADCIRC for: (a) fixed tuning strategy, and; (b) dynamic tuning strategy, with the location of array deployment depicted by group of dashed lines.

full-width arrays), the dynamic boost appears to increase as function of B_L and N_R for all simulated cases.

In particular, it is found that the local blockage effect is more beneficial, with respect to the dynamic boost, when a dynamic strategy is employed. For instance, when comparing the maximum $\overline{P}_{av}$ for configurations of actuator discs using the dynamic strategy with different B_L and a fixed $N_R = 10$ (Figure 8.4a), PW_1 ($B_L =$ 0.2) and PW_3 ($B_L = 0.33$) produce an additional $\approx 5.7\%$ and $\approx 1.1\%$ of power on top of the full-width configuration of FW_3 ($B_L = 0.1$). In contrast, with the fixed strategy implemented, the change in $\overline{P}_{av}$ is $\approx 2.7\%$ and $\approx$ -7.2% for PW_1 ($B_L =$ 0.2) and PW_3 ($B_L = 0.33$). Furthermore, the decline of $\overline{P}_{av}$ with respect to N_R (Figure 8.4b) is more gradual with the dynamic strategy, meaning that a series configuration of turbines is less unfavourable with dynamic tuning. The advantages of dynamic tuning are also apparent for tidal rotors, but the difference between the two strategies is less significant when compared to their application using the actuator disc. According to Figure 8.6, the configuration PW_3 responds best to dynamic tuning as it has the largest percentage of dynamic boost; however, this configuration also has one of the lowest $\overline{P}_{av}$ out of all the layouts due to the excessive reduction of the flow through the array and array-scale mixing caused by its high N_R and B_L. Despite the power production, the response of such a configuration to dynamic tuning can be explained by a superimposed 'dynamic and reversal boost' effect, which is discussed in the following section.

A final point of interest is the importance of the tuning with the dynamic strategy for a partial-width array, which is indicated in Figure 8.11. As before, the results of $\overline{P}_{av}$ for both of the patient tuning strategies are normalised by the corresponding values from the impatient strategy. It is clear from the figures that, just as the importance of tuning is observed to increase with increasing B_L and N_R for the fixed strategy, a similar trend is true for the dynamic strategy. As well, both patient

turbine tuning strategies are still found to be less significant for the more realistic tidal rotor.

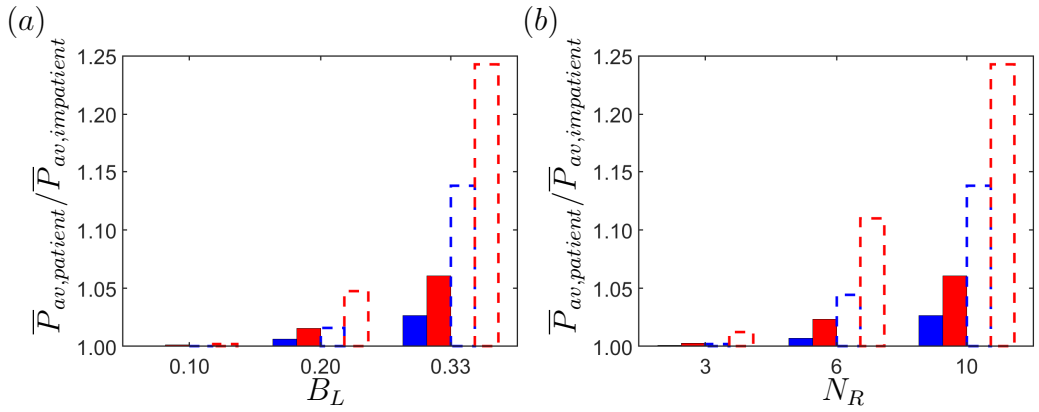

Figure 8.11: Variations in normalised $\overline{P}_{av}$ with: (a) varying B_L and fixed $N_R = 10$, and; (b) varying N_R and fixed $B_L = 0.33$, with actuator discs (dashed bars) and tidal rotors (solid bars) for the fixed (blue bars) and dynamic (red bars) tuning strategies with different array configurations.

8.3.3 Dynamic and reversal boost

Having examined the dynamic boost in both partial-width and full-width arrays, more detailed investigation is undertaken to determine how this performance enhancement and the detailed behaviour of dynamic strategy are affected by array layout as it varies from a full-width to a partial-width array. As highlighted by Nishino and Willden (2012*b*) and Bonar et al. (2019), if an array of turbines does not span the full width of the channel, the flow physics becomes more complex with addition flow features comprising: flow diversion around the array, resulting in array-scale mixing, and the reversal boost, caused by the different inertia and drag balance between array-scale core and bypass flows. In order to accommodate these effects, it may be necessary to change the optimal operation of the dynamic tuning strategy, which will in turn affect the results of the dynamic boost when changing from full-width to partial-width configurations.

With an aim to examine the altered effects of the dynamic boost, turbine config-

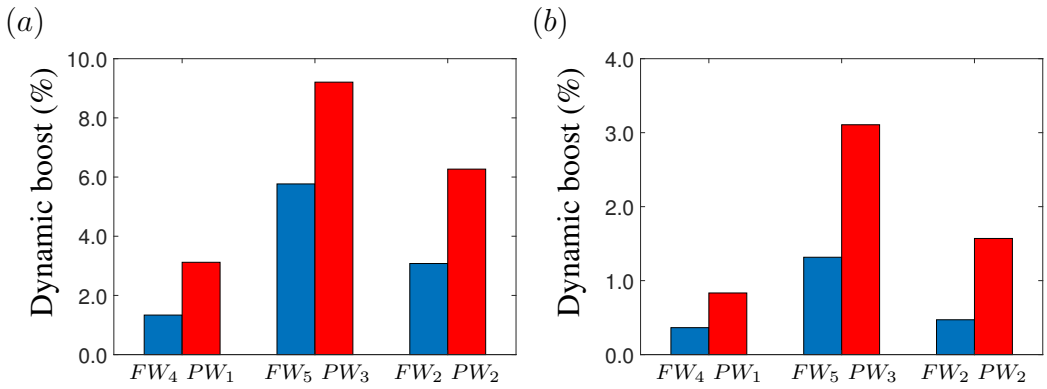

Figure 8.12: Comparison of the dynamic boost between equivalent partial-width (red bars) and full-width (blue bars) array configurations with the same N_R and B_L for: (a) actuator discs, and; (b) tidal rotors.

urations with constant N_R and B_L are compared against each other for full-width and partial-width arrays as shown in Figure 8.12. The results presented in this bar graph show the side-by-side comparisons of the increase in $\overline{P}_{av}$ achieved through implementing the dynamic strategy, or the dynamic boost. The findings suggest that, for all array configurations tested, a larger dynamic boost can be achieved in partial-width arrays than in full-width arrays.

In order to better understand the complexity of the dynamic strategy operation with partial-width arrays, 2D flow fields are produced for the PW_3 configuration using actuator discs with both patient strategies. Four time steps are selected in the transition between the operating phases of the dynamic strategy, as shown in Figure 8.13, for a complete tidal period of T. The tuning curves (α_4) for both strategies are plotted at the lower right corner of Figures 8.13a_2-d_2.

Observing Figures 8.13a, as the tide reverses, the core flow is phase-shifted forward and has already reversed ahead of the bypass flow. When the bypass flow does eventually change direction, the effect of the inertia forces some of the bypass flow to divert into the core region. The phase shift between array-scale core and bypass flows has been identified by Bonar et al. (2019) as the underlying driver for the reversal boost. This phenomenon is found to be more pronounced in Figure 8.13a_2,

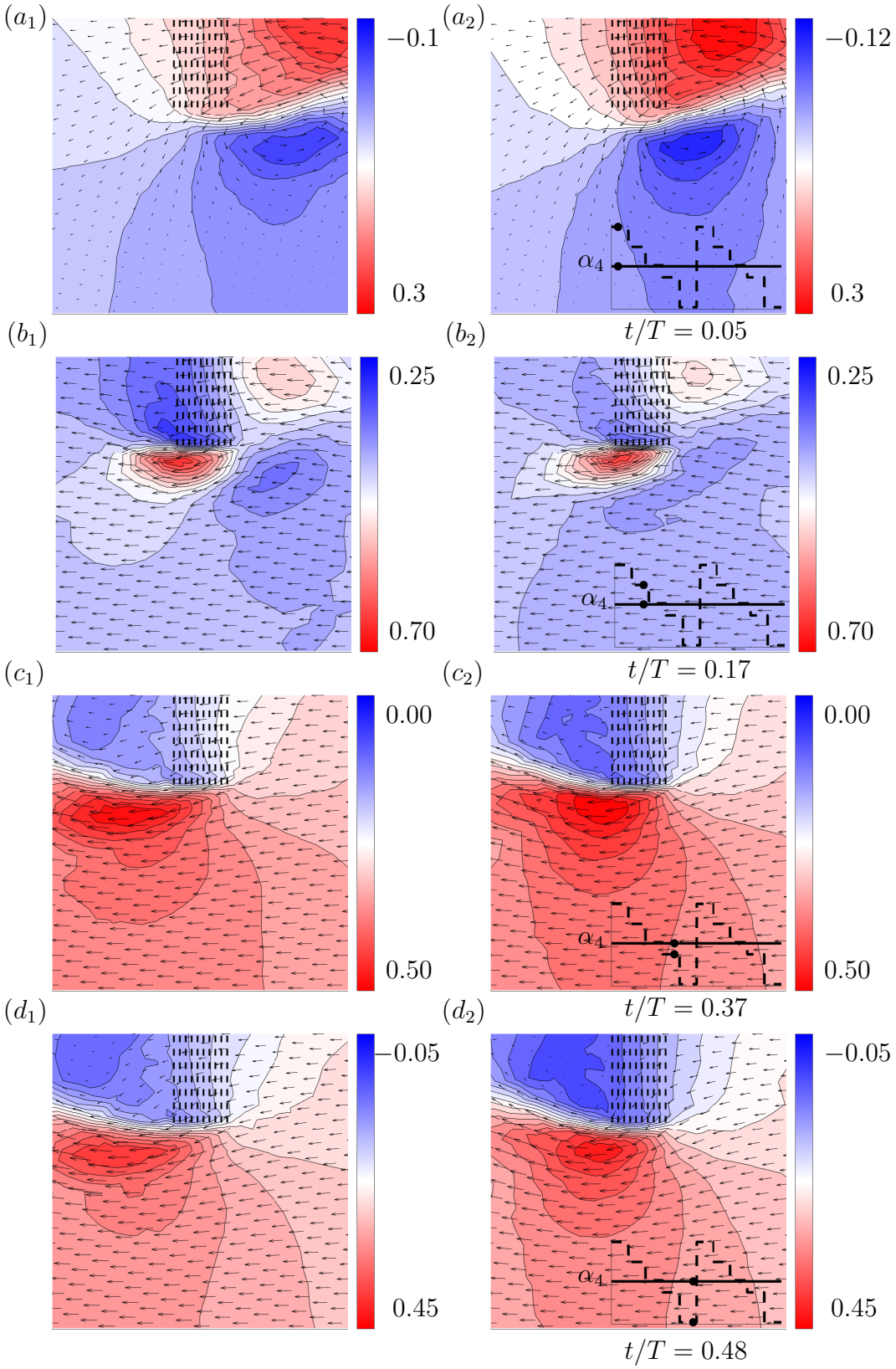

Figure 8.13: Contours of streamwise depth-averaged velocity (m/s), for: (a_1)-(d_1) fixed tuning strategy, and; (a_2)-(d_2) dynamic tuning strategy, with the location of array deployment depicted by group of dashed lines. Thin black arrows illustrate the magnitudes and directions of velocity vectors u and v. Each set of figures (a)-(d) show the transition period between successive phases, from phase 1-2 in figure set (a) to phase 4-1 in figure set (d).

where the lower C_T proposed in phase 1 of the dynamic strategy allows for the array-scale core flow to build up without inhibition (Vennell, 2016); furthermore, the path through the array core becomes the path of least resistance, facilitating the diversion of the lagging array-scale bypass flow into the array itself (more so than the fixed strategy). The combination of these two effects leads to an enhanced reversal boost being generated during each change of flow direction. Following phase 1, the flow acceleration phase in Figures 8.13b shows stronger array-scale core flow accompanied by less array-scale flow diversion in Figure 8.13b_2. This is due to the lower resistance that is experienced by the core flow as the dynamic strategy employs a moderate C_T and higher η during phase 2. As such, the aim is to extract power in the most efficient manner by avoiding the reduction of flow acceleration through the array core as well as decreasing array-scale flow diversion.

Figures 8.13c and 8.13d illustrate the later stages of the half tidal cycle, when approaching slack water, for two instances showing strong flow diversion around the array with the dynamic strategy. Array-scale core flow is found to reverse earlier in Figure 8.13d_2 while it continues in the same direction at the end of the last phase in Figure 8.13d_1, which has been demonstrated in Figures 8.8 and 8.10. The additional flow diversion and earlier turn of the array-scale core flow in the dynamic strategy are expected due to the additional resistance applied by the array in increasing the C_T within phase 4. As a result, the dynamic balance of the array-scale core flow further differs from the fixed strategy in that the reduction in phase difference between the core flow velocity curve and the pressure forcing allows the beginning of the next half tidal cycle to experience an extended period of flow acceleration. Simultaneously, and more importantly for partial-width arrays, the enhanced phase difference between the array-scale core flow and array-scale bypass flow promotes greater funnelling of the bypass flow into the array core when the tide turns, driving a larger reversal boost.

With the key physical processes of the dynamic strategy and how they are distinguished from the fixed strategy now understood for partial-width arrays, the next step is to analyse how the operational phases may change in context of the alteration from a full-width to partial-width array. Figures 8.14-8.16 illustrate the optimal tuning curves for each partial-width configuration and their respective initial guesses from the generate-and-test method, showing their deviation from the curves originally produced for the corresponding full-width configurations of the same N_R and B_L. Throughout all comparisons made, a lower optimal k (i.e. higher α_4 and lower TSR) over the first 3 phases is observed while the same value of k, or even higher, is required in phase 4; this finding is observed to be true regardless of array configuration and turbine representations. The reason why a lower k is required in phase 1 for the partial-width configuration is to optimise the benefits of the reversal boost as the tide turns: the enhanced acceleration of the array-scale core flow and addition of phase-shifted bypass flow add to the advantage of a partial-width array in the early operational phases of a half tidal cycle, leading to a lower k to be deemed optimal. Both phase 2 and phase 3 (where power production is concentrated) also require a more moderate k with high η for a partial-width array in order to better accommodate the reversal boost and, just as importantly, balance the desired power extraction with the negative impact of greater flow diversion and array-scale mixing if too much resistance should be applied. As a result of the lower k and higher η needed for power extraction, phase 2 tends to outweigh phase 3 in terms of importance within the tidal cycle for a partial-width array. At the same time, maximisation of the reversal boost is dependent on the enlargement of the phase difference between the flows of the array core and its bypass regions; this is achieved by increasing the resistance of the array as discussed in Chapter 7. Thus, it makes sense that a high value of k remains the more optimal choice in phase 4, given that more resistance is required and that it can compensate for the lower k needed during phase 1. The

combination of change in phase 4 and phase 1 during the turn of the tide ensures that the benefit of the reversal boost is maintained or, more appropriately, increased.

To confirm the above, Figures 8.17-8.19 are presented: these figures further examine the power production and dynamic boost by plotting the normalised available power, P_{av}, over a tidal cycle. This is calculated as the P_{av} produced using the patient strategies for partial-width and full-width arrays, normalised by their corresponding $P_{av,max}$ of the dynamic strategy. As can be observed from the figures, power production has been further concentrated into the periods of phase 2 and phase 3 for partial-width configurations using the dynamic strategy, especially in the case of actuator discs in the highly packed configuration PW_3, as indicated in Figure 8.18a. This is generally expected given that adjustments of k are made in phase 1 and phase 4 to focus on maximising the reversal boost, narrowing down the effective period of power production. It is notable that, in this situation, more of the concentrated power production has shifted to phase 2, resulting from the enhanced reversal boost and the compromise made between power extraction and flow diversion, as noted previously.

From the discussion above, this section has clearly identified and examined the superimposed dynamic and reversal boost effect that has been found to occur in partial-width turbine arrays. Revisiting the interesting conundrum from Section 8.3.2, it can be concluded that, while an increase in B_L and N_R with a constant turbine total swept area will lead to greater flow diversion from the array core and array-scale mixing, it also leads to a higher resistance that increases the dynamic and reversal boost effect and results in a superior performance enhancement with the dynamic strategy. However, it should be noted that the dynamic and reversal boost does not completely overcome the array choking effect, as observed in the overall performance of PW_3 when compared to other configurations in terms of its resulting $\overline{P}_{av}$. Furthermore, the importance of the combined effect may be sig-

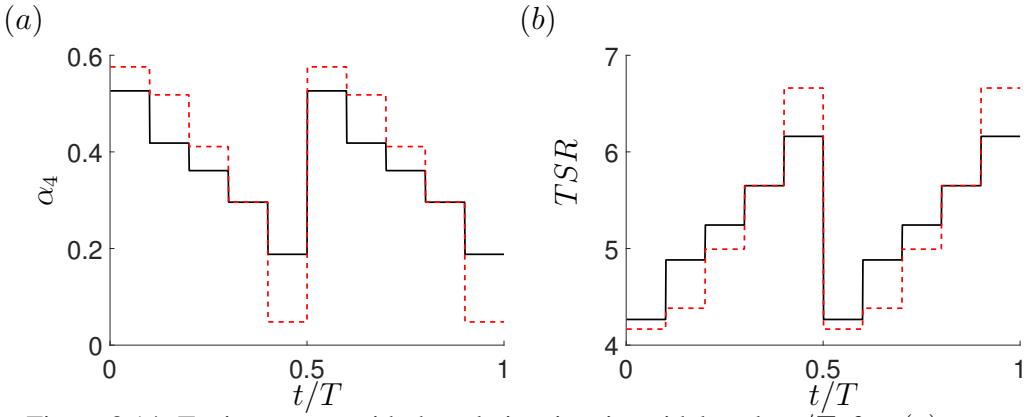

Figure 8.14: Tuning curves with the relative time in a tidal cycle, t/T, for: (a) actuator discs, and; (b) tidal rotors, for the configuration FW_4 (black solid lines) and PW_1 (red dashed lines).

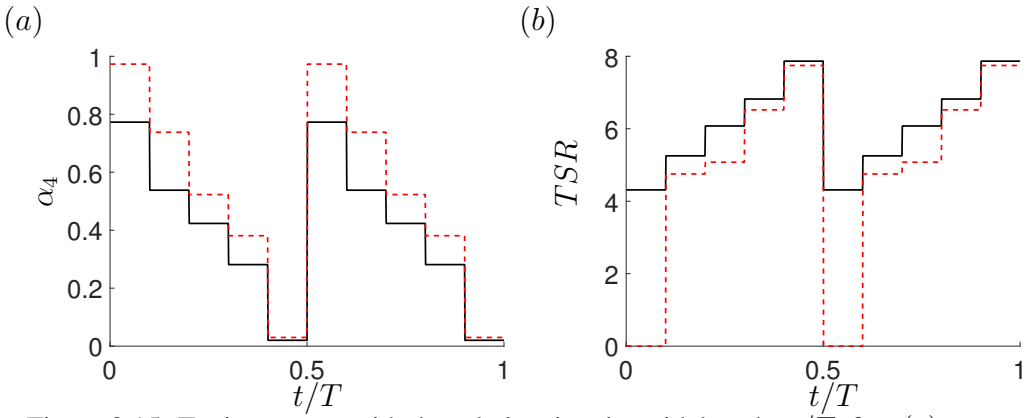

Figure 8.15: Tuning curves with the relative time in a tidal cycle, t/T, for: (a) actuator discs, and; (b) tidal rotors, for the configuration FW_5 (black solid lines) and PW_3 (red dashed lines).

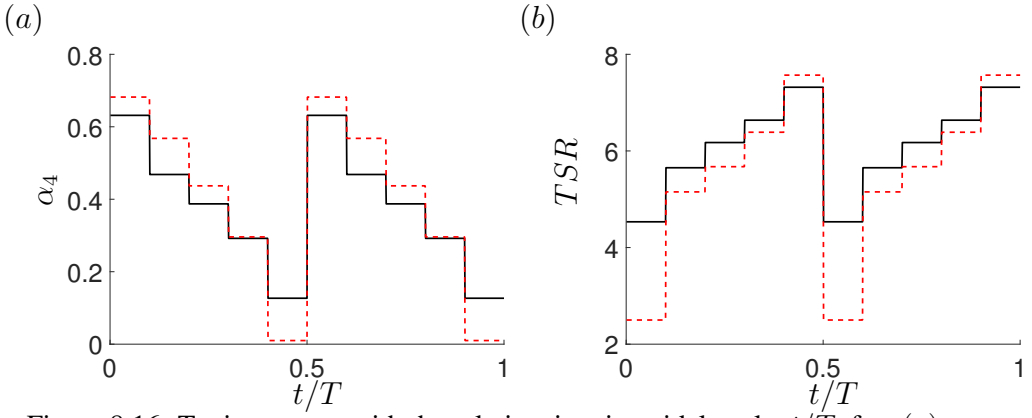

Figure 8.16: Tuning curves with the relative time in a tidal cycle, t/T, for: (a) actuator discs, and; (b) tidal rotors, for the configuration FW_2 (black solid lines) and PW_2 (red dashed lines).

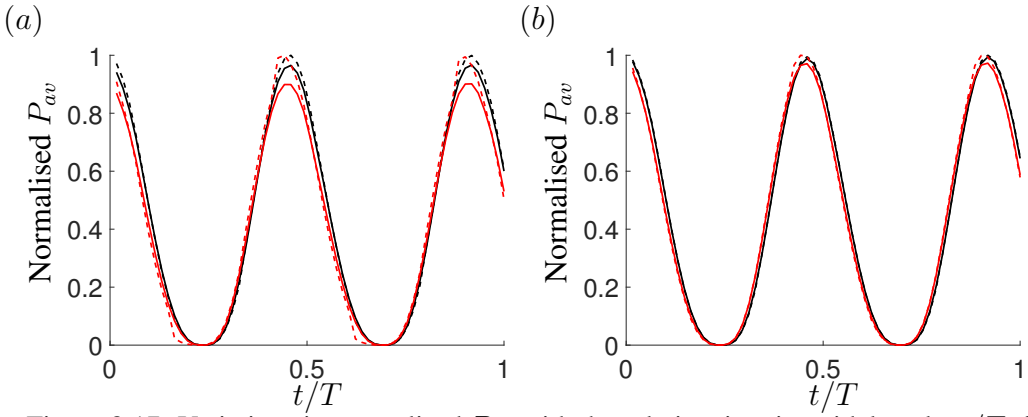

Figure 8.17: Variations in normalised P_{av} with the relative time in a tidal cycle, t/T, for: (a) actuator discs, and; (b) tidal rotors, for the configuration FW_4 (black lines) and PW_1 (red lines) with fixed (solid lines) and dynamic (dashed lines) tuning strategies.

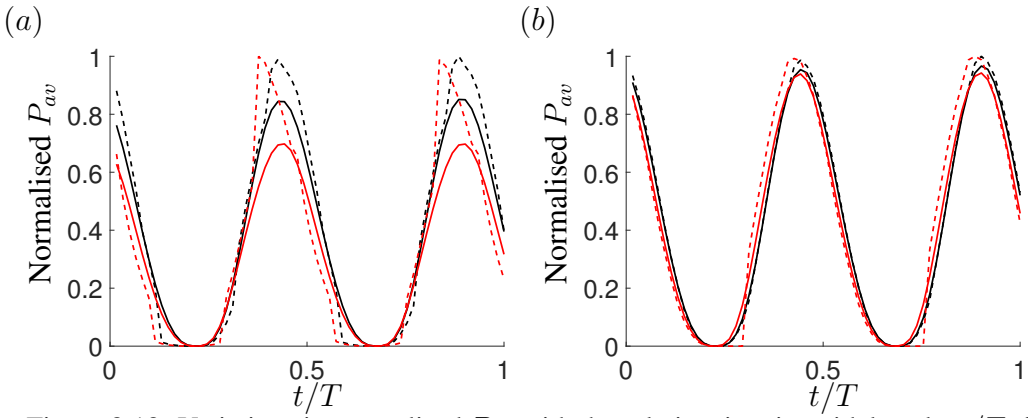

Figure 8.18: Variations in normalised P_{av} with the relative time in a tidal cycle, t/T, for: (a) actuator discs, and; (b) tidal rotors, for the configuration FW_5 (black lines) and PW_3 (red lines) with fixed (solid lines) and dynamic (dashed lines) tuning strategies.

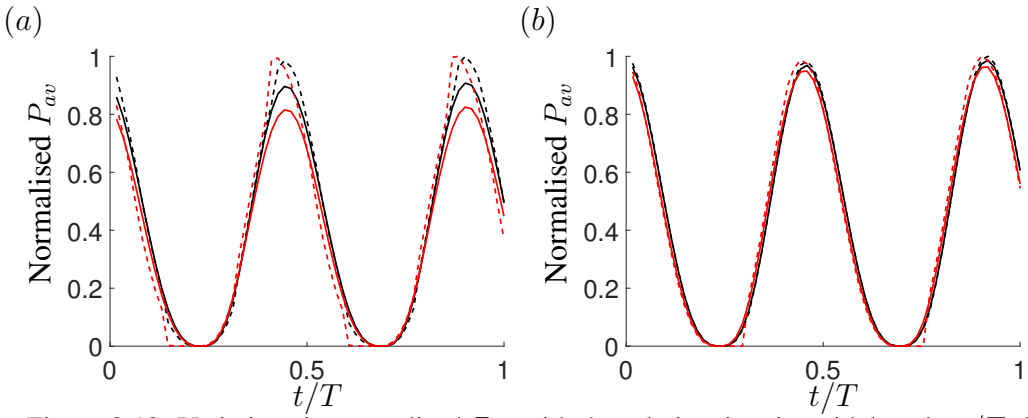

Figure 8.19: Variations in normalised P_{av} with the relative time in a tidal cycle, t/T, for: (a) actuator discs, and; (b) tidal rotors, for the configuration FW_2 (black lines) and PW_2 (red lines) with fixed (solid lines) and dynamic (dashed lines) tuning strategies.

nificantly reduced with a realistic turbine representation (limited to a maximum of 3% in dynamic boost for the different cases considered in this chapter, as shown in Figure 8.12) and it is uncertain as to whether the enhancement of the dynamic and reversal boost effect is worth the operational complexity.

Overall, it should be noted that the precise optimal tuning strategy may not be guaranteed with the optimisation process adopted in this chapter due to the resolution of the time steps and the tuning parameters used. However, the systematic approach of the generate-and-test method in conjunction with the convergence check have provided confidence that the solution is near the optimum. Despite this approximation of the optimal solution, leading order physics for the dynamic and reversal boost effect has been captured by the higher-order hydrodynamic model with the more realistic partial-width array configuration. In addition, only one specific channel dynamic has been considered in this chapter, yet Vennell and Adcock (2014) and Bonar et al. (2019) have respectively claimed that the phenomenon of the dynamic boost and the reversal boost may be further diminished in more drag-dominated channels; thus more insight on this combined effect can be gained with the consideration of additional channel dynamics.

8.4 Conclusions

This chapter has investigated the optimal operation of a large tidal turbine array using both fixed and dynamic tuning strategies to explore the power available to, and the performance of, different array configurations. The advanced dynamic strategy of Vennell (2016) has been implemented using a 2D numerical scheme and has been verified against the 0D model. This process has confirmed that the 2D hydrodynamic model is able to accurately reproduce the predictions from the analytical model for a full-width array, verifying the existence of the dynamic boost and the ability to capture this phenomenon. The numerical model has further been extended

to describe, for the first time, the effectiveness of the dynamic strategy with an array of turbines partially spanning a tidal channel. Specifically, a generate-and-test method has been adopted to derive the optimal tuning curve for each partial-width configuration.

Both partial-width and full-width arrays have shown performance improvement by using a dynamic tuning strategy over a fixed strategy, with partial-width arrays benefiting more. In order to achieve their optimal performance with the dynamic strategy, operations of the four phases are altered to enhance the beneficial reversal boost and balance the trade-off between power extraction and flow diversion, resulting in an overall power increase over a smaller time period. These effects have been identified in 2D hydrodynamic simulations using both actuator disc and tidal rotor turbine representations with a less pronounced improvement in the latter. The importance of tuning is also generally low for the rotor when compared to the disc. Furthermore, similar to full-width arrays, the amount of dynamic boost has been shown to be an increasing function of N_R and B_L for partial-width configurations when the total swept area of the array is kept constant, which can be explained by the combined dynamic and reversal boost. Therefore, by replacing fixed tuning with a dynamic strategy, the significance of local blockage effects and a series array configuration (relative to parallel) have been enhanced. Lastly, the 60-70% power correction for the disc from the predictions of the rotor still holds.

Chapter 9

Conclusions

The optimal design and operation of a tidal turbine array present a great challenge to engineers, particularly given the complex interactions between turbines and the unsteady tidal flow. This thesis has explored the complicated problem of optimally arranging and operating large numbers of tidal turbines in arrays across different length scales, ranging from the individual device scale to the larger array scale and eventually up to the basin scale, with the aim to maximise power output. In order to address thoroughly the existing research questions, steps have been taken towards comparing different array-building methodologies at a real site in China, as well as using simple analytical and numerical models to extend existing theories while using a more realistic turbine representation.

In the first part of this thesis, a comprehensive study of a real site has been conducted for a candidate tidal energy site in the Bohai Strait of south-eastern China. New design strategies for constructing a tidal turbine array based on the kinetic energy flux profiles of tidal flow have been used to explore the optimal arrangement of tidal stream turbines. This particular study has highlighted the difficulties of optimising turbine deployments at actual sites at regional scale, where it is difficult to isolate key physical effects and to draw general conclusions on array design and operation. These complex interactions have motivated the further detailed examination

of the underlying physics involved in the multi-scale modelling and optimisation of tidal arrays with deeper understanding provided of various key flow phenomena.

The remainder of this thesis has focused on both zero-dimensional and two-dimensional representations of an idealised site-scale channel model containing a tidal turbine array. A pragmatic approach was taken to explore the fundamental aspects of turbine arrangements and operation due to the simpler geometry of this model. Using the simplified model, iterations have been made towards defining a more generalised optimal solution for maximum power capture by means of a parametric study. The present thesis is distinctive from previous work in its inclusion of more realistic representations of tidal stream turbines. To achieve this, an alternative, more sophisticated turbine model based on the BC-BEMT was implemented in combination with idealised channel models. The resulting combined model has enabled re-examination of findings drawn from existing theories and provided further insight into the practical significance of various turbine tuning approaches and turbine arrangement strategies for better power capture.

Section 9.1 presents the fundamental findings of this thesis and recommendations for further work are given in Section 9.2.

9.1 Concluding Remarks

Sections 9.1.1 and 9.1.2 present findings on array configuration and operation for a fully blocked channel with varying swept area ($N_R B_G$) and a partially blocked channel with constant total swept area, respectively. Section 9.1.3 lists the conclusions regarding array power output.

9.1.1 Full-width array operation and arrangement

- A turbine array operating with either a fixed or dynamic tuning strategy, in which turbines are tuned specifically for each individual configuration, yields more power than an identical array operating using the impatient strategy,

where turbines continuously operate at $C_{P,max}$ and thus the tuning is constant across varying configurations (Vennell, 2010, 2016). For both fixed and dynamic strategies, optimally tuned turbine arrays observe an increase in $\overline{P}_{av}$ with the addition of new turbines, represented in this study by an increment in either B_L or N_R. However, this improvement in performance is not directly proportional to the increase in array size, as additional turbine rows see a diminishing return of power increment per row (Vennell, 2010), which has been observed to reduce slightly when adopting the dynamic strategy.

- The relative importance of tuning (i.e. the performance improvement in power output resulting from tuning the turbine operation), when comparing the fixed strategy to the impatient strategy and similarly the dynamic strategy to the fixed strategy, has been shown to increase with a larger array (larger N_R or B_L) (Vennell, 2016). In addition, the importance of tuning has an inverse relationship with the dynamic balance λ_0 — this leads to an inertia-dominated channel having the most significant benefit from tuning for both fixed and dynamic strategies (Vennell and Adcock, 2014).

- The variable-pitch (VP) rotor can serve as a favourable option as it improves operational efficiency and power production when compared to the fixed-pitch (FP) rotor. With the VP rotor, for the fixed strategy, pitching the blades to feather allows k to be reduced with a much smaller reduction in TSR and η. For the dynamic strategy, both pitch-to-feather and pitch-to-stall operations are carried out to allow for the VP rotor to more closely approximate the optimal k variations observed for the idealised disc over the tidal cycle. The VP rotor performs better than the FP rotor particularly for situations with small λ_0.

- For the more realistic tidal rotor turbine representation of both FP and VP

rotors adopted in this thesis, the performance improvement, and hence the importance of tuning, using both the fixed and dynamic strategies, are generally low when compared to the more idealistic actuator disc. Therefore, for most practical scenarios with the rotors, the impatient strategy, which has served as the baseline scenario for dynamic strategy comparison, may still remain a cost-effective option if the performance enhancement from tuning is deemed to be insignificant. Furthermore, the effect of the diminishing return on power gain as turbines are added to the array will likely be reduced for the rotor when compared to the disc.

- For a large turbine array (high N_R and B_L) operating with a fixed tuning strategy in an inertia-dominated channel, an under-designed rotor ($c_x < c_{x,optimal}$) may be a more desirable option for power production. In contrast, an optimally-designed rotor ($c_x = c_{x,optimal}$) is expected to have the optimal performance in a drag-dominated channel. It has also been found that in most practical scenarios, with a realistic range of N_R, B_L and λ_0, the turbine drag will be sufficiently small such that an under-designed rotor may produce a similar amount of power compared to an optimally-designed rotor, though the former will experience lower thrust and therefore have lower structural costs and higher extraction efficiency. For the dynamic strategy, the choice of rotor design is complicated by the specific tuning requirement, as it varies throughout the tidal cycle.

9.1.2 Partial-width array operation and arrangement

- The power delivered by adopting a fixed or dynamic strategy has been shown to be higher than that achieved using the impatient strategy, which is similar to the result for the full-width array. With respect to turbine arrangement,

when the total turbine swept area is kept constant and the optimal tuning is applied with a fixed N_R, having the turbines at a closer spacing has been confirmed as a more effective arrangement than having the turbines spread uniformly across the channel (Nishino and Willden, 2012*b*). Furthermore, when B_L is fixed, an increase in array length (parallel arrangement) achieves greater performance improvement than deploying arrays in series (Garrett and Cummins, 2007). However, for a real site, this finding may not achieve the optimal outcome due to the varied kinetic energy distribution along the width of the channel, especially in a drag-dominated site.

- The predictions derived from coupling an analytical partial-width array model with a simple channel model are only partially supported by the 2D numerical simulations. The analytical model has been observed to underestimate the contribution of the local blockage effect on the available power, while overestimating the importance of tuning (fixed strategy relative to the impatient strategy). The poorest comparison between the 0D and 2D models has been observed when simulating an inertia-dominated channel, though the predictions of the analytical model have been found to closer align with the numerical model as λ_0 increases (Bonar et al., 2019). For realistic values of N_R and B_L, the 2D numerical model has suggested that additional power output can be achieved by densely packing turbines into a small fraction of the channel cross-section. In this regard, although the assumption of steady flow adopted by the analytical partial-array model of Nishino and Willden (2012*b*) should be treated with caution, their suggested array arrangement remains a useful tool.

- As observed in the case of a full-width array, for a partial-width turbine array with a fixed total turbine swept area, a greater relative importance in tuning,

when comparing the fixed strategy to the impatient strategy and again the dynamic strategy to the fixed strategy, is achieved with both increasing N_R and B_L. This enhancement in performance, and thus the necessity of tuning, is also seen for the partial-width case when compared to the corresponding full-width case with the same N_R and B_L for the dynamic strategy. As such, in both circumstances with a fixed N_R while increasing B_L (higher packing density and thus increasing local blockage effect) as well as fixed B_L while increasing N_R (transition from parallel to series configuration), the application of a dynamic strategy can further improve performance, though the strategy may introduce additional operational complexity and equipment costs. However, this enhancement, the dynamic and reversal boost, does not seem to provide enough power gain to lessen the disadvantage of the series configuration and the preference for a parallel configuration ultimately remains.

- Across all the different partial-width array arrangements, the effect of tuning, as in the full-width cases, has been observed to be relatively inconsequential between fixed and dynamic strategies for the realistic turbine representation. This is a worthwhile result as it is easier to operate using an impatient or fixed strategy rather than a dynamic strategy, which requires careful timing and controls to be implemented thus increasing the cost of power production.

9.1.3 Resource assessment correction

- It has been observed for a fully-blocked channel that the actuator disc tends to over-predict the available power compared to the tidal rotors for both fixed and dynamic strategies. The results obtained using the actuator disc tend to agree more with those from the rotor for low λ_0 and similarly for increasing N_R and decreasing B_L. However, for sufficiently large N_R and B_L operating using the dynamic strategy, as λ_0 approaches zero, the actuator disc approach

leads to substantial over-predictions, in comparsion with the rotor approach.

- For partial-width arrays, similarly to the fully-blocked channel configuration, the actuator disc consistently overestimates the available power when compared to the more realistic rotor for the range of array layouts modelled with both fixed and dynamic strategies. The level of over-prediction by the actuator disc has been found to increase with increasing B_L (though if the array size is large, the agreement is slightly better in comparison) as well as with decreasing N_R when B_L is fixed (transitioning from series to parallel array configuration).

- For the full, realistic range of B_L and N_R values considered in all simulations in this thesis (regardless of turbine arrangement or operation strategies), the power production determined using the rotor is typically 60-70% of that determined by the actuator disc. This finding can provide a useful reference for power generation adjustments between actuator disc and tidal rotor turbine representations. The correction can potentially be adopted for existing and ongoing tidal resource assessments with actuator discs, under the assumption that array configurations (i.e. N_R, B, layout etc.) and locations remain unchanged, only altering the turbine representations. Moreover, the rotor is also likely to cause less flow reduction and impact on the tidal environment due to the lower thrust it exerts on the flow.

9.2 Future Work

As this thesis primarily examines turbine array design and operation across different length scales, the future work is also considered in terms of these scales of interest: the device, the array, and the basin.

9.2.1 Device scale

Simplifications made in the blade element momentum theory typically result in a misrepresentation of the flow near the blade root and tip sections due to 3D flow effects. Additional difficulties may be experienced when operating in extreme off-design operation conditions. Correction factors derived from empirical and semi-empirical investigations are usually applied in BEMT to account for the root and tip losses as well as stall delay under strongly retarded flow conditions and turbulent wake states due to the high axial induction factor. These correction factors have not been fully investigated for tidal turbines given that a different formulation is required to account the effect of blockage. Further development of these correction models accompanied with robust numerical schemes will enable the BC-BEMT model to serve as a more useful and cost-efficient tool for tidal rotor modelling and design.

The power output and thrust applied to the flow from the tidal farm have been obtained using the low-order analytical turbine model presented in this thesis, and for the purpose of simplicity, this model excludes a number of realistic turbine characteristics, such as parasitic drag from support structures. The detailed description of real turbines and the response of the flow-field to energy extraction can be explored by using results extracted from high-fidelity 3D blade-resolved simulations or experimental results obtained under various design and off-design operation conditions (e.g. cut-in and out, power capping). The extracted data can be applied as performance input files (C_P and C_T curves or surfaces) for both analytical and numerical models to further improve the estimates of power output from arrays.

9.2.2 Array scale

As mentioned previously, the end effect — the lower power and thrust experienced by turbines towards the ends of a turbine array as a result of taking advantage of

the local blockage effect — is not explicitly accounted for in the two-scale separation model, and this effect may be more significant with higher B_L. An attempt was made by Cooke (2016) to account analytically for this effect by using a revised partial-width array model that is analogous to a BEM model. This method attempted to improve the estimate for the end effect but it failed to capture the reduction in thrust towards the edge turbine as it ignored the variation in incoming velocity and the flow diversion around the ends of the array. It may prove useful to incorporate a factor that is analogous to a tip loss correction within such a BEM analogy framework, which requires an additional experimental measurement, to gain better understanding of the flow mechanics around the edges of the array (Draper et al., 2013a). A similar extension can also be applied to the work of Nishino and Willden (2013), which improved the two-scale theory for short row arrays but still assumed that, across the array, all individual devices have identical performance and that the expansion factor of the local flow is uniform. In addition, for large multi-row arrays, the mixing rate m and the corresponding inter-row spacing have been shown by Nishino and Draper (2019) to be important in determining the optimal arrangement of turbines. As such, further amendment of the three-parameter (m, B, k) array model to include an additional wake mixing model would allow for the effect of wake mixing to be further investigated.

The DG-ADCIRC model has been used alongside a line momentum sink turbine modelling approach (smearing the turbine drag over an element) throughout this research to balance the model complexity and computational demands with accuracy. These methods have provided estimates for the array-scale effects but are unable to describe completely the interactions between the turbines and the flow (e.g. vortex formation and turbulent mixing). More detailed exploration of the local blockage effect can be accomplished by employing sophisticated modelling techniques such as 3D actuator line and blade-resolved RANS simulations or by performing exper-

iments with tidal rotors. Such simulations or experiments can be used to further investigate the local blockage effect with varied micro-siting configurations (in line versus staggered) and inter-row spacing.

9.2.3 Basin scale

As discussed in this thesis, the analytical combined partial-array model of Nishino and Willden (2012*b*) and Garrett and Cummins (2005) is incomplete due to the model not being able to fully capture some key physics involved in oscillatory flow. As such, in order to investigate partial-array behaviour under oscillatory flow, and to estimate the power generation as well as the optimum arrangement and operation of turbines within different channel dynamics, the formulation of a new theoretical framework would be a major development. With this consideration in mind, a new model may be formed by further extending the electrical analogy model of Draper el al., 2014a) to incorporate a common shear force or mass transfer term associated with the velocity gradient between the array-scale core and bypass flows as an additional tuning factor. This is done to replicate the amplitude and phase difference, as well as to describe the interaction (e.g. array-scale core and bypass flow mixing) between the two separated flows in the channel (Nishino and Draper, 2019).

There is also significant scope to improve the modelling techniques in order to better simulate the hydrodynamics for resource assessment at real sites. Through implementing the line momentum sink turbine scheme into more sophisticated numerical models such as a 3D sigma-layer or hybrid-sigma-layer model, additional flow effects can be investigated resulting in improved tidal stream energy assessments. This includes superior estimates of the hydrodynamic impacts, analysis of power extraction in vertically sheared flow, the ability to derive design conditions for extreme weather events, and better modelling of turbine wakes (with validation from higher-resolution numerical models and physical experiments). Furthermore,

the optimisation of a tidal array at a real candidate site currently provides many challenges in obtaining the optimal combination of key design parameters, such as the number of turbines and their installation cost, array arrangement, overall farm profit and levelised cost of energy, etc. Although the computation may presently be impractical, the combination of an efficient optimisation software (e.g. OpenTidalFarm) and an accurate model representation of both oscillating tidal flow and tidal rotors could achieve to create an effective optimisation tool. From an energy payback perspective, the target of the array design is to optimise the ratio of the embodied energy (total energy required for the manufacture, installation, maintenance and eventual decommission of the devices) to the energy produced. This can be achieved through improving the array performance (as discussed above) or extending the service life of the devices. Further investigation into the complete life cycle assessment of the devices may be required to highlight risk factors, improve long-term resource estimates and extend device lifespan (Douglas et al., 2008).

References

Adcock, T. A. A. (2012), On the Garrett & Cummins limit, *in* Proc. 1st Oxford Tidal Energy Workshop, Oxford, UK.

Adcock, T. A. A. and Draper, S. (2014), Power extraction from tidal channels - multiple tidal constituents, compound tides and overtides, *Renew. Energy* **63**, 797–806.

Adcock, T. A. A., Draper, S., Houlsby, G. T., Borthwick, A. G. L. and Serhadlıoğlu, S. (2013), The available power from tidal stream turbines in the Pentland Firth, *Proc. R. Soc. A* **469**(2157).

Adcock, T. A. A., Draper, S., Houlsby, G. T., Borthwick, A. G. L. and Serhadlıoğlu, S. (2014), Tidal stream power in the Pentland Firth – long-term variability, multiple constituents and capacity factor, *Proc. IMechE A: J. Power Energy* **228**(8), 854–861.

Adcock, T. A. A., Draper, S. and Nishino, T. (2015), Tidal power generation – a review of hydrodynamic modelling, *Proc. IMechE A: J. Power Energy* **229**(7), 755–771.

Afgan, I., McNaughton, J., Rolfo, S., Apsley, D. D., Stallard, T. and Stansby, P. (2013), Turbulent flow and loading on a tidal stream turbine by LES and RANS, *Int J. Heat Fluid Flow* **43**, 96–108.

Agnarsson, J., Sunde, M. and Ermilova, I. (2013), Parallel optimization in MATLAB, *Project in Computational Science Report, Department of Information Technology, Uppsala University, Sweden* .

Ahmadian, R. and Falconer, R. A. (2012), Assessment of array shape of tidal stream turbines on hydro-environmental impacts and power output, *Renew. Energy* **44**, 318–327.

Apsley, D. D., Stallard, T. and Stansby, P. K. (2018), Actuator-line CFD modelling of tidal-stream turbines in arrays, *J. Ocean Eng. and Mar. Energy* **4**(4), 259–271.

Bahaj, A. S., Molland, A. F., Chaplin, J. R. and Batten, W. M. (2007b), Power and thrust measurements of marine current turbines under various hydrodynamic flow conditions in a cavitation tunnel and a towing tank, *Renew. Energy* **32**(3), 407–426.

Bahaj, A. S., Myers, L. E., Thomson, M. D. and Jorge, N. (2007a), Characterising the wake of horizontal axis marine current turbines, *in* Proc. 7th European wave and tidal energy conference (EWTEC), p. 9.

Bai, L., Spence, R. R. G. and Dudziak, G. (2009), Investigation of the influence of array arrangement and spacing on tidal energy converter (TEC) performance using a 3-dimensional CFD model, *in* Proc. 8th European wave and tidal energy conference

(EWTEC), Uppsala, Sweden, pp. 654–660.

Bak, C., Johansen, J. and Andersen, P. B. (2006), Three-dimensional corrections of airfoil characteristics based on pressure distributions, *in* European Wind Energy Conference & Exhibition (EWEC), pp. 1–10.

Batten, W. M. J., Harrison, M. E. and Bahaj, A. S. (2013), Accuracy of the actuator disc-rans approach for predicting the performance and wake of tidal turbines, *Phil. Trans. R. Soc. A* **371**(1985), 20120293.

Belloni, C. S. (2013), Hydrodynamics of ducted and open-centre tidal turbines. DPhil Thesis, University of Oxford, UK.

Betz, A. (1920), Das Maximum der Theoretisch Möglichen Ausnützung des Windes durch Windmotoren, *Zeitschrift für das gesamte Turbinenwesen* **26**, 307–309.

Bian, C., Jiang, W., Pohlmann, T. and Sündermann, J. (2016), Hydrography-physical description of the Bohai Sea, *J. Coast. Res.* **74**(sp1), 1–12.

Black and Veatch (2005), Phase II. UK tidal stream energy resource assessment, *Carbon Trust Marine Energy Challenge* .

Blanchfield, J., Garrett, C., Wild, P. and Rowe, A. (2008), The extractable power from a channel linking a bay to the open ocean, *Proc. IMechE A: J. Power Energy* **222**(3), 289–297.

Blanckaert, K. and de Vriend, H. J. (2005), Turbulence characteristics in sharp open-channel bends, *Phys. Fluids* **17**(5), 055102.

Blunden, L. S. and Bahaj, A. S. (2006), Initial evaluation of tidal stream energy resources at Portland Bill, UK, *Renew. Energy* **31**(2), 121–132.

Blunden, L. S. and Bahaj, A. S. (2007), Tidal energy resource assessment for tidal stream generators, *Proc. IMechE A: J. Power Energy* **221**(2), 137–146.

Bonar, P. A. J. (2017), Toward best practice in the design of tidal turbine arrays. PhD Thesis, University of Edinburgh, UK.

Bonar, P. A. J., Chen, L., Schnabl, A. M., Venugopal, V., Borthwick, A. G. L. and Adcock, T. A. A. (2019), On the arrangement of tidal turbines in rough and oscillatory channel flow, *J. Fluid Mech.* **865**, 790–810.

Bonar, P. A. J., Schnabl, A. M., Lee, W.-K. and Adcock, T. A. A. (2018), Assessment of the Malaysian tidal stream energy resource using an upper bound approach, *J. Ocean Eng. and Mar. Energy* **4**(2), 99–109.

Borthwick, A. G. L. (2016), Marine renewable energy seascape, *Engineering* **2**(1), 69–78.

Borthwick, A. G. L. and Barber, R. W. (1992), River and reservoir flow modelling using the transformed shallow water equations, *Int. J. Numer. Methods Fluids* **14**(10), 1193–1217.

Boukhezzar, B., Lupu, L., Siguerdidjane, H. and Hand, M. (2007), Multivariable control strategy for variable speed, variable pitch wind turbines, *Renew. Energy* **32**(8), 1273–1287.

Buckland, H. C., Masters, I., Orme, J. A. C. and Baker, T. (2013), Cavitation inception and

simulation in blade element momentum theory for modelling tidal stream turbines, *Proc. IMechE A: J. Power Energy* **227**(4), 479–485.

Buhl, Jr., M. L. (2005), New empirical relationship between thrust coefficient and induction factor for the turbulent windmill state.

Bunya, S., Kubatko, E. J., Westerink, J. J. and Dawson, C. (2009), A wetting and drying treatment for the Runge–Kutta discontinuous Galerkin solution to the shallow water equations, *Comput Methods Appl Mech Eng.* **198**(17-20), 1548–1562.

Burton, T., Jenkins, N., Sharpe, D. and Bossanyi, E. (2011), *Wind energy handbook*, John Wiley & Sons.

Cao, B., Willden, R. H. J. and Vogel, C. R. (2018), Effects of blockage and freestream turbulence intensity on tidal rotor design and performance, *in* Proc. 3rd International Conference on Renewable Energies Offshore (RENEW 2018), Lisbon, Portugal, CRC Press, p. 127.

Chaviaropoulos, P. K. and Hansen, M. O. L. (2000), Investigating three-dimensional and rotational effects on wind turbine blades by means of a quasi-3D Navier-Stokes solver, *J. Fluid Eng.* **122**(2), 330–336.

Chen, Y., Lin, B., Lin, J. and Wang, S. (2015), Effects of stream turbine array configuration on tidal current energy extraction near an island, *Computers & geosciences* **77**, 20–28.

Chen, Y., Lin, B., Lin, J. and Wang, S. (2017), Experimental study of wake structure behind a horizontal axis tidal stream turbine, *Appl. Energy* **196**, 82–96.

Churchfield, M. J., Li, Y. and Moriarty, P. J. (2013), A large-eddy simulation study of wake propagation and power production in an array of tidal-current turbines, *Phil. Trans. R. Soc. A* **371**(1985), 20120421.

Coles, D. S., Blunden, L. S. and Bahaj, A. S. (2017b), Assessment of the energy extraction potential at tidal sites around the channel islands, *Energy* **124**, 171–186.

Coles, D. S., Kramer, S., Piggott, M., Avdis, A. and Angeloudis, A. (2017a), Optimisation of tidal stream turbine arrays within Alderney Race.

Cooke, S. (2016), Enhanced array design for tidal power generation. DPhil Thesis, University of Oxford, UK.

Creed, M. J., Draper, S., Nishino, T. and Borthwick, A. G. L. (2017), Flow through a very porous obstacle in a shallow channel, *Proc. R. Soc. A* **473**(2200), 20160672.

Dick, C. G., Tromble, E. M., Dresback, K. M. and Kolar, R. L. (2013), Implementation and analysis of a partial-element wetting and drying framework for generalized wave continuity equation-based hydrodynamic models, *Int. J. Numer. Methods Fluids* **72**(10), 1015–1033.

Divett, T., Vennell, R. and Stevens, C. (2013), Optimization of multiple turbine arrays in a channel with tidally reversing flow by numerical modelling with adaptive mesh, *Phil. Trans. R. Soc. A* **371**(1985), 20120251.

Divett, T., Vennell, R. and Stevens, C. (2014), Channel scale optimisation of large tidal

turbine arrays in packed rows using large eddy simulations with adaptive mesh, *in* Proc. 2nd Asian Wave and Tidal Energy Conference, Tokyo, Japan.

Douglas, C. A., Harrison, G. P. and Chick, J. P. (2008), Life cycle assessment of the Seagen marine current turbine, *Proc. Inst. Mech. Eng. Part M J. Eng. Marit. Environ.* **222**(1), 1–12.

Draper, S. (2011), Tidal stream energy extraction in coastal basins. DPhil Thesis, University of Oxford, UK.

Draper, S., Adcock, T. A. A., Borthwick, A. G. L. and Houlsby, G. T. (2014b), Estimate of the tidal stream power resource of the Pentland Firth, *Renew. Energy* **63**, 650–657.

Draper, S., Borthwick, A. G. L. and Houlsby, G. T. (2013a), Energy potential of a tidal fence deployed near a coastal headland, *Phil. Trans. R. Soc. A* **371**(1985), 20120176.

Draper, S., Houlsby, G. T., Oldfield, M. L. G. and Borthwick, A. G. L. (2010), Modelling tidal energy extraction in a depth-averaged coastal domain, *IET Renew. Power Gener.* **4**(6), 545.

Draper, S. and Nishino, T. (2014), Centred and staggered arrangements of tidal turbines, *J. Fluid Mech.* **739**, 72–93.

Draper, S., Nishino, T. and Adcock, T. A. A. (2014a), Turbine blockage in non-uniform flow, *in* Proc. 19th Australasian Fluid Mechanics Conference, Melbourne, Australia.

Draper, S., Stallard, T., Stansby, P., Way, S. and Adcock, T. A. A. (2013b), Laboratory scale experiments and preliminary modelling to investigate basin scale tidal stream energy extraction, *in* Proc. 10th European Wave and Tidal Energy Conference (EWTEC), Aalborg, Denmark.

Du, Z. and Selig, M. (1998), A 3-D stall-delay model for horizontal axis wind turbine performance prediction, *in* 1998 American Society of Mechanical Engineers Wind Energy Symposium, p. 21.

Dumitrescu, H., Cardoş, V. and Dumitrache, A. (2007), Modelling of inboard stall delay due to rotation, *in* Journal of Physics: Conference Series, Vol. 75, IOP Publishing, p. 012022.

Egbert, G. D., Bennett, A. F. and Foreman, M. G. G. (1994), TOPEX/POSEIDON tides estimated using a global inverse model, *J. Geophys. Res.: Oceans* **99**(C12), 24821–24852.

Eggleston, D. M. and Stoddard, F. (1987), Wind turbine engineering design.

EMEC (2009), "Assessment of Tidal Energy Resource". Marine Renewable Energy Guides.

Falconer, R. A. (1993), An introduction to nearly-horizontal flows, *Coastal, Estuarial and Harbour Engineers's reference book, E and FN Spon Ltd, London* pp. 27–36.

Fang, G., Wang, Y., Wei, Z., Choi, B. H., Wang, X. and Wang, J. (2004), Empirical cotidal charts of the Bohai, Yellow, and East China Seas from 10 years of TOPEX/Poseidon altimetry, *J. Geophys. Res.: Oceans* **109**(C11).

Flores Mateos, L. (2019), Tidal stream energy assessment with and without a shock capture scheme-Incorporating a non-constant thrust force coefficient, PhD thesis, National University of Ireland, Galway, Republic of Ireland.

Froude, R. E. (1889), On the part played in propulsion by differences of fluid pressure, *Transactions of the Institude of Naval Architects* **30**, 390–405.

Funke, S. W., Farrell, P. E. and Piggott, M. D. (2014), Tidal turbine array optimisation using the adjoint approach, *Renew. Energy* **63**, 658–673.

Funke, S. W., Kramer, S. C. and Piggott, M. D. (2016), Design optimisation and resource assessment for tidal-stream renewable energy farms using a new continuous turbine approach, *Renew. Energy* **99**, 1046–1061.

Gao, C. and Adcock, T. A. A. (2017), On the tidal resonance of the Bristol Channel, *27th International Journal of Offshore and Polar Engineering (ISOPE 2017), San Francisco, USA* .

Garrett, C. and Cummins, P. (2004), Generating power from tidal currents, *J. Waterw Port Coast* **130**(3), 114–118.

Garrett, C. and Cummins, P. (2005), The power potential of tidal currents in channels, *Proc. R. Soc. A* **461**(2060), 2563–2572.

Garrett, C. and Cummins, P. (2007), The efficiency of a turbine in a tidal channel, *J. Fluid Mech.* **588**, 243–251.

Garrett, C. and Cummins, P. (2008), Limits to tidal current power, *Renew. Energy* **33**(11), 2485–2490.

Glauert, H. (1935), Airplane propellers, *in* Aerodynamic theory, Springer, Berlin, Heidelberg, pp. 169–360.

Glauert, H. (1983), *The elements of aerofoil and airscrew theory*, Cambridge University Press.

Gong, X., Li, Y. and Lin, Z. (2018), Effects of blockage, arrangement, and channel dynamics on performance of turbines in a tidal array, *J. Renew. Sust. Energy* **10**, 014501.

Goss, Z. L., Kramer, S. C., Avdis, A., Cotter, C. J. and Piggott, M. D. (2019), Variations in the optimal design of a tidal stream turbine array with costs, *in* Proc. 7th Oxford Tidal Energy Workshop, Oxford, UK.

Guntur, S. (2013), A detailed study of the rotational augmentation and dynamic stall phenomena for wind turbines. PhD Thesis, Technical University of Denmark, Denmark.

Harrison, M. E., Batten, W. M. J., Myers, L. E. and Bahaj, A. S. (2010), Comparison between CFD simulations and experiments for predicting the far wake of horizontal axis tidal turbines, *IET Renew. Power Gener.* **4**(6), 613–627.

Hau, E. and von Renouard, H. (2003), *Wind turbines: fundamentals, technologies, application, economics*, Springer, Berlin, Heidelberg.

Hesthaven, J. S. and Warburton, T. (2007), *Nodal discontinuous Galerkin methods: algorithms, analysis, and applications*, Springer Science & Business Media.

Himmelskamp, H. (1945), Profile investigations on a rotating airscrew. PhD Thesis, Goettingen University, Germany.

Hooper, T. and Austen, M. (2013), Tidal barrages in the UK: Ecological and social impacts,

potential mitigation, and tools to support barrage planning, *Renew. Sust. Energy Rev.* **23**, 289–298.

Hou, F., Bao, X., Li, B. and Liu, Q. (2015), The assessment of extactable tidal energy and the effect of tidal energy turbine deployment on the hydrodynamics in Zhoushan, *Acta Oceanologica Sinica* **34**(5), 86–91.

Houlsby, G. T., Draper, S. and Oldfield, M. L. G. (2008), Application of linear momentum actuator disc theory to open channel flow, Technical report, reportno. OUEL 2296/08, Department of Engineering Science, University of Oxford, UK.

Jacobs, C. T., Piggott, M. D., Kramer, S. C. and Funke, S. W. (2016), On the validity of tidal turbine array configurations obtained from steady-state adjoint optimisation, *European Congress on Computational Methods in Applied Sciences and Engineering (ECCOMAS), Crete, Greece* .

Joukowsky, N. E. (1920), Windmill of the NEJ Type, *Transactions of the Central Institute for Aero-Hydrodynamics of Moscow* **1**, 57.

Kärnä, T., Kramer, S. C., Mitchell, L., Ham, D. A., Piggott, M. D. and Baptista, A. M. (2017), Thetis coastal ocean model: discontinuous Galerkin discretization for the three-dimensional hydrostatic equations, *arXiv preprint arXiv:1711.08552* .

Karsten, R. H., McMillan, J. M., Lickley, M. J. and Haynes, R. D. (2008), Assessment of tidal current energy in the Minas Passage, Bay of Fundy, *Proc. IMechE A: J. Power Energy* **222**(5), 493–507.

Kreitmair, M. J., Draper, S., Borthwick, A. G. L. and van den Bremer, T. S. (2019), The effect of uncertain bottom friction on estimates of tidal current power, *R Soc Open Sci.* **6**(1), 180941.

Kubatko, E. J., Bunya, S., Dawson, C. and Westerink, J. J. (2009), Dynamic p-adaptive Runge–Kutta discontinuous Galerkin methods for the shallow water equations, *Comput Methods Appl Mech Eng.* **198**(21-26), 1766–1774.

Kubatko, E. J., Dawson, C. and Westerink, J. J. (2008), Time step restrictions for Runge–Kutta discontinuous Galerkin methods on triangular grids, *J. Comput. Phys.* **227**(23), 9697–9710.

Kubatko, E. J., Westerink, J. J. and Dawson, C. (2006), hp discontinuous Galerkin methods for advection dominated problems in shallow water flow, *Comput Methods Appl Mech Eng.* **196**(1-3), 437–451.

Lagarias, J. C., Reeds, J. A., Wright, M. H. and Wright, P. E. (1998), Convergence properties of the Nelder-Mead simplex method in low dimensions, *Society for Industrial and Applied Mathematics Journal on optimization* **9**(1), 112–147.

Larsen, L. H., Cannon, G. A. and Choi, B. H. (1985), East China Sea tide currents, *Cont. Shelf Res.* **4**(1-2), 77–103.

Lavaroni, L., Watson, S. J., Cook, M. J. and Dubal, M. R. (2014), A comparison of actuator disc and BEM models in CFD simulations for the prediction of offshore wake losses, *in*

J. of Phys.: Conference Series, Vol. 524, IOP Publishing, p. 012148.

Le Provost, C., Genco, M.-L. and Lyard, F. (1995), Modeling and predicting tides over the World Ocean, *Coast. Estuar. Stud.* **47**, 175–201.

Lewis, M., Neill, S. P., Robins, P. E. and Hashemi, M. R. (2015), Resource assessment for future generations of tidal-stream energy arrays, *Energy* **83**, 403–415.

Li, D., Wang, S. and Yuan, P. (2010), An overview of development of tidal current in China: energy resource, conversion technology and opportunities, *Renew. Sust. Energy Rev.* **14**(9), 2896–2905.

Li, Y., Zhang, H., Tang, C., Zou, T. and Jiang, D. (2016), Influence of rising sea level on tidal dynamics in the Bohai Sea, *J. Coast. Res.* **74**(sp1), 22–31.

Lindenburg, C. (2004), Modelling of rotational augmentation based on engineering considerations and measurements, *in* European Wind Energy Conference, London, UK.

Luettich, R. A. and Westerrink, J. J. (2000), ADCIRC user manual: a (parallel) advanced circulation model for oceanic, coastal and estuarine waters, *University of North Carolina at Chapel Hill, Chapel Hill, USA and University of Notre Dame, Notre Dame, USA* .

Marshall, J. and Plumb, R. A. (1989), *Atmosphere, ocean and climate dynamics: an introductory text*, Academic Press.

Martin-Short, R., Hill, J., Kramer, S. C., Avdis, A., Allison, P. A. and Piggott, M. D. (2015), Tidal resource extraction in the Pentland Firth, UK: potential impacts on flow regime and sediment transport in the Inner Sound of Stroma, *Renew. Energy* **76**, 596–607.

McAdam, R. A. (2011), Studies into the technical feasibility of the transverse horizontal axis water turbine. DPhil Thesis, University of Oxford, UK.

McIntosh, S. C., Fleming, C. F. and Willden, R. H. J. (2011), Embedded RANS-BEM tidal turbine design, *in* Proc. 9th European Wave and Tidal Energy Conference (EWTEC), Southampton, UK.

McNaughton, J. (2013), Turbulence modelling in the near-field of an axial flow tidal turbine in code_saturne, PhD thesis, University of Manchester, UK.

McNaughton, J., Cao, B., Vogel, C. R. and Willden, R. H. J. (2019), Experimental study on interactions between two closely spaced rotors, *in* Proc. 7th Oxford Tidal Energy Workshop, Oxford, UK.

Medeiros, S. C. and Hagen, S. C. (2013), Review of wetting and drying algorithms for numerical tidal flow models, *Int. J. Numer. Methods Fluids* **71**(4), 473–487.

MeyGen Ltd. (2014), Decommissioning programme, Technical report.

Miglio, E., Quarteroni, A. and Saleri, F. (1999), Finite element approximation of quasi-3d shallow water equations, *Comput Methods Appl Mech Eng.* **174**(3-4), 355–369.

Muchala, S. (2018), Impact of tidal turbine support structures on realizable turbine farm power. DPhil Thesis, University of Oxford, UK.

Muchala, S. and Willden, R. H. J. (2018), Influence of support structures on tidal turbine power output, *J. Fluids Struct.* **83**, 27–39.

Mycek, P., Gaurier, B., Germain, G., Pinon, G. and Rivoalen, E. (2014), Experimental study of the turbulence intensity effects on marine current turbines behaviour. Part II: Two interacting turbines, *Renew. Energy* **68**, 876–892.

Nishino, T. (2016), Two-scale momentum theory for very large wind farms, *in* Journal of Physics: Conference Series, Vol. 753, IOP Publishing, p. 032054.

Nishino, T. and Draper, S. (2015), Local blockage effect for wind turbines, *in* Journal of Physics: Conference Series, Vol. 625, IOP Publishing, p. 012010.

Nishino, T. and Draper, S. (2019), Theoretical prediction of the efficiency of very large turbine arrays: combined effects of local blockage and wake mixing, *in* Proc. 7th Oxford Tidal Energy Workshop, Oxford, UK.

Nishino, T. and Willden, R. H. J. (2012*a*), Effects of 3-D channel blockage and turbulent wake mixing on the limit of power extraction by tidal turbines, *Int J. Heat Fluid Flow* **37**, 123–135.

Nishino, T. and Willden, R. H. J. (2012*b*), The efficiency of an array of tidal turbines partially blocking a wide channel, *J. Fluid Mech.* **708**, 596–606.

Nishino, T. and Willden, R. H. J. (2013), Two-scale dynamics of flow past a partial cross-stream array of tidal turbines, *J. Fluid Mech.* **730**, 220–244.

Nuernberg, M. and Tao, L.-B. (2018), Three dimensional tidal turbine array simulations using OpenFOAM with dynamic mesh, *Ocean Eng.* **147**, 629–646.

Olczak, A., Stallard, T., Feng, T. and Stansby, P. K. (2016), Comparison of a RANS blade element model for tidal turbine arrays with laboratory scale measurements of wake velocity and rotor thrust, *J. Fluids Struct.* **64**, 87–106.

Owen, A. (1980), The tidal regime of the Bristol Channel: a numerical modelling approach, *Geophys. J. Int.* **62**(1), 59–75.

Pearce, N. (2005), Worldwide tidal current energy developments and opportunities for Canada's Pacific coast, *Int. J. Green Energy* **2**(4), 365–386.

Perez-Campos, E. and Nishino, T. (2015), Numerical validation of the two-scale actuator disc theory for marine turbine arrays, *Proc. 11th European wave and tidal energy conference (EWTEC), Nantes, France* .

Pugh, D. T. (1987), *Tides, surges and mean sea level*, John Wiley and Sons Inc., New York, NY.

Rahman, A., Venugopal, V. and Thiebot, J. (2018), On the accuracy of three-dimensional actuator disc approach in modelling a large-scale tidal turbine in a simple channel, *Energies* **11**(8), 2151.

Rankine, W. J. M. (1865), On the mechanical principles of the action of propellers, *Transaction of the Institute of Naval Architects* **6**, 13–19.

Rodi, W. (1984), *Turbulence models and their application in hydrodynamics—A state of the art review*, Univ. of Karlsruhe, Karlsruhe, Germany.

Rourke, F. O., Boyle, F. and Reynolds, A. (2010), Tidal energy update 2009, *Appl. Energy*

87(2), 398–409.

Schluntz, J. (2014), Tidal turbine array modelling. DPhil Thesis, University of Oxford, UK.

Schluntz, J. and Willden, R. H. J. (2015), The effect of blockage on tidal turbine rotor design and performance, *Renew. Energy* **81**, 432–441.

Schmitz, S. and Maniaci, D. C. (2016), Methodology to determine a tip-loss factor for highly loaded wind turbines, *AIAA Journal* **55**(2), 341–351.

Schnabl, A. M., Moreira, T. M., Wood, D., Kubatko, E., Houlsby, G. T. and Adcock, T. A. A. (2019), Implementation of tidal stream turbines and tidal barrage structures in DG-SWEM, *in* ASME 38th International Conference on Ocean, Offshore and Arctic Engineering, Glasgow, UK.

Serhadlıoğlu, S. (2014), Tidal stream resource assessment of the Anglesey Skerries and the Bristol Channel. DPhil Thesis, University of Oxford, UK.

Serhadlıoğlu, S., Adcock, T. A. A., Houlsby, G. T., Draper, S. and Borthwick, A. G. L. (2013), Tidal stream energy resource assessment of the Anglesey Skerries, *Int. J. Mar. Energy* **3**, e98–e111.

Shen, W. Z., Mikkelsen, R., Sørensen, J. N. and Bak, C. (2005), Tip loss corrections for wind turbine computations, *Wind Energy* **8**(4), 457–475.

Shu, C. W. (1987), TVB uniformly high-order schemes for conservation laws, *Mathematics of Computation* **49**(179), 105–121.

Smeaton, M., Vennell, R. and Harang, A. (2016), The effect of channel constriction on the potential for tidal stream power, *Renew. Energy* **99**, 45–56.

Snel, H. and van Holten, T. (1995), Review of recent aerodynamic research on wind turbines with relevance, *AGARD Report CP 552* pp. 1–11.

Sørensen, J. N. and Shen, W. Z. (2002), Numerical modeling of wind turbine wakes, *J. Fluid Eng.* **124**(2), 393–399.

Soulsby, R. (1997), *Dynamics of marine sands: a manual for practical applications*, Thomas Telford.

Stansby, P. K. (2003), A mixing-length model for shallow turbulent wakes, *J. Fluid Mech.* **495**, 369–384.

Stansby, P. K. (2006), Limitations of depth-averaged modeling for shallow wakes, *J. Hydraul Eng.* **132**(7), 737–740.

Su, M., Yao, P., Wang, Z.-B., Zhang, C.-K. and Stive, M. J. F. (2015), Tidal wave propagation in the Yellow Sea, *Coast. Eng. J.* **57**(03), 1550008.

Sun, X., Chick, J. P. and Bryden, I. G. (2008), Laboratory-scale simulation of energy extraction from tidal currents, *Renew. Energy* **33**(6), 1267–1274.

Sutherland, G., Foreman, M. G. G. and Garrett, C. (2007), Tidal current energy assessment for Johnstone Strait, Vancouver Island, *Proc. IMechE A: J. Power Energy* **221**(2), 147–157.

Teng, F., Fang, G.-H., Wei, Z.-X., Xu, X.-Q., Cui, X.-M. and Wu, D. (2016), Tidal sim-

ulation in Chezy-type and generalized Manning-type friction for Chinese Eastern Shelf Seas, *Oceanologia et Limnologia Sinica* **P731.23**.

Thongam, J. S. and Ouhrouche, M. (2011), MPPT control methods in wind energy conversion systems, *in* Fundamental and advanced topics in wind power, IntechOpen.

Turnock, S. R., Phillips, A. B., Banks, J. and Nicholls-Lee, R. (2011), Modelling tidal current turbine wakes using a coupled RANS-BEMT approach as a tool for analysing power capture of arrays of turbines, *Ocean Eng.* **38**(11-12), 1300–1307.

Uihlein, A. and Magagna, D. (2016), Wave and tidal current energy - a review of the current state of research beyond technology, *Renew. Sust. Energy Rev.* **58**, 1070–1081.

Vennell, R. (1998), Oscillating barotropic currents along short channels, *J. Phys. Oceanogr.* **28**(8), 1561–1569.

Vennell, R. (2010), Tuning turbines in a tidal channel, *J. Fluid Mech.* **663**, 253–267.

Vennell, R. (2011), Tuning tidal turbines in-concert to maximise farm efficiency, *J. Fluid Mech.* **671**, 587–604.

Vennell, R. (2012), The energetics of large tidal turbine arrays, *Renew. Energy* **48**(C), 210–219.

Vennell, R. (2016), An optimal tuning strategy for tidal turbines, *Proc. R. Soc. A* **472**(2195), 20160047.

Vennell, R. and Adcock, T. A. A. (2014), Energy storage inherent in large tidal turbine farms, *Proc. R. Soc. A* **470**(2166), 20130580.

Vennell, R., Funke, S., Draper, S., Stevens, C. and Divett, T. (2015), Designing large arrays of tidal turbines: A synthesis and review, *Renew. Sust. Energy Rev.* **41**, 454–472.

Vogel, C. R. (2014), Theoretical limits to tidal stream energy extraction. DPhil Thesis, University of Oxford, UK.

Vogel, C. R. and Willden, R. H. J. (2018), Designing multi-rotor tidal turbine fences, *Int. Mar. Energy J.* **1**(1), 61–70.

Vogel, C. R., Willden, R. H. J. and Houlsby, G. T. (2013), A correction for depth-averaged simulations of tidal turbine arrays, *in* Proc. 10th European wave and tidal energy conference (EWTEC), Aalborg, Denmark.

Vogel, C. R., Willden, R. H. J. and Houlsby, G. T. (2018), Blade element momentum theory for a tidal turbine, *Ocean Eng.* **169**, 215–226.

Vogel, C. R., Willden, R. H. J. and Houlsby, G. T. (2019), Tidal stream turbine power capping in a head-driven tidal channel, *Renew. Energy* **136**, 491–499.

Walters, R. A., Tarbotton, M. R. and Hiles, C. E. (2013), Estimation of tidal power potential, *Renew. Energy* **51**, 255–262.

Wang, T. and Adcock, T. A. A. (2018), Power and Thrust Capping of Tidal Stream Turbines: A Case Study of the Pentland Firth, *in* 37th International Conference on Ocean, Offshore and Arctic Engineering, Madrid, Spain.

Wang, T. and Adcock, T. A. A. (2019), Combined power and thrust capping in the design

of tidal turbine farms, *Renew. Energy* **133**, 1247 – 1256.

Wang, Z.-F., Zhou, L.-M., Zhang, G.-B. and Wang, A.-F. (2010), Tidal stream energy assessment in specific channels of Zhoushan sea area, *Periodical of Ocean University of China* **8**(005).

Whelan, J. I., Graham, J. M. R. and Peiró, J. (2009), A free-surface and blockage correction for tidal turbines, *J. Fluid Mech.* **624**, 281–291.

White, F. M. (2009), *Fluid Mechanics*, McGraw Hill Publishers.

Willden, R. H. J., Nishino, T. and Schluntz, J. (2014), Tidal stream energy: Designing for blockage, *3rd Oxford Tidal Energy Workshop, Oxford, UK* .

Wimshurst, A. (2018), Tip flow corrections for horizontal axis wind and tidal turbine rotors. DPhil Thesis, University of Oxford, UK.

Wimshurst, A. and Willden, R. H. J. (2016*a*), Computational analysis of blockage designed tidal turbine rotors, *Proc. 2rd International Conference on Renewable Energies Offshore (RENEW 2016), Lisbon, Portugal* pp. 587–597.

Wimshurst, A. and Willden, R. H. J. (2016*b*), Validation of an actuator line method for tidal turbine rotors, *in* 26th International Ocean and Polar Engineering Conference, Rhodes, Greece.

Wimshurst, A. and Willden, R. H. J. (2017), Analysis of a tip correction factor for horizontal axis turbines, *Wind Energy* **20**(9), 1515–1528.

Wright, J., Colling, A. and Park, D. (1999), *Waves, tides and shallow-water processes*, Gulf Professional Publishing.

Wu, H., Wu, Y.-N., Bai, Y. and Wu, G.-W. (2017), Reviews of Resource Assessment on Tidal Current Energy of China, *Proc. 2nd 2016 International Conference on Sustainable Development (ICSD), Shaanxi, China* .

Wu, H., Zhao, S. M., Zhang, S., Wang, X. and Ma, Z.-Z. (2011), Preliminary assessment of tidal energy in Lao Tieshan channel, *Mar. Sci. Bull.* **30**(3), 310–314.

Wu, H., Zhao, S., Xu, H. F. and Zhang, Z. H. (2010), Preliminary Assessment of Tidal Current Energy on Chengshantou Area, *Ocean Technology* **29**(3), 98–100.

Xu, H., Deng, G., Li, Y., Wang, X., Wu, H., Zhou, Q. and Jiang, B. (2016), Numerical simulation for tidal current turbine siting metrics of Zhoushan Archipelago, *in* OCEANS 2016-Shanghai, IEEE.

Yang, H.-Y., Chen, B., Barter, M., Piersma, T., Zhou, C.-F., Li, F.-S. and Zhang, Z.-W. (2011), Impacts of tidal land reclamation in Bohai Bay, China: Ongoing losses of critical Yellow Sea waterbird staging and wintering sites, *Bird Conserv. Int.* **21**(3), 241–259.

Yao, Z., He, R., Bao, X., Wu, D. and Song, J. (2012), M 2 tidal dynamics in Bohai and Yellow Seas: a hybrid data assimilative modeling study, *Ocean Dyn.* **62**(5), 753–769.

Yu, Z., Zhang, J., Zhai, Y., Zhang, T. and Zheng, J. (2017), Numerical hydrodynamics study around turbine array of tidal stream farm in Zhoushan, China, *Journal of Ocean University of China* **16**(4), 703–708.

Zhang, H., Li, Y., Zou, T. and Tang, C. (2014a), Interaction between coastline change and tidal system of the Bohai Sea, *2014 Ocean Sciences Meeting, Honolulu, HI, USA* .

Zhang, Y.-L., Lin, Z. and Liu, Q.-L. (2014b), Marine renewable energy in China: Current status and perspectives, *Water Science and Engineering* **7**(3), 288–305.

Zheng, J., Dai, P. and Zhang, J. (2015), Tidal stream energy in China, *Procedia Engineering* **116**, 880–887.

Appendix A

Power Capping

In order both to facilitate direct comparison between theoretical models that predict maximum power capture and to achieve simplicity, many practical considerations have been neglected in this thesis. One such key consideration is power capping. Fully maximising the time-averaged available power from a tidal turbine array is ideal but also generally infeasible in terms of economic viability since the maximum kinetic energy flux is only experienced over a short period of time. Designing for that condition will require particularly high-capacity electric cables and generators, as well as a robust design of turbine structure, which are not utilised efficiently for most of the time. In practice, the application of a 'power cap' enables a suitable and economical compromise between adequate power generation and affordability (Wang and Adcock, 2019). Thus, power capping plays an important role in the estimation of realistic maximum available power and the establishment of optimal tuning strategies. During rated power operation, the control of turbines is achieved by tuning the rotor to move away from the point of the peak power coefficient. It can be inferred from the discussion in Chapter 4 that, for a tidal rotor with realistic performance characteristics, it may have different power capping operations for fixed and dynamic tuning strategies when compared to the actuator disc model used

in other research (e.g. Adcock et al., 2014; Vennell, 2016; Wang and Adcock, 2019) and will therefore result in different capacity factors (defined below). This suggests that when investigating power capping strategies in this work, it is informative to analyse the difference between the actuator disc and the tidal rotor.

A common power capping strategy for FP turbines is to vary the rotational speed of the rotor, which can be achieved by using over-speed or under-speed control mechanisms (Vogel et al., 2018). As discussed by Adcock et al. (2014), the under-speed control is likely to be the preferred option as the structure would experience less fatigue loading and the likelihood of cavitation is reduced when compared to over-speed control. Alternatively, with a VP turbine, a blade pitch angle adjustment to feathering can achieve a similar power capping result; whilst this may be a more desirable option due to the low turbine loading and torque stability, by adding to the complexity and computational time, the inclusion of the VP mechanism in a dynamic strategy may limit the number of idealised scenarios that can be explored. As this mechanism also has a higher capital cost and risk of failure (Vogel, 2014), VP rotors will not be considered further here. With the actuator disc, a similar approach has typically been adopted by increasing its value of α_4 to achieve power capping.

Actuator disc and BC-BEMT models have been used by the author to explore the effect of power capping controls on the performance of porous discs and tidal rotors, respectively. If the flow through the turbine at any time over the tidal cycle leads to the power exceeding the designated rated power $P_{av,rated}$, the turbine characteristics (α_4 and TSR for the disc and rotor, respectively) are altered accordingly to maintain the $P_{av,rated}$, forming a flat power-capping zone within the power curve. Following the work by Wang and Adcock (2019), a linear approximated root finding method is implemented to accelerate the computing when determining the turbine characteristics within the power capping zone. It is worth noting that the im-

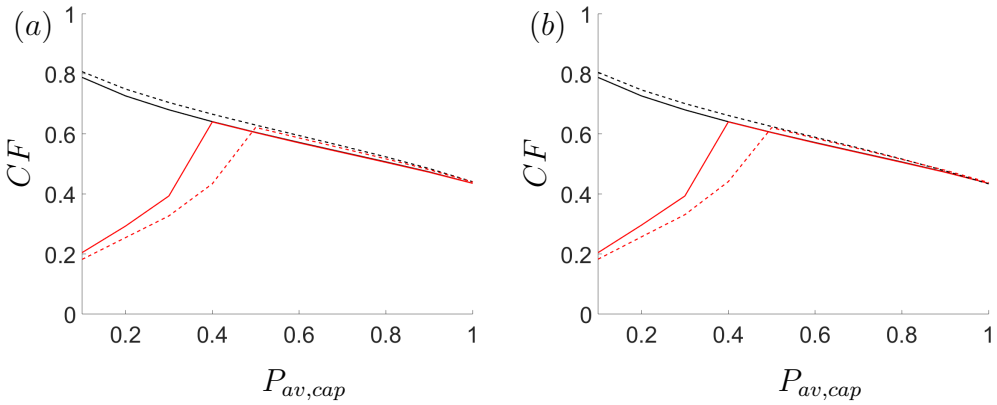

Figure A.1: Variations in the capacity factor with the normalised rated power $P_{av,cap}$ for $\lambda_0 = 1$, with: (a) fixed tuning strategy, and; (b) dynamic tuning strategy, for one (solid lines) and five (dashed lines) rows of actuator discs (black lines) and FP rotors (red lines) in moderately blocked ($B = 0.16$) flow.

plication of power capping in a real tidal channel site, as highlighted by Wang and Adcock (2018), is further complicated due to the variation in flow velocity along the channel cross-section and with varying water depth. This means that certain turbines across the array will likely be capped more often than others or at different times.

Figure A.1 presents a comparison of the capacity factor between actuator discs and tidal rotors, conducted in an idealised 0D channel based on the Pentland Firth for both fixed and dynamic tuning strategies. The value of $P_{av,rated}$ is normalised by an uncapped maximum power to define a normalised rated power, $P_{av,cap}$. It should be noted that the large divergence observed when $P_{av,cap}$ is small is due to the fact that the rotor is set to fail below certain values of TSR since the inner limitation of the BC-BEMT does not allow the rotor to reach the practically-zero C_T value of the disc. Apart from this difference, the discrepancy between the actuator disc and tidal rotor are almost indistinguishable, suggesting the principle power capping behaviour remains similar between the two turbine representations, with both tuning strategies. It is therefore unsurprising that the available power when using tidal rotors is still 60-70% of the actuator disc after the implementation of power capping.

Furthermore, it is determined that the importance of tuning is reduced (excluding the tuning operations governed by the power capping process) for both turbine representations with the inclusion of power capping. This is evidenced by the stronger similarities observed between the tuning curves of the impatient and fixed strategies as well as the fixed and dynamic strategies outside of the power capping regime, which is more prominent with decreasing $P_{av,cap}$. Therefore, there is greater confidence in the findings summarised in the conclusions of Section 9.1, which should still be generally applicable with the implementation of power capping.

Appendix B

Potential Implication for a Real Site

This section examines the implication of the foregoing findings summarised in Chapter 9 on a actual tidal stream power site, the Pentland Firth, which separates the mainland of Scotland from the Orkney Islands, and provides general recommendations on the optimal tidal array design and operation. The Pentland Firth experiences a significant phase difference between its western and eastern ends as the tide sweeps in from the Atlantic Ocean to the North Sea, funnelling through the Firth. This drives remarkably fast tidal currents with peak velocity exceeding 5 m/s, making the Pentland Firth a location of interest for tidal energy extraction and accompanying research (Adcock et al., 2013). A number of previous studies investigating the potential for power generation from the Pentland Firth have been undertaken with widely varying assessments of the resources. Perhaps the most comprehensive study of this location was performed by Adcock et al. (2013) and Draper et al. (2014b), investigating the power output using the method of an array arrangement parametric study. Specifically, their investigation used a similar depth-averaged numerical model as the one adopted in this thesis to analyse the introduction of turbine rows placed either across the whole Pentland Firth with a full-width array between mainland Scotland and Hoy (referenced as 'A') or as a series of arrays in sub-channels within the Firth. These sub-channels are formed

by the two islands of Stroma and Swona in between mainland Scotland and South Ronaldsay, as well as between the island Muckle Skerry and South Ronaldsay (for convenience, the four sub-channels are referenced as 'B', 'C', 'D' and 'E'). All channels are shown in Figure B.1, together with the prediction of the major axis currents of the M_2 tidal constituent across the Firth.

B.1 Arrays spanning the Pentland Firth

For the range of N_R and B_L simulated by Adcock et al. (2013), the application of a dynamic strategy may suggest that $\overline{P}_{av}$ is likely to increase with an expected dynamic boost of between $\approx$ 3-7%, while it may also generate a less severe case of diminishing return in available power. However, under the same simulation conditions, the dynamic and fixed tuning strategies may be insufficiently different and will likely recommend a similar maximum N_R value that is economically suitable for the Firth. More importantly, with the update of a more realistic turbine represen-

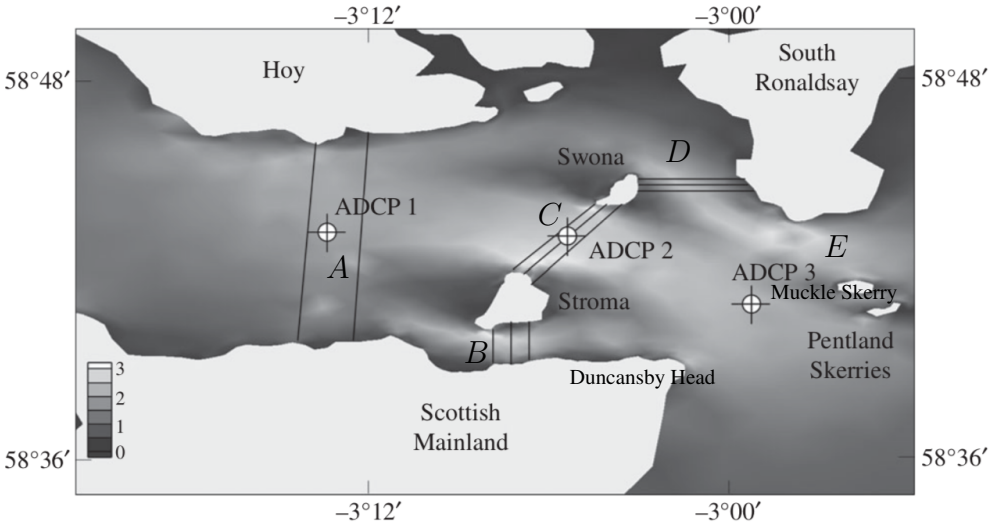

Figure B.1: Contours of M_2 major axis currents predicted by the depth-averaged numerical model adapted from Adcock et al. (2013). The locations of the turbine rows used in this study are indicated by solid lines.

tation, the significance of tuning may greatly reduce and the gain from the dynamic boost is expected to be limited to $\approx$ 1-2%. As such, the standard temporally-fixed tuning (impatient or fixed strategy) should still be used as the recommended operation strategy. In terms of physical site development, the negative effect to earlier developers after later additions of tidal arrays due to the diminishing return should also be less of a concern as this phenomenon is over-predicted by the actuator disc model when compared to the more realistic rotor.

B.2 Arrays spanning sub-channel(s) of the Pentland Firth

For the partially-blocked Pentland Firth (i.e. without completely blocking the entire width of the Pentland Firth — between one and three of the sub-channels B, C, D and E), $\overline{P}_{av}$ can be expected to increase with the implementation of a dynamic strategy due to the beneficial combination of the reversal and dynamic boost, but this increase may not be very substantial due to the moderate value of λ_0 at the site, categorising it as less of an inertia-dominated channel. The exact amount of dynamic boost will also vary with the array arrangement due to the different dynamics of the sub-channels and the inter-dependent nature of three of the sub-channels (Draper et al., 2014a,b). Similarly to the discussion in Section B.1, when replacing actuator discs with a more realistic turbine representation, the tidal rotors will not benefit as significantly with tuning for both fixed and dynamic strategies. Due to the smaller thrust applied to the flow leading to less flow disruption, it is likely that the potential downside of not collaborating between site developers in different sub-channels has been overestimated by the actuator disc, as the magnitude of potential interaction between turbines in different sub-channels may be smaller than suggested by Adcock et al. (2013) and Draper et al. (2014b). However, for this case, the general

finding that arrays in parallel perform better than arrays in series should still hold for both fixed and dynamic strategies (Garrett and Cummins, 2007).

B.3 Arrays spanning partial sub-channel(s) of the Pentland Firth

Given a realistic constraint on the number of turbines feasible for a project, it would be more effective to design a partial-width array for a sub-channel with the turbines packed tightly together in order to take advantage of performance enhancement from the increased local blockage effect. Adopting a dynamic strategy in this case may further support the choice of a densely packed partial-width array (referring to the conclusion that the importance of tuning increases with higher B_L), as such an arrangement can achieve higher performance enhancement with the dynamic and reversal boost, though the exact improvement will vary with different locations within the sub-channel.

It is critical to account for the variation in current velocities within the Pentland Firth so as to optimise the power output from small arrays. For partial-width arrays in the sub-channels, it is highly recommended for turbines to be packed towards locations that exhibit large current velocities, which include regions such as the shallow areas around the Swona and Stroma islands and near the headlands (e.g. Duncansby Head), as shown in Figure B.1. The currently approved four regions for development (see Figure 1 by Draper et al., 2014b) in the area of the Pentland Firth agree with the suggested locations found above. Additionally, as mentioned in Sections B.1 and B.2, it is also true here that both fixed and dynamic tuning are less important when a realistic turbine representation is used. As to which configuration is preferable in this case between parallel and series placement, it is likely to be highly dependent on the site geometry and flow dynamics as well as the proposed

number of turbines, as was the case with the Bohai Strait study in Chapter 3.

B.4 Resource assessment on the Pentland Firth

Previous work by Adcock et al. (2013) to determine the power resource within the Pentland Firth was carried out using only the highly idealised actuator disc model, which is likely to overestimate the resource potential. With the introduction of the more realistic turbine representation while maintaining the same array location and all configurations parameters, both the upper-bound power estimate of 1.9 GW across the entire Pentland Firth (three-row array extending across the width blocking 40% of the channel cross-section) and the range of power estimations for different cases of tidal arrays spanning one or more sub-channels, made in Adcock et al. (2013), can be possibly reduced by 30-40% using the correction factor suggested in Section 9.1.3. The appropriate correction factor will depend on a combination of the array configuration, turbine arrangement, as well as the channel dynamics of sub-channels and the complex interaction between the sub-channels. Whilst the revised estimates produce smaller values than the predictions determined using actuator discs, the tidal arrays are still able to deliver more power per turbine swept area than offshore wind farms around the UK. For example, after a conservative performance correction, a single-row array filling up to 40% of the Pentland Firth's cross-section delivers higher power per swept area than the upper-end calculation of offshore wind turbines (see Adcock et al., 2013); however, it is possible that the maximum number of turbine rows that is economically viable for the Pentland Firth may be reduced. Lastly, the reduction in power output when using the rotor can be partially compensated by the reduction in thrust on the flow, which reduces the significant changes to natural hydrodynamics and associated environmental impacts as suggested by Adcock et al. (2013).

Appendix C

Publications arising from this thesis

P1. Bonar, P. A. J., Chen, L., Schnabl, A. M., Venugopal, V., Borthwick, A. G. L. and Adcock, T. A. A. (2019), On the arrangement of tidal turbines in rough and oscillatory channel flow, *J. Fluid Mech.* [status: Published]

P2. Chen, L., Bonar, P.A.J., Vogel, C.R. and Adcock, T. A. A. (2019a), A note on the tuning of tidal turbines in channels, *J. Ocean Eng. and Mar. Energy* [status: Published]

P3. Chen, L., Bonar, P. A. J., and Adcock, T. A. A. (2018b), Design of a tidal turbine array for the Bohai Strait, China. *37th International Conference on Ocean, Offshore and Arctic Engineering, Madrid, Spain* [status: Published]

P4. Chen, L., Bonar, P. A. J., Vogel, C. R. and Adcock, T. A. A. (2019b), Local blockage effect of tidal stream turbines in channels modelled with a constrained blade element method. *38th International Conference on Ocean, Offshore and Arctic Engineering, Glasgow, UK* [status: Published]

P5. Chen, L., Bonar, P. A. J., Vogel, C. R. and Adcock, T. A. A., A note on dynamic tuning strategy in Channels [status: In preparation]

P6. Chen, L., Bonar, P. A. J., Vogel, C. R. and Adcock, T. A. A. (2018a), A basin-scale comparison of constrained BEM and actuator disc models. *6th Oxford Tidal Energy Workshop, Oxford, UK* [status: Published]